

Springer Water

Rasel Das
Bidyut Baran Saha *Editors*

Rapid Refrigeration and Water Protection

Next Generation Adsorbents

 Springer

Springer Water

Series Editor

Andrey Kostianoy, Russian Academy of Sciences, P. P. Shirshov Institute of Oceanology, Moscow, Russia

Editorial Board

Angela Carpenter, School of Earth & Environment, University of Leeds, Leeds, West Yorkshire, UK

Tamim Younos, Green Water-Infrastructure Academy, Blacksburg, VA, USA

Andrea Scozzari, Area della ricerca CNR di Pisa, CNR Institute of Geosciences and Earth Resources, Pisa, Italy

Stefano Vignudelli, CNR - Istituto di Biofisica, Pisa, Italy

Alexei Kouraev, LEGOS, Université de Toulouse, TOULOUSE CEDEX 9, France

The book series Springer Water comprises a broad portfolio of multi- and interdisciplinary scientific books, aiming at researchers, students, and everyone interested in water-related science. The series includes peer-reviewed monographs, edited volumes, textbooks, and conference proceedings. Its volumes combine all kinds of water-related research areas, such as: the movement, distribution and quality of fresh-water; water resources; the quality and pollution of water and its influence on health; the water industry including drinking water, wastewater, and desalination services and technologies; water history; as well as water management and the governmental, political, developmental, and ethical aspects of water.

More information about this series at <https://link.springer.com/bookseries/13419>

Rasel Das · Bidyut Baran Saha
Editors

Rapid Refrigeration and Water Protection

Next Generation Adsorbents

 Springer

Editors

Rasel Das
Department of Chemistry
Stony Brook University
Stony Brook, NY, USA

Bidyut Baran Saha
WPI-I2CNER
Kyushu University
Fukuoka, Japan

ISSN 2364-6934

ISSN 2364-8198 (electronic)

Springer Water

ISBN 978-3-030-93844-4

ISBN 978-3-030-93845-1 (eBook)

<https://doi.org/10.1007/978-3-030-93845-1>

© The Editor(s) (if applicable) and The Author(s), under exclusive license to Springer Nature Switzerland AG 2022

This work is subject to copyright. All rights are solely and exclusively licensed by the Publisher, whether the whole or part of the material is concerned, specifically the rights of translation, reprinting, reuse of illustrations, recitation, broadcasting, reproduction on microfilms or in any other physical way, and transmission or information storage and retrieval, electronic adaptation, computer software, or by similar or dissimilar methodology now known or hereafter developed.

The use of general descriptive names, registered names, trademarks, service marks, etc. in this publication does not imply, even in the absence of a specific statement, that such names are exempt from the relevant protective laws and regulations and therefore free for general use.

The publisher, the authors and the editors are safe to assume that the advice and information in this book are believed to be true and accurate at the date of publication. Neither the publisher nor the authors or the editors give a warranty, expressed or implied, with respect to the material contained herein or for any errors or omissions that may have been made. The publisher remains neutral with regard to jurisdictional claims in published maps and institutional affiliations.

This Springer imprint is published by the registered company Springer Nature Switzerland AG
The registered company address is: Gewerbestrasse 11, 6330 Cham, Switzerland

Preface

In this book, authors have discussed their experiences and how they changed our thoughts in understanding the fundamentals of adsorption-based rapid refrigeration and water purification systems. You will find experimental and theoretical knowledge that we hope will help you to overcome the research problems. Adsorbents have secured a special place in rapid refrigeration and pose huge advantages for ultra-grade water purification. Besides bulk adsorbents, various nanoadsorbent materials are of interest due to their nano-confinement effects, resulting in superior surface area, high reactivity, and other leapfrogging properties to build complex nanostructures. This book contains nine chapters in which Chap. 1 introduces the essential background of the book and covers a nutshell of all the chapters. Chapter 2 shows the synthesis technique to prepare silica gel-based high-quality consolidated adsorbents. Chapter 3 highlights new functional adsorbents and investigates their interactions with water under the adsorption desalination cycle's operating parameters. Chapter 4 represents the significance of specific heat capacity, detailed experimental procedure, and the parent materials at the operating temperature range of adsorption heat pump and adsorption desalination cycles. Chapter 5 focuses on atomic force microscopy, a recent characterization technique that uses nanoprobles to extract three-dimensional images of surfaces. The authors discuss two new adsorption methods in Chap. 6 to increase water harvesting from the atmosphere and heat and moisture recovery in ventilation systems. Chapter 7 presents thermochemical methods for powder-activated carbon preparation from abundant and cheap biomasses. Some crucial nanocarbon-based adsorbent materials for water purification are well corroborated in Chap. 8. Chapter 9 explores the potential applications of various nanoparticles-based adsorbents with special reference to nano zero-valent iron, iron oxide, titanium, alumina, and silica in the field of adsorptive removal of inorganic and organic pollutants from water. These nano adsorbents show good adsorption capacity, reaction rate, and competence for diverse pollutants removal.

Most of these book chapters are contributed by a collection of authors from different research groups worldwide including the USA, Japan, Bangladesh, Singapore, Republic of Korea, Russia, Malaysia, Australia, and India; mainly focused on

the uses of nanomaterial for adsorptive refrigeration and water treatment applications. It ensures a broad view of each topic, rather than reflecting the work of specific research groups. We are thankful to the authors who produced these preceding excellent chapters that will greatly benefit the potential readers interested in different adsorbents for rapid cooling/refrigeration and water purification applications.

New York, USA
Fukuoka, Japan

Rasel Das
Bidyut Baran Saha

Contents

1 Introduction	1
Rasel Das and Bidyut Baran Saha	
2 Towards the Development of Compact and High Efficiency Adsorption Heat Pumps	7
Md. Amirul Islam, Mahbubul Muttakin, Kaiser Ahmed Rocky, and Bidyut Baran Saha	
3 Synthesis and Characterization of Various MOFs and MOFs-Zeolite Composites: Water Adsorption and Rapid Cooling Production	29
Bo Han and Anutosh Chakraborty	
4 Specific Heat Capacity of Carbon-Based Composites for Adsorption Heat Pump and Desalination Applications	87
Kaiser Ahmed Rocky, Md. Amirul Islam, Animesh Pal, Bidyut Baran Saha, Hyun-Sig Kil, Seong-Ho Yoon, and Jin Miyawaki	
5 Characterizing Adsorbent Materials Employing Atomic Force Microscopy	113
Mujib L. Palash, Animesh Pal, Mir Shariful Islam, and Bidyut Baran Saha	
6 Advanced Adsorbents for Ecological Applications: Water Harvesting from the Atmosphere and Recuperation of Heat and Moisture in Ventilation Systems	133
Larisa G. Gordeeva and Yuri I. Aristov	
7 Thermochemical Conversion of Lignocellulosic Waste to Activated Carbon: A Potential Resource for Industrial Wastewater Treatment	153
Ahmed Elsayid Ali, Zaira Zaman Chowdhury, Abu Nasser Faisal, Rasel Das, Yasmin Abdul Wahab, and Seeram Ramakrishnan	

- 8 Carbon Nanomaterial-Based Adsorbents for Water Protection 193**
Umma Habiba and Tawsif Ahmed Siddique
- 9 Nanoparticles-Based Adsorbents for Water Pollutants Removal 237**
Ayushi Jain, Shweta Wadhawan, and S. K. Mehta

Chapter 1

Introduction



Rasel Das and Bidyut Baran Saha

Abstract This chapter defines common terms and discusses some fundamental concepts for adsorption-based refrigeration and water pollutants removal systems. It also summarizes important topics of every chapter that has been published in this book entitled, ‘Rapid Refrigeration and Water Protection—Next Generation Adsorbents.’

Keywords Adsorbent · Refrigeration · Water pollution

1.1 Background

The adsorbent is a mass-separating agent because of its capability to separate solutes present in the vapor and liquid phases or both phases to the solid matrices. This process can be expedited by choosing an appropriate adsorbent with desired physicochemical properties. For example, activated carbon, zeolite, silica gel, activated alumina, and other materials have been extensively used commercially for cooling [1], refrigeration [2], heat pump [3], desalination [4, 5], separation, and purification [6]. Adsorbents can be implemented in different columns or fixed-bed on continuous and/or discontinuous processes. Since the solutes have sufficient contact time with the sorbent in the discontinuous process, the adsorption is more favorable as compared with a discontinuous method. However, this is not true for all cases, especially in a situation where an adsorbent with a high-affinity binder is used for solutes adsorption.

R. Das (✉)

Department of Chemistry, Stony Brook University, Stony Brook NY11794-3400, USA
e-mail: raseldas@daad-alumni.de; rasel.das@stonybrook.edu

B. B. Saha

International Institute for Carbon-Neutral Energy Research (WPI-I2CNER), Kyushu University,
744 Motoooka, Nishi-ku, Fukuoka 819-0395, Japan
e-mail: saha.baran.bidyut.213@m.kyushu-u.ac.jp

Mechanical Engineering Department, Kyushu University, 744 Motoooka, Nishi-ku, Fukuoka
819-0395, Japan

The research and development of adsorption refrigeration system should be on material science and heat transfer enhancement techniques. For the former, synthesis of adsorbent materials having (i) adsorption of a large amount of adsorbate under low-temperature conditions typically below 100 °C, (ii) high packing density, (iii) high thermal conductivity, (iv) non-corrosive and non-toxic, and (v) low cost and widely available. Also, the adsorbent and adsorbate pairs should have broad uptake and offtake changes with a slight change of temperature. The reversibility of the process for many thousand cycles is also desired. The research efforts to find an alternative system for refrigeration application have been intensified worldwide since the imposition of international restrictions on production and use of refrigerants accountable for environmental degradation. Recently, the demand for adsorption refrigeration systems has also increased due to safeguarding the adverse environmental effects, resulting in additional consumption of electrical energy and ecological problems. The use of an adsorption system is considering as one of the promising alternatives. The adsorbent material's low heat and mass transfer coefficient is the main bottleneck of the adsorption refrigeration system, resulting in a large footprint and poor performance. The appropriate choice of adsorbent and design of adsorber/desorber beds with enhanced heat and mass transfer is essential to overcome this limitation. Figure 1.1 shows a schematic diagram of an anticipated adsorber/desorber heat exchanger with an enhanced heat transfer mechanism as listed below:

- a. Adsorbent should have a high thermal conductivity
- b. Reduced thermal contact resistance between adsorbent material and heat exchanger tube
- c. Good contact between heat exchanger tube and fin

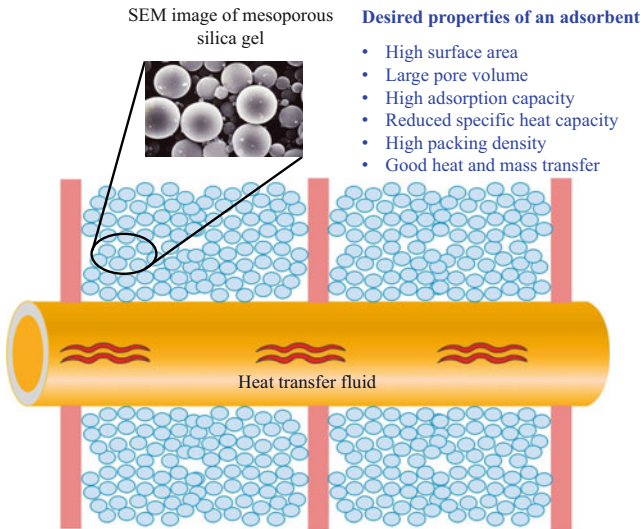


Fig. 1.1 Schematic of anticipated adsorber/desorber bed for refrigeration applications

- d. Reduced thermal contact resistance between adsorbent material and fin
- e. Optimized number of fin pieces
- f. Optimized fin height.

Besides securing these properties, special emphasis should be given to developing efficient, low-cost, thermally powered systems that will allow small (several watts) to largescale (a few 100 kW) capacity refrigeration systems.

For water purification, the adsorption process is typically better than the other methods such as filtration, catalysis, separations, and so on due to their highly porous networks, which typically ensure high removal efficiency. Different materials have different adsorption sites, and for example, carbon nanotube bundles typically have four types of adsorption sites, as shown in Fig. 1.2. Overall, there are four ways through which most of the nanoparticles adsorb pollutants that entail (a) water pollutants transport from the bulk solution to the external adsorbent surface, (b) film diffusion of the pollutant ions through the boundary around the surface, (c) migration of pollutants within the sorbent internal pores or intraparticle diffusion and (d) chemical interaction between pollutant ions and active sites of the sorbent.

Solutes can be adsorbed by either physisorption and/or chemisorption processes. The former one exists where intact electronic orbital remained, whereas the latter process occurs through electron transfer between the adsorbate and adsorbent, as shown in Fig. 1.3. Generally, physisorption is less selective and stable as compared with chemisorption. Equilibrium would be reached after adsorbing/absorbing sufficient amounts of pollutants or refrigerants. Adsorption isotherms commonly express this. Studying isotherms and reaction kinetics is especially important for an adsorbent's industrial application, from where one can measure the maximum adsorption capacity of a tested adsorbent. Different mathematical models, such as Langmuir, Freundlich, Halsey, Henderson, Smith, Elovich, Lagergren, and so on, can express these reaction behaviors [5].

Fig. 1.2 Schematic illustration of four possible adsorption sites of carbon nanotubes

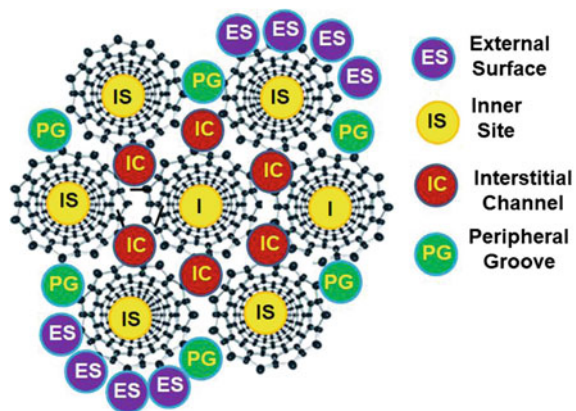
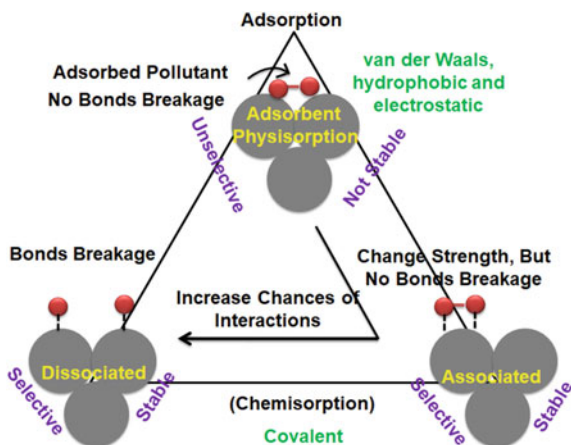


Fig. 1.3 Common adsorption forces that participate in adsorbent-adsorbate interactions



1.2 Conclusions

Various adsorbent materials are used for adsorption-based refrigeration as well as water purification. Studies are there to increase refrigeration and/or cooling performances of adsorbent materials, such as the requirement of low specific power, low mass transfer, and heat. Alternatively, pore size tuning, high surface area, and greater chemical reactivity are needed to ensure using various novel materials for water pollutants adsorption. In this book, authors from cross-disciplinary research fields are nicely evaluated and highlighted the properties of different adsorbent materials with a special focus on refrigeration and water purification processes.

Chapter 2 presents the synthesis technique to prepare silica gel-based high-quality consolidated adsorbents. This chapter provides a detailed comparison of numerous thermophysical parameters of parent silica gel and silica gel-based composite adsorbents. Finally, modeling studies are used to examine and optimize the performance of the adsorption cooling system. The aim of Chap. 3 is to create new functional adsorbents and investigate their interactions with water under the adsorption desalination cycle's operating parameters. The authors give a basic grasp of metal-organic frameworks (MOFs) synthesization and functionalization in this chapter. The hydrothermal reaction process is used to make a variety of MOFs. The porosities, thermal properties of original and modified MOFs/zeolite-MOF composite are characterized by X-ray diffraction, thermo-gravimetric analysis, scanning electron microscopy, and N_2 adsorption. Water uptake/offtake in an adsorption desalination system has also been studied under equilibrium and dynamic conditions. The following Chap. 4 presents the significance of specific heat capacity, detailed experimental procedure, and the cp of composites and the parent materials at the operating temperature range of adsorption heat pump (AHP) and adsorption desalination (AD) cycles. All of the experimentally measured data is thoroughly examined and correlated with the cp equations. The fitted parameters and the supplied experimental cp data are critical in designing

AHP and AD cycles. Chapter 5 focuses on Atomic Force Microscopy (AFM), a recent characterization technique that uses nanoprobes to extract three-dimensional (3-D) images of surfaces. These three-dimensional images include both qualitative and quantitative data. The authors provided a concise overview of image extraction strategies for various porous materials, including silica gel, activated carbon, along with quantitative analysis of the obtained images. The authors discuss two new adsorption methods in Chap. 6 to increase water harvesting from the atmosphere and heat and moisture recovery in ventilation systems. Both systems are open-type, and they may be analyzed as a whole by looking at a thermodynamic cycle of the process to account for different climatic circumstances. The authors proposed a nano-tailoring strategy for selecting or synthesizing improved adsorbents for atmospheric water harvesting and heat and moisture recovery in the ventilation systems.

Chapter 7 shows thermochemical methods for powder-activated carbon preparation from abundant and cheap biomasses. At the beginning of the chapter, the authors nicely illustrated different routes for thermochemical processing of lignocellulosic waste. Then, some of the simple pyrolysis reactors and the obtained products are highlighted. As a byproduct, some of the value-added products (bio-gases and bio-fuels) could be generated during pyrolysis, which is also shown in the chapter. The authors nicely tabulated most carbon activation processes such as physical activation, chemical activation, and physiochemical activation. They discuss some factors, gas flow rate and temperature, which directly affect activated carbon production. At the end of the chapter, the removal of both metallic and non-metallic water pollutants using this prepared activated carbon is demonstrated. Chapter 8 highlights some crucial nanocarbon-based adsorbent materials for water purification. At the beginning of their chapter, they discuss the fundamental of adsorption isotherms, which are essential to understand the adsorption phenomena at the atomic level. The highlighted carbon nanostructures are carbon nanotube, carbon nanofiber, graphene-family member, etc. They also tabulated many reinforcing materials such as polymers, nanoparticles (e.g., SiO_2 , Fe_3O_4 , MnO_2 , etc.), 2D nanosheets like MOS_2 , and other materials, which directly help to accelerate the rate of pollutants adsorption. The preparation methods of these nanocomposites are also well corroborated. Chapter 9 explores the potential applications of various nanoparticles-based adsorbents with special reference to nano zero-valent iron (NZVI), iron oxide, titanium, alumina, and silica in the field of adsorptive removal of inorganic and organic pollutants from water. These nano adsorbents show good adsorption capacity, reaction rate, and competence for diverse pollutants removal. The recyclability and reusability of some adsorbents are discussed. This chapter gives an overview of the progress and application of bare and functionalized metal and metal oxide nanoparticles for this purpose. Moreover, the mechanism of heavy metal ions, dyes, and organic chlorinated compounds removal by nanoparticles has also been discussed. The present chapter offers advanced information about the imperative characteristics of some metal and metal oxide-based nanoparticles and demonstrates their advantages as adsorbents in water remediation.

References

1. Ghazy M et al (2021) Performance enhancement of adsorption cooling cycle by pyrolysis of Maxsorb III activated carbon with ammonium carbonate. *Int J Refrig* 126:210–221
2. Ambarita H, Kawai H (2016) Experimental study on solar-powered adsorption refrigeration cycle with activated alumina and activated carbon as adsorbent. *Case Stud Thermal Eng* 7:36–46
3. Srivastava N, Eames I (1998) A review of adsorbents and adsorbates in solid–vapour adsorption heat pump systems. *Appl Therm Eng* 18(9–10):707–714
4. Mustafa MA et al (2019) Embedded high-hydrophobic CNMs prepared by CVD technique with PVDF-co-HFP membrane for application in water desalination by DCMD. *Desalin Water Treat* 142:37–48
5. Das R et al (2017) Recent advances in nanomaterials for water protection and monitoring. *Chem Soc Rev* 46(22):6946–7020
6. Das R et al (2020) High flux and adsorption based non-functionalized hexagonal boron nitride lamellar membrane for ultrafast water purification. *Chem Eng J*: 127721

Chapter 2

Towards the Development of Compact and High Efficiency Adsorption Heat Pumps



Md. Amirul Islam, Mahbul Muttakin, Kaiser Ahmed Rocky, and Bidyut Baran Saha

Abstract A set of thermal compressors (often referred to as adsorption beds) is employed in an adsorption heat pump (AHP) system to achieve the desired cooling, whereas electricity-driven compressors are used in a conventional vapor compression refrigeration system (VCRS). Although an AHP is much more environmentally friendly than VCRS, its massive size is one of the major hindrances towards its commercial application. The primary reason for this bulkiness is the huge amount of adsorbents that are being used in the adsorption beds. A remedy to this major flaw can be the use of composite adsorbents instead of loosely packed powders. Another colossal issue is the poor efficiency of this system which can be partially resolved by (i) proper selection of adsorbent, adsorbate, binder, thermal conductivity enhancer and optimizing their composition; (ii) applying optimum pressure in the consolidation process; (iii) determining the thermophysical properties of adsorbents to select the most suitable one, and (iv) ensuring efficient operation of the

Md. A. Islam · K. A. Rocky · B. B. Saha (✉)
International Institute for Carbon-Neutral Energy Research (WPI-I2CNER), Kyushu University,
744 Motoooka, Nishi-ku, Fukuoka 819-0395, Japan
e-mail: saha.baran.bidyut.213@m.kyushu-u.ac.jp

Md. A. Islam
e-mail: islam.md.amirul.240@m.kyushu-u.ac.jp; toha_apece@yahoo.com

K. A. Rocky
e-mail: kaiserrocky@du.ac.bd

Md. A. Islam
Department of Electrical and Electronic Engineering, Bangabandhu Sheikh Mujibur Rahman
Science & Technology University, Gopalganj 8100, Bangladesh

M. Muttakin
Department of Mechanical and Production Engineering, Ahsanullah University of Science and
Technology, Tejgaon, Dhaka 1208, Bangladesh
e-mail: muttakin.mpe@aust.edu

K. A. Rocky · B. B. Saha
Department of Mechanical Engineering, Kyushu University, 744 Motoooka, Nishi-ku, Fukuoka
819-0395, Japan

K. A. Rocky
Department of Physics, University of Dhaka, Dhaka Dhaka-1000., Bangladesh

© The Author(s), under exclusive license to Springer Nature Switzerland AG 2022
R. Das and B. B. Saha (eds.), *Rapid Refrigeration and Water Protection*,
Springer Water, https://doi.org/10.1007/978-3-030-93845-1_2

system by optimizing the duration of different recovery schemes. In this chapter, the synthesis technique to prepare silica gel-based high-quality consolidated adsorbents is demonstrated, a comparison of several thermophysical properties of the parent and composite adsorbents is presented, and finally, the system operation is investigated and optimized through simulation studies.

Keywords Adsorption · Consolidated adsorbent · Heat pump · MATLAB Simulation · Thermophysical properties

2.1 Introduction

Nowadays, heating, ventilation, air-conditioning, and refrigeration (HVAC&R) systems have become an integrated part of our daily life. The temperature must be maintained within a certain range for specific applications [1]. For example, fresh vegetables can be preserved between -5 and 15 °C, for fresh fish and meat, the temperature range is between -5 and 0 °C, long time preservation temperature for certain products including fish/meat is -30 to -20 °C [2, 3], the data centers require less than 20 °C to prevent damage of the servers and equipment [4]. An air-conditioning unit is usually operated between 20 and 25 °C to attain thermal comfort; industries, and chemical factories require a certain level of cooling/heating to manufacture their products; power generation plants especially nuclear reactors require huge heat removal for smooth operation; automobiles interior is cooled/heated by burning the fuel. Conventional cooling systems suffer from various issues such as fossil fuel-based energy consumption, which is indirectly responsible for global warming. Besides, high-GWP (high global warming potential) refrigerants used in the system directly contribute to global warming due to leakage or during the disposal of the system after its lifetime [5]. Researchers are earnestly trying to replace conventional cooling systems with alternative technologies such as an adsorption cooling system (ACS). These ACSs are far better than the traditional coolers in terms of electricity consumption (<90%), environmentally benign refrigerant usage, low-temperature waste heat utilization, longer lifetime (~3 times), lower maintenance requirement and so on. However, these systems also have some major drawbacks, such as, bulkiness, being expensive, having a low thermal coefficient of performance (COP), and having insufficient data about the working pairs [6]. Numerous researchers investigated the feasibility of building a compact system by consolidating the adsorbent by compressing and adding binders. In order to enhance the performance of the ACS, thermally conductive materials are also added. Bauer et al. [7] prepared zeolite/aluminum composites. They found that alteration of the structure by using hydrophilic materials can reduce the mass of adsorbent by a factor of 4. Besides, kinetics, specific cooling power (SCP), COP, and thermal behavior also improve. El-Sharkawy et al. [8] studied activated carbon-based composites by mixing Maxsorb III with expanded graphite of type EC500 as thermal conductivity enhancer and polyvinyl alcohol (PVA) as a binder at various compositions. According to their results, the packing density of the composite adsorbent (50% Maxsorb III, 40% EG, 10% PVA) is 11 times higher than the powder adsorbent, and the thermal conductivity

is 8 times. Pal et al. [9, 10] investigated various composites made with the adsorbent Maxsorb III, binder PVA, and thermal conductivity enhancer expanded graphite and graphene nanoplatelets. They found up to 23.5 times thermal conductivity improvement along with 23% volumetric uptake capacity increase. Younes et al. [11] synthesized silica gel-based consolidated composite with four types of binder hydroxyethyl cellulose (HEC), PVA, polyvinylpyrrolidone (PVP), and gelatin at various compositions. Their results show up to 32% thermal conductivity enhancement. Since the amount of binder is small, there was no compromise on net uptake. Despite that, there was 12.5% volumetric uptake improvement than the parent silica gel powder.

Thermophysical and adsorption characteristics changes due to the consolidation. Researchers have reported many important properties of consolidated adsorbents such as specific heat capacity, thermal conductivity, thermal diffusivity, packing density, net adsorption uptake, volumetric adsorption uptake, adsorption kinetics, and so on [11–19]. It is infeasible to build adsorption cooling systems by employing all these parent and composite adsorbents to determine the actual system performances. Therefore, computer programs are designed to simulate the operation of an actual adsorption cooling system. Cho and Kim [20] modeled the operation of a two bed silica gel–water adsorption chiller. But their model did not include the heat and mass recovery processes. However, these processes were included in several other models [21, 22], and the performance of the chiller was also investigated in those models. One of the major objectives of this chapter is to utilize a similar model in order to investigate the performance of an adsorption-based cooling system that uses (i) silica gel powder and (ii) silica gel powder +2 wt% PVP (composite) as adsorbent materials. Such an investigation indicates whether or not the use of this composite material as an adsorbent of such a cooling system is justified.

2.2 Methodology to Develop Composite Adsorbents

Adsorbent materials are considered as the core element of an adsorption heat pump. The widely used adsorbents, namely silica gel (SG), zeolite, activated carbon (AC), and metal–organic framework (MOF), all have a high surface area and pore volume that result in high adsorption capacity of refrigerants. However, these materials are commonly used in powdered form and possess low packing density and heat transfer coefficient, which in turn cause the system to be bulky and poor heat transfer in adsorption bed. Consolidation of the adsorbents may improve the packing density as well thermal conductivity because through the process of consolidation, the particles of the adsorbents are brought closer to each other, and the thermal resistance, thus, gets reduced. Nevertheless, most of the adsorbents are dispersive in nature and cannot be consolidated by applying only pressure. In effect, nowadays, researchers are focusing on the development of consolidated composite adsorbents. Here, the binder material is mixed with adsorbent material to make it solid form, which will result in improved packing density and heat transfer. Besides, thermally conductive materials are also added with adsorbent and binder to enhance the packing density and thermal conductivity significantly. However, binders and thermal conductivity

enhancers (TCE) have almost no adsorption capacity. One strong positive point is that consolidated composite adsorbent contributes to the improvement of volumetric adsorption capacity, which would result in developing a compact system. Thus, the selection of suitable binders and TCE will play a vital role in the synthesis of composite adsorbents. PVA, PVP, HEC, polytetrafluoroethylene (PTFE), gelatin, polymerized ionic liquid (PIL), etc., are the widely used binders. On the other hand, expanded graphite (EG), graphene nanoplatelets (GNPs), carbon nanotube (CNT), zinc oxide, boron nitride, etc., are considered as promising TCEs.

Sharkawy et al. [8] and Pal et al. [9] developed consolidated composite adsorbents employing AC of type Maxsorb III as a parent adsorbent, EG of type EC-500 as a TCE and PVA as a binder for ethanol and CO₂ adsorption, respectively. They showed that their developed composite have 2.2 and 11 times higher packing density and thermal conductivity, respectively than that of parent Maxsorb III. Zheng et al. [23] synthesized a highly conductive compact composite by combining SG with sulfuric acid-treated EG and showed that the consolidated composite exhibits 270 times higher thermal conductivity than that of parent SG. Pal et al. [10, 24] also developed AC–GNPs–PVA based composites for ethanol and CO₂ adsorption. Here, the authors reported that their fabricated composite possesses 3.2 times higher packing density and 23.5 times higher thermal conductivity than that of parent AC. Besides, the composite exhibits 23% enhancement of effective volumetric adsorption uptake of ethanol. Sharafian et al. [12] synthesized SG–PVP composite for adsorption cooling system applications, which results in 78.6% higher thermal conductivity than that of dry SG. Besides, several researchers developed composite adsorbents employing PTFE [25], HEC [26], PIL [13, 27] as a binder to improve packing density, thermal conductivity, and volumetric adsorption capacity. Moreover, Younes et al. [11] performed a comparative study among the SG-based composites developed using four types of binders, namely HEC, PVA, PVP, and gelatin. Here, the authors showed that SG–PVP composite exhibits 32% higher thermal conductivity and 12.5% higher volumetric adsorption uptake than that of parent SG.

Some of the thermophysical properties of promising binders and TCEs are summarized in Table 2.1.

Synthesis of consolidated composite adsorbents draws special attention for developing a compact and efficient AHP. There are two processes to synthesize composite adsorbents—(i) chemical process, (ii) physical mixing process.

In the chemical process, a chemical reaction occurs at any of the steps of the synthesis. Several researchers synthesized composite adsorbents by a chemical process. Zheng et al. [33] developed an activated carbon fiber composite by chemically activating a phenolic precursor on a glass fiber substrate using ZnCl₂ as the catalyst. Sukhyy et al. [34] fabricated silica gel–sodium sulphate composites from Na₂SO₄, tetraethoxysilane, hydrochloric acid, and ethanol employing the sol–gel method. Palash et al. [35] synthesized MOF composite by doping metallic ions in parent MOF. Besides, several notable researches regarding the synthesis of composite adsorbents can be found elsewhere [36–39].

In the physical mixing process, after the suitable heat treatment of the constituent elements of a composite, the elements are mixed physically in such a way that

Table 2.1 Thermophysical properties of promising binders and thermal conductivity enhancers

Type	Material	Short name	Surface area (m ² g ⁻¹)	Total pore volume (cm ³ g ⁻¹)	Specific heat capacity* (kJ kg ⁻¹ K ⁻¹)
Binder	Hydroxyethyl cellulose	HEC	117 [11]	0.104 [11]	–
	Polyvinyl alcohol	PVA	125 [11]	0.104 [11]	1.428 [16]
	Polyvinyl pyrrolidone	PVP	148 [11]	0.125 [11]	1.220 [16]
	Polytetrafluoroethylene	PTFE	11.67 [28]	–	0.926 [29]
	Gelatin	Gelatin	126 [11]	0.108 [11]	2.25 [30]
	Poly vinylbenzyltrimethyl ammonium alanate	Poly[VBTMA] [Ala]	–	–	1.400
	Poly vinylbenzyltrimethyl ammonium serinate	Poly[VBTMA] [Ser]	–	–	1.187
TCE	Multiwalled carbon nanotube	MWCNT	640 [31]	1.151 [31]	0.878
	Graphene nanoplatelets	H25-GNPs	44 [32]	0.065 [32]	0.698 [16]
		C750-GNPs	777 [32]	1.097 [32]	0.860 [16]
	Expanded graphite	EC-100	–	–	0.775 [16]
		EC-500	99 [32]	0.002 [32]	0.757 [16]
EC-1500		–	–	0.738 [17]	

* At room temperature

the mixture will be uniform. Sometimes, researchers use the planetary ball milling process to obtain the homogenous distribution of the elements in a composite. The detailed synthesis procedure of composite adsorbents adopting a physical mixing process can be found in the literature [8, 27, 40–43].

In this study, a silica gel-based consolidated composite adsorbent has been synthesized employing physical mixing process. Here, the parent materials are RD type silica gel and PVP procured from Fuji Silysia Chemical Ltd., Japan, and Sigma-Aldrich Chemistry Co., USA, respectively. For developing a consolidated composite adsorbent, initially, SG powder is dried at 100 °C in a vacuum oven for 4 h to remove moisture. Meanwhile, a certain amount of PVP is added to water to make a viscous solution. After that, the dried SG and the viscous solution are mixed properly to get a homogeneous mixture. Hereafter, the mixture is placed in the compression chamber of a pressing machine and compressed at 10 MPa. This step results in a consolidated composite adsorbent. Finally, the consolidated composite is placed in a vacuum oven at 100 °C for 6 h to eliminate water content. Figure 2.1 shows the steps involved in the synthesis of SG-PVP composite. The dry mass of the composite is 0.30 g, where SG holds 98wt% of the total mass and PVP possesses the remaining 2wt%. The diameter of the pellet shape composite is 17 mm, and thickness is 1.45 mm.

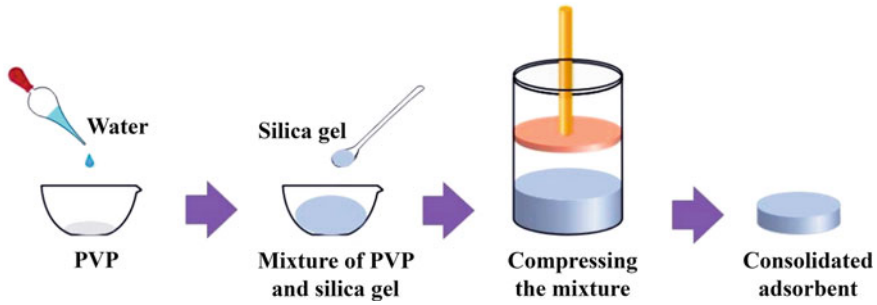


Fig. 2.1 Synthesis of silica gel and PVP-based consolidated composite adsorbent

2.3 Thermophysical Characterization

An ideal adsorbent has a high surface area, large pore volume, high thermal conductivity/diffusivity. When an adsorbent is consolidated, some properties change positively, and some of them are altered to the negative direction of the expectation. For example, the surface area change after the consolidation is negligible. However, the addition of binders affects the adsorption uptake. The uptake of per unit mass of the adsorbent is lower after consolidation, since the contribution of binders in adsorption is negligible. However, the volumetric uptake increases tremendously since a larger amount of adsorbent can be accommodated in a smaller volume. Contrarily, the thermal conductivity increases with the packing density due to the closeness of the adsorbent particles. Since very high packing density causes the adsorption kinetics to become slower, the degree of compactness should be optimized for better results.

2.3.1 Specific Heat Capacity

Calorimetric method is the most employed technique to measure the specific heat capacity of any substance. Figure 2.2 shows the basic components of a heat flux type differential scanning calorimetry (DSC) apparatus. The basic principle is that the reference and sample are heated at a constant temperature increment rate. The empty reference crucible requires less amount of heat to maintain the temperature increment rate than the crucible with the sample. The power consumption of each side is recorded. Therefore, the specific heat capacity of the target material can be assessed from Eqs. (2.1) and (2.2) based on three measurements (baseline, standard sample, and target sample) [44].

$$c_p = \frac{\text{Signal difference (sample - baseline)}}{\text{Sample mass} \times \text{Heating rate} \times \text{Sensitivity}} \quad (2.1)$$

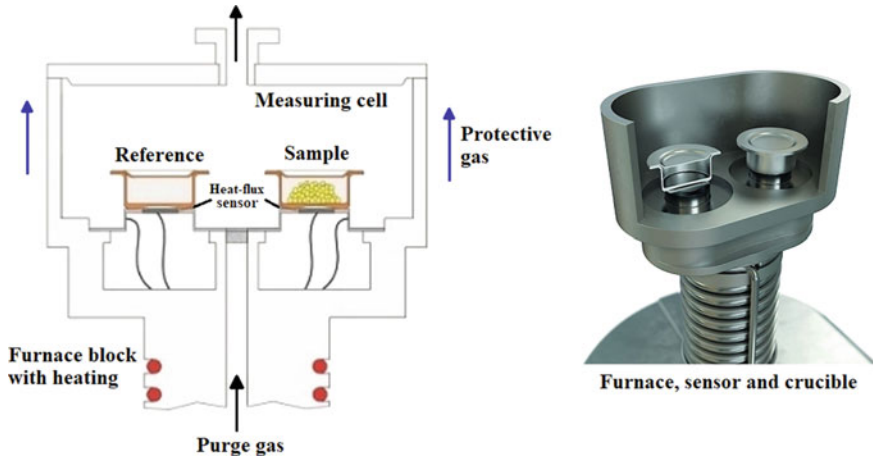


Fig. 2.2 Illustration of working principle of the DSC apparatus [44]

where,

$$\text{Sensitivity} = \frac{\text{Signal difference (standard} - \text{baseline)}}{\text{Mass (standard)} \times \text{Heating rate} \times \text{theoretical } C_p(\text{standard})} \quad (2.2)$$

2.3.2 Thermal Conductivity and Thermal Diffusivity

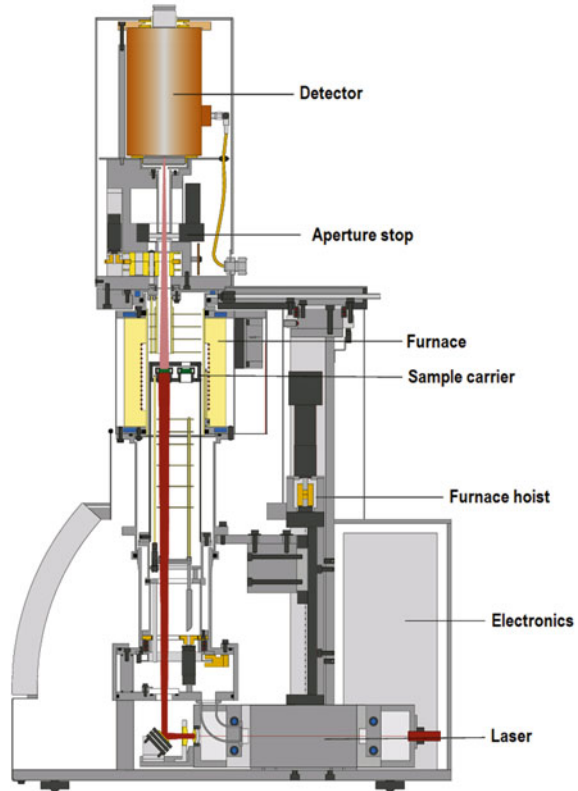
An advanced apparatus designed by NETZSCH is employed to measure the thermal diffusivity of the solid samples. The apparatus is named laser flash analyzer (LFA), and the schematic is shown in Fig. 2.3. The LFA technique is a fast, non-destructive, and non-contact method to determine thermal diffusivity. A short energy light pulse is applied on the front surface (surface and pulse are perpendiculars) of the sample (Fig. 2.4). The resulting temperature emission from the rear face is measured with an infrared (IR) detector. Thermal conductivity can be determined from the Eq. (2.3).

$$\lambda(T) = a(T) \times C_p(T) \times \rho \quad (2.3)$$

Here,

- λ Thermal conductivity [$\text{W m}^{-1} \text{K}^{-1}$].
- a Thermal diffusivity [$\text{m}^2 \text{s}^{-1}$].
- C_p Specific heat capacity [$\text{J kg}^{-1} \text{K}^{-1}$].
- ρ Packing density [kg m^{-3}].

Fig. 2.3 Laser flash analyzer (NETZSCH LFA 457) apparatus for thermal diffusivity measurement [45]



2.3.3 Porous Properties Measurement

Surface area, pore volume, and pore width are the most significant properties of an adsorbent. These properties are determined by the volumetric method with N_2 gas adsorption at 77 K temperature (boiling point Nitrogen). The internal schematic of the porous properties' measurement apparatus is shown in Fig. 2.5. The basic principle is that the vapor adsorbate is brought into contact with the solid adsorbent. Hence, the adsorbent pores soak a part of the adsorbate, and the rest remains attached to the outer surface of the adsorbent. It is assumed that physisorption occurs between the adsorbate and adsorbent where a weak Van der Waals attraction force exists.

2.3.3.1 BET Surface Area

Brunauer, Emmett and Teller (BET) is the most common method used to describe the specific surface area. The equation can be written as follows:

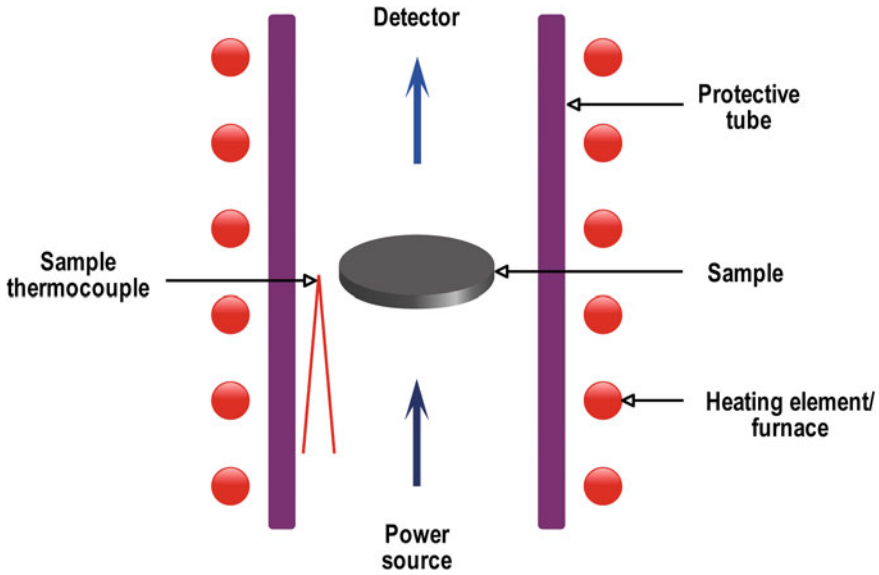


Fig. 2.4 Laser flash technique to measure thermal diffusivity

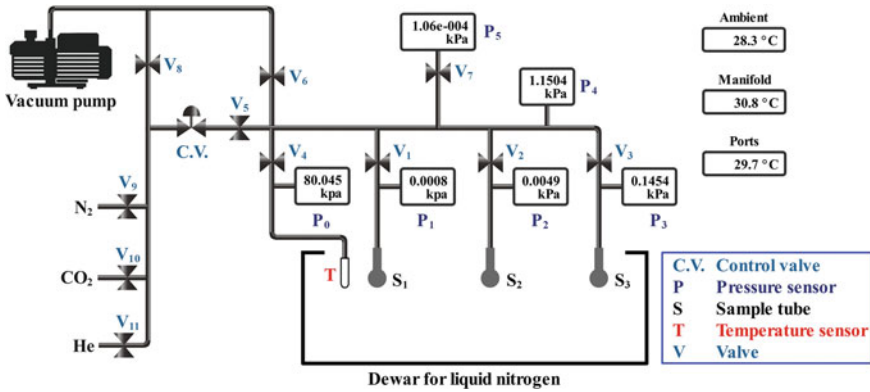


Fig. 2.5 Schematic of porous properties measurement apparatus (Micromeritics 3FLEX) [46]

$$\frac{1}{W \left(\left(\frac{P_0}{P} \right) - 1 \right)} = \frac{1}{W_m C} + \frac{C - 1}{W_m C} \left(\frac{P}{P_0} \right) \tag{2.4}$$

where,

- W weight of adsorbed gas.
- P/P_0 relative pressure.
- W_m adsorbate weight as monolayer.

C BET constant.

The BET Eq. (2.4) requires a linear plot of $\frac{1}{w\left(\left(\frac{P_0}{P}\right)-1\right)}$ versus $\frac{P}{P_0}$ where the slope (s), intercept (i), with y-axis and weight of monolayer (W_m) can be written as Eqs. (2.5), (2.6), and (2.7), respectively.

$$s = \frac{C - 1}{W_m C} \quad (2.5)$$

$$i = \frac{1}{W_m C} \quad (2.6)$$

$$W_m = \frac{1}{s + i} \quad (2.7)$$

Total surface area (S_t) can then be derived from Eq. (2.8),

$$S_t = \frac{W_m N A_{cs}}{M} \quad (2.8)$$

where,

N Avogadro's number (6.023×10^{23}).

M Molecular weight of adsorbate.

A_{cs} Cross sectional area of adsorbate (16.2 \AA^2 for Nitrogen).

Specific surface area is then determined by dividing the total surface area by sample weight:

$$S = \frac{S_t}{w} \quad (2.9)$$

2.3.3.2 Pore Volume

Total pore volume can be estimated from the amount of vapor adsorbed at a relative temperature close to unity (assuming pores are filled with liquid adsorbate). A mathematical expression can be written as Eq. (2.10),

$$V_{liq} = \frac{P_a V_{ads} V_m}{R T} \quad (2.10)$$

where,

V_{ads} volume of adsorbed gas.

V_{liq} volume of liquid N_2 in pores.

V_m molar volume liquid adsorbate.

P_a ambient pressure.

T ambient temperature.

R universal gas constant.

2.3.3.3 Pore Radius

The average pore size can be estimated from the pore volume by Eq. (2.11). In this case, the pore geometry is considered as cylindrical (type A hysteresis).

$$r_p = \frac{2V_{liq}}{S} \quad (2.11)$$

2.3.4 Summarization of Thermophysical Properties

Table 2.2 shows the variation of the thermophysical properties of some silica gel-based composite samples [11]. Their results clearly indicate that the change of surface area and total pore volume is not so significant; still, the increment in thermal conductivity and thermal diffusivity are substantial.

2.4 Computer Simulations

The consolidation of SGP with 2 wt% PVP certainly improves its volumetric uptake capacity. However, on the other hand, it loses its equilibrium uptake capacity as PVP does not contribute to the adsorption process. The rate of adsorption, i.e., the kinetics, also deteriorates with the consolidation. Hence, the combined effects of all these parameters need to be investigated, and this is accomplished through simulation studies. A MATLAB model that simulates the operation of an adsorption chiller, employing mass and heat recovery schemes, is utilized to serve this purpose.

A typical adsorption chiller contains two beds filled with an adsorbent material. Each bed goes through (i) adsorption/desorption, (ii) mass recovery, and (iii) heat recovery processes. The operation cycle time may be defined as the total time required by all these processes. A detailed description of all these processes, including their model equations, can be found in literature [21]. In the present investigation, the same mathematical model is used to compare the performance of two types of adsorbents—(i) SGP and (ii) SGP with 2% PVP. In the previous study [21], granular particles of silica gel were used as the adsorbent material. It is further assumed in this study that the adsorber beds are of the same type as described in the previous investigation.

Table 2.2 Thermophysical properties of the consolidated samples [11]

Composition (wt%)	Packing density (kg m ⁻³)	Total surface area (m ² g ⁻¹)	Total pore volume (cm ³ g ⁻¹)	Thermal conductivity (W m ⁻¹ K ⁻¹)	Thermal diffusivity (m ² s ⁻¹)
Parent silica gel powder 100%	810	601 ± 15	0.284	0.119	1.60 × 10 ⁻⁷
SGP 98%, PVA 2%	~900	576 ± 13	0.272	0.145	1.74 × 10 ⁻⁷
SGP 95%, PVA 5%	~900	548 ± 12	0.253	–	–
SGP 90%, PVA 10%	~900	493 ± 15	0.234	–	–
SGP 98%, PVP 2%	~900	572 ± 12	0.274	0.158	1.88 × 10 ⁻⁷
SGP 95%, PVP 5%	~900	558 ± 12	0.262	–	–
SGP 93%, PVP 7%	~900	550 ± 11	0.257	–	–
SGP 90%, PVP 10%	~900	520 ± 12	0.252	–	–
SGP 98%, HEC 2%	834	570 ± 15	0.265	–	–
SGP 98%, HEC 2%	911	562 ± 15	0.266	0.157	1.88 × 10 ⁻⁷
SGP 98%, HEC 2%	949	564 ± 14	0.268	–	–
SGP 98%, HEC 2%	975	568 ± 13	0.268	–	–
SGP 95%, HEC 5%	~900	557 ± 12	0.257	–	–
SGP 98%, Gelatin 2%	~900	553 ± 13	0.254	0.157	1.88 × 10 ⁻⁷
SGP 95%, Gelatin 5%	~900	486 ± 14	0.230	–	–

SGP—Silica gel powder; PVA—Polyvinyl alcohol; HEC—Hydroxyethyl cellulose; PVP—Polyvinyl pyrrolidone

2.4.1 Isotherm Model

The maximum amount of adsorbate (water in the present investigation) that the unit mass of adsorbent can adsorb at a specified temperature is termed as equilibrium uptake. Several researchers presented different models, such as Dubinin-Astakhov (D-A) model, Dubinin-Raduskevich (D-R) model, Tóth model, Freundlich model, Saha, Boelman and Kashiwagi (S-B-K) model, etc., to mathematically determine this

equilibrium uptake values [6]. These models are known as isotherm models. In this investigation, Tóth model [47] is used to determine the vapor adsorption capacity of the two adsorbents at a particular temperature. The model equation is given below,

$$w^* = w_s \frac{bP}{[1 + (bP)^t]^{\frac{1}{t}}} \quad (2.12)$$

where w^* and w_s are the equilibrium uptake and saturation adsorption capacity, respectively; P is the equilibrium pressure; b and t are the adjustable parameters. The constant b can be determined by the following equation,

$$b = k_0 \exp\left(\frac{Q_{st}}{RT}\right) \quad (2.13)$$

where k_0 is the pre-exponential constant, Q_{st} is the isosteric heat of adsorption, R is the gas constant, and T denotes the adsorption temperature.

Younes et al. [11] experimentally investigated the adsorption of water vapor by both SGP and SGP + 2wt%PVP adsorbents. They fitted their experimental data with the Tóth model and determined the values of the constants of Eqs. (2.12) and (2.13). In our simulation studies, Tóth model is used to determine the equilibrium uptake capacity of both the adsorbents, and the values of the equation parameters (from literature [11]) are presented in Table 2.3.

2.4.2 Kinetics Model

It represents the rate of adsorption, which is also important as it determines the cycle time of the system. The commonly used kinetics models used by the scientists are the Langmuir model, linear driving force (LDF) model, Fickian diffusion (FD) model, semi-infinite model and so on [6]. In this investigation, LDF model is utilized to determine the rate of adsorption of water vapor by the adsorbents. The model assumes that the rate of adsorption at any point of time is proportional to the difference between the equilibrium uptake capacity and the uptake at that point of time. Mathematically it can be presented by,

Table 2.3 Tóth equation parameters for adsorption of water vapor by SGP and SGP + 2wt% PVP

Adsorbent	k_0 (kg kPa ⁻¹)	Q_{st} (kJ kg ⁻¹)	w_s (kg kg ⁻¹)	t (-)
SGP	1.1739×10^{-9}	2592	0.3	4.15
SGP + 2wt% PVP	1.2975×10^{-9}	2580	0.3	4.35

$$\frac{dw}{dt} = k_1[w * -w(t)] \quad (2.14)$$

where k_1 is the overall mass transfer coefficient. In the current study, both SGP and SGP + 2wt%PVP adsorbents are assumed to possess spherical shaped particles. Hence the value of k_1 can be determined by [48–50], $k_1 = \frac{15D_s}{R_p^2}$, where D_s is the diffusion time constant and R_p represents the particle radius. D_s depends on temperature, T , by the following relation,

$$D_s = D_{so} \exp\left(\frac{-E_a}{RT}\right) \quad (2.15)$$

where E_a represents the activation energy. Hence, the final form of Eq. (2.14) can be written as,

$$\frac{dw}{dt} = \frac{15D_{so}}{R_p^2} \left\{ \exp\left(\frac{-E_a}{RT}\right) \right\} (w * -w) \quad (2.16)$$

Younus et al. [11] determined the values of kinetics parameters for both SGP – water and SGP + 2wt% PVP—water pairs, and they are presented in Table 2.4.

As can be seen in Eq. (2.16), the adsorption rate is directly proportional to the value of D_{so}/R_p^2 . Furthermore, from Table 2.4, it is observed that D_{so}/R_p^2 decreases with the consolidation of SGP for synthesizing the composite adsorbent. Furthermore, a higher value of E_a is reported in the case of composite material as compared to SGP, which also contributes to the reduction of kinetics in SGP + 2%PVP—water pair. And based on the kinetics data alone, it can be opined that a reduced specific cooling capacity will be observed with the SGP + 2wt% PVP, when they will be used as the adsorbent material in an adsorption heat pump system, as compared to SGP.

On the other hand, due to the consolidation, the volumetric uptake of the adsorbent is improved by 12.5% [11]. Since PVP has no contribution to the adsorption of water vapor, we can state that a specific volume of space of an adsorption bed of the chiller can accommodate 12.5% more mass of SGP, as in the case of composite adsorbent. This will eventually increase the uptake and will contribute to the enhancement of the cooling capacity of the chiller. So, the cumulative effects of reduction of kinetics and improvement of volumetric efficiency on the performance of chiller are investigated in the present article through simulation studies.

Table 2.4 LDF parameters for adsorption of water vapor by SGP and SGP with 2 wt% PVP

Adsorbent	D_{so}/R_p^2 (s ⁻¹)	E_a (kJ kg ⁻¹)
SGP	3.56×10^{-3}	434.2
SGP + 2wt% PVP	3.13×10^{-3}	442.8

2.4.3 Energy Balance Equation and Chiller Specification

A typical adsorption chiller consists of two adsorption beds, one evaporator, and one condenser. During adsorption/desorption stage, one bed goes through adsorption, and desorption occurs in the other bed. The hot water and cold water flow through the tubes of the desorbing and adsorbing beds, respectively, which in turn heat or cool the fins of the heat exchangers. Again, heat transfer between these fins and the adsorbent materials takes place as the adsorbents are packed between these fins Fig. 2.6.

On the other hand, evaporation and condensation of the refrigerant take place in the evaporator and condenser, respectively. The incoming chilled water transfers its heat to the evaporating water. And cold water from the exit of the adsorber bed enters the condenser and causes the condensation of the refrigerant vapor. The energy balance equation for all the components and different stages of operation can be generalized as,

$$[MC_p]_{H.Ex} \frac{dT_k}{dt} = M_{bed} h_{ads} \frac{dw}{dt} + [\dot{m} C_p (T_{in} - T_{out})]_{H.Ex.fluid} \quad (2.17)$$

where subscript k stands for different components of the chiller, i.e., adsorbing/desorbing bed, evaporator or condenser; subscripts $H.Ex$ and $H.Ex.fluid$ represent heat exchanger and heat transfer fluid, respectively. The left-hand side of the equation indicates the rate of change of enthalpy of the component k . For the adsorption bed, the thermal mass MC_p includes the thermal masses of tubes, fins, as well as, adsorbents. As reported in literatures [11, 14], the specific heat capacity, C_p , of SGP is $918.2 \text{ J kg}^{-1} \text{ K}^{-1}$, and that of SGP + 2wt% PVP is $933.8 \text{ J kg}^{-1} \text{ K}^{-1}$. Thus, the thermal mass of the adsorbent is increased as both specific heat and mass (by 12.5%) are increased due to consolidation, and this contributes to the enhancement of the performance of the chiller.

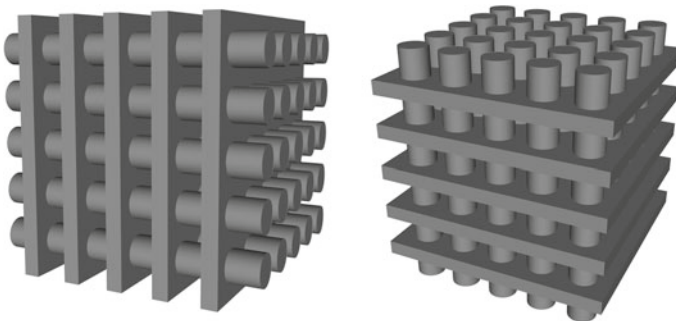


Fig. 2.6 The side view and top view of a commonly used finned tube type heat exchanger in an adsorption bed

Again, since M_{bed} stands for the mass of adsorbent used in each bed, the total amount of heat released or absorbed in each bed during adsorption or desorption is represented by the first term of the right-hand side. And from the last term, the outlet temperature, T_{out} , of the heat transfer fluid, i.e., chilled water, cooling water, or hot water, can be determined after its sensible heat transfer with the respective component.

A detailed description of all the components of the chiller and their respective model equations can be found in literature [21, 22]. Furthermore, in the present investigation, the same specifications of the chiller, as used in literature [21], are assumed to be applicable for both the adsorbents under consideration, and they are presented in Table 2.5.

The specifications of chiller necessarily remain the same for both SGP—water and SGP + 2wt% PVP—water pairs. But for the composite adsorbent, 12.5% more mass is considered in the investigation as compared to the parent SGP adsorbent.

Table 2.5 Specifications of the different components of the chiller used in the modelling

<i>Ad/desorber bed</i>	
Number of modules, N_m	10
Length of each module, L_m	3.65 m
Tube material	Copper
Number of tubes in each module, N_t	3
Outside diameter of tube, $D_{m,o}$	16.6 mm
Inside diameter of tube, $D_{m,i}$	15 mm
Fin material	Aluminium
Number of fins in each module, N_f	3310
Length of fin, L_f	342 mm
Height of fin, H_f	30 mm
Width of fin, W_f	0.105 mm
<i>Evaporator</i>	
Tube material	Copper
Number of tubes, $N_{t,evap}$	115
Length of tube, $L_{t,evap}$	3.9 m
Mass per tube, $M_{t,evap}$	1.4 kg
Inner diameter of tube, $D_{e,i}$	17.65 mm
<i>Condenser</i>	
Tube material	Copper
Number of tubes, $N_{t,cond}$	220
Length of tube, $L_{t,cond}$	2.65 m
Mass per tube, $M_{t,cond}$	0.96 kg
Inner diameter of tube, $D_{e,i}$	17.65 mm

2.4.4 Specific Cooling Capacity and Coefficient of Performance

The specific cooling capacity, Q_c , is defined as the cooling effect produced by the chiller and can be determined by,

$$Q_c = \frac{\int_0^{t_{cycle}} \dot{m}_{ch} C_{p,ch} (T_{in,ch} - T_{out,ch}) dt}{t_{cycle}} \quad (2.18)$$

where t_{cycle} is the operation cycle time considered, and subscript ch represents chilled water. The SI unit of Q_c is kW. Another commonly used unit is ‘Ton of refrigeration (TR)’, which relates to kW by, $TR = 3.517$ kW.

The coefficient of performance (COP) indicates the efficiency of the chiller. It is defined as the ratio of the cooling effect produced to the energy input to the chiller. In an adsorption chiller, heat is the principal form of energy, provided as input to the chiller through the hot water circulation. Thus, the amount of energy input can be calculated by,

$$Q_h = \frac{\int_0^{t_{cycle}} \dot{m}_{hot} C_{p,hot} (T_{in,hot} - T_{out,hot}) dt}{t_{cycle}} \quad (2.19)$$

where hot represents hot water. Hence COP can be expressed as,

$$COP = \frac{Q_c}{Q_h - Q_{rec}} \quad (2.20)$$

where Q_{rec} is the amount of heat energy saved due to the inclusion of the heat recovery process. It needs mentioning that during the heat recovery stage, there is no cooling effect produced by the chiller, but this stage can significantly improve the COP , as can be seen from Eq. (2.20). Hence the optimum duration of the heat recovery stage needs to be carefully determined in order to obtain a higher COP at the minimum cost of cooling capacity.

2.4.5 Simulation Results and Discussion

The simulation studies are carried out for both SGP—water and SGP + 2wt% PVP—water pairs. As observed in Table 2.5, the value of D_{so}/R_p^2 for both the cases is of the order of 10^{-3} , which is 10^7 orders less than that of the RD (regular density) silica gel, as can be seen in literature [51]. Due to this poor kinetics of the adsorbents under consideration, the operation cycle time, t_{cycle} , of the chiller needs to be sufficiently

high in order to achieve around 80% of the equilibrium uptake and a moderately high coefficient of performance. In the current investigation, a cycle time of 745 s is considered, of which 700 s is for ad/desorption stage, 30 s is spent for mass recovery, and 15 s is the duration of heat recovery stage.

The specific cooling capacity of the chiller is then determined for both the adsorbent-adsorbate pairs, and the result is depicted in Fig. 2.7. It is observed that a reduced cooling capacity is observed in the case of composite adsorbent, although a 12.5% higher mass can participate in the adsorption/desorption process, as compared to the parent SGP adsorbent. Hence, the decrease in equilibrium uptake and kinetics parameters due to consolidation are playing the dominant role here. The average chilling capacities obtained with SGP and SGP + 2wt% PVP adsorbents are 7.32 TR and 6.88 TR, respectively, at COP of 0.52 and 0.48, respectively. Simulation results further indicate that an enhancement of 23% in the volumetric uptake capacity of the composite as compared to that of the parent SGP could produce a similar cooling capacity as demonstrated with the parent SGP. Results show that a composite with 23% improved volumetric uptake would produce a cooling capacity of 7.33 TR at a COP of 0.48. It needs mentioning that, apart from the increased mass of adsorbent for the composite, all other parameters (e.g., specific heat capacity, isotherm, and kinetics parameters) are assumed to be the same as those used for SGP + 2wt% PVP.

Thus, based on the reported isotherm and kinetics data [11], it can be opined that a 12.5% increase in volumetric efficiency and a nominal increase in the specific heat capacity are not sufficient enough to employ this composite as the primary adsorbent material in an adsorption chiller. Because it demonstrates a poorer performance in terms of both, cooling capacity and COP when compared to parent SGP.

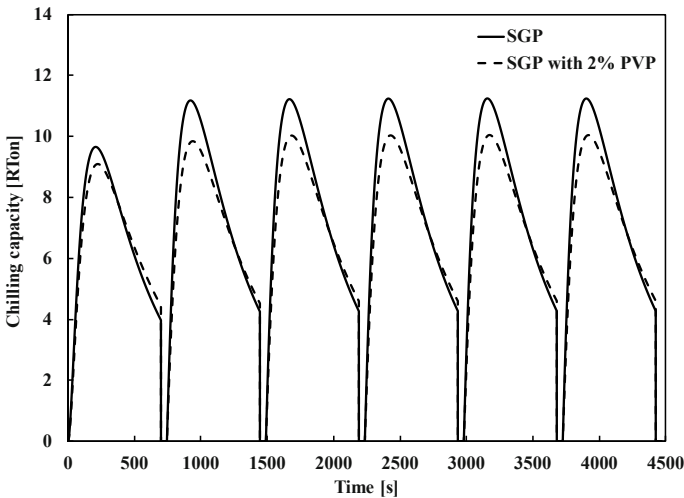


Fig. 2.7 Instantaneous chilling capacity of the chiller operating with SGP and SGP + 2wt% PVP

2.5 Conclusions

In this chapter, the synthesis of consolidated adsorbent and thermophysical properties improvement/measurement techniques is focused. Moreover, a mathematical model is utilized to simulate the performance of an actual cooling system with the synthesized composites. A nominal amount of binder (2 wt%) is required to consolidate the adsorbent (silica gel powder). Hence, there is no significant change in the net adsorption uptake and specific heat capacity. Besides, there is 32% improvement in the thermal conductivity and 12.5% increase in the volumetric uptake. However, the simulation results indicate that both chilling capacity and COP of the system decrease due to the consolidation. The reason is that a volumetric uptake of 12.5% is not enough to improve the system performance. The simulation results also suggest that the consolidation will enhance the system performance if the improvement in the volumetric uptake exceeds 23%, provided all other parameters for the composite remain the same.

References

1. Islam MA., Pal A, Kyaw T, Saha BB (2019) Study on performance and environmental impact of supermarket refrigeration system in japan, evergr. *Jt J Nov Carbon Resour Sci Green Asia Strateg*, 6:168–176. <https://doi.org/10.5109/2321014>
2. Liu D-K, Xu C-C, Guo C-X, Zhang X-X (2020) Sub-zero temperature preservation of fruits and vegetables: A review. *J Food Eng*, 275 109881. <https://doi.org/10.1016/j.jfoodeng.2019.109881>
3. Lonergan SM, Topel DG, Marple DN (2019) Fresh and cured meat processing and preservation. S.M. Lonergan, D.G. Topel, D.N.B.T.-T.S. of A.G. and M.T. (Second E. Marple (eds.). *Sci Anim Growth Meat Technol*, Elsevier, 205–228. <https://doi.org/10.1016/B978-0-12-815277-5.00013-5>
4. Ebrahimi K, Jones GF, Fleischer AS (2014) A review of data center cooling technology, operating conditions and the corresponding low-grade waste heat recovery opportunities. *Renew Sustain Energy Rev* 31:622–638. <https://doi.org/10.1016/j.rser.2013.12.007>
5. Islam MA, Saha BB (2020) TEWI assessment of conventional and solar powered cooling systems. In: H. Tyagi (Ed.). *Sol Energy*, Springer Nature Singapore Pte Ltd,147–177. https://doi.org/10.1007/978-981-15-0675-8_9
6. Islam MA (2019) Thermophysical and adsorption characterization of functional and pore modified adsorbents. Kyushu University. <http://hdl.handle.net/2324/2534480>
7. Bauer J, Herrmann R, Mittelbach W, Schwieger W (2009) Zeolite/aluminum composite adsorbents for application in adsorption refrigeration. *Int J Energy Res* 33:1233–1249. <https://doi.org/10.1002/er.1611>
8. El-Sharkawy II, Pal A, Miyazaki T, Saha BB, Koyama S (2016) A study on consolidated composite adsorbents for cooling application. *Appl Therm Eng* 98:1214–1220. <https://doi.org/10.1016/j.applthermaleng.2015.12.105>
9. Pal A, El-Sharkawy II, Saha BB, Jribi S, Miyazaki T, Koyama S (2016) Experimental investigation of CO2 adsorption onto a carbon based consolidated composite adsorbent for adsorption cooling application. *Appl Therm Eng* 109:304–311. <https://doi.org/10.1016/j.applthermaleng.2016.08.031>

10. Pal A, Uddin K, Thu K, Saha BB (2019) Activated carbon and graphene nanoplatelets based novel composite for performance enhancement of adsorption cooling cycle. *Energy Convers Manag* 180:134–148. <https://doi.org/10.1016/j.enconman.2018.10.092>
11. Younes MM, El-sharkawy II, Kabeel AE, Uddin K, Pal A, Mitra S, Thu K, Saha BB (2019) Synthesis and characterization of silica gel composite with polymer binders for adsorption cooling applications. *Int J Refrig* 98:161–170. <https://doi.org/10.1016/j.ijrefrig.2018.09.003>
12. Sharafian A, Fayazmanesh K, McCague C, Bahrami M (2014) Thermal conductivity and contact resistance of mesoporous silica gel adsorbents bound with polyvinylpyrrolidone in contact with a metallic substrate for adsorption cooling system applications. *Int J Heat Mass Transf* 79:64–71. <https://doi.org/10.1016/j.ijheatmasstransfer.2014.07.086>
13. Pal A, Shahrom MSR, Moniruzzaman M, Wilfred CD, Mitra S, Thu K, Saha BB (2017) Ionic liquid as a new binder for activated carbon based consolidated composite adsorbents. *Chem Eng J* 326:980–986. <https://doi.org/10.1016/j.cej.2017.06.031>
14. Islam MA, Pal A, Saha BB (2020) Experimental study on thermophysical and porous properties of silica gels. *Int J Refrig* 110:277–285. <https://doi.org/10.1016/j.ijrefrig.2019.10.027>
15. Jahan I, Islam MA, Palash ML, Rocky KA, Rupam TH, Saha BB (2021) Experimental study on the influence of metal doping on thermophysical properties of porous aluminum fumarate. *Heat Transf Eng*, 42. <https://doi.org/10.1080/01457632.2020.1777005>
16. Rocky KA, Islam MA, Pal A, Ghosh S, Thu K, Nasruddin, Saha BB (2020) Experimental investigation of the specific heat capacity of parent materials and composite adsorbents for adsorption heat pumps. *Appl Therm Eng*, 164:114431. <https://doi.org/10.1016/j.applthermaleng.2019.114431>
17. Uddin K, Islam MA, Mitra S, Lee J, Thu K, Saha BB, Koyama S (2018) Specific heat capacities of carbon-based adsorbents for adsorption heat pump application. *Appl Therm Eng*, 129:117–126. <https://doi.org/10.1016/j.applthermaleng.2017.09.057>
18. Aristov YI, Tokarev MM, Freni A, Glaznev IS, Restuccia G (2006) Kinetics of water adsorption on silica Fuji Davison RD. *Microporous Mesoporous Mater* 96:65–71. <https://doi.org/10.1016/j.micromeso.2006.06.008>
19. Chakraborty A, Saha BB, Aristov YI (2014) Dynamic behaviors of adsorption chiller: Effects of the silica gel grain size and layers. *Energy* 78:304–312. <https://doi.org/10.1016/j.energy.2014.10.015>
20. Cho S, Kim J (1992) Modeling of a silica Gel-water adsorption cooling system. *Energy* 17:829–839
21. Muttakin M, Ito K, Saha BB *Solar Thermal-Powered Adsorption Chiller*. Himanshu Tyagi Prodyut R. Chakraborty Satvasheel Powar, Springer, 117
22. Rezk ARM, Al-Dadah RK (2012) Physical and operating conditions effects on silica gel/water adsorption chiller performance. *Appl Energy* 89:142–149. <https://doi.org/10.1016/j.apenergy.2010.11.021>
23. Zheng X, Wang LW, Wang RZ, Ge TS, Ishugah TF (2014) Thermal conductivity, pore structure and adsorption performance of compact composite silica gel. *Int J Heat Mass Transf* 68:435–443. <https://doi.org/10.1016/j.ijheatmasstransfer.2013.09.075>
24. Pal A, Uddin K, Rocky KA, Thu K, Saha BB (2019) CO₂ adsorption onto activated carbon-graphene composite for cooling applications. *Int J Refrig*. <https://doi.org/10.1016/j.ijrefrig.2019.04.022>
25. Cacciola G, Restuccia G, Mercadante L (1995) Composites of activated carbon for refrigeration adsorption machines. *Carbon N Y* 33:1205–1210. [https://doi.org/10.1016/0008-6223\(95\)00051-E](https://doi.org/10.1016/0008-6223(95)00051-E)
26. Berdenova B, Pal A, Muttakin M, Mitra S, Thu K, Saha BB, Kaltayev A (2019) A comprehensive study to evaluate absolute uptake of carbon dioxide adsorption onto composite adsorbent. *Int J Refrig* 100:131–140. <https://doi.org/10.1016/j.ijrefrig.2019.01.014>
27. Rocky KA, Pal A, Moniruzzaman M, Saha BB. (2019) Adsorption characteristics and thermodynamic property fields of polymerized ionic liquid and polyvinyl alcohol based composite/CO₂ pairs. *J Mol Liq*, 111555. <https://doi.org/10.1016/j.molliq.2019.111555>

28. Graham D (1962) Physical adsorption on low energy solids. I. Adsorption of carbon tetrafluoride, argon, and nitrogen on polytetrafluoroethylene. *J Phys Chem*, 66 1815–1818. <https://doi.org/10.1021/j100816a009>
29. Polymer Properties Database, Polymerdatabase.Com. (2018). https://polymerdatabase.com/polymer_physics/Cp_Table.html (accessed May 20, 2020)
30. Kon JY, Miyawaki O, Nakamura K, Yano T (1982) The “intrinsic” thermal conductivity of some wet proteins in relation to their hydrophobicity: Analysis on gelatin gel. *Agric Biol Chem* 46:783–788. <https://doi.org/10.1080/00021369.1982.10865135>
31. Rocky KA, Pal A, Saha BB (2019) Adsorption Characteristics of CO₂ onto Carbon Nanotube for Adsorption Cooling / Capturing Applications. In: Proceeding international exchange innovations conference engineering science, Kyushu University, Fukuoka, Japan, pp. 67–69. <https://doi.org/10.15017/2552939>
32. Pal A (2018) Study on novel functional activated carbon and composites for adsorption heat pump systems, Kyushu University. <http://hdl.handle.net/2324/1959153%0D>
33. Zheng W, Hu J, Rappeport S, Zheng Z, Wang Z, Han Z, Langer J, Economy J (2016) Activated carbon fiber composites for gas phase ammonia adsorption. *Microporous Mesoporous Mater* 234:146–154. <https://doi.org/10.1016/j.micromeso.2016.07.011>
34. Sukhyy KM, Belyanovskaya EA, Kozlov YN, Kolomiets EV, Sukhyy MP (2014) Structure and adsorption properties of the composites “silica gel-sodium sulphate”, obtained by sol-gel method. *Appl Therm Eng* 64:408–412. <https://doi.org/10.1016/j.applthermaleng.2013.12.013>
35. Palash ML, Jahan I, Rupam TH, Harish S, Saha BB (2020) Novel technique for improving the water adsorption isotherms of metal-organic frameworks for performance enhancement of adsorption driven chillers. *Inorganica Chim Acta*, 501:119313. <https://doi.org/10.1016/j.ica.2019.119313>
36. Chan KC, Chao CYH, Wu CL (2015) Measurement of properties and performance prediction of the new MWCNT-embedded zeolite 13X/CaCl₂ composite adsorbents. *Int J Heat Mass Transf* 89:308–319. <https://doi.org/10.1016/j.ijheatmasstransfer.2015.05.063>
37. Qin Y, Long M, Tan B, Zhou B (2014) RhB adsorption performance of magnetic adsorbent Fe₃O₄/RGO composite and its regeneration through a fenton-like reaction. *Nano-Micro Lett* 6:125–135. <https://doi.org/10.5101/nml.v6i2.p125-135>
38. Py X, Daguette E, Menard D (2002) Composites of expanded natural graphite and in situ prepared activated carbons. *Carbon N Y* 40:1255–1265. [https://doi.org/10.1016/S0008-6223\(01\)00285-8](https://doi.org/10.1016/S0008-6223(01)00285-8)
39. Sun Z, Yao G, Liu M, Zheng S (2017) In situ synthesis of magnetic MnFe₂O₄/diatomite nanocomposite adsorbent and its efficient removal of cationic dyes. *J Taiwan Inst Chem Eng* 71:501–509. <https://doi.org/10.1016/j.jtice.2016.12.013>
40. Wang LW, Tamainot-Telto Z, Thorpe R, Critoph RE, Metcalf SJ, Wang RZ (2011) Study of thermal conductivity, permeability, and adsorption performance of consolidated composite activated carbon adsorbent for refrigeration. *Renew Energy* 36:2062–2066. <https://doi.org/10.1016/j.renene.2011.01.005>
41. Wang LW, Metcalf SJ, Critoph RE, Thorpe R, Tamainot-Telto Z (2012) Development of thermal conductive consolidated activated carbon for adsorption refrigeration. *Carbon N Y* 50:977–986. <https://doi.org/10.1016/j.carbon.2011.09.061>
42. Ghosh S, Harish S, Rocky KA, Ohtaki M, Saha BB (2019) Graphene enhanced thermoelectric properties of cement based composites for building energy harvesting. *Energy Build* 202:1–7. <https://doi.org/10.1016/j.enbuild.2019.109419>
43. Zajackowski B, Królicki Z, Jezowski A (2010) New type of sorption composite for chemical heat pump and refrigeration systems. *Appl Therm Eng* 30:1455–1460. <https://doi.org/10.1016/j.applthermaleng.2010.03.005>
44. NETZSCH Differential Scanning Calorimetry, (n.d.). <https://www.netzsch-thermal-analysis.com/en/products-solutions/differential-scanning-calorimetry/dsc-204-fi-phoenix/> (Accessed June 14 2020)
45. Netzsch, Laser Flash Apparatus LFA 457 MicroFlash®, (2018). https://www.netzsch-thermal-analysis.com/media/thermal-analysis/brochures/LFA_457_MicroFlash_en_web_01.pdf (Accessed May 12, 2020)

46. 3FLEX—Surface Characterization Analyzer (2016) 12. https://www.micromeritics.com/Repository/Files/3flex_brochure_2016_v8.pdf (Accessed May 7, 2019)
47. Terzyk AP, Chatlas J, Gauden PA, Rychlicki G, Kowalczyk P (2003) Developing the solution analogue of the Toth adsorption isotherm equation. *J Colloid Interface Sci* 266:473–476. [https://doi.org/10.1016/S0021-9797\(03\)00569-1](https://doi.org/10.1016/S0021-9797(03)00569-1)
48. Niazmand H, Dabzadeh I (2012) Numerical simulation of heat and mass transfer in adsorbent beds with annular fins. *Int J Refrig* 35:581–593. <https://doi.org/10.1016/j.ijrefrig.2011.05.013>
49. Saha BB, El-Sharkawy II, Koyama S, Lee JB, Kuwahara K (2006) Waste heat driven multi-bed adsorption chiller: Heat exchangers overall thermal conductance on chiller performance. *Heat Transf Eng* 27:80–87. <https://doi.org/10.1080/01457630600560742>
50. Mahdavikhah M, Niazmand H (2013) Effects of plate finned heat exchanger parameters on the adsorption chiller performance. *Appl Therm Eng* 50:939–949. <https://doi.org/10.1016/j.applthermaleng.2012.08.033>
51. Saha BB, Boelman EC, Kashiwagi T (1995) Computational analysis of an advanced adsorption-refrigeration cycle. *Energy* 20:983–994. [https://doi.org/10.1016/0360-5442\(95\)00047-K](https://doi.org/10.1016/0360-5442(95)00047-K)

Chapter 3

Synthesis and Characterization of Various MOFs and MOFs-Zeolite Composites: Water Adsorption and Rapid Cooling Production



Bo Han and Anutosh Chakraborty

Abstract This chapter begins with the synthesis of methyl-functionalized-MOF-801 (Zr) and Aluminium Fumarate-zeolite/alkali metal cations composites. The porous structures are characterized by XRD, TGA, SEM, and N_2 adsorption analysis. Later water adsorption on these synthesized materials is measured gravimetrically. Based on the experimental results, the adsorption chiller performance adopting modified fumarate-based MOFs as adsorbents is predicted by thermodynamic modeling. Enhanced hydrophilicity and faster water adsorption kinetics are observed for MOFs-zeolite/alkali metal cations composites. It is also observed that the methyl functional groups ($-CH_3$) enhance the thermal stability of MOF structures as well as increase the water uptake/offtake kinetics. Under adsorption-assisted cooling system operating conditions, the water transfer per cooling cycle for methyl functionalized MOF-801 (Zr) is found 25% higher as compared with the original MOF-801 (Zr) materials. On the other hand, modified fumarate MOFs improve the water loading rates significantly up to two folds. Therefore, the SCP and COP are also found higher for modified fumarate-based MOF-801 (Zr) and Al-Fum MOFs.

Keywords Cooling · Metal organic frameworks · Water adsorption

Nomenclature

A	Area (m^2)
c_p	Specific heat capacity [$kJ/(kg \cdot K)$]
COP	Coefficient of performance –
E_a	Energy activation (J/mol)

B. Han · A. Chakraborty (✉)
School of Mechanical and Aerospace Engineering, Nanyang Technological University, 50
Nanyang Avenue, 639798 Nanyang, Singapore
e-mail: AChakraborty@ntu.edu.sg

B. Han
e-mail: ha0002bo@e.ntu.edu.sg

h_{fg}	Latent heat of evaporation (kJ/kg)
h	Enthalpy/heat transfer coefficient (kJ/kg)
K	Isotherm coefficient –
k_{ads}	Adsorption rate (1/s)
k_{des}	Desorption rate (1/s)
L	Length (m)
m	Mass/heterogeneity coefficient ($kg/-$)
dm/dt	Mass flow rate of heat transfer fluid (kg/s)
P	Pressure (kpa)
Q	Heat input/output ($kW \cdot horkW$)
Q_{st}	Isosteric heat of adsorption (kJ/kg)
q	Amount of adsorbate uptake (kg/kg)
q^0	Limiting adsorbate uptake (kg/kg)
R	Gas constant ($J/(mol \cdot K)$)
r	Radial direction (m)
r_0	Radius of adsorption bed (m)
SCP	Specific cooling capacity (kw/kg)
T	Temperature ($^{\circ}C$)
t	Time (s)
U	Overall heat transfer coefficient ($W/(m^2 \cdot K)$)
u	Velocity (m/s)
v	Specific volume (m^3/kg)
V	Volume (m^3)
z	Axial direction (m)
ΔT	Temperature lifts (between condenser and evaporator ($^{\circ}C$))

Symbols

α	Pre-exponential coefficient
β_0	Sticking coefficient –
λ	Thermal conductivity ($W/(m \cdot K)$)
τ	Half cycle time (s)
ϕ	Porosity of bed –
ψ	Flag for defining switching and operation modes

Subscripts/Superscripts

a	Adsorbed phase
ads	Adsorption
bed	Adsorption bed
cc	Cooling capacity

chill	Chilled water
cond	Condenser
cool,in	Cooling fluid at inlet
cw	Cooling water
cw,in	Cooling water inlet
des	Desorption
eff	Effective
evap	Evaporator
f	Fluids
f-m	Fluid to metal (heat transfer)
fin	Fin
fin-b	Fin to bed (heat transfer)
g	Gaseous phase
heating	Heat transfer fluids
hot,in	Heating fluid at inlet
in	Inlet/input
i	Heating/cooling water
l	Liquid phase
m	Metal
m-b	Metal to bed (heat transfer)
m-M	Metal to MOFs (heat transfer)
mt	Metal tube
MOF	Metal organic framework adsorbents
ref	Refrigerant (water vapor)
s	Surface/saturated
tube	Heat exchanger tube
w-bed	Water to bed heat transfer

3.1 Introduction

The major needs for daily life are electric power, cooling, heating, and drinkable fresh water, and these needs are traditionally obtained by the combustion of natural gas and fossil fuels in power plants (to generate heating energy sources and electricity). On the other hand, the thermal and cooling requirements are achieved by employing energy-efficient chillers and boilers [1, 2]. All processes for generating these major needs involve irreversible resource exhaustion and environmental pollution. For example, serious atmosphere degradation such as global climate change, acid rain, and smog is due to the excessive emission of greenhouse gas and other pollutants [1]. In addition, the abuse and improper disposal of refrigerants also lead to the global warming potential (GWP) [2]. On the other hand, more than 70% of the earth's surface is covered by water, and only 2.5% of the drinkable water is available. Therefore, the desalination technology for converting seawater to fresh water

is essential. However, the production and supply of clean, potable water consume energy from various energy sources, such as fossil fuel, natural gas, and coal, and result in the GWP. The implementation of the adsorption cycle for desalination can be applied as the adsorption-assisted desalination system is environmentally friendly and requires renewable energy such as solar to operate [3]. Therefore, for the development of a green environment with less carbon footprint, researches on innovative heat transformation systems to produce cooling, heating, and desalting water has become much more popular [4–8].

The adsorption-assisted cooling (ADC) system is energy-efficient and environmentally friendly. The ADC shows no noise or vibration with low maintenance cost and a long system life. In addition, the adsorption heat can be regeneratively re-cycled during the operation. Water is adopted as the refrigerant (adsorbate) due to higher evaporation heat. Furthermore, conventionally adsorbents such as silica gel, graphite, and zeolites are chosen as adsorbents. Furthermore, good number of research activities on the performances of ADC are investigated, both experimentally and theoretically [3, 4, 9, 10].

In an adsorption-assisted heat transmission system, both heating and cooling effects are generated by the unique assembly of adsorption-initiated-evaporation and condensation-activated-desorption [11], and the scheme of cooling/heating with water uptake-off take processes are shown in Fig. 3.1. The adsorption cooling (ADC) comprises two or multi adsorption beds, which are switchable from adsorption to desorption or vice-versa. For continuous cooling in ADC, the adsorption heat exchanger adsorbs water vapor generated from the evaporator due to the cooling

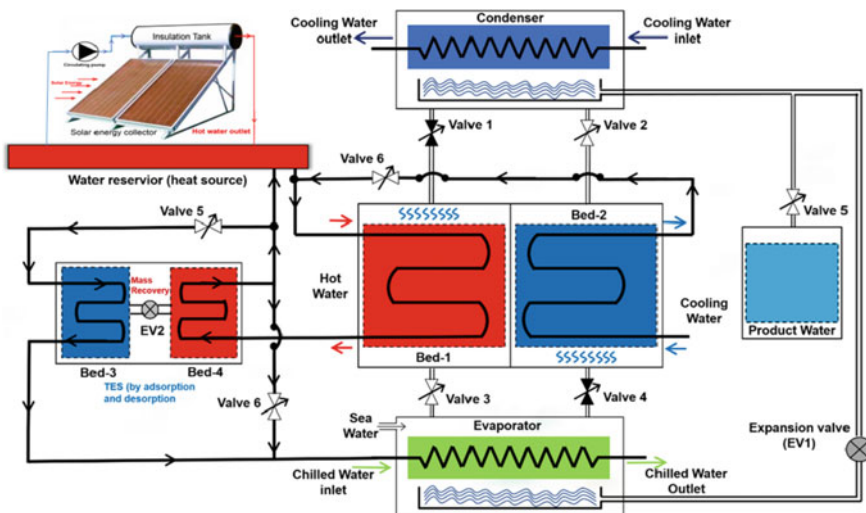


Fig. 3.1 The scheme of an adsorption device under cooling, heating, and desalination. *Source* Energy Conversion and Management 213 (2020) 112, 825

load (Q_{evap}) supplied in the evaporator with lower vapor pressure. The bed temperature increases due to the isosteric heat of adsorption, the cooling water flow through the heat exchanger of the adsorption bed releases the heat generated during the adsorption process (Q_{ads}) to the heat sink. Furthermore, the heating water is supplied to the heat exchanger of the desorption bed to release heat (Q_{des}). Therefore, water vapor is desorbed and, later, is condensed in the condenser, where the heat generated during the condensation process is released into the environment. Both the temperature and the pressure increase during desorption and pre-heating periods. Finally, the condensed fluid transfers back to the evaporator through a u-tube or expansion valve, which drops the pressure from the condenser to the evaporator. The heat generated during the condensation (Q_{cond}) is released into the heat sink by the flowing of cooling water through the heat exchanger of the condenser. In the next cycle, all beds are switched i.e., adsorption to desorption and desorption to adsorption moods. These processes are continuously repeated for the generation of heating and cooling power. Here, (i) the amalgamation of adsorption and condensation enthalpies are calculated for heat-pumping purposes, and (ii) the required cooling power depends on the latent heat of evaporation. In addition, the condensed liquid is stored as desalinated water. The TES (thermal energy storage) combining both the mass and heat recovery between the adsorption heat-exchanger enhances the cooling effects and heating capacity (or the overall efficiencies characterized by the cooling/heating power and specific water production).

3.1.1 Motivation of the Chapter

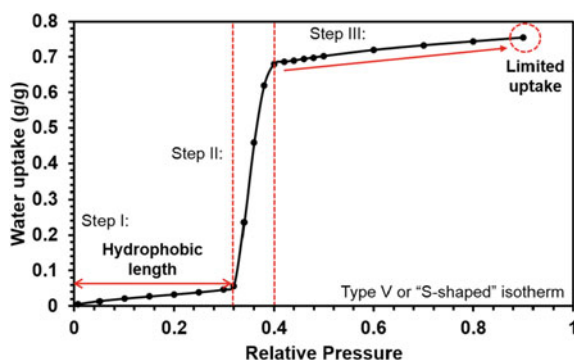
The isotherms shapes and kinetics behaviors of adsorbent plus adsorbate systems depend on pore characteristics, porosity, and interaction between adsorbate and adsorbent [5], and these are used to predict the thermal performances of the ADC. Water adsorption on the conventional adsorbents (for example, zeolite and silica gel) is used for heat pumps and cooling applications [6, 7]. However, these are suffered from some disadvantages related to highly hydrophilic, the requirement of a relatively higher temperature for desorbing water from the pore-structures of the adsorbent, and high operational cost [8]. On the other hand, silica gel shows less hydrophilic with lower water uptake capabilities at the relative pressures ranging from 0.1 to 0.3 as compared with zeolite adsorbents [12]. Therefore, both zeolite and silica gel structures achieve the lower water vapor transfer (Δq) per adsorption cooling cycle, which leads to the bulky size of adsorption-bed with lower specific heating/ cooling capacity (SHP/SCP) and coefficient of performance (COP). As can be found from the experimental observation that the higher Δq is obtained with “S-shaped” isotherm as compared with that of the type I isotherms for adsorption chiller application. As a result, the ADC driven under the lower regeneration temperature ($<60\text{ }^{\circ}\text{C}$) could be achieved by employing “S-shaped” adsorbents [13]. The interactions between water vapor and adsorbent are governed by adsorbent porosity, hydrothermal stability, water adsorption capacity, recyclability and hydrophilicity/hydrophobicity [14]. As

compared with chiller/heat pump performances employing silica gel and zeolites plus-plus water systems, water adsorption on metal–organic frameworks (MOFs) shows more potentials recently for adsorption bed design and development [15–19]. MOFs are metal-containing nodes with organic ligands. Qualified adsorbents such as zirconium-based MOF-801 (Zr) [18], MIL-160 [20], MIL-68 [21], CAU-10 [22] and Al-Fumarate [23] etc. deliver high Δq with fast kinetics per adsorption–desorption cycle. Currently, a number of MOFs such as HKUST-1, MIL-53, and Ni-MOF-74 are synthesized and tested widely [24–27] for various applications.

The foremost problem with the parent MOFs is their defective hydrophobicity/hydrophilicity behaviors in the low-pressure region. Normally, a three-step uptake should be found in a typical “S-shaped” or type V water adsorption isotherm, which is shown in Fig. 3.2. Firstly, rarely any water vapor is adsorbed onto the MOFs structure at a low-pressure region, and the water uptake is extremely low (nearly zero). Secondly, as the pressure increase to a certain point, an intense rise of water uptake is observed with a steep slope (approximately vertical). Finally, with the continues of the adsorption process, some more water is adsorbed onto the MOFs, and the slope of the isotherm becomes smooth. For water adsorption with “S-shaped” isotherm, the hydrophobic length is evaluated in terms of the relative pressure, which is measured from the beginning of adsorption ($P/P_s = 0$) to the point where a rapid increase of water uptake is observed.

For example, for Al-Fum, a relative long hydrophobic length is found ($P/P_s \approx 0.23$) and it results in a low Δq (water uptake-offtake difference) per adsorption chiller operation cycle, which results in unfavorable impact on practical ADC applications. Even longer hydrophobic lengths are found for Zr-UiO-66 ($P/P_s \approx 0.33$). Different from the MOFs discussed above, the key problem with MOF-801(Zr) is that its hydrophobic length is too short. Although MOF-801 (Zr) exhibits a “S-shaped” or type V water adsorption isotherm, the isotherm shape behaviors more like Type I due to its extremely short hydrophobic length; therefore, it requires high regeneration temperature up to 85 or 90 °C for the ADC applications. Besides the hydrophobicity/hydrophilicity performance issue at low pressure region, some other problems also exist. For example, the adsorption kinetics for the original Al-Fum and

Fig. 3.2 A typical example of “S-shaped” water adsorption isotherm



Zr-UiO-66 is too slow, and a long cycle time is required for the ADC operation. These constraints prevent the parent MOFs from being used in the adsorption-assisted heat transmission system.

It is noted here that the porosity of MOFs influences the adsorption behaviors strongly. For example, MOFs with extensively larger pore volume and higher BET surface area such as MIL-101 (Cr) could achieve an impressive water uptake capacity (up to 1.0 g/g); however, it results in a pretty long step pressure or hydrophobic length (up to $P_s/P \approx 0.4$) [16, 28, 29], which leads to a poor performance outcome in cooling/heat pump application. Therefore, direct or post-modification by adding the alkali metal dopants (such as Li^+ , Na^+ , K^+) into the parent Zn/Cr-based MOFs reconstructs the microstructure of the parent MOFs so that more water can be adsorbed and desorbed under the operating conditions of the ADC cycle [28, 30]. Another method involves the replacement of the original organic ligands with the polar chemical-functionalized ligands. For example, Bae et al. [31] achieved a promising improvement of N_2/CO_2 selectivity by introducing the highly polar ligands to the original MOF's framework. In addition, by implanting ethylenediamine (ED) and ethylene glycols (EG), the unsaturated metal sites of MIL-101 (Cr) are activated, and enhanced water selectivity is achieved in the low-pressure region [32]. Other modification approaches such as ligand functionalization, hydrothermal post-synthesis treatment, colloidal crystallization, decane injection or acid immersion [33–36] are used for adsorbents micro-structure reconstruction (pore size enlargement, micropore generation, and so on) purposes.

The performances of the ADC system can be projected employing adsorption isotherms and kinetics for an ideal case. The water uptake/offtake on MOFs under equilibrium and non-equilibrium conditions are explained thermodynamically by isotherms [37–39] and kinetics models [23, 40]. Combining the thermodynamic frameworks and theoretical models of various adsorbent-adsorbate system, the ADC performances are predicted and simulated. The ADC-modelling is derived with respect to the working principles for each component (such as the evaporator, condenser, and beds) of the adsorption cooling as well as the chilled/ cooling water loops and the heat sink/ source.

3.1.2 Research Objectives and Scope

The overall aims of this Chapter are to develop novel functional adsorbents and study their behaviors with water under the operating conditions of ADC. The objective and scope are listed as follows:

- (1) Fundamental understanding of MOFs synthesization and functionalization-Various MOFs are synthesized via the hydrothermal reaction method. The original MOFs are modified with the additions of functional groups, alkali ion dopants or mixing with conventional adsorbents.

- (2) The porosities, thermal properties of original and modified MOFs/zeolite-MOF composite are characterized by XRD (X-ray diffraction), TGA (thermo-gravimetric analysis), SEM (scanning electron microscopy), and N₂ adsorption.
- (3) Experimental investigation for water uptake/offtake under equilibrium and dynamic conditions and the thermodynamic modeling of ADC system.
- (4) Evaluation of the adsorption cooling performance employing various MOFs/composites plus water in terms of the SCP (specific cooling power) and COP (coefficient of performance) employing experimentally confirmed adsorption kinetics and isotherms data.

3.2 Literature Review

3.2.1 MOFs for Cooling/Heat Pump

MOFs (metal–organic-frameworks) are a class of crystalline meso-microporous hybrid structures, comprise metals or metal clusters and organic building linkers [41]. Normally, divalent (Cu, Mg, etc.), trivalent (Al, Fe, Cr, etc.) or tetravalent (Zr, Ti, etc.) metals are chosen as the metallic component, and the organic ligand with multidentate chains are usually used to connect the metal clusters [42–48]. Research on metal–organic frameworks (MOFs) took off in the late decades as it became more accessible to various synthesis approaches such as electrochemistry (EC), conventional electric (CE) heating, ultrasonic (US), mechanochemistry (MC) and microwave (MW) heating methods [49]. MOFs with three-dimensional networks usually attains massive pore volumes, large surface areas, uniform pore sizes, and stable pore structures. These highly porous materials have been widely adopted in the area of gas separation, liquid adsorption/purification, filtration and catalysis. Among these applications, water plus MOFs-based heat transmission systems for heat pump, cooling, and desalination purposes have met with much success and gradually broadened into commercial use. A detailed literature survey of MOFs-based cooling/heat pump/desalination applications is furnished in Table 3.1. In this chapter, series of metal–organic frameworks (MOFs) adsorbents are synthesized and investigated thoroughly for their performance regarding water adsorption via both simulation and experimental methods.

3.2.2 Current Research Activities in Parent MOFs

Al fumarate (Al-Fum) MOFs are chosen for desirable “S-shaped” isotherms with water adsorption plus the impressive hydrothermal stability [50]. Normally, Al-Fum with the monoclinic lozenge-shaped inner cell has a relatively larger pore volume (0.87–0.99 cm³/g) and higher specific surface area (750–1200 m²/g) [105, 109,

Table 3.1 A summarization of the adsorption-assisted heat transmission (for cooling and heat pump purposes) systems employing various MOFs plus water pairs

MOFs-type	Adsorption characteristics	Performance factors	Applications
MIL-101 (Cr) [16]	Isotherms with 'S' type showing long-hydrophobic-length from $P/P_s \rightarrow 0.4$ to 0.5 with higher limiting-uptake of 1.01g/g	Water transfer 0.94 kg/kg with 40 °C of the adsorption temperature and 90 °C of regeneration temperature Shows the poorer SCP	Not suitable for heat pump/ cooling but suitable for desalination and dehumidification
Al-Fum [50]	Isotherms with 'S' shaped, narrow hysteresis and limiting uptake of 0.45kg/kg. Provides better hydrothermal stability within 5000 water uptake/offtake cycles	Thermal conductivity of 0.13 W/(mK) with the heat capacity ranging from 1.05 to 1.35 kJ/(kg.K)	Cooling/ Heat pump
CAU-10-H [51, 52]	Surface area (BET) of 660 m ² /g Pore volume of 0.28 cm ³ /g showing the 'S' type isotherms and the limiting uptake equivalent to 0.25g/g.	Both numerical and experiments study with the adsorption enthalpy of 49 kJ/mol	Heat pump/ thermal storage
UiO-66 [53]	Isotherms with type IV, and the step pressure up to $P/P_s \rightarrow 0.20$ with the water uptake capacity of 0.4 g/g -NH ₂ implanted UiO-66 (Zr) shows 0.37 g/g of the water limiting capacity With promising cyclic stability	Enthalpy of adsorption: 89.5 kJ/mol for NH ₂ -UiO-66 (Zr) and 41.3 kJ/mol for UiO-66 (Zr)	Heat pump, cooling and thermal energy storage
MIL-160 [51]	Surface area = 1070 m ² /g Pore volume = 0.40 cm ³ /g Showing type I isotherms with the limiting capacity of 0.35 g/g at 30 °C	Experimental investigation with GCMC simulation Isothermic heat of adsorption is 54 kJ/mol COP = 1.6	Mainly heat pump

(continued)

Table 3.1 (continued)

MOFs-type	Adsorption characteristics	Performance factors	Applications
MOF-801 (Zr) [54]	Type 'S' isotherms with short hydrophobic length $0.05 < P/P_s < 0.1$. Relatively faster uptake/offtake rates < 600 s for the temperature varying from 20 °C to 90 °C	Water vapor transfer Δq of 0.31 kg/kg with SCP = 2 kW/kg and COP = 0.67 (under the conditions of $T_{ads} = 303K$ and $T_{des} = 353to358K$). Highly ambitious results	Heat pump/cooling/thermal storage
MIL-125 [53]	'S' type isotherms with hydrophobic length up to $P/P_s \rightarrow 0.32$. Water capacity equals to 0.33 kg/kg. Secondly Amine-functionalized MIL-125 exhibits the water capacity of 0.37 kg/kg with the rapid rise of water uptakes from $P/P_s = 0.1$ to $P/P_s = 0.25$	Enthalpy of adsorption = 56.0 kJ/mol for NH_2 -MIL-125 + water systems	Desalination/heat pump
fam-Al-Fum [55]	Water uptake capacity of 0.45 kg/kg with hydrophobic length up to $P/P_s = 0.2$, and higher water uptake/offtake rates	Water vapor transfer per thermal compression increases up to 12% as compared with that of the parent materials	Cooling / heat pump
COP-27(Ni) and MIL-101(Cr) MOF [15]	MIL-101(Cr) provides the maximum uptake capacity of 1.46 kg/kg. On the other hand, COP-27(Ni) possesses the limiting water uptake of 0.47 kg/kg	Modelling and simulation of adsorption assisted desalination system CPO-27(Ni) is found applicable at relatively lower evaporation temperature (<5 °C)	Adsorption desalination and dehumidification

110]. By using Al-Fum as an adsorbent, Youssef et al. [56] simulated 3.4 m³ water per tonne of Al-Fum MOFs and 20.0 Rton cooling energy per tonne of Al-Fum MOFs per day at 65 °C heating water temperature with the evaporator temperature of 10 °C, which is almost three times higher as compared with zeolite and silica gel adsorbents. Karmakar et al. [55] used Al-Fum as the clean agent to extract fluoride from water, and potable water was obtained at room temperature. Furthermore, Marta et al. [57] developed one continuous process to achieve large-scale Al-Fum production at

a rate of 5.6 kg/h and space–time-yields of 97,159 kg/m³ per day. Besides experimental investigations, some inherent simulation works were performed to study the interaction between Al-Fum with various adsorbates in molecular aspects [58, 59]. On the other hand, MOF-801 (Zr) is selected for fast kinetics and moderate water adsorption limiting uptakes (0.3 g/g of adsorbent) [18]. For example, Kim et al. [18] adsorbed water from the atmosphere employing solar energy as the driven heat force, and they obtained 2.8-L water/ kg of MOF-801 (Zr) daily employing the moist air of 20% relative humidity. Furukawa et al. [60] addressed the relationship between the MOF-801 (Zr) (Zr) adsorbent-water molecules' interaction with water adsorption sites by the powder neutron diffraction study. Furthermore, UiO-66 (Zr), a zirconium-based microporous material, should be considered as a qualified candidate for ADC applications for its high adsorption heat and good recyclability [53]. For example, Liu et al. [61] used UiO-66 polycrystalline membranes to desalinate water, and the membranes exhibited impressive ion rejection, good permeability with high water stability. Felix et al. [53] obtained high water adsorption heat up to 90 kJ/mol by using UiO-66 based MOFs as adsorbents. It should be noted here that UiO-66 having a face-centered cubic topology, which provides considerable pore volume (~0.49 cm³/g) and specific surface area (~1200 m²/g). Additionally, UiO-66 (Zr) plus water adsorption system gives 'S' type isotherms indicating the possibility of low regeneration temperature in adsorption cooling/heat pump application. Collectively, MOFs presented in this thesis exhibit diversified metal cation types, different topologies (from face-centred cubic to inner-caged) and various water adsorption behaviours.

3.2.3 *Modified MOFs and MOFs-Zeolite Composites*

To revise the water adsorption behaviours of the parent MOFs and optimize the MOFs-based ADC system performance, structural modification on the parent MOFs is necessary. Numbers of direct or post-synthesis modification methods are available to reconstruct MOFs pore topologies, and metal-doping is one of them. For example, by adding alkali metal ion dopants (such as lithium cations), Benjamin et al. [28] shorten the hydrophobic length of the parent MIL-101 (Cr), and improved uptake/offtake rates are observed. Yang et al. [62] doped Ni (II) ions into the MOF-5 structure, and adsorbents with larger Langmuir surface area, enhanced hydro-stability, and higher pore volume are obtained. Additionally, Zhu et al. [63] proved that the porosity and hydrophobicity of the parent MOF STU-1 are revised by doping various metal ions such as Fe²⁺, Cd²⁺ or Cu²⁺. Another popular MOFs modification method is functionalization. By implanting organic ligands with hydrophilic/hydrophobic functional groups onto the parent MOFs, the pore-structures are re-constructed, and the water adsorption behaviours on the functionalized MOFs are revised. For example, Jeremias et al. [53] showed that amino-functionalized MIL-125 exhibits much-enhanced hydrophilicity at the low-pressure region as compared with the original MIL-125, and it has huge potentials for heat

storage and heat transmission applications. It is also found that a great improvement of water uptakes is obtained by introducing $-\text{NH}_2$ functional groups onto the original UiO-67 at a low-pressure region. Furthermore, Ortiz et al. [64] proposed that the hydrophobicity/hydrophilicity traits of MOFs are determined by the geometry, porosity and structural flexibility of the MOFs, which could be tailored by functionalization.

In this chapter, the original MOFs is mainly modified with three following approaches: (1) post-mixing with conventional zeolite-based (AFI/CHA type) adsorbents; (2) post-doping with hydrophilic alkali dopants (Li^+) and (3) direct-implanting with various of hydrophobic/hydrophilic functional groups. The functional group additives involving in this chapter are: Pyridine group ($-\text{N}$), is used as a crucial media to affecting the shape of adsorption isotherm [65]. Hydroxyl group ($-\text{OH}$), a versatile polar functional group, has already been used to enhance the MOFs' affinity with various adsorbates [66, 67]. Amine group ($-\text{NH}_2$), another efficient functional group, plays an important role in MOFs' hydrophilic enhancement at low-pressure region [68, 69]. The nonpolar hydrophobic methyl functional group ($-\text{CH}_3$) for its impressive water capture stability [70, 71].

3.3 Methodology and Experiments

3.3.1 Synthesis

3.3.1.1 MOF-801 (Zr)

Zr assisted MOF-801 is synthesized by hydrothermal reaction method [72], in which 0.005 mol of zirconium oxide chloride octahydrate ($\text{ZrOCl}_2 \cdot 8\text{H}_2\text{O}$, 99%) and 0.005 mol of fumaric acid ($\text{C}_4\text{H}_4\text{O}_4$, 99%) are mixed in the formic acid-DMF solution (volume ratio: $v/v = 7:20$, 27 ml totally). Next, the suspension is put into the sealed autoclave for heating for 24 h at 130 °C. The white materials are then separated from the waste reagent and purified with DMF (three times) and with ethanol (two times). The humid fumarate-based MOFs are dried at 80 °C for 12 h and then transferred to the vacuum oven for activation purposes (150 °C, 5 h). The fabrication processes and purification procedures stay the same for methyl functionalized MOF-801 (Zr) except for substituting the original ligand with 2,3-Dimethylfumaric acid.

3.3.1.2 Al Fumarate MOFs

The Al Fumarate (Al-Fum) is fabricated via the reflux reaction method under ambient pressure [58]. Firstly, 0.01 mol aluminium chloride hexahydrate ($\text{AlCl}_3 \cdot 6\text{H}_2\text{O}$, 99%) and 0.01 mol fumaric acid ($\text{C}_4\text{H}_4\text{O}_4$, 99%) are added into the beaker, 50 ml of N, N-dimethylformamide (DMF, 99.8%) is used here as a reagent. The mixture

is stirred for four days at a constant temperature (130 °C). Secondly, the mixture is separated by a centrifugal spinning machine with a speed of 10,000 rpm. Next, the condensed solid is washed twice with acetone then twice with methanol for purification purposes. After purification, the moist synthesized adsorbent is heated at 80 °C overnight for drying. Finally, the white power is heated in the vacuum oven (150 °C, 3 h). This activation procedure is aimed for further removal of residual unreacted organic ligands, reagents, water vapor, or any impurities. It is noted that the activation process is necessary for fully unlocking the potentials of MOFs. It is also important in minimizing the side reactions during the post-synthesis process. The whole synthesis procedure for Al-Fum is shown schematically in Fig. 3.3.

3.3.1.3 Methyl Functionalized MOF-801 (Zr)

The original MOF-801 (Zr) is synthesized via the hydrothermal reaction method. For $(\text{CH}_3)_2$ -MOF-801 (Zr), the fabrication environment/conditions and purification processes are the same as compared with the original materials except substituting the original organic ligand (Fumaric acid, $\text{C}_4\text{H}_4\text{O}_4$) with two-methyl-groups functionalized linker (2,3-Dimethylfumaric acid, $\text{C}_6\text{H}_8\text{O}_4$). Later, the manufactured $(\text{CH}_3)_2$ -MOF-801 (Zr) is heated at 80 °C for 12 h, and put them in a vacuum oven for activation purpose (150 °C, 5 h). Hence, any other residual moisture, unreacted reagent, or acid is removed. Figure 3.4 displays the scheme of the synthesization process for the original and $-\text{CH}_3$ implanted MOF-801 (Zr).

3.3.1.4 AFI/CHA-Zeolite Plus Al-Fum Composites

For the fabrication of composite materials, the activation of the parent Al-Fum is performed before the mixing procedure. Firstly, 2 g of synthesized Al-Fum is

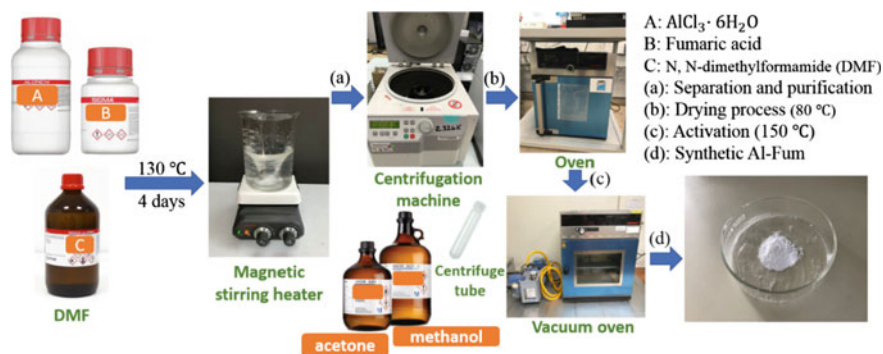


Fig. 3.3 Synthesis process (reflux reaction) of MOF Al-Fum. *Source* Energy Conversion and Management 240 (2021) 114, 264

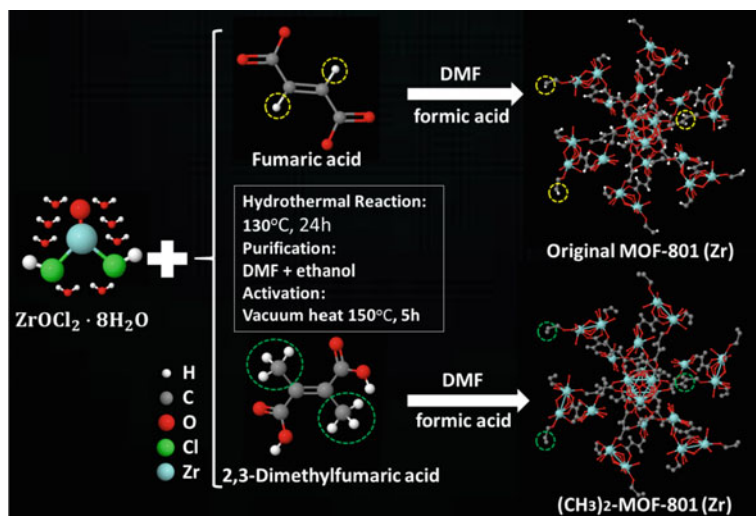


Fig. 3.4 The schematic diagram of the original and $-\text{CH}_3$ implanted MOF-801 (Zr) MOFs

dissolved into 50 ml hexane (C_6H_{14} , 95% Sigma-Aldrich) or distilled water. Next, the suspension is stirred at 90°C for 30 min, and a certain weight of zeolite-based adsorbent (type AFI or CHA) is added to the suspension. The mixture is stirred for one hour for complete physi-mix purpose. After stirring, the post-synthesized zeolite-AI-Fum adsorbent is extracted by the filter method and heated at 80°C overnight for drying. Hence, zeolite-based adsorbents with various weight concentration ratios (from 10 to 90%) are synthesized and investigated.

3.3.1.5 Alkali Ions Doped AI-Fum Composites

Before the doping process, the 2 mg of activated AI-Fum sample is mixed with 50 ml of hexane. The suspension is mixed for half an hour at 80°C . During the stirring procedure, liquor contains alkali metal ions is pouring into the mixture carefully. The alkali ions such as Li^+ , Na^+ , K^+ solutions contain alkaline-metal-salt having 5% concentration in weight, and distilled water (1 ml). After doping, the suspension is separated, and the post-synthesized-AI-Fum is dried at 80°C overnight.

The adsorbent structures such as AI Fum, Li-AI-Fum, CHA-AI-Fum, and AFI-AI-Fum composites are shown in Fig. 3.5. This Figure also presents the snapshots of the 30% CHA/AFI plus AI-Fum composites from various angles, which also indicate the random mixing structure of adsorbents.

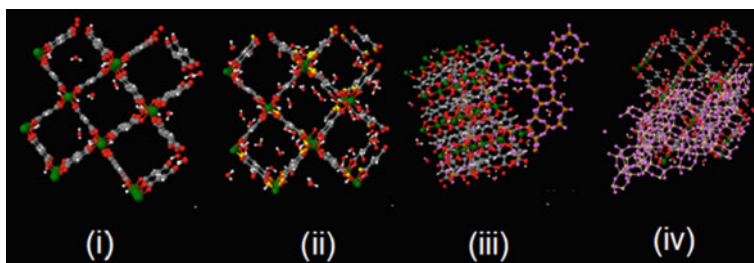


Fig. 3.5 Snap shots representing the molecular structure of (i) Al-Fum MOF (ii) 5% Li-Al-Fum MOF (iii) 30% AFI-Al-Fum MOF and (iv) 30% CHA-Al-Fum. Hence 'Al-Fum' means 'aluminium fumarate'. (red is O₂ in H₂O and for aluminium fumarate, white means H₂, grey is C, yellow shows lithium, violet indicates O₂ in CHA or AFI zeolites, orange represents phosphorus, cream-color indicates silicon, and green stands for aluminum). *Source* Microporous and Mesoporous Materials 288 (2019) 109, 590

3.3.2 Characterization

3.3.2.1 X-ray Diffraction

The X-ray diffraction (XRD) characterization is performed to investigate the crystallography of MOF adsorbents. The XRD apparatus is fitted with a 0.2 mm Cu Attenuator by detecting the protection of direct beam and is functioned at 40 mA and 40 kV, employing Cu radiation prefix with parallel beam X-ray mirror. It should be noted here that the divergence slit with respect to 1/6 or 1/4 degree is recommended and depends on the maximum peak.

3.3.2.2 Scanning Electron Microscopy

The microstructures, particle sizes, and morphology of MOFs-structures are evaluated by the scanning-electron-microscopy or SEM technique. Pre-platinum-coating work on MOF powders is performed to enhance the electrical conductivity of the sample. The investigation voltage range is 2–10 kV.

3.3.2.3 Thermogravimetric Measurement

Thermogravimetric characterization is applied to test the thermal stability of MOFs and composite adsorbents. Before the utilization of the TGA apparatus, the MOFs and composites are dried at 80 °C in a vacuum chamber. Later, in order to make sure that the original and modified MOFs reach the fully-hydrated state, these adsorbents are exposed to the atmosphere at ambient conditions for one day. Finally, the MOF-power is heated from 30 °C up to 600 °C, including the ramp rate of 10 °C per minute. In the apparatus, the air flow rate is maintained steady. During experimentation, the weight

change of the hydrated material is logged temporarily (from dynamic to equilibrium state) as a function of temperature. Technically, MOF adsorbents are considered as thermally stable if no evident weight loss is observed at high temperature.

3.3.3 Adsorption Uptake Investigation

Generally, the amount of adsorbate uptakes under equilibrium and dynamic states are measured by volumetric (manometric), gravimetric and dynamic flow adsorption methods. The CVVP (constant volume variable pressure) or volumetric method is used to calculate the adsorptive uptakes with respect to various pressures at a given temperature. The pressure changes are achieved by partial vacuum conditions within the confined adsorbent volume. Hence, pressure transducers with high accuracy are required. The volumetric gas adsorption becomes a mature technique to characterize the porosities of adsorbent materials. Nitrogen is recommended to be the guest gas as compared with other gases such as argon, krypton or carbon dioxide for its distinct advantages. For example, nitrogen has a similar buoyancy to atmospheric air, and it is easily available. Due to its non-polar feature, the adsorption is not affected by the surface charge of the adsorbent. Furthermore, the gravimetric method is preferred for water adsorption, where the adsorption uptakes are monitored by varying the relative humidity or concentration of water vapor and measuring the mass change of the adsorbent.

3.3.3.1 Nitrogen Adsorption

The N_2 assisted adsorption–desorption experiments are carried on by Autosorb instrument at 77.4 K to determine the average pore size with pore size distribution (PSD curves), specific surface area (by BET analysis), and micro and mesopore volume of the assorted MOFs adsorbents. The outgassing station, analysis station and the main instrument accessories of the N_2 adsorption apparatus are shown in Fig. 3.6. Before N_2 adsorption experiment, the sample is outgassed at 160 °C for 3 h to remove any undesirable adsorbed vapors and water. The nitrogen adsorption isotherm data can be converted into the specific surface area of MOFs by Brunauer-Emmet-Teller or BET equation, and the pore volume is calculated relating to saturation conditions ($P/P_s = 1$) i.e., the pore volume of the MOF powder sample is equivalent to the total liquid nitrogen adsorbed onto the MOF sample. The liquid volume is calculated by $V_{liq} = \frac{P_a V_{ads} V_m}{RT}$, where P_a is the ambient pressure, V_{ads} denotes the adsorbed phase volume of nitrogen, V_m is the molar volume of liquid N_2 with a value of $3.47 \times 10^{-5} m^3/mol$, R indicates the gas constant, and T defines the temperature. Moreover, the average pore size (r_p) is calculated by $r_p = \frac{2V_{liq}}{A_s}$, where A_s represents the specific surface area of the MOF-sample.

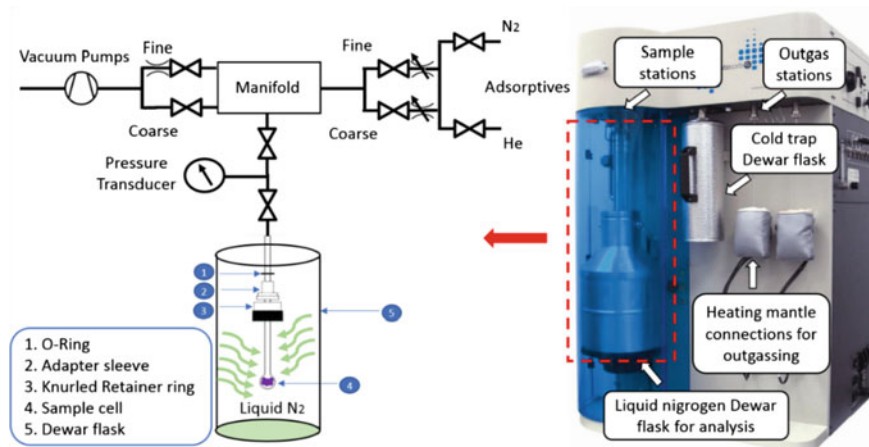


Fig. 3.6 Main components and schematic diagram of N_2 adsorption machine

3.3.3.2 Water Adsorption

The experimental investigation on the water adsorption/desorption on MOFs materials at various temperatures (from 25 °C to 75 °C) and pressures ($0 < P/P_s < 1$) are performed by a thermogravimetric analyzer (TGA), and its scheme is displayed in Fig. 3.7. The TGA apparatus is made up of six main components, and these are sample cell, micro-balance, humidifier, pumps, temperature sensor, and humidity probe. At the very beginning of the experiment, the purified and water-free MOFs sample is put on the sample cell held by the microbalance. The microbalance is located at the top of the temperature-controlled chamber. The microbalance possesses a limiting load capacity of 5 g ($\pm 0.1 \mu\text{g}$). The sample cell and the microbalance are connected

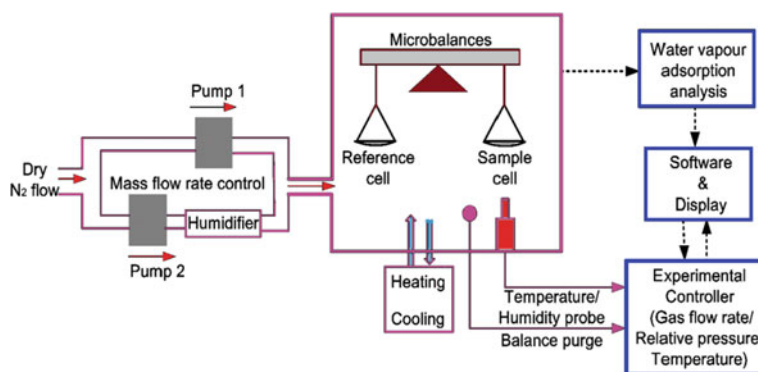


Fig. 3.7 Schematic diagram of the gravimetric equipment for the investigation of water adsorption isotherms and kinetics. *Source* Energy Conversion and Management 213 (2020) 112, 825

by an extension wire which makes the TGA give a direct measurement of water vapor uptake during the water uptake/offtake processes. The mass of water vapor gain or loss on MOFs sample is measured directly by the microbalance and recorded in the data logger. These data are then deduced to the water adsorption isotherms. The water adsorption investigation is performed under different relative humidity or relative pressure (P/P_s) under isothermal conditions over time. The temperature sensor (class A RTD, accuracy ± 0.15 °C) is installed inside the TGA, and by controlling the furnace heating system, the isothermal condition is maintained. To maintain the pressure same inside the TGA apparatus, the adsorption system is vacuumed and purged by the vacuum pump at the beginning of the experiment. Maintaining the temperature and regulate the relative pressure inside the chamber are considered as two key procedures for the adsorption experiment. Before the experiment, the adsorbent materials are heated at 80 °C by a heater as installed hermetically around the reaction chamber.

The temperature is regulated by the balance process employing the combination of radiant heater heat and the cooling air flows into the chamber. To prevent possible condensation effects, the temperature of adsorption chamber is maintained 10 °C higher than the experimental conditions of the gravimetric apparatus. The dry nitrogen (99.999% purity) is supplied across the adsorption chamber continuously to maintain the control of the microbalance buoyancy effect and to remove the residual moisture on the MOFs adsorbents. In addition, the relative humidity inside the chamber is regulated by adjusting the flow of dry nitrogen into the adsorption chamber and is measured by the humidity probe. When the relative humidity is lower than the expected value, the flow of nitrogen with additional water vapor (generated from the humidifier) is pumped to the adsorption chamber. On the other hand, dry nitrogen is injected to the adsorption chamber when the relative humidity of water vapor is higher than the desired value. Thus the relative pressure is controlled experimentally in the adsorption chamber. During water adsorption procedure, the overall mass of the adsorbent sample is increased due to the fact that water vapor adsorbs onto the adsorbent. The change of mass in the adsorbent-adsorbate system is detected and recorded by the build-in microbalance. The mass of the water vapor adsorbate is evaluated by $m_{a,i} = M_s(P_i) - M_s(P_0)$, where $M_s(P_0)$ is the initial recorded mass of the MOF-material, and $M_s(P_i)$ is the overall sample mass as a function of the relative pressure at certain temperature. In addition, the gravimetric water uptake is calculated by $q_i = m_{a,i}/M_s$. During the adsorption process, the mass changes are varied from the dynamic state to static condition, and all uptake values are recorded by the build-in software, and they could be deduced to analyze the adsorption isotherms, kinetics, and the isosteric heat of adsorption under dynamic and equilibrium conditions.

3.4 Results for Surface Characterization

3.4.1 Functional MOF-801 (Zr)

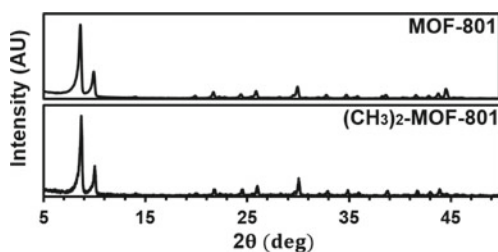
3.4.1.1 Power X-ray Diffraction (PXRD)

Figure 3.8 illustrates the Powder X-ray diffraction (PXRD) curves of the original and methyl functionalized MOF-801 (Zr). The $(\text{CH}_3)_2$ -MOF-801 (Zr) exhibits similar XRD trends as compared with the parent MOF-801 (Zr) [18], indicating that the MOFs are fabricated correctly, and the functional group additives do not destroy MOFs' structural integrity. The distinct reflection for MOF-801 (Zr) and $(\text{CH}_3)_2$ -MOF-801 (Zr) is observed at around 8.65° . The peaks correlate with the intensity of Zr ions. It is noted here that few additional peaks are found for $(\text{CH}_3)_2$ -MOF-801 (Zr) at certain angles, which is related to the addition of unreacted metal/organic acid in the pore-structures of MOFs, and inadequate purification work are conducted after the synthesization procedure. However, methyl functional group-assisted MOF-801 (Zr) is a stable structure.

3.4.1.2 Thermogravimetric Analysis (TGA)

The TGA curves for the parent and $-\text{CH}_3$ implanted MOF-801 (Zr) are displayed in Fig. 3.9, where the weight losses of MOFs are observed in terms of three stages as a function of temperature. At first, water vapors depart from the outer cages of MOF-801 (Zr) based materials. Thus, the first stage of weight loss occurs between 50 and 80°C . It should be noted here that 14% weight loss of $(\text{CH}_3)_2$ -MOF-801 (Zr) indicates the smaller pore volume. This result agrees with N_2 adsorption analysis as found in Table 3.2. In the second stage, the weight loss is obtained for the temperature ranging from 80 to 260°C , which is mainly because of the release of water vapor from the inner pores. The decomposition of the organic ligands is found [73] as the temperature increases up to 260°C . Therefore, weight losses occur both in the MOF-801 (Zr) and $(\text{CH}_3)_2$ -MOF-801 (Zr) samples. Hence, the final stage of the weight loss is due to the decomposition of MOFs structures at a higher temperature. The final weight loss in MOF-801 (Zr) is found at 355°C whilst it occurs at 380°C

Fig. 3.8 The XRD (X-ray diffraction) diagrams for the parent and $-\text{CH}_3$ implanted MOF-801 (Zr) materials.
Source Applied Thermal Engineering 175 (2020) 115, 393



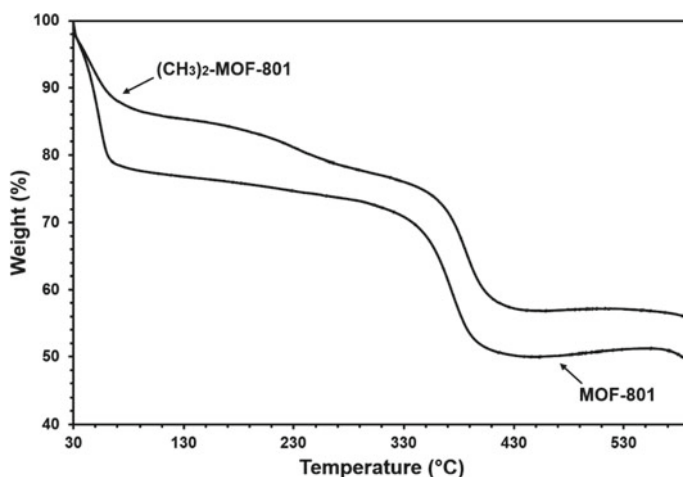


Fig. 3.9 TGA analysis for the parent and $-\text{CH}_3$ implanted MOF-801 (Zr) samples. *Source* Applied Thermal Engineering 175 (2020) 115, 393

Table 3.2 The porosities of the original and $-\text{CH}_3$ implanted MOF-801 (Zr) materials employing N_2 adsorption technique

Samples	BET surface area (m^2/kg)	Pore volume (cm^3/g)	Average pore radius (\AA)
MOF-801 (Zr)	864.0	0.37	10.8
$(\text{CH}_3)_2$ -MOF-801 (Zr)	756.2	0.30	11.0

for $-\text{CH}_3$ implanted MOF-801 (Zr). Therefore, the thermal stability of the original MOF-801 (Zr) is improved by the $-\text{CH}_3$ functionalization work.

3.4.1.3 Scanning Electron Micrography (SEM)

Figure 3.10 shows the SEM diagrams for fumarate-based MOFs. The shape and the size of the methyl functionalized MOF-801 (Zr) sample are similar to those of the original MOF-801 (Zr). In addition, strong agglomeration behaviors are observed for both the original and $-\text{CH}_3$ implanted MOF-801 (Zr) samples with typical rounded particle presents. Therefore, the morphologies of the MOFs are not disrupted by adding a methyl-functional-group.

3.4.1.4 N_2 Adsorption for Measuring Pore Size Distribution

Figure 3.11 shows N_2 adsorption isotherm results. All the functionalized adsorbents show the similar N_2 adsorption performance without major differences. It is found

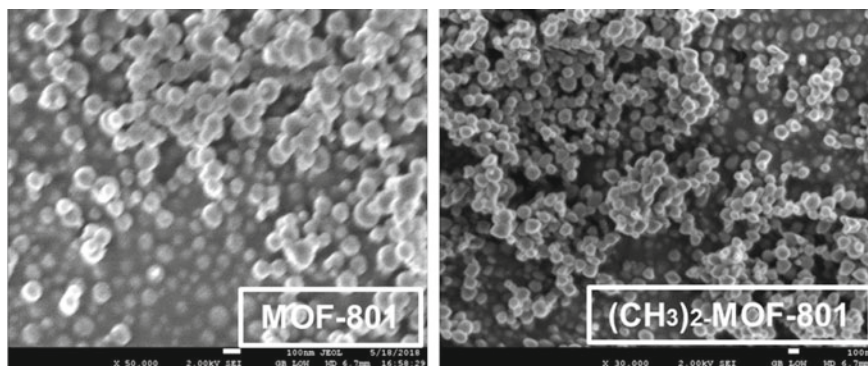


Fig. 3.10 Scanning electron microscopy (SEM) of functionalized fumarate-based MOFs

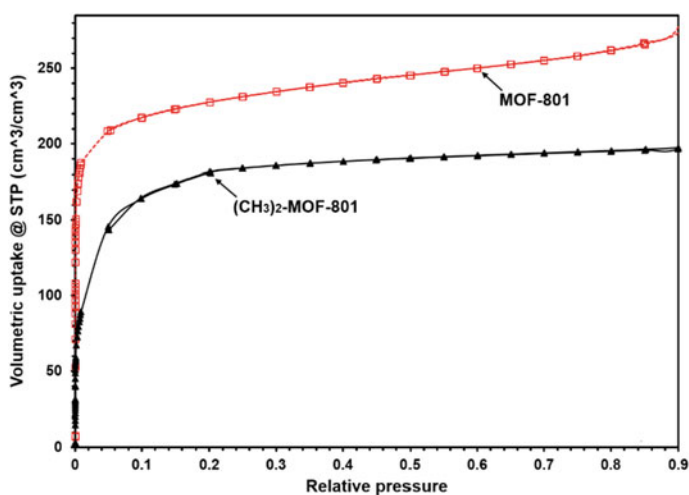
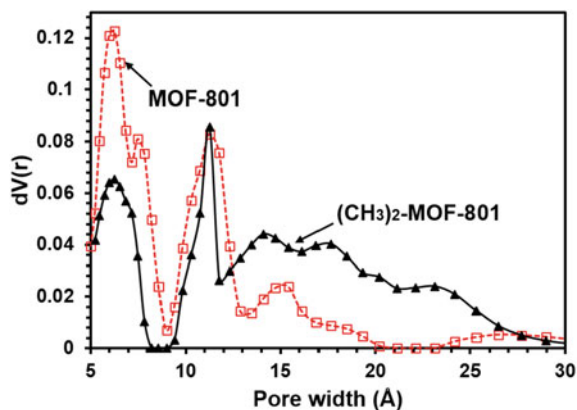


Fig. 3.11 Isotherms curves showing N₂ adsorption on two different MOFs. Here, (□) is MOF-801 (Zr), and (▲) indicates (CH₃)₂-MOF-801 (Zr). *Source* Applied Thermal Engineering 175 (2020) 115, 393

that the original MOF-801 (Zr) has a higher N₂ uptake as compared with functionalized MOF-801 (Zr) adsorbent, which indicates that the additional methyl functional groups may obstruct the N₂ molecules from being adsorbed into the pores of the MOFs framework.

The PSD (pore size distribution) diagram of the -CH₃ implanted MOF-801 (Zr) is displayed in Fig. 3.12, and the parent MOF is presented for comparison purposes. It is observed that the pore width mainly varies from 5.0 to 15 Å, which indicates that fumarate-based MOFs consist majority of micropores through their surface. It

Fig. 3.12 Pore size distribution of functionalized fumarate-based MOFs adsorbents employing DFT analysis. Here, (□) is MOF-801 (Zr), and (▲) indicates (CH₃)₂-MOF-801 (Zr).
 Source Applied Thermal Engineering 175 (2020) 115, 393



is found that the dual methyl functional group i.e. (CH₃)₂-MOF-801 (Zr) increases the number of micro-pores. The PSD graph indicates that the pore distributions of the -CH₃ implanted MOF-801 (Zr) are found with the pore size varying from 12.0 Å to 20 Å.

3.4.2 Al Fumarate and MOF-Zeolite Composites

3.4.2.1 Thermogravimetric Analysis (TGA)

The TGA curves of the 5% doped Li⁺, Na⁺, K⁺ Al-Fum, 30% mixed AFI/CHA-Al-Fum is displayed in Fig. 3.13 and original aluminium fumarate (Al-Fum) for comparison purposes. Generally, all samples, as presented in Fig. 3.13 provides the weight loss in three stages for the temperature increasing from 30 °C to 550 °C.

The weight loss for the first stage is due to the water vapor release from the outer cage of Al-based adsorbents. The weight loss for the second stage due to the water vapor release from the sample- inner cage. After that, the final weight decrement is due to the collapse of the material pore-structure. The final weight loss process for all the post-synthesis Al-Fum occurs around the temperature range from 400 to 450 °C, which is lower as compared with the parent MOFs (around 460 °C). Hence, the post-synthesis process slightly reduced the thermal stability of Al-Fum.

3.4.2.2 Scanning Electron Micrography (SEM)

Figure 3.14 shows the SEM diagrams for parent Al-Fum and the post-synthesis Al-Fum (5% doped Li⁺, Na⁺, K⁺ and 10%, 50%, 90% mixed AFI/CHA). The shape and pore size of the alkali metal cations doped materials are similar to the original Al-Fum samples, which indicates that the pore structure of the original Al-Fum

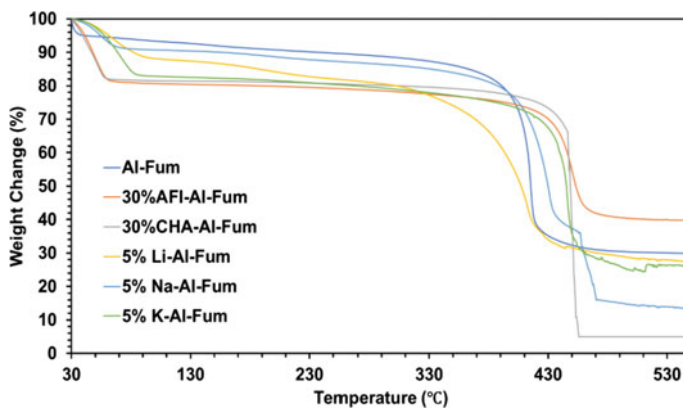


Fig. 3.13 TGA graphs showing the thermal stabilities for the parent, alkali ions doped and zeolite mixed Al-Fum composites based MOFs. *Source* Microporous and Mesoporous Materials 288 (2019) 109, 590

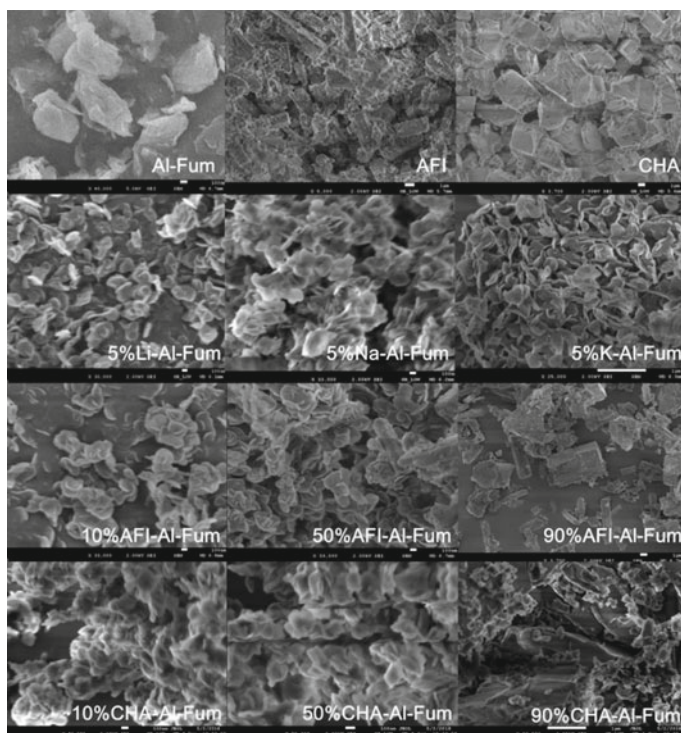


Fig. 3.14 Scanning electron microscopy (SEM) of Al-Fum (top left), AFI (top middle), and CHA (top right). The second row shows the SEMs of 5% Li^+ , Na^+ and K^+ doped Al-Fum (from the left side). The third row shows the SEMs of 10%, 50%, and 90% AFI mixed Al-Fum (from the left side). The fourth row shows the SEMs of 10%, 50%, and 90% CHA mixed Al-Fum (from left-hand side). *Source* Microporous and Mesoporous Materials 288 (2019) 109, 590

is not destroyed by the doping of alkali cations. The coexistence of quadra-hedral and rod-like shape in the 50%AFI/CHA-Al-Fum sample indicates that there is only homogenous physical mixing inside the samples without any chemical reaction.

3.4.2.3 N_2 Adsorption for Measuring Pore Size Distribution

Figure 3.15 shows N_2 adsorption isotherms of 5% doped Li^+ , Na^+ , K^+ Al-Fum, 10%, 30%, 50% mixed CHA/AFI-Al-Fum and parent Al-Fum MOFs is shown here for comparison purpose. It is observed that the original Al-Fum exhibits the largest N_2 limiting capacity as compared to post-synthesized adsorbent samples. This is because of the fact that some of the doped alkali metal cations may obstruct the N_2 molecules from being adsorbed into the pores of the adsorbents, and the poor affinity between the AFI/CHA zeolite and nitrogen also results in a lower N_2 uptake. Furthermore, all the post-synthesized Al-Fum adsorbents (10%, 30%, 50% mixed AFI/CHA-Al-Fum and 5% doped Li^+ , Na^+ , K^+ Al-Fum) shares the similar N_2 adsorption performance without any major difference.

Figure 3.16a–c shows pore size distribution (PSD) graphs of both the original and the post-synthesized adsorbents. It is found that the pore widths of alkali metal cations doped and zeolite-based adsorbent mixed Al-Fum adsorbents vary from 6 Å to 15 Å with a similar amount of increment in pore volume, which implies the majority of micropores throughout the material surface.

The existence of alkali dopants or zeolite results in the decrement of adsorbent-mesopores distribution, which indicates that the post-synthesis process could be a reliable approach to generate the “S-shaped” water adsorption isotherm with a shorter hydrophobic length. Based on N_2 adsorption measurement, the pore volume, the average pore radius, and the BET surface area of all the parent and modified Al-Fum-based MOFs are calculated and furnished in Table 3.3. As can be found

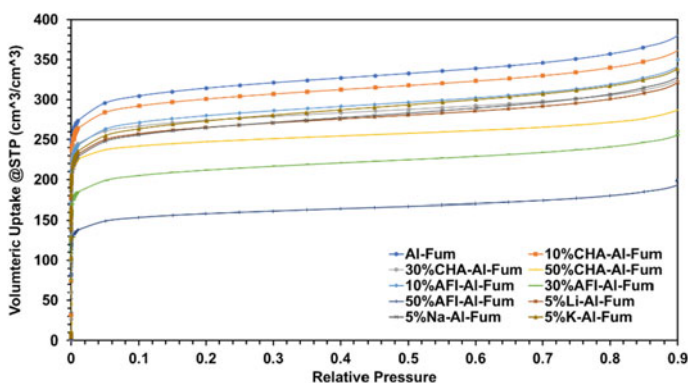


Fig. 3.15 N_2 adsorption isotherm for the original and post-synthesis Al-Fum adsorbents. *Source* Microporous and Mesoporous Materials 288 (2019) 109, 590

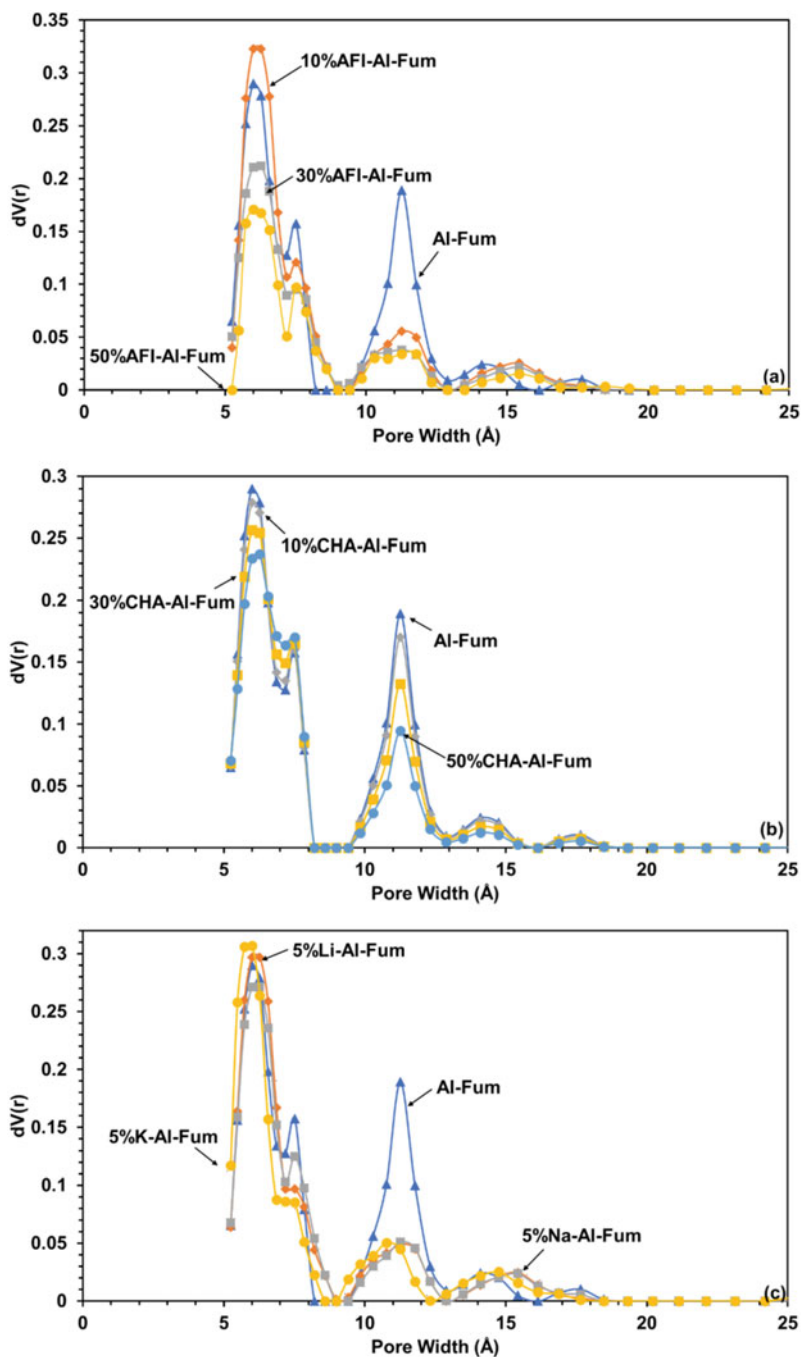


Fig. 3.16 Pore size distribution of the original and post-synthesis Al-Fum adsorbents employing DFT analysis. *Source* Microporous and Mesoporous Materials 288 (2019) 109, 590

Table 3.3 N₂ adsorption measurement (pore volume, average pore radius, and BET surface area) of samples

Samples	BET surface area (m ² /kg)	Pore volume (cm ³ /g)	Average pore radius (Å)
Al-Fum	1093.3	0.93	11.75
Li-Al-Fum (5%)	1061.4	0.43	11.80
Na-Al-Fum (5%)	1061.7	0.44	11.78
K-Al-Fum (5%)	1059.8	0.43	11.78
AFI-Al-Fum (10%)	1089.4	0.45	11.78
AFI-Al-Fum (30%)	822.0	0.34	11.79
AFI-Al-Fum (50%)	598.4	0.25	11.78
CHA-Al-Fum (10%)	1058.7	0.87	11.84
CHA-Al-Fum (30%)	983.5	0.76	11.83
CHA-Al-Fum (50%)	905.8	0.58	11.84

from Table 3.3, the micro-structure properties of alkali metal ions doped Al-Fum are almost the same (pore volume $\approx 0.43\text{cm}^3/\text{g}$, BET surface area $\approx 1060\text{ m}^2/\text{g}$ and pore size $\approx 11.78\text{ \AA}$). However, mixing different amounts of AFI/CHA zeolite results in different BET surface area with a range from $598\text{ m}^2/\text{g}$ to $1089\text{ m}^2/\text{g}$.

3.5 Water Adsorption Isotherms and Kinetics

3.5.1 Functional MOF-801 (Zr) Plus Water

The plots of adsorption and desorption processes on the original and $-\text{CH}_3$ implanted MOF-801 (Zr) adsorbents are displayed in Fig. 3.17. The experiments are performed at $25\text{ }^\circ\text{C}$ with pressures extending from the low-pressure region ($P/P_s \approx 0$) to the saturated condition ($P/P_s = 0.9$). Hence, MOF-801 (Zr) is detected by the solid black line, whereas the brown dotted line defines the $(\text{CH}_3)_2$ -MOF-801 (Zr) adsorbent. The experiments for the measurement of water uptakes are performed at least three times for reliability and error analysis purposes. The hysteresis phenomena are observed in the low-pressure region, which is similar to other research findings [72]. It is found that the hydrophobic length in Henry's region is slightly increased even though the maximum uptake of water vapor on $(\text{CH}_3)_2$ -MOF-801 (Zr) drops slightly as

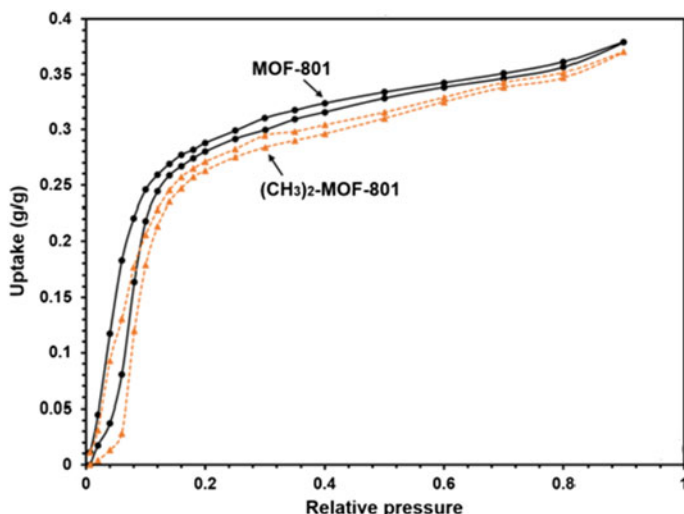


Fig. 3.17 Adsorption–desorption isotherms show the hysteresis phenomena for the original MOF-801 (Zr) (solid black line) and $(\text{CH}_3)_2\text{-MOF-801}$ (Zr) (color dotted line) at the experimental temperature of 25 °C. *Source* ATE 175 (2020) 115, 393

compared with that of the original material. This is because of the fact that the implantation of the $-\text{CH}_3$ additives into the parent MOF-801 (Zr) not only reduces the size of the pore openings and the surface area of the MOF-801 (Zr) but also degrades the effect of interactions between water and $(\text{CH}_3)_2\text{-MOF-801}$ (Zr).

The adsorption isotherms of water plus MOF-801 (Zr) and water plus $(\text{CH}_3)_2\text{-MOF-801}$ (Zr) systems under equilibrium conditions are illustrated in Fig. 3.18a, b. The isotherms diagrams are shown here for the temperature varies from 25 °C to

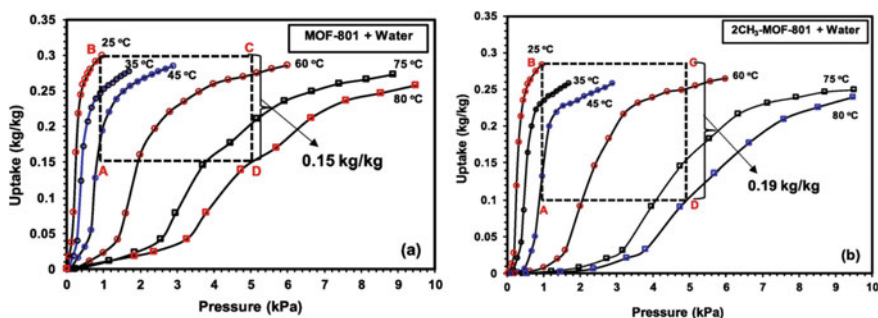


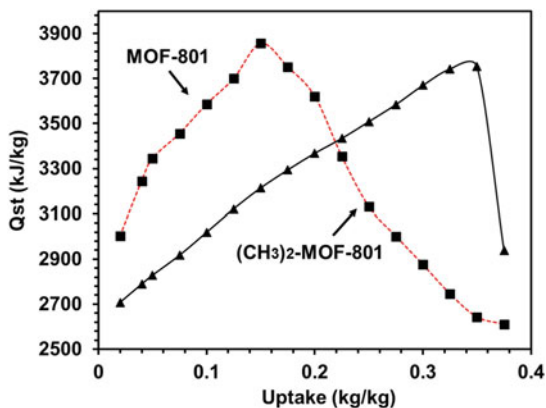
Fig. 3.18 Experimental results for water adsorption isotherms on **a** the parent MOF-801 (Zr) (Zr) and **b** $(\text{CH}_3)_2\text{-MOF-801}$ (Zr) adsorbents from 25 °C to 80 °C. Hence A-B-C-D loop indicates the thermal compression process under adsorption and desorption conditions, where C-D is the pre-cooling process, D-A defines the adsorption process, A-B indicates the pre-heating process, and B-C shows the desorption process. *Source* ATE 175 (2020) 115, 393

80 °C, and the pressure ranges from the low-pressure region to the saturated state. The adsorption-cooling performances can be predicted from the water adsorption isotherm analysis. However, the effects of adsorption kinetics should be considered. The performance in terms of cooling/heat pump is calculated by water storage capacity (Δq) per adsorption cooling cycle. In Fig. 3.18, the Δq ($= q_{ads} - q_{des}$) for both the original and $-\text{CH}_3$ implanted MOF-801 (Zr) are displayed with respect to adsorption chiller operating conditions, in which adsorption experiment is performed at 1 kPa and 25 °C, and desorption investigation is conducted at 5 kPa and 80 °C.

The Δq of $(\text{CH}_3)_2$ -MOF-801 (Zr) is found 25% more as compared to that of the original MOF-801 (Zr), which is due to very enhanced interactions between water and $-\text{CH}_3$ implanted MOF i.e., the space-loss effects are observed in the original materials. Additionally, it is found that at the heat source temperature of 75 °C, the Δq is found to be 0.09 kg/kg for the original MOF-801 (Zr), and the Δq for the water plus $(\text{CH}_3)_2$ -MOF-801 (Zr) system is 0.14 kg/kg at the same operating conditions. Hence, $-\text{CH}_3$ functional group in MOF-801 (Zr) reduces the pore volume and pore size of the parent MOF-801 (Zr). Still, it increases the water interaction, which does not override the smaller pore-openings (i.e., more micro-pores are generated) of methyl functionalized MOF-801 (Zr) pore. Therefore, a significant decrease of the water uptake (q) is observed at higher regeneration temperatures (> 60 °C). On the other hand, the Δq increases.

The isosteric heat of adsorption (Q_{st}) evaluated on the basis of Clausius Clapeyron equation for water adsorption on various fumarate-based MOFs systems are shown in Fig. 3.19. A rapid increase in Q_{st} is found for MOF-801 (Zr) at the low uptake region, and it is mainly because abundant water molecules are adsorbed violently onto the high-energy pore site at the beginning of adsorption. As the pressure increases, a continuous decrement of Q_{st} is observed. Similar trends are found for $(\text{CH}_3)_2$ -MOF-801 (Zr) except that there is a quick drop-in Q_{st} at the saturation pressure point, which indicates abundant meso and macro pores are available in $(\text{CH}_3)_2$ -MOF-801 (Zr) structure. This can also be observed from the PSD distribution curves, as shown in N_2 characterization section. Generally, by implanting the methyl functional group

Fig. 3.19 Isosteric heat of water adsorption on original and $-\text{CH}_3$ implanted MOF-801 (Zr) based systems. Here, (■) is MOF-801 (Zr) plus Water, and (▲) indicates $(\text{CH}_3)_2$ -MOF-801 (Zr) plus water adsorption systems



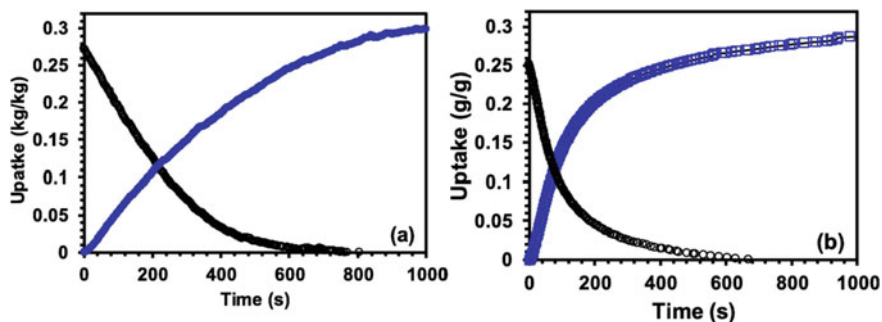


Fig. 3.20 Under dynamic conditions, water adsorption kinetics on (a) MOF-801 (Zr) and (b) $(\text{CH}_3)_2$ -MOF-801 (Zr) at 1 kPa and 30 °C for adsorption and 5 kPa and 60 °C for desorption conditions of a thermal compression system. *Source* ATE 175 (2020) 115, 393

into MOF-801 (Zr), the water plus $(\text{CH}_3)_2$ -MOF-801 (Zr) interaction is increased. Therefore, as the pressure (water uptake) increases, the additional interaction between MOFs-framework and water vapor will result in the increment of Q_{st} .

Under dynamic conditions, the amount of the water vapor uptakes as a function of time for both the original and $-\text{CH}_3$ implanted MOF-801 (Zr) materials are displayed in Fig. 3.20a, b, in which the kinetics data are plotted under the operation conditions of an adsorption chiller, where the adsorption occurs at 1 kPa and 30 °C, and desorption takes place at 5 kPa and 60 °C. The adsorption kinetics data are obtained from $t = 0$ up to the equilibrium condition. As can be shown in Fig. 3.20 that up to 600 s, $(\text{CH}_3)_2$ -MOF-801 (Zr) shows twice faster adsorption kinetics as compared to that of the original MOF-801 (Zr). It takes the parent MOF-801 (Zr) about 1000 s to reach the equilibrium.

It is noted here that the interactions between the adsorbate and adsorbent depend on pore chemistry and topology [74, 75]. By embedding $-\text{CH}_3$ in the pore-structure of MOF-801 (Zr), the pore topologies in the original MOF structure can be changed, i.e., the total pore volume is lessened and more narrow pores are generated. Hence, the narrow pores enhance the binding energies between the $(\text{CH}_3)_2$ -MOF-801 (Zr) and water vapor, which could also be explained by the interatomic mechanisms. At first, the water molecules move inside the “methyl functional group-blocked pores” and lead to the higher electrostatic potential, LJ (Lennard-Jones) potential, the induction interaction as well as the high order interactions. Additionally, the lateral attractions between adsorbed water molecules in MOFs pores are also enhanced at higher pressure due to the existence of methyl functional group-blocked pore walls. All these factors enhance the overall interactions between the $(\text{CH}_3)_2$ -MOF-801 (Zr) and water, as compared to that of the original MOF-801 (Zr) adsorbent. Therefore, with the injecting of methyl functional group, (i) the pore-blocking effect is resulted, (ii) the stronger interaction potentials are achieved, and (iii) the faster adsorption/desorption kinetics are obtained. However, the reduction of pore volume reduces the limiting uptake slightly.

From the kinetic theory of gas, the desorption kinetics should be faster than that of adsorption as at relatively higher pressure and temperature, and water vapor moves in the adsorbent-pores quickly. As can be observed from Figs. 3.20 (a) and 20 (b) that the desorption-equilibrium is reached less than 600 s for the parent MOF-801 (Zr), and it is observed that up to 200 s, methyl functionalized MOF-801 (Zr) provides twice faster desorption kinetics.

3.5.2 *Al Fumarate and MOF-Zeolite Composite Plus Water*

Figure 3.21a–c shows water adsorption isotherms on the synthesized Al-Fum-based materials at 30 °C for various relative pressures. The maximum water vapor uptake on aluminium fumarate is found to be 0.4 kg/kg, which can be compared with published work available in the literature [23, 76]. The porosities of Al-Fum MOFs define the nature of water interactions, which also calculates the shape of the adsorption isotherm. Generally, water vapor firstly adsorbs onto the pore sites of the MOFs with higher energy; however, it is not equivalent to the strong binding energy between the adsorbent and the adsorbate. When the pore size is too big as compared with the water molecule, the interactions become weaker, and relatively lower water uptakes are the result. For example, the weaker interactions between the larger pores and the water vapors at the low-pressure region are the main cause for the hydrophobic behavior of the water plus the Al-Fum adsorption system. Due to the increment of relative pressure in the adsorption bed up to $P/P_s \approx 0.20$, more water molecules penetrate into the micro-pores of the Al-Fum. As a result, the binding energy dominates, and the water uptake increases sharply in the low pressure or at the beginning of adsorption. Secondly, at moderate and higher pressure, some water vapors are adsorbed onto the lower energy pore sites. Therefore, the interactions between the adsorbate and adsorbent become slower, and the slope of uptake versus pressure becomes more gentle. For Al-Fum plus water system, the hydrophobic length is found up to the relative pressure (P/P_s) up to 0.2. Furthermore, more micro-pores are generated by the combination of parent Al-Fum MOFs and zeolites or doping MOFs with lithium cations. Hence, the interaction between the water and modified Al-Fum-based adsorbent can be improved from the low-pressure region, which thereby, the hydrophilicity is enhanced and the hydrophobic length is reduced. For example, the hydrophobic length of the modified Al-Fum-based adsorbents can be decreased up to $P/P_s \rightarrow 0.15$ by mixing 10% to 50% (in weight basis) AFI/CHA based zeolites on parent aluminium fumarate.

Experimentally, it is found that the water uptake capacity of the zeolite mixed adsorbents decreases. On the other hand, the water transfer on these composite structures is found better for the relative pressure varying from 0.2 to 0.25 with respect to chiller-operating conditions. Hence 50% AFI-Al-Fum composite provides the higher water transfer. As can be shown in Fig. 3.21b that the same trends are observed CHA-Al-Fum composites too. Additionally, Fig. 3.21c shows the impacts of alkali-ions on MOFs structure, and 5% Li-Al-Fum adsorbent exhibits better performances in terms

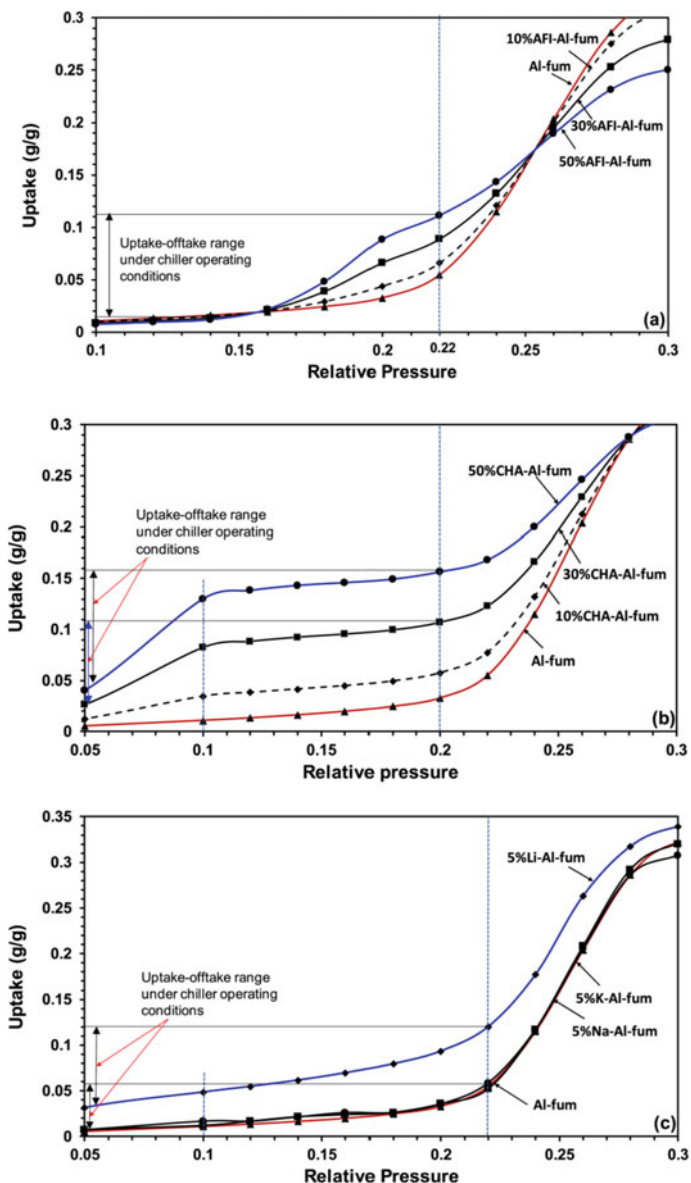


Fig. 3.21 Isotherms for water uptakes on **a** the parent and 10%, 30%, and 50% AFI-Al-Fum MOFs, **b** parent and 10%, 30%, and 50% CHA-Al-Fum MOFs, (c) parent and 5% Li^+ , Na^+ and K^+ doped Al-Fum MOFs at the adsorption temperature of 30 °C (Source: Microporous and Mesoporous Materials 288 (2019) 109,590)

of higher Δq under adsorption assisted cooling system working conditions. Higher water uptake is presented with the relative pressure varies from 0 to 0.25 as Li^+ dopants provide hydrophilic behaviors. On the other hand, Na^+ and K^+ dopants do not provide significant improvements on the original Al-Fum for higher water transfer per cycle, which is because of the larger size of Na^+ / K^+ ions as compared to Li^+ ions.

The uptake data in the form of adsorption isotherms or (uptake vs. pressure) coordinate system is displayed in Fig. 3.22a–d for (a) the original aluminium fumarate, (b) 5% Li-Al-Fum, (c) 30% CHA-Al-Fum, and (d) 30% AFI-Al-Fum composites plus water systems. These results are provided here for the temperatures ranging from 30 to 60 °C. In Fig. 3.22, the water uptake-offtake loop (A-B-C-D) is illustrated in the form of both adsorption and desorption, where the water transfer per thermal compression cycle i.e., Δq per operation cycle, is depicted with respect to adsorption (1 kPa and 30 °C) and desorption (5 kPa and 60 °C) conditions. As shown in Fig. 3.22a, b, the Δq values of the original and Li cations added Al-Fum MOFs plus water per cycle are found almost the same. Furthermore, the Δq /cycle for 30% AFI-Al-Fum and 30% CHA-Al-Fum MOFs composites plus water systems are calculated 12% and 17% lower as compared to that of the original Al-Fum material, and these

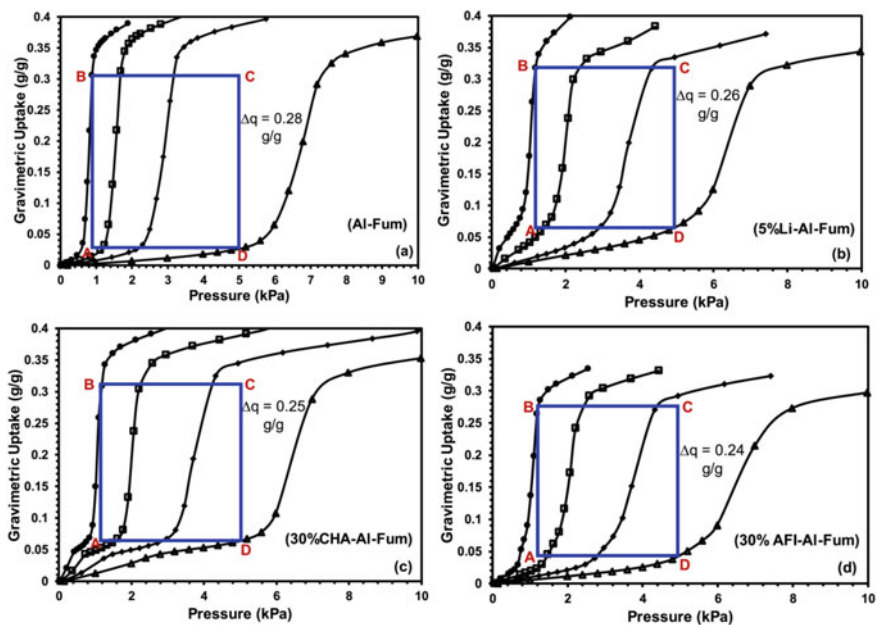


Fig. 3.22 Plots of adsorption isotherms for parent and modified Al-Fum plus water systems, where temperatures range from 30 to 60 °C: **a** original Al-Fum MOFs, **b** 5% Li Al-Fum MOFs, **c** 30% CHA-Al-Fum MOFs, **d** 30% AFI-Al-Fum MOFs. Hence, (●) indicates 30 °C, (□) stand for 40 °C, (◆) represents 50 °C and (Δ) is 60 °C. *Source* Microporous and Mesoporous Materials 288 (2019) 109, 590

results are shown in Fig. 3.22c, d. It should be noted here that the $\Delta q/\text{cycle}$ for AFI-type zeolites and CHA-type plus water systems are observed to be 0.15 kg/kg and 0.05 kg/kg, respectively.

The experimental data for water uptakes on Al-Fum based adsorbents are shown in Fig. 3.22 for pressures from Henry's regions to the saturated regions and temperatures ranging from 30 °C to 60 °C (30 °C, 40 °C, 50 °C, 60 °C), which will be deduced to the isosteric adsorption heat. Figure 3.23 illustrates the isosteric heat (Q_{st}) of water adsorption on the original and post-synthesis Al-Fum MOFs based on Clausius–Clapeyron relation $\ln(P)/dT = -Q_{st}/RT^2$ with a wide temperature range from 30 °C to 60 °C, where P indicates the adsorption pressure, R stands for the gas constant for water, and T represents the experiment temperature. A sharp increase of Q_{st} for Al-Fum and 5% Li-Al-Fum is observed at low water uptake region, which is due to the rapid adsorbed process of the water molecules onto the higher energy pore sites.

Therefore, the post-synthesis process enhances the sample affinity to water molecules. A relative steady Q_{st} level is found for the water uptakes from 0.1 kg/kg to 0.3 kg/kg for all the adsorption systems. This is because of the fact that as the adsorption process continues, more water vapors are adsorbed onto lower energy sites of the Al-Fum-based material pores. Furthermore, an increase in Q_{st} is observed for both 30% AFI-Al-Fum and 30% CHA-Al-Fum MOFs near the saturated regions as the interactions between water molecules are increased.

The water adsorption–desorption rates on the synthesized-Al-Fum-based MOFs at 30 and 60 °C are displayed in Fig. 3.24a–d. The practical working criteria of the adsorption assisted chiller are applied as a reference in the water adsorption experiments for a better investigation of the Al-Fum-based MOFs kinetics performance. Firstly, the water adsorption kinetics is characterized at 30 °C, where the

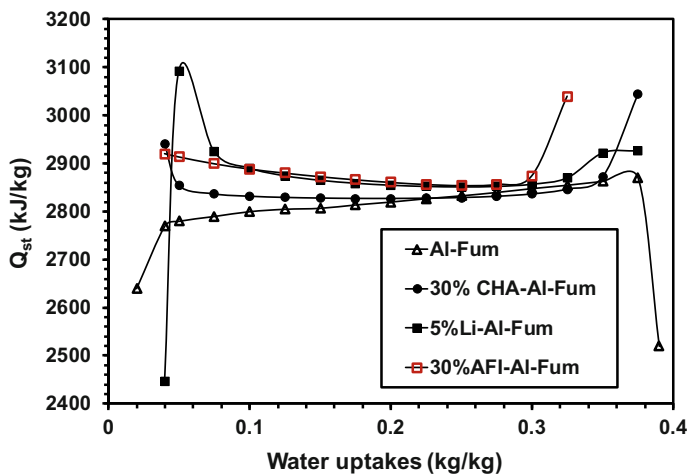


Fig. 3.23 Isosteric heats for the water adsorption on the parent Al-Fum, 5% Li-Al-Fum, 30% AFI-Al-Fum and 30% CHA-Al-Fum for temperature from 30 to 60 °C. *Source* Microporous and Mesoporous Materials 288 (2019) 109, 590

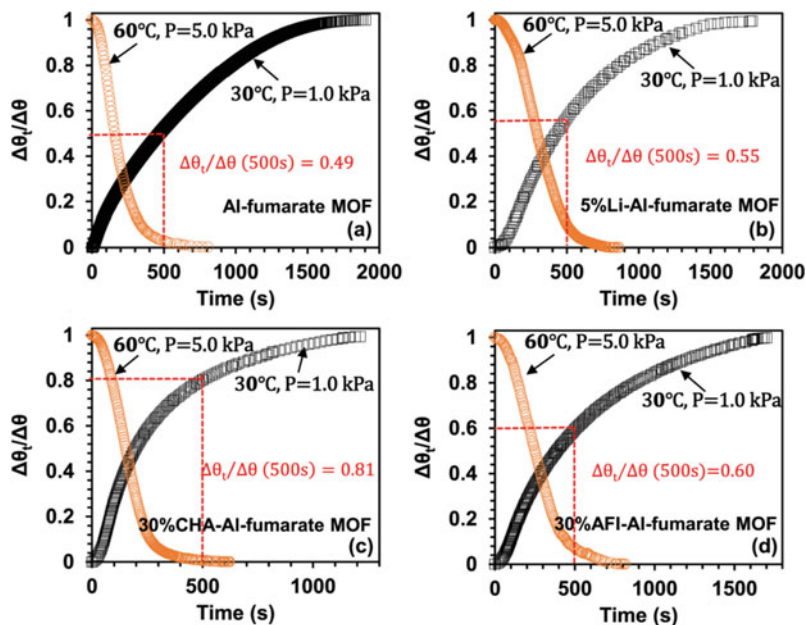


Fig. 3.24 The kinetics diagram of the water adsorption/desorption on the original and modified Al-Fum-based MOFs at the temperature of 30 °C and 60 °C. Here **a** original Al-Fum, **b** 5% Li-Al-Fum **c** 30% CHA-Al-Fum, and **d** 30% AFI-Al-Fum. *Source* Microporous and Mesoporous Materials 288 (2019) 109, 590

pressure is rising from extremely low pressure ($P/P_s \leq 0.05$) to 1 kPa ($P/P_s \approx 0.24$) directly. Secondly, the desorption kinetics is tested at 60 °C, where the AL-Fum based MOFs are immediately desorbed at 60 °C, 5.0 kPa ($P/P_s \approx 0.25$). To minimize uncertainties, all the experiments are conducted three times. The adsorption–desorption kinetics results are displayed from the beginning to the equilibrium state, from where one can conclude that the adsorbent structures have great effects on the adsorption–desorption period. It is found that the water uptake/offtake rates of the original Al-Fum MOFs are significantly improved by the alkali cations adding or conventional zeolite-based adsorbent mixing method. The overall kinetics ranking of all the parent and modified Al-Fum-based MOFs could be summarized as CHA-Al-Fum > AFI- Al-Fum > Li dope Al-Fum > original Al-Fum. It is observed that 30% CHA-Al-Fum adsorbent exhibits higher performances in terms of water adsorption (30 °C) and desorption (60 °C) kinetics (Fig. 3.24) as compared to those of the original Al-Fum material. The addition of the AFI/CHA zeolite leads to numbers of micro-pores generation in the parent Al-Fum MOF structure. Therefore, enhanced electrostatic and interatomic interaction potentials have resulted between water and zeolite-MOF composite. Experimentally, it is observed for adsorption kinetics investigation (30 °C), (i) the original Al-Fum requires about 1900s to reach equilibrium

Table 3.4 Total experimental duration (in the unit of hours) needed for one complete adsorption-desorption cycle employing the parent and modified Al-Fum MOFs as adsorbent

Samples	30 °C	40 °C	50 °C	60 °C
Al-Fum MOF	94.2	77.9	63.2	43.1
Li-Al-Fum MOF (5%)	90.2	72.8	59.3	30.7
AFI-Al-Fum MOF (30%)	84.0	60.3	43.2	36.1
CHA-Al-Fum MOF (30%)	29.2	26.3	18.7	12.5

(Fig. 3.24a), (ii) the modified 5% Li-Al-Fum MOF needs the 1790s for steady conditions (Fig. 3.24b), (iii) 30% CHA-Al-Fum reaches equilibrium at 1214 s and 30% AFI-Al-Fum requires 1702s to reach equilibrium states (Figs. 3.24 c, d), (iv) for practical adsorption assisted cooling system working conditions (i.e., half-cycle time = 500 s), the original Al-Fum completes 49% of the overall adsorption process, whilst 5% Li-doped Al-Fum, 30% AFI-Al-Fum and 30% CHA-Al-Fum accomplish 55%, 60% and 81% of the overall adsorption process, respectively. Furthermore, it is found that the water offtake rates are faster as compared to that of the water uptake rates at higher temperatures for all the adsorption cases.

All the desorption experiments for Al-Fum-based materials could be finished within 1000 s, especially for CHA/ Al-Fum (around 500 s). The doubts about whether the experiment reaches the full equilibrated state are mainly caused by the limitation of the apparatus. For one step of the adsorption experiment under certain pressure and temperature, the adsorbents (Al-Fum-based materials) will keep adsorbing water, and the mass of the Al-Fum-based MOFs will keep increasing. The current adsorption step will continue if the increase of the adsorbent mass is detected within the weight change tolerance and short time interval (which depends on the machine's characteristics and could not be changed). However, the experiment process will move on to the next adsorption set point automatically if there is no significant mass change of the adsorbent detected by the machine. Therefore, some of the kinetics graphs at the equilibrium state may behave stiffly rather than asymptotic even the curve is reaching coverage 1. Nonetheless, in that case, the current adsorption process should be fully equilibrated. Table 3.4 shows the total times need for one complete uptake-offtake cycle employing parent and modified Al-Fum MOFs, from where one can understand that the overall uptake/offtake kinetics is improved by employing the alkali ion-doped or zeolite-based adsorbent mixed Al-Fum materials.

3.6 Thermodynamic Frameworks of Adsorption Assisted Cooling

Two-bed adsorption assisted cooling (ADC) system is structured by an evaporator, a condenser, and a pair of adsorption/desorption beds. For a complete ADC operation cycle, four steps, namely isosteric cooling, isobaric adsorption, isosteric heating, and

isobaric desorption, are involved. By monitoring the valve states and the direction of the cooling/hot water supply, the adsorbent beds are refreshed, and continuous cooling is achieved in the evaporator. The adsorption-triggered-evaporation procedure and the desorption-activated-condensation process are shown schematically in Fig. 3.1. Hence, specific amounts of solid porous adsorbents (original or modified MOFs) are installed in the fin-tube adsorption beds. For the adsorption process, as a result of the supply of chiller water (cooling load, Q_{evap}) to the evaporator, the refrigerant (water here) is kept releasing from the evaporator and being adsorbed by the porous adsorbent placed in adsorption-bed (mass transfer from the evaporator). The adsorption heat (Q_{ads}) is removed by circulating the cooling water. Water vapor is adsorbed onto the bed until the bed pressure is equivalent to the evaporator pressure.

During the desorption process, the desorption-bed is constantly heated up (by Q_{des} amount) by circulating hot water through the heat exchanger tubes at the regeneration temperature of T_{des} . Therefore, the water vapor is dehydrated from the porous adsorbent by the driving heat source Q_{des} . The released water vapor enters into the condenser and condenses at condenser pressure P_{cond} and the heat rejection temperature of T_{cond} . The condensation heat Q_{cond} is removed by the cooling water at the same time. Both adsorption and desorption processes require some-times to reach equilibrium. After adsorption and desorption, all mass-transfer valves between beds and evaporator/condenser are closed, and the whole ADC system changes into a pre-heating or pre-cooling state. The cooling and hot water are redirected inside the two adsorption beds, and the role of the two adsorption/desorption beds are switched. After switching, the normal adsorption–desorption process continues to complete the batch operation of the ADC. In the ADC cycle, the enthalpy of evaporation is used for cooling purposes. The combined effects of enthalpies of condensation and adsorption are used as the required heating effect.

3.6.1 Adsorption Isotherms and Kinetics Fitting

The experimental MOFs and MOFs-zeolite composite plus water adsorption show type I and type V (“S-shaped”) isotherms which could be well fitted by the following isotherm equation [77].

$$\theta = \frac{K \left(\frac{P}{P_s} \right)^m}{1 + (K - 1) \left(\frac{P}{P_s} \right)^m} \quad (3.1)$$

where $\theta = q/q^0$ indicates the surface coverage, q^0 is the limiting uptake, and q represents the uptake under equilibrium state as a function of pressure and temperature. The adsorption equilibrium constant $K = \alpha \exp[m(Q_{st}^* - h_{fg})/RT]$, where m stands for the heterogeneous coefficient, α represents the pre-exponential coefficient, h_{fg}

denotes the evaporation-enthalpy and Q_{st}^* defines the isosteric heat at zero coverage. Furthermore, R represents the universal gas constant.

Based on the Langmuir analogy [78], $K = k_{ads}/k_{des}$, Where k_{ads} indicates the adsorption rate coefficient and k_{des} denotes the desorption rate coefficient. Under the equilibrium states of adsorption/desorption process, substituting $K = k_{ads}/k_{des}$ into Eq. (3.1), the surface coverage becomes:

$$k_{ads}(1 - \theta) \left(\frac{P}{P_s} \right)^m = k_{des} \theta \left[1 - \left(\frac{P}{P_s} \right)^m \right] \quad (3.2)$$

where $k_{ads} = W\beta A_s$, A_s indicates the BET surface area of the adsorbent. β represents the sticking coefficient, and it is given by $\beta = [\beta_0 \exp(E_a/RT)]$, where β_0 is the pre-exponential or frequency factor with unit value for monolayer; E_a resembles the activation energy. W stands for the adsorbate molecule-collision with the adsorbent surface per unit time and it is given by $W = MP/\sqrt{2\pi MRT}$, where M denotes the adsorbate molecular weight. Therefore, the water vapor uptakes with respect to time can be calculated under non-equilibrium conditions

$$\frac{dq}{dt} = k_{ads}(1 - q) \left(\frac{P}{P_s} \right)^m - k_{des}q \left[1 - \left(\frac{P}{P_s} \right)^m \right] \quad (3.3)$$

$$\frac{dq}{dt} = k_{ads} \left(\frac{P}{P_s} \right)^m - q \left\{ k_{ads} \left(\frac{P}{P_s} \right)^m \text{ plus } k_{des} \left[1 - \left(\frac{P}{P_s} \right)^m \right] \right\} \quad (3.4)$$

Hence the time constant is given as $\frac{1}{\tau} = k_{ads} \left(\frac{P}{P_s} \right)^m \text{ plus } k_{des} \left[1 - \left(\frac{P}{P_s} \right)^m \right]$, therefore Eq. (3.4) becomes

$$\frac{dq}{dt} = k_{ads} \left(\frac{P}{P_s} \right)^m - q \frac{1}{\tau} \quad (3.5)$$

Tables 3.5 and 3.6 show the water adsorption kinetics and isotherms fitting parameters on the original and $-\text{CH}_3$ implanted MOF-801 (Zr). On the other hand, the kinetics and isotherms fitting parameters for the parent Al-Fum/lithium ions added Al-Fum/Al-Fum-zeolite composite plus water systems are furnished in Tables 3.7 and 3.8, respectively.

Table 3.5 Parameters of isotherm fitting for water adsorption on various parent and modified MOF-801 (Zr) adsorbents

System	q^0 (kg/kg)	Q_{st}^* (kJ/kg)	m	α
MOF-801 (Zr) plus Water	0.31	3132.5	3.2	4.54×10^{-3}
$(\text{CH}_3)_2$ -MOF-801 (Zr) plus Water	0.30	3110.5	3.3	7.78×10^{-4}

Table 3.6 Kinetics fitting parameters for water adsorption on various parent and modified MOF-801 (Zr) adsorbents

System	k_{ads} (1/s)	$E_a@30^\circ\text{C}$ (J/mol)	β_0	k_{des} (1/s)	$E_a@60^\circ\text{C}$ (J/mol)
MOF-801 (Zr) plus Water	1.694	39,800	1	0.0037	43,300
(CH ₃) ₂ -MOF-801 (Zr) plus Water	3.193	37,900	1	0.0061	42,000

Table 3.7 Parameters of isotherm fitting for water adsorption on parent and modified Al-Fum-based adsorbents

System	q^0 (kg/kg)	Q_{st}^* (kJ/kg)	m	α
Al-Fum plus Water	0.40	2786.5	6.8	9.98×10^{-5}
5%Li-Al-Fum plus Water	0.41	2861.4	5.7	1.86×10^{-5}
30%AFI-Al-Fum plus Water	0.34	2877.5	5.6	1.12×10^{-5}
30%CHA-Al-Fum plus Water	0.39	2781.2	5.9	3.49×10^{-4}

Table 3.8 Kinetics fitting parameters for water adsorption on parent and modified Al-Fum-based adsorbents

System	k_{ads} (1/s)	$E_a@30^\circ\text{C}$ (J/mol)	β_0	k_{des} (1/s)	$E_a@60^\circ\text{C}$ (J/mol)
Al-Fum plus Water	1.177	41,200	1	0.0041	40,100
5%Li-Al-Fum plus Water	1.183	41,100	1	0.0039	43,500
30%AFI-Al-Fum plus Water	1.122	42,700	1	0.0052	42,600
30%CHA-Al-Fum plus Water	2.177	39,500	1	0.0068	40,780

3.6.2 ADC System Modelling

Numbers of papers describing the thermodynamic frameworks of the adsorption–desorption process for various heat transformation applications such as heat pump, cooling and distillation/ desalination are available in the literature. For simplicity, the lumped thermal capacity model is considered. The limitations of the thermodynamic modelling are (i) the adsorption bed temperature depends on time, i.e., the temperature is independent of space and position of bed, and (ii) the simulation domain begins with initial conditions and stops by setting a tolerance or error between the last two values as a function of time.

It should be noted here that (i) the chilled water flows through the heat exchanger in the evaporator, and (ii) the high heat sink temperature ($>25^\circ\text{C}$) generating from the TES (thermal energy storage) provide the extra cooling loads to the AHT system.

For the generation of continuous cooling, heating, and desalination, the refrigerant (hence water vapor) under low-pressure conditions is evaporated and flows into the porous adsorbents of the bed. The combination of sensible and latent heat flow is involved in the evaporator by (i) the transfer of heat from cooling/chilled water to the refrigerant via the copper tubes and (ii) energy transmission from the evaporated water vapor to the adsorption bed. Both the mass and heat interactions between the adsorption bed and the evaporator evolve the energy balance within the evaporator as given by the following equation

$$(Mc_p)_e \frac{dT_e}{dt} = -h_{fg} M_s \frac{dq_a}{dt} + (UA)_e \frac{1}{N} \sum_{i=1}^N (T_e - T_i) - h_f M_s \frac{dq_d}{dt} \quad (3.6)$$

The water uptake and offtake rates $\frac{dq_a}{dt}$ and $\frac{dq_d}{dt}$ are evaluated by the adsorption kinetics and isotherms models. Secondly, the heat capacity of the copper tube-heat exchanger, as presented on the left-hand side of Eq. (5.1), becomes $(Mc_p)_e [= M_{ehx}c_{p,ehx} + M_w c_{p,w}]$. Thirdly, the first item of the right-hand-side of Eq. (5.1) shows the latent heat involved during evaporation, the second terms present the liquid phase enthalpy in the evaporator generation from condensate liquid, and the third term stands for the load generating from the supply of chilled/warm/cooling water. The chilled water temperature for each segment of the heat exchanger tube (T_i) becomes

$$\frac{V_e(\rho c_p)_{cw}}{N} \frac{dT_i}{dt} = (\dot{m}c_p)_{cw}(T_{i-1} - T_i) + \frac{(UA)_e}{N}(T_e - T_i) \quad (3.7)$$

The heat is evolved as the water vapor enters into the bed during adsorption. The generated heat in the bed-heat-exchanger is removed by flowing cooling water through the heat exchanger tubes. Furthermore, during pre-heating and desorption periods, the hot water is transferred to the heat-exchanger tubes of the bed. Therefore, the water vapor is rejected from the surface of porous adsorbents, i.e., the water vapor mass transfer takes place. All these phenomena as observed in the adsorption bed can be expressed mathematically by the following equation

$$(Mc_p)_b \frac{dT_{b,k}}{dt} = \psi \cdot M_s \frac{dq_{b,k}}{dt} \Delta H - \frac{(UA)_{b,k}}{N} \sum_{j=1}^N (T_{b,k} - T_j) \quad (3.8)$$

where k shows either water uptake (adsorption) or offtake (desorption) condition with flag $\psi = 1$ (for adsorption) and $\psi = -1$ (for desorption). The thermal heat capacity of the bed is shown on the left-hand side of Eq. (5.3) and is calculated with respect to the summation of heat and mass capacity of tube-fin-adsorbent heat exchanger plus the amount of water vapor in the adsorbed phase, e.g. $(Mc_p)_b [= M_{bhx}c_{p,bhx} + M_s(c_{p,s} plus q \cdot c_{p,a})]$. On the other hand, the right-hand side of Eq. (3.8) is related to the amount of energy input and output in the bed

control volume, in which the first term represents the latent-heat transfer due to the heat of adsorption, and the second term indicates the rejection of heat energy from the bed to the coolant fluid (during adsorption and pre-cooling periods) or the addition of heat to the bed by the driving heat source (hot water) during pre-heating and desorption periods. The amount of water vapor in the bed is calculated with respect to the bed temperature and evaporator/condenser pressure. The valves effects are considered to calculate the bed pressure under adsorption and desorption conditions. However, the bed pressure is based on isosteric conditions during pre-cooling and pre-heating periods. All these phenomena, as mentioned above, depending on the flow rates and temperature of the heat transfer fluid. Hence the temperature, T_i of the heat transfer fluid (hence hot and cooling water) for the N segment of heat-exchanger tubes is evaluated as

$$\frac{V_b(\rho c_p)_f}{N} \frac{dT_j}{dt} = (\dot{m}c_p)_f (T_{j-1} - T_j) + \frac{(UA)_{b,k}}{N} (T_b - T_j) \quad (3.9)$$

The term $V_b(\rho c_p)_f$ as shown on the left-hand side defines the total heat capacity of cooling/heating water passing through the tubes. On the other hand, the right-hand side relates to the heat input and output involved in fluid control volume in tubes. The water vapor is desorbed from the porous adsorbents by the supply of heating fluid to the heat exchanger tubes of the bed. The desorbed water vapor enters into the condenser, and condensation occurs. Cooling water flows through the condenser tubes, and heat is rejected to the environment simultaneously. Finally, the condensed fluid reflux-back to the evaporator via a U-tube or an expansion valve, which maintains the pressure difference between the condenser and the evaporator. In the present modeling, it is assumed that the condenser tube holds some liquid condensate. Therefore, the energy balance in the condenser is calculated based on (i) heat input from the desorbed water vapor as shown in the first term of the right-hand side of Eq. (3.9), (ii) the heat transfer from the condenser to the heat sink as indicated by the second term of the right-hand side, and (iii) the transfer of warm condensate through the expansion valve (3rd term of Eq. (3.9)). The condenser temperature (T_c) is calculated by

$$(Mc_p)_c \frac{dT_c}{dt} = -h_{fg}M_s \frac{dq_d}{dt} \text{ plus } \frac{(UA)_c}{N} \sum_{i=1}^N (T_i - T_c) + h_f M_s \frac{dq_d}{dt} \quad (3.10)$$

Hence $(Mc_p)_c$ is the total heat capacity of condensed water and heat exchanging tubes of condenser, and is defined by $[M_{chx}c_{p,chx} + M_w c_{p,w}]$. The cooling water temperature at each segment (total N segment) of the condenser heat exchanger tube is calculated by the following equation

$$\frac{V_c(\rho c_p)_c}{N} \frac{dT_i}{dt} = (\dot{m}c_p)_{cw} (T_{i-1} - T_i) + \frac{(UA)_c}{N} (T_c - T_i) \quad (3.11)$$

The amount of water uptake/offtake per adsorption–desorption cycle is obtained by the mass interaction during adsorption–desorption operation and the switching periods. The amount of sea water in the evaporator decreases as the evaporation of water vapor continues. Therefore, the mass balance in the evaporator becomes $\frac{dM_e}{dt} = -M_s \frac{dq_a}{dt} - M_s \frac{dq_d}{dt}$. The mass and energy balance equations are solved numerically, and a finite difference method is applied with the boundary and initial conditions. The computational region is discretized into many discrete elements having equal steps. In the programming code, the fins and MOFs adsorbents are considered as the same temperature at the initial condition and considered as a control volume. In the modeling, a one-dimensional transfer is assumed for the heat transfers through the fin. The temperature difference in the heat-exchanging tubes is approximated by a forward difference scheme. Double precision is used with the tolerance of 1×10^{-6} . The adsorption kinetics and isotherms are correlated by a series of subroutines. The simulated variables such as the temperature of adsorption/desorption beds and the amount of the water vapor uptake/offtake are continuously updated by numerical integration momentarily. The overall simulation of the AHT system begins with the initial conditions, and subsequent simulation automatically performs, from the dynamic state to the cyclic steady condition. The parameters [5, 79] for mass and energy balance frameworks are furnished in Table 3.9.

During the operation of the ADC system, both the heating and cooling power are generated simultaneously. Furthermore, the enthalpy of evaporation is applied for cooling purposes. In addition, the combined effects of enthalpies of the condensation (in the condenser) of working fluid and the adsorption (in the adsorption bed) could be used for heat pump applications. Mathematically, these useful effects for continuous cooling productions such as COP (coefficient of performance) and SCP (specific cooling power) can be evaluated under cyclic steady-state conditions. The calculation is time-based, where the total cycle time (t_{cycle}) comprises the switching period and adsorption–desorption operation period. The energy required for evaporation (Q_e) and desorption (Q_h) are calculated as

$$Q_e = \int_0^{t_{cycle}} \frac{(\dot{m}c_p)_{cw}(T_{cw,i} - T_{cw,o})dt}{t_{cycle}} \quad (3.12)$$

$$Q_h = \int_0^{t_{cycle}} \frac{(\dot{m}c_p)_{hw}(T_{hw,i} - T_{hw,out})dt}{t_{cycle}} \quad (3.13)$$

The performances of adsorption cooling such as SCP and COP are calculated by

$$SCP = \int_0^{t_{cycle}} \frac{(\dot{m}c_p)_{cw}}{M_s} \frac{(T_{cw,i} - T_{cw,o})dt}{t_{cycle}} \quad (3.14)$$

Table 3.9 The mass and energy balance parameters for the simulation of the ADC system

Parameter	Numerical description
c_p	750 J/(kg · K) at 300 K
M_s	18 kg
$(Mc_p)_b$	184.1 W/(m ² · K) [38]
$(Mc_p)_e$	(24 kg × 386 J/(kg · K) plus 5 kg × 4180 J/(kg · K)) [38]
$(Mc_p)_e$	(8.9 kg × 386 J/(kg · K) plus 40 kg × 4180 J/(kg · K)) [38]
T_f^i	30 °C
T_f^j	60 ~ 80 °C
T_{chill}^{in}	14.8 ~ 30 °C (Maintained by TES)
$(UA)_e$	(2557 W/(m ² · K) × 1.37 m ²) [6]
$(UA)_c$	(4115 W/(m ² · K) × 3.71 m ²) [6]
$(UA)_b$	10.3 kW/K (experimental investigation)
$(UA)_b$	9.85 kW/K (experimental investigation)
u_{cw}	0.20 m/s
u_{cw}	0.15 m/s (chilled water)
u_f	0.20 m/s (for heating)
$V_b = \pi r_0^2 L_t$	$r_0 = 8.6$ mm, $L_t = 2.5$ m
$V_e = \pi r_0^2 L_e$	$L_e = 2.0$ m, $r_0 = 8.6$ mm
$V_c = \pi r_0^2 L_c$	$L_c = 2.0$ m, $r_0 = 8.6$ mm
\dot{m}_f	2.08 kg/s for both beds
\dot{m}_{cw}	1.4 kg/s

$$COP = \frac{Q_e}{Q_h} \quad (3.15)$$

3.6.3 ADC Performance Analysis

3.6.3.1 Heat Transfer Fluid Dynamic Profile

Employing the proposed modelling, the temperature changes with respect to the operation time of the heat transfer fluids and the major components of the AHT (here, Al-Fum plus water pair as an example) are shown in Fig. 3.25. Hence, adequate cycles are run to minimize any single structure effects, and two half-cycles of the adsorber (Bed-1 and Bed-2) are exhibited under cyclic-steady-state. The regeneration temperature, chilled water temperature inlet, and cold water inlet temperature are kept at 80 °C, 14.8 °C, and 30 °C, respectively. The half-cycle time is fixed at 500 s. Initially,

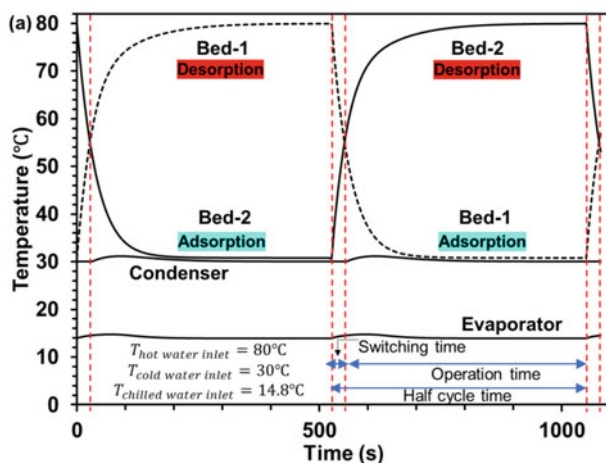


Fig. 3.25 Cyclic-steady-state overall temperature profiles of the Al-Fum—water ADC system as a function of time. Here, **a** temperature profiles of the evaporator, condenser, adsorption, and desorption chamber

Bed-1 is designed as the desorber where its temperature increases steeply from 32 to 76 °C by the heating processes with the external flow of hot water. In addition, Bed-2 is used as the adsorber, and a quick temperature decrease is observed due to the cooling effect by the supply of the coolant. Both the switching time and operation time are labeled in Fig. 3.25. During the switching periods, heat transfer fluids (cold and hot water) redirect, and the role of the two beds switches and temperature surges are found especially in sorption-beds. For the first half cycle, the hot/cold water outlet temperature reaches the regeneration/cooling water inlet temperature (80/30 °C) at about 300 s. The evaporator and condenser temperatures are also shown. Under the steady-state condition, it is found that the evaporator water outlet distributes around 13 °C (< 14.8 °C). Hence, continuous cooling power production is achieved. Furthermore, the heat generation in the adsorber and condenser could be applied in the adsorption heat pump application, and the condensed water can be used for water distillation purposes.

The variations of pressure with respect to temperature for Al-Fum and water-assisted cooling cycle are shown in Fig. 3.26, which is known as the Dühring diagram. Here, regeneration temperature, chilled water temperature inlet, and cold water inlet temperature are kept at 80 °C, 14.8 °C, and 30 °C, respectively. On the other hand, the operation and switching periods are optimized 500 s and 25 s for the best performance in COP and SCP. Four ADC operation stages, namely pre-cooling, adsorption, pre-heating, and desorption, are also provided in Fig. 3.26, from which one could understand the transient water vapor transfers under various pressure and temperature conditions. It is found that the maximum water vapor Δq per cooling cycle for the parent Al-Fum and zeolite-Al-Fum composites could be ranked as 5% Li-Al-Fum >30% CHA-Al-Fum >30% AFI Al-Fum > parent Al-Fum. During the switching

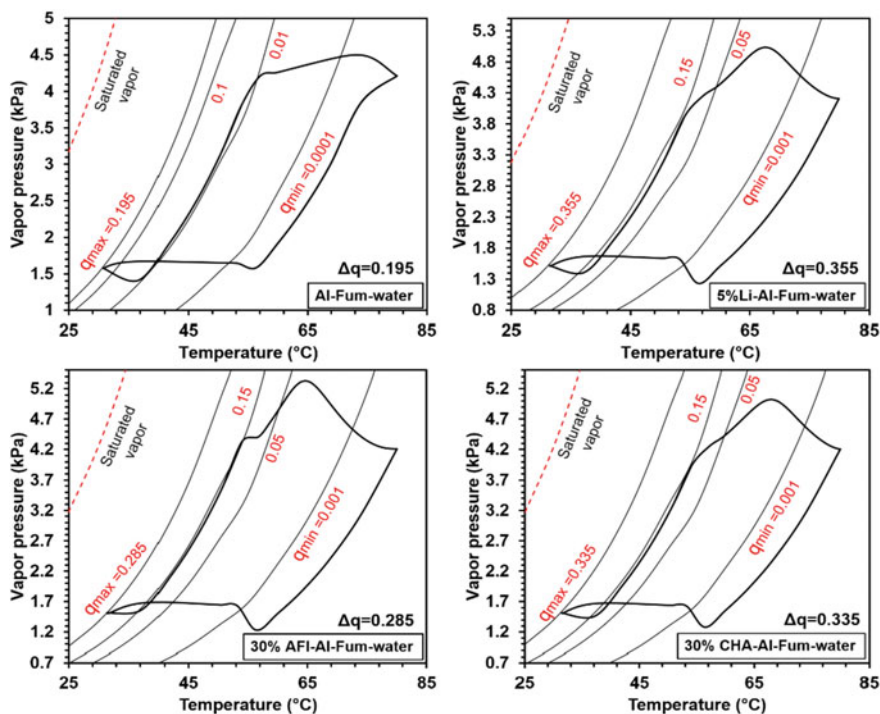


Fig. 3.26 The Dühring diagram (pressure versus temperature, P–T) for the original Al-Fum and zeolite-Al-Fum composites plus water-based ADC under cyclic-steady-state

time, the entire bed follows the isosteric path. It is noted here that the rise in pressure is observed during the adsorption process due to the presence of more water vapor with isosteric heat in the adsorption bed. Additionally, both the temperature and pressure increase at the end of the cold-to-hot thermal swing process in the bed. Hence, the desorption process occurs within the bed.

The Δq per adsorption cooling cycle for the original Al-Fum and composites plus water-based ADC system at various regeneration temperatures (60 to 90 °C) is furnished in Table 3.10. It is found that the regeneration temperature of 60 °C suits well for the original Al-Fum MOFs for its hydrophobic trait at the low-pressure region ($\Delta q = 0.192$ g/g). The maximum cooling capacity of the original Al-Fum is achieved at the regeneration temperature of 70 °C ($\Delta q = 0.195$ g/g), and no improvement of Δq is found when the regeneration temperature increases (> 80 °C). On the other hand, higher Δq under higher regeneration temperatures are found for all the modified Al-Fum-based MOFs for their enhanced hydrophilicity. For example, at the regeneration temperature of 60 °C, the Δq for 5% Li-Al-Fum, 30% AFI-Al-Fum, and 30% CHA-Al-Fum are 0.311 g/g, 0.255 g/g, and 0.285 g/g, respectively. As the regeneration temperature increases up to 70 °C, the Δq for 30% AFI-Al-Fum, 5%

Table 3.10 Water uptake-offtake difference (Δq) at various regeneration temperatures (from 60 to 90 °C) for original and modified Al-Fum based ADC systems (cold water inlet temperature/chilled water inlet temperature/switching time/half-cycle time = 30 °C/14.8 °C/25 s/500 s)

	Δq ($T_{regen} = 60$ °C)	Δq ($T_{regen} = 70$ °C)	Δq ($T_{regen} = 80$ °C)	Δq ($T_{regen} = 90$ °C)
Al-Fum	0.192	0.195	0.195	0.195
5% Li-Al-Fum	0.311	0.353	0.355	0.355
30%AFI-Al-Fum	0.255	0.284	0.285	0.285
30%CHA-Al-Fum	0.285	0.333	0.335	0.335

Li-Al-Fum and 30% CHA-Al-Fum are 0.284 g/g (plus 11.4%), 0.353 g/g (plus 13.5%) and 0.333 g/g (plus 16.8%), respectively.

3.6.3.2 Performance Factors: Influence of Heat Transfer Fluids

The hot water (driving heat source) inlet temperature (55–90 °C) affects the COP and the SCP for various original and modified MOF-based ADC systems, and these results are shown in Fig. 3.27. Here, the cooling water and the chilled water inlet temperature are 30 and 14.8 °C, while the half-cycle time is fixed at 400 s. For the parent (such as Al-Fum and MOF-801 (Zr)) and modified (Al-Fum–zeolite composites and functional MOF-801 (Zr)) adsorbents plus water systems, the best COP is obtained at the hot water inlet temperatures between 55 and 60 °C. The COP starts to drop when the regeneration temperature is higher than 60 °C. The reason is that all the Al-Fum based materials show “S-shaped” water adsorption isotherms with a medium hydrophobic length ($P/P_s > 0.22$); therefore, no evident enhancement of the water vapor transfer per thermal compression cycle is achieved at $T_{des} > 60$ °C. The maximum COP for 30% CHA-Al-Fum composite is 0.39 ($T_{des} = 60$ °C) while the maximum COP for 5% Li-Al-Fum, 30% AFI-Al-Fum and the parent Al-Fum are 0.37, 0.32, and 0.27, respectively ($T_{des} = 55$ °C). On the other hand, the SCP rises sharply between the regeneration temperature of 55 °C and 65 °C as the water vapor delivery per adsorption cooling cycle increases. When $T_{des} > 65$ °C, the SCP drops due to incomplete utilization of applied heat to the desorption bed for the rejection of water vapor. Therefore, the decrease of the Δq thermal compression cycle has resulted. At 65 °C, the maximum SCP for the functional MOFs and MOFs-zeolite composites (such as 30% CHA-Al-Fum, 5% Li-Al-Fum, 30% AFI-Al-Fum, and Al-Fum MOFs) are found to be 0.54, 0.45, 0.37, and 0.31 kW/kg, respectively. Unlike the Al-Fum group, MOFs such as MOF-801 (Zr) and $(\text{CH}_3)_2$ -MOF-801 (Zr) present type I resemble isotherms with water adsorption, and high regeneration temperature is required for a completed desorption process. Therefore, the evident increases of SCP and COP are found as the regeneration temperature increases. Additionally, MOF-801 (Zr) (0.498, $T_{des} = 90$ °C) and $(\text{CH}_3)_2$ -MOF-801 (Zr) (0.603, $T_{des} = 85$ °C) shows the maximum COP at higher heat source temperature due to the higher

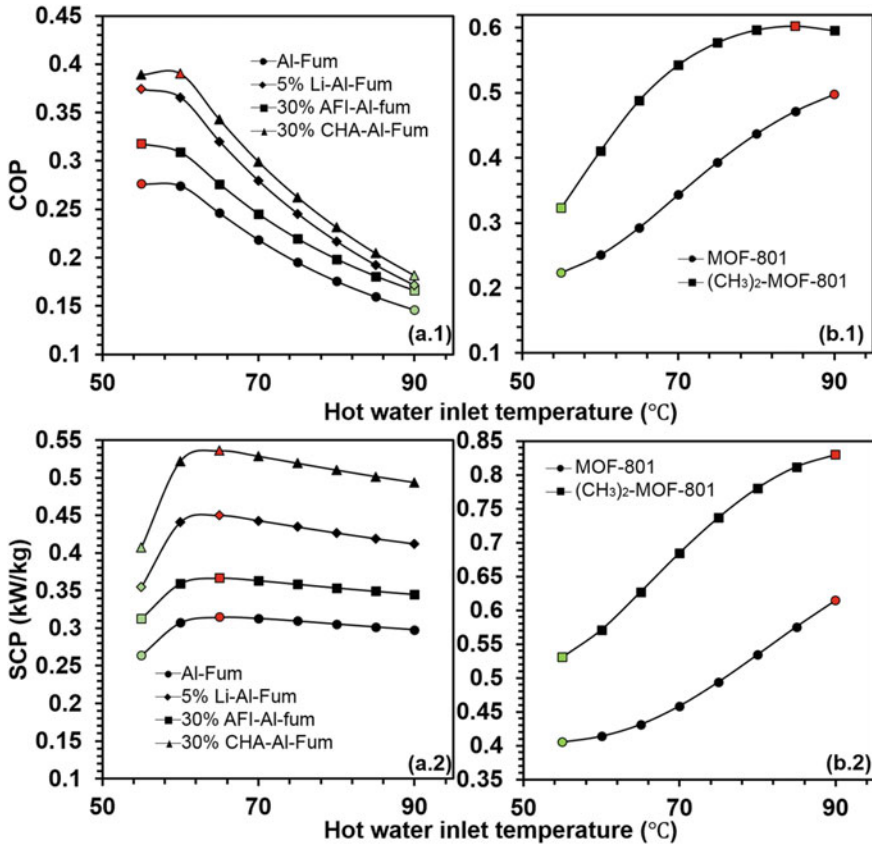


Fig. 3.27 Effects of regeneration temperatures on SCP (kW/kg) and COP for original and modified MOFs plus water-based adsorption chillers at the half-cycle time of 400 s and the cooling water inlet temperature of 30 °C

transfer of water vapor per thermal compression cycle. Similarly, at higher regeneration temperatures ($T_{des} > 80\text{ }^{\circ}\text{C}$), the functional $(\text{CH}_3)_2\text{-MOF-801}$ (Zr) adsorbent provides the highest SCP with the value of 0.83 kW/kg as compared with the parent MOFs.

It is found that all the modified MOFs present substantially better results as compared with the original MOFs. For example, at a lower regeneration temperature of 60 °C, 42.3% higher COP, and 70.0% more SCP are observed for 30% CHA-Al-Fum as compared with that of the parent Al-Fum. At the same time, similar results are found for 5% Li-Al-Fum (33.3% more COP and 43.5% more SCP) and 30% AFI-Al-Fum (12.6% higher COP and plus 17.0% higher SCP). Hence, the impressive ADC performances are obtained by the post-modification of the parent MOF materials. By balancing the ADC performances in terms of the SCP and COP, the optimal regeneration temperature is found between 55 °C and 65 °C (for Al-Fum

MOFs and zeolite plus Al-Fum composites adsorbent). In addition, higher COP and SCP are obtained by methyl-functionalized MOF-801 (Zr) adsorbents even at a lower regeneration temperature of 55 °C.

Figure 3.28 illustrates the effects of heat sink temperature (varying from 20 to 35 °C) on the ADC performances. Generally, the coolant fluid flowing through the adsorbent-heat exchanger absorbs heat from the adsorbent, which increases the water uptake capabilities. As furnished in Fig. 3.28, both the SCP and COP drop monotonously for all the assorted MOF adsorbents plus water systems as the heat sink temperature increases. The main reason is that the higher heat sink temperature leads to the decrement of Δq (water transfer) per adsorption cooling cycle. Due to higher heat sink temperature, the water uptake drops, and the water offtake increases, and the SCP decreases. Generally, water at room temperature is used as the heat sink for energy-saving purposes. At 25 °C, the original Al-Fum MOF delivers moderate performance with the SCP of 0.43 kW/kg and COP of 0.39. By doping the lithium

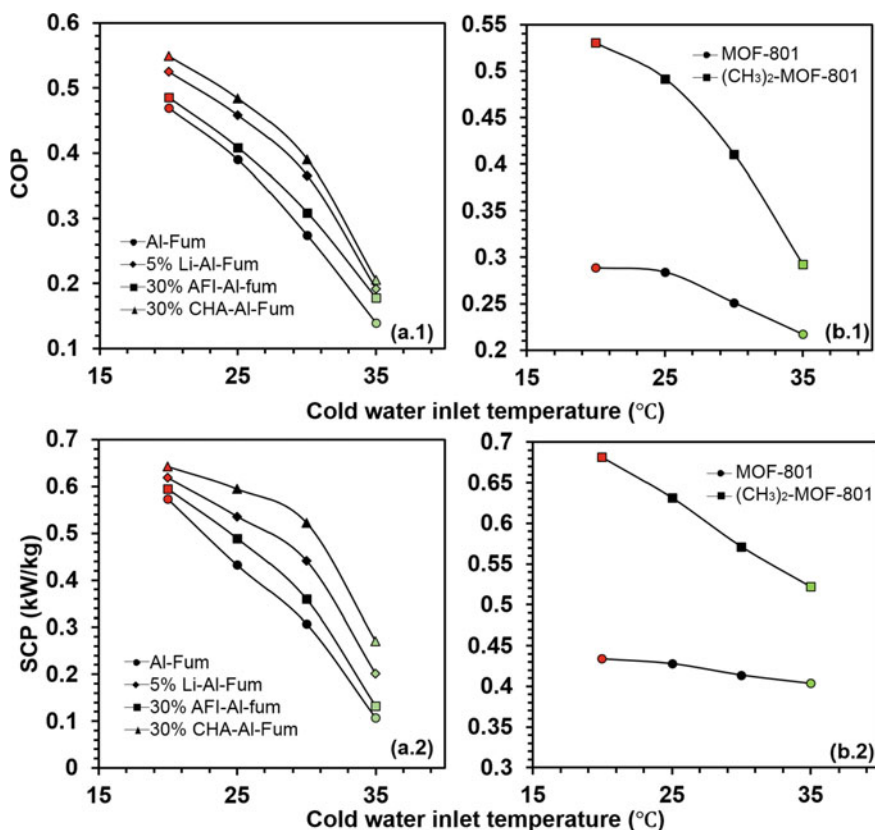


Fig. 3.28 The COP and SCP (kW/kg) at various cooling water inlet temperature original and modified MOFs—water adsorption chillers with the half-cycle time of 400 s and regeneration temperature of 60 °C

ions onto the Al-Fum structure (for 5% Li-Al-Fum), 17.5% higher COP (0.46) and 23.9% larger SCP (0.54 kW/kg) are obtained. In addition, 30% AFI-Al-Fum shows 4.7% higher COP (0.41) and 17.5% larger SCP (0.49 kW/kg) as compared with the parent Al-Fum. The best performance is found for 30% CHA-Al-Fum.

Water adsorption chiller, where the COP is 0.48 (24.1%), and the SCP is 0.59 kW/kg (37.6%). On the other hand, the functionalized MOFs also yield extensively better results in terms of COP and SCP as compared with original materials. As for the hydrophilic materials such as MOF-801 (Zr), the effect of the heat sink temperature on chiller behaviors is not significant. For example, only 7.4% drop of SCP (from 0.434 kW/kg to 0.404 kW/kg) is found for water plus MOF-801 (Zr) ADC system when the heat sink temperature increases from 20 °C to 35 °C. On the other hand, The cooling water inlet temperature provides significant effects on (CH₃)₂-MOF-801 (Zr) adsorbents, where the COP decreases 81.6% (from 0.53 to 0.29) and the SCP drops 30.6% (from 0.681 kW/kg to 0.522 kW/kg) when the heat sink temperature increases from 20 °C to 35 °C.

3.6.3.3 Effect of Half-Cycle Time

Figure 3.29 shows the SCP and COP of the original and modified MOF-based adsorbent–water adsorption assisted cooling system for the heat sink temperature of 30 °C and heat source (hot water) temperature of 60 °C at the various half-cycle time (τ). As shown in Fig. 3.29, the COP increases monotonically with τ for all the adsorbents. This is because that the water uptake/offtake process is not finished with a short half-cycle time, the heating energy is poorly utilized, and the Δq per thermal compression cycle is very low; hence, low COP has resulted. As the cycle time increases, the use of the heat energy is reduced significantly as compared with the reduction in the production of the cooling power, which results in a favorable impact on the COP. Hence, higher COP is obtained. From this standpoint, saturated COP is exceeded when a relatively long cycle time is considered. For Al-Fum-based adsorbent system, the largest COP ($\tau=1000$ s) for Al-Fum, 5% Li-Al-Fum, 30% AFI-Al-Fum and 30% CHA-Al-Fum is 0.446, 0.476, 0.539 and 0.564, respectively. Furthermore, 71.2% increase in terms of COP is found for (CH₃)₂-MOF-801 (Zr) (0.437, $\tau=1000$ s) as compared with that of original MOF-801 (Zr) (0.255, $\tau=1000$ s). It should be noted that the effect of the half-cycle time is considered negligible for MOF-801 (Zr) and (CH₃)₂-MOF-801 (Zr) when a longer cycle time is applied ($\tau > 600$ s). It is because that both of these materials exhibit impressively fast water adsorption kinetics, and 80% of the equilibrium state could be reached within 600 s (as shown in Fig. 3.20). Hence, no evident COP improvement is found when longer half-cycle time is employed ($600 < \tau < 1000$ s).

Unlike COP, the SCP (cycle average specific cooling power) delivers the nonmonotonic behaviors with the change of τ for the majority of the adsorbents. For the Al-Fum-based ADC system, the SCP increases rapidly up to 300 s, and the slope becomes more gentle when longer half-cycle time is applied (>500 s), where even a slight decrease is found for 5% Li-Al-Fum and 30% CHA-Al-Fum based

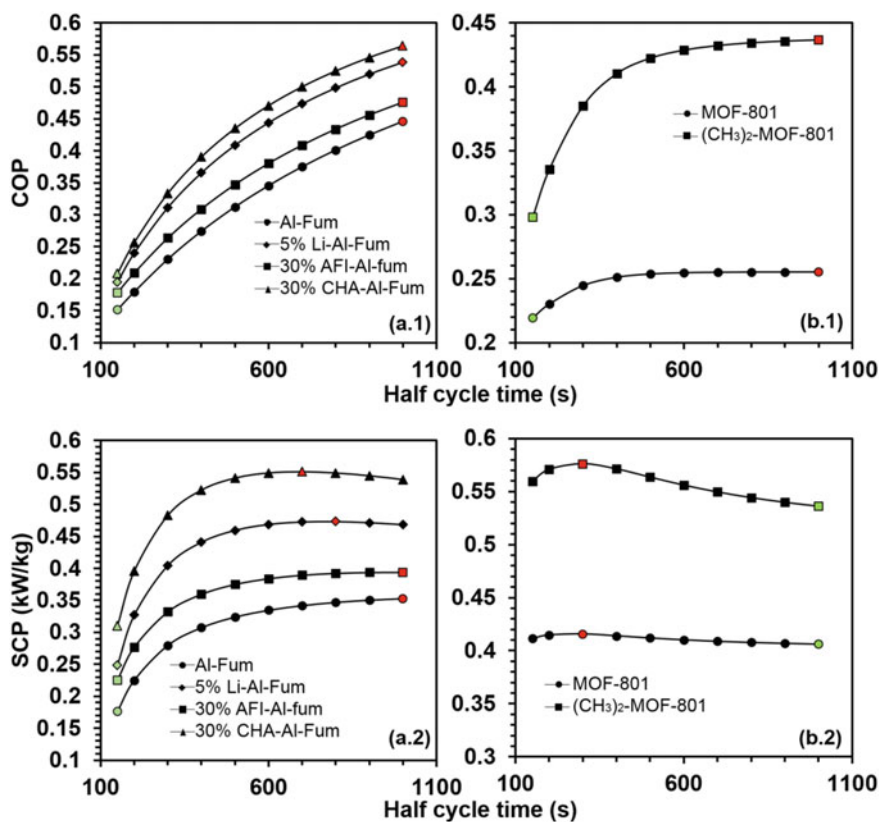


Fig. 3.29 Effects of half-cycle time on SCP (kW/kg) and COP for original and modified Al-Fum or MOF-801 (Zr) based adsorption chiller at the heat source o temperature of 60 °C and heat sink temperature of 30 °C. *Source* ATE 175 (2020) 115, 393

adsorption chiller. Hence, the highest SCP is labeled in red color, and the lowest SCP is marked in green. Lower SCP is found when a shorter half-cycle time (150 to 300 s) is applied, which is because that the adsorption and desorption processes are not fully complete with the scanty cooling and heating of the bed (lower Δq is caused). At the longer half-cycle time, more heat energy is utilized in the adsorption beds, and all the Al-Fum-based adsorbents approach their adsorption limit. Furthermore, reverse-adsorption may also be found for the MOF-801 (Zr) plus water system if a longer desorption cycle time is used, which is because of the strong adsorbent plus adsorbate interaction.

These constraints will lead to unfavorable cooling capacity and poor SCP. Hence, a decrease of SCP is found for MOF-801 (Zr) and $(\text{CH}_3)_2\text{-MOF-801}$ (Zr) when a longer half-cycle time is applied ($\tau > 400$ s). The highest SCP for all the systems with various MOF adsorbents is summarized as (a) Al-Fum, 5% Li-Al-Fum, 30% AFI-Al-Fum and 30% CHA-Al-Fum is 0.353 ($\tau=1000$ s), 0.394 ($\tau=1000$ s), 0.473 ($\tau=800$ s)

and 0.551 ($\tau=700$ s), respectively; (b) MOF-801 (Zr) and $(\text{CH}_3)_2$ -MOF-801 (Zr) is 0.416 ($\tau=300$ s) and 0.576 ($\tau=300$ s), respectively. The results demonstrate that the performance of the ADC system could be enhanced significantly by employing the modified MOFs as adsorbent as compared with the original MOFs. For example, among the four Al-Fum-based adsorbents, the original Al-Fum shows the poorest ADC performance (COP and SCP) for its slow adsorption/desorption kinetics as well as the strong hydrophobic performance under low-pressure conditions. By mixing the parent Al-Fum with the AQSOA-Z02 (CHA type) zeolite, the modified 30% CHA-Al-Fum delivers the best adsorption performance.

ADC performance with the highest COP of 0.564 ($\tau=1000$ s) and SCP of 0.551 ($\tau=700$ s). Significant enhancements are also found for 5% Li-Al-Fum and 30% AFI-Al-Fum for their enhanced hydrophilicity at the low-pressure region, faster adsorption–desorption rates, and higher Δq per adsorption cooling cycle. For example, at a half cycle time of 300 s, a 14.3% larger COP and 18.8% higher SCP are found for 30% AFI-Al-Fum as compared with the original Al-Fum. Even better results are obtained for 5% Li-Al-Fum (plus 35.0% COP and plus 44.7% SCP) and 30% CHA-Al-Fum (plus 35.0% COP and plus 44.7% SCP). At other half cycle times such as 500 s, obvious enhancements of ADC performance are also found, which is shown in Fig. 3.30. The overall performance for different Al-Fum-based adsorbent–water adsorption chiller in terms of SCP and COP could be summarized as 30% CHA-Al-Fum > 5% Li-Al-Fum > 30% AFI-Al-Fum > Al-Fum. Similar results are also found for MOF-801 (Zr) based ADC systems.

3.6.4 Comparison Study

Figure 3.30 shows a comparative study of the effects of various types of adsorbents on the adsorption chiller performances. Here, original and modified Al-Fum based MOFs, original and $-\text{CH}_3$ implanted MOF-801 (Zr) based MOFs, conventional silica gel and AQSOA-Z01/Z02 type zeolite-based adsorption assisted cooling system are studied, and the results are listed in Table 3.11. The SCP of conventional materials is found relatively lower as compared with the parent MOF-801 (Zr) based MOFs as a result of the low water vapor transfer ($M_s \times \Delta q$) per thermal compression cycle. In addition, it is noted that the COP of the silica gel is comparable to that of the original MOF-801 (Zr), which is mainly because of the stronger hydrophilic performance of MOF-801 (Zr) (0.25 g/g of the water uptake at $P/P_s = 0.1$). It is also observed that all the Al-Fum-based MOFs could operate with relatively low regeneration temperatures (55 to 60 °C). These results could be compared with the published literatures. For example, it is reported that at the regeneration temperature of 82.1 °C, conventional silica gel could deliver a moderate SCP (0.2 kW/kg) and COP (0.49). Significant enhancement is achieved when silica/ CaCl_2 plus activated carbon composites are used, where 90% and 32.7% of increment are resulted for the SCP and the COP as compared with those of the RD-type silica gel. It is noted here that a higher hot water inlet temperature (85 °C) is needed. In addition, the original MOF-801 (Zr)

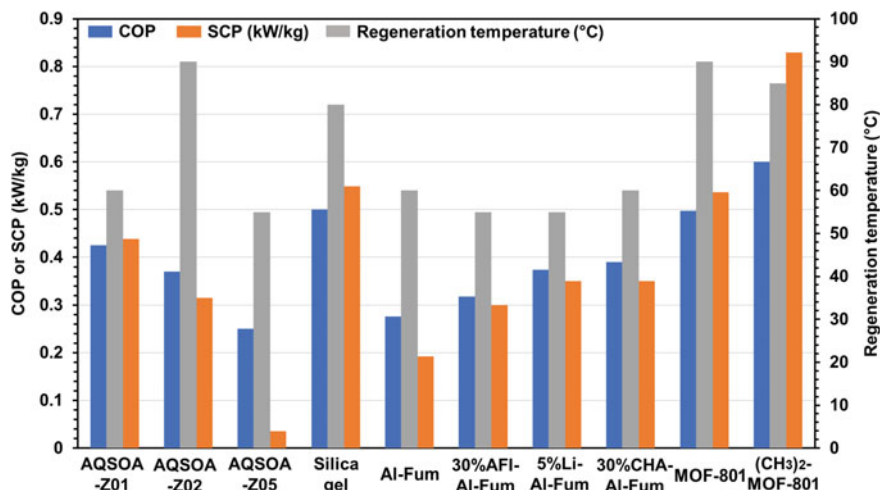


Fig. 3.30 The SCP and COP of the adsorption assisted chiller employing various adsorbents plus water pairs under the optimal regeneration temperature conditions

Table 3.11 The COPs and SCPs for conventional adsorbent and parent/modified MOFs based adsorption assisted chiller

Material	Optimal COP	Optimal SCP	Regeneration temperature (°C)
AQSOA-Z01	0.43	0.44	60
AQSOA-Z02	0.37	0.31	90
AQSOA-Z05	0.25	0.04	55
Silica gel	0.50	0.55	80
Al-Fum	0.28	0.19	60
30% AFI-Al-Fum	0.32	0.30	55
5% Li-Al-Fum	0.37	0.35	55
30% CHA-Al-Fum	0.39	0.35	60
MOF-801 (Zr)	0.50	0.54	90
(CH ₃) ₂ -MOF-801 (Zr)	0.6	0.83	85

shows the comparable higher COP ($0.47 > 0.44$) and SCP ($0.54 > 0.51$ kW/kg) as compared with those of the FAM Z01 type zeolite. By optimizing the hydrophilicity behaviors of the parent MOFs at low-pressure region with modification procedures (alkali ions doping, functionalization, or mixing with conventional zeolite adsorbent), the hydrophilicity of the original Al-Fum or MOF-801 (Zr) is revised. Higher COP and SCP are found for the modified fumarate-based MOFs as compared with those of the original ones. Collectively, these results prove that the modified Al-Fum or MOF-801 (Zr) based MOFs are promising candidates for adsorption-assisted cooling applications.

3.7 Conclusions

In this chapter, fumarate-based MOFs, namely Al-Fum and MOF-801 (Zr) are modified with zeolite composites/alkali cations/ $-\text{CH}_3$ additives. The parent and modified adsorbents are characterized by XRD, TGA, SEM, and N_2 adsorption. Water adsorption investigations on parent and modified MOFs are performed both theoretically and experimentally. It is observed that the synthesized MOFs exhibit improved stability properties with enhanced micro-porosities. Noteworthy, faster adsorption—desorption kinetics with the higher water vapor transfer per adsorption cooling cycle are found for modified materials as compared with parent Al-Fum or MOF-801 (Zr) adsorbents. The water adsorption kinetics and isotherms are fitted with the Langmuir-based equation, and the critical parameters are applied to analyze adsorption chiller (ADC) performance. The adsorption chillers employing various original and modified MOF adsorbents—water pairs are successfully modeled, and the performances in terms of the SCP (specific cooling power) and COP (coefficient of performance) are presented. The effects of the operation conditions on the ADC performance are investigated regarding the different regeneration temperatures (55–90 °C), cold water inlet temperature (20–35 °C), and half-cycle time (150–1000 s). Superior results are seen for modified MOFs-based adsorption chiller. Collectively, the ranking in terms of the ADC performance (SCP and COP) is summarized as: (a) 30% CHA-Al-Fum > 5% Li-Al-Fum > 30% AFI-Al-Fum > parent Al-Fum; (b) $(\text{CH}_3)_2$ -MOF-801 (Zr) > MOF-801 (Zr). The simulated results indicate that:

- (a) Overall, the optimal half-cycle time (τ) for all the original and modified adsorbents ranges from 400 to 800 s, which is related to the water adsorption kinetics. The original Al-Fum and 30% AFI-Al-Fum achieve the maximum SCP at 1000 s while 5% Li-Al-Fum and 30% CHA-Al-Fum require a much shorter time (800 s and 700 s, respectively). For MOF-801 (Zr) based MOFs, both MOF-801 (Zr) and $(\text{CH}_3)_2$ -MOF-801 (Zr) could achieve 90% of the maximum SCP within 600 s.
- (b) The modified MOF-based adsorbent–water adsorption chiller could be driven readily by the low-grade heat source, for example, solar energy or waste heat. At a low regeneration temperature of 75 °C, all the modified MOF adsorbents achieve optimized SCP, and the maximum COP is obtained at even lower temperatures (55–65 °C) for some materials. Furthermore, inlet cold water at room temperature (25–30 °C) is suitable for cooling purposes.
- (c) Among all the Al-Fum-based MOFs, 30% CHA-Al-Fum exhibits the best ADC performance. For the heat sink temperature of 30 °C and heat source temperature of 60 °C, 30% CHA-Al-Fum presents a promising SCP of 0.52 kW/kg and COP of 0.39, which is 42.3% and 70% higher as compared with the original Al-Fum. Furthermore, $(\text{CH}_3)_2$ -MOF-801 (Zr) is suitable for ADC applications for a wide regeneration temperature range (70–90 °C).

Hence the simulation results are based on experimentally confirmed MOFs plus water adsorption isotherms and kinetics data. The conclusion provides a potential

guideline for the optimization and design of the parent and modified MOF—water adsorption chiller. Further research should be devoted to the development of practical adsorption chiller experiments to confirm these novel findings. Additionally, the original MOFs could be further revised by other modification methods such as the pore size enlargement to deliver higher water uptake—offtake difference (Δq) with faster kinetics per adsorption cooling cycle.

Acknowledgements The authors acknowledge the financing support from Ministry of Education (MOE), Singapore (grant no. MOE Tier1: 2021-T1-001-041).

References

1. Woolf D, Amonette JE, Street-Perrott FA, Lehmann J, Joseph S (2010) Sustainable biochar to mitigate global climate change. *Nat Commun* 1:56. [https://doi.org/10.1038/ncomms1053\(2010\)](https://doi.org/10.1038/ncomms1053(2010))
2. Kang SM, Polvani L, Fyfe J, Sigmond M (2011) Impact of polar ozone depletion on subtropical precipitation. *Science* 332(6032):951–954. <https://doi.org/10.1126/science.1202131>
3. Zhai X, Wang R (2010) Experimental investigation and performance analysis on a solar adsorption cooling system with/without heat storage. *Appl Energy* 87(3):824–835. <https://doi.org/10.1016/j.apenergy.2009.10.002>
4. Chan KC, Chao CY, Sze-To G, Hui KS (2012) Performance predictions for a new zeolite 13X/CaCl₂ composite adsorbent for adsorption cooling systems. *Int J Heat Mass Transf* 55(11–12):3214–3224. <https://doi.org/10.1016/j.ijheatmasstransfer.2012.02.054>
5. Teo HWB, Chakraborty A, Han B (2017) Water adsorption on CHA and AFI types zeolites: Modelling and investigation of adsorption chiller under static and dynamic conditions. *Appl Therm Eng* 127:35–45. <https://doi.org/10.1016/j.applthermaleng.2017.08.014>
6. Grabowska K, Krzywanski J, Nowak W, Wesolowska M (2018) Construction of an innovative adsorbent bed configuration in the adsorption chiller-Selection criteria for effective sorbent-glue pair. *Energy* 151:317–323. <https://doi.org/10.1016/j.energy.2018.03.060>
7. Shmroukh AN, Ali AHH, Ookawara S (2015) Adsorption working pairs for adsorption cooling chillers: A review based on adsorption capacity and environmental impact. *Renew Sustain Energy Rev* 50:445–456. <https://doi.org/10.1016/j.rser.2015.05.035>
8. Freni A, Bonaccorsi L, Calabrese L, Capri A, Frazzica A, Sapienza A (2015) SAPO-34 coated adsorbent heat exchanger for adsorption chillers. *Appl Therm Eng* 82:1–7. <https://doi.org/10.1016/j.applthermaleng.2015.02.052>
9. Hassan H, Mohamad A, Bennacer R (2011) Simulation of an adsorption solar cooling system. *Energy* 36(1):530–537. <https://doi.org/10.1016/j.energy.2010.10.011>
10. Solmuş İ, Yamalı C, Kaftanoğlu B, Baker D, Çağlar A (2010) Adsorption properties of a natural zeolite–water pair for use in adsorption cooling cycles. *Appl Energy* 87(6):2062–2067. <https://doi.org/10.1016/j.apenergy.2009.11.027>
11. Han B, Chakraborty A (2020) Advanced cooling heat pump and desalination employing functional UiO-66 (Zr) metal-organic frameworks. *Energy Convers Manage* 213. <https://doi.org/10.1016/j.enconman.2020.112825>
12. Pan Q, Peng J, Wang H, Sun H, Wang R (2019) Experimental investigation of an adsorption air-conditioner using silica gel-water working pair. *Sol Energy* 185:64–71. <https://doi.org/10.1016/j.solener.2019.04.054>
13. Myat A, Choon NK, Thu K, Kim Y-D (2013) Experimental investigation on the optimal performance of Zeolite–water adsorption chiller. *Appl Energy* 102:582–590. <https://doi.org/10.1016/j.apenergy.2012.08.005>

14. Han B, Chakraborty A (2019) Water adsorption studies on synthesized alkali-ions doped Al-Fumarate MOFs and Al-Fumarate plus zeolite composites for higher water uptakes and faster kinetics. *Microporous Mesoporous Mater* 288. <https://doi.org/10.1016/j.micromeso.2019.109590>
15. Elsayed E, Raya A-D, Mahmoud S, Anderson PA, Elsayed A, Youssef PG (2017) CPO-27 (Ni), aluminium fumarate and MIL-101 (Cr) MOF materials for adsorption water desalination. *Desalination* 406:25–36. <https://doi.org/10.1016/j.desal.2016.07.030>
16. Ehrenmann J, Henninger SK, Janiak C (2011) Water adsorption characteristics of MIL-101 for heat-transformation applications of MOFs. *Eur J Inorg Chem* 2011(4):471–474. <https://doi.org/10.1002/ejic.201001156>
17. Zhao Z, Wang S, Yang Y, Li X, Li J, Li Z (2015) Competitive adsorption and selectivity of benzene and water vapor on the microporous metal organic frameworks (HKUST-1). *Chem Eng J* 259:79–89. <https://doi.org/10.1016/j.cej.2014.08.012>
18. Kim H, Yang S, Rao SR, Narayanan S, Kapustin EA, Furukawa H, Umans AS, Yaghi OM, Wang EN (2017) Water harvesting from air with metal-organic frameworks powered by natural sunlight. *Science* 356(6336):430–434. <https://doi.org/10.1126/science.aam8743>
19. Hu G, Li W, Li S (2019) Effects of functionalization on the performance of metal-organic frameworks for adsorption-driven heat pumps by molecular simulations. *Chem Eng Sci* 208. <https://doi.org/10.1016/j.ces.2019.08.001>
20. Permyakova A, Skrylnyk O, Courbon E, Affram M, Wang S, Lee UH, Valekar AH, Nour F, Mouchaham G, Devic T (2017) Synthesis Optimization, Shaping, and Heat Reallocation Evaluation of the Hydrophilic Metal-Organic Framework MIL-160 (Al). *Chemsuschem* 10(7):1419–1426. <https://doi.org/10.1002/cssc.201700164>
21. Canivet J, Bonnefoy J, Daniel C, Legrand A, Coasne B, Farrusseng D (2014) Structure–property relationships of water adsorption in metal–organic frameworks. *New J Chem* 38(7):3102–3111. <https://doi.org/10.1039/C4NJ00076E>
22. Fröhlich D, Pantatosaki E, Kolokathis PD, Markey K, Reinsch H, Baumgartner M, van der Veen MA, De Vos DE, Stock N, Papadopoulos GK (2016) Water adsorption behaviour of CAU-10-H: a thorough investigation of its structure–property relationships. *Journal of Materials Chemistry A* 4(30):11859–11869. <https://doi.org/10.1039/C6TA01757F>
23. Teo HWB, Chakraborty A, Kitagawa Y, Kayal S (2017) Experimental study of isotherms and kinetics for adsorption of water on Aluminium Fumarate. *Int J Heat Mass Transf* 114:621–627. <https://doi.org/10.1016/j.ijheatmasstransfer.2017.06.086>
24. Zlotea C, Phanon D, Mazaj M, Heurtaux D, Guillermin V, Serre C, Horcajada P, Devic T, Magnier E, Cuevas F (2011) Effect of NH₂ and CF₃ functionalization on the hydrogen sorption properties of MOFs. *Dalton Trans* 40(18):4879–4881. <https://doi.org/10.1039/C1DT10115C>
25. Prestipino C, Regli L, Vitillo JG, Bonino F, Damin A, Lamberti C, Zecchina A, Solari P, Kongshaug K, Bordiga S (2006) Local structure of framework Cu (II) in HKUST-1 metallorganic framework: spectroscopic characterization upon activation and interaction with adsorbates. *Chem Mater* 18(5):1337–1346. <https://doi.org/10.1021/cm052191g>
26. Liu J, Wang Y, Benin AI, Jakubczak P, Willis RR, LeVan MD (2010) CO₂/H₂O adsorption equilibrium and rates on metal–organic frameworks: HKUST-1 and Ni/DOBDC. *Langmuir* 26(17):14301–14307. <https://doi.org/10.1021/la102359q>
27. Glover TG, Peterson GW, Schindler BJ, Britt D, Yaghi O (2011) MOF-74 building unit has a direct impact on toxic gas adsorption. *Chem Eng Sci* 66(2):163–170. <https://doi.org/10.1016/j.ces.2010.10.002>
28. Teo HWB, Chakraborty A, Kayal S (2017) Post synthetic modification of MIL-101 (Cr) for S-shaped isotherms and fast kinetics with water adsorption. *Appl Therm Eng* 120:453–462. <https://doi.org/10.1016/j.applthermaleng.2017.04.018>
29. Küsgens P, Rose M, Senkovska I, Fröde H, Henschel A, Siegle S, Kaskel S (2009) Characterization of metal-organic frameworks by water adsorption. *Microporous Mesoporous Mater* 120(3):325–330. <https://doi.org/10.1016/j.micromeso.2008.11.020>

30. Mulfort KL, Hupp JT (2008) Alkali metal cation effects on hydrogen uptake and binding in metal-organic frameworks. *Inorg Chem* 47(18):7936–7938. <https://doi.org/10.1021/ic800700h>
31. Bae Y-S, Farha OK, Hupp JT, Snurr RQ (2009) Enhancement of CO₂/N₂ selectivity in a metal-organic framework by cavity modification. *J Mater Chem* 19(15):2131–2134. <https://doi.org/10.1039/B900390H>
32. Wickenheisser M, Jeremias F, Henninger SK, Janiak C (2013) Grafting of hydrophilic ethylene glycols or ethylenediamine on coordinatively unsaturated metal sites in MIL-100 (Cr) for improved water adsorption characteristics. *Inorg Chim Acta* 407:145–152. <https://doi.org/10.1016/j.ica.2013.07.024>
33. Khushalani D, Kuperman A, Ozin GA, Tanaka K, Coombs N, Olken MM, Garcés J (1995) Metamorphic materials: restructuring siliceous mesoporous materials. *Adv Mater* 7(10):842–846. <https://doi.org/10.1002/adma.19950071005>
34. Sayari A, Liu P, Kruk M, Jaroniec M (1997) Characterization of large-pore MCM-41 molecular sieves obtained via hydrothermal restructuring. *Chem Mater* 9(11):2499–2506. <https://doi.org/10.1021/cm970128o>
35. Velev O, Jede T, Lobo R, Lenhoff A (1997) Porous silica via colloidal crystallization. *Nature* 389(6650):447–448. <https://doi.org/10.1038/38921>
36. Yadav M, Xu Q (2013) Catalytic chromium reduction using formic acid and metal nanoparticles immobilized in a metal-organic framework. *Chem Commun* 49(32):3327–3329. <https://doi.org/10.1039/C3CC00293D>
37. Toth J (1971) State equation of the solid-gas interface layers. *Acta chim hung* 69:311–328
38. Langmuir, I., The constitution and fundamental properties of solids and liquids. Part I. Solids. *Journal of the American chemical society*, 1916. 38(11): p. 2221–2295. doi: <https://doi.org/10.1021/ja02268a002>
39. Chakraborty A, Saha BB, Ng KC, Koyama S, Srinivasan K (2009) Theoretical insight of physical adsorption for a single-component adsorbent plus adsorbate system: I. Thermodynamic property surfaces. *Langmuir* 25(4):2204–2211. <https://doi.org/10.1021/la803289p>
40. Ritchie, A., Alternative to the Elovich equation for the kinetics of adsorption of gases on solids. *Journal of the Chemical Society, Faraday Transactions 1: Physical Chemistry in Condensed Phases*, 1977. 73: p. 1650–1653. doi: <https://doi.org/10.1039/F19777301650>
41. Kitagawa S (2014) Metal-organic frameworks (MOFs). *Chem Soc Rev* 43(16):5415–5418. <https://doi.org/10.1039/C4CS90059F>
42. Zhang X, Qin W, Li D, Yan D, Hu B, Sun Z, Pan L (2015) Metal-organic framework derived porous CuO/Cu₂O composite hollow octahedrons as high performance anode materials for sodium ion batteries. *Chem Commun* 51(91):16413–16416. <https://doi.org/10.1039/C5CC06924F>
43. Sun L, Campbell MG, Dincă M (2016) Electrically conductive porous metal-organic frameworks. *Angew Chem Int Ed* 55(11):3566–3579. <https://doi.org/10.1002/anie.201506219>
44. Lo S-H, Chien C-H, Lai Y-L, Yang C-C, Lee JJ, Raja DS, Lin C-H (2013) A mesoporous aluminium metal-organic framework with 3 nm open pores. *Journal of Materials Chemistry A* 1(2):324–329. <https://doi.org/10.1039/C2TA00030J>
45. Wang K, Feng D, Liu T-F, Su J, Yuan S, Chen Y-P, Bosch M, Zou X, Zhou H-C (2014) A series of highly stable mesoporous metalloporphyrin Fe-MOFs. *J Am Chem Soc* 136(40):13983–13986. <https://doi.org/10.1021/ja507269n>
46. Teo HWB, Chakraborty A, Kayal S (2017) Evaluation of CH₄ and CO₂ adsorption on HKUST-1 and MIL-101 (Cr) MOFs employing Monte Carlo simulation and comparison with experimental data. *Appl Therm Eng* 110:891–900. <https://doi.org/10.1016/j.applthermaleng.2016.08.126>
47. Cirujano, F.G., A. Corma, and F.L. Xamena, Conversion of levulinic acid into chemicals: synthesis of biomass derived levulinate esters over Zr-containing MOFs. *Chemical Engineering Science*, 2015. 124: p. 52–60. doi: <https://doi.org/10.1016/j.ces.2014.09.047>
48. Gao J, Miao J, Li P-Z, Teng WY, Yang L, Zhao Y, Liu B, Zhang Q (2014) A p-type Ti (IV)-based metal-organic framework with visible-light photo-response. *Chem Commun* 50(29):3786–3788. <https://doi.org/10.1039/C3CC49440C>

49. Stock N, Biswas S (2011) Synthesis of metal-organic frameworks (MOFs): routes to various MOF topologies, morphologies, and composites. *Chem Rev* 112(2):933–969. <https://doi.org/10.1021/cr200304e>
50. Jeremias F, Fröhlich D, Janiak C, Henninger SK (2014) Advancement of sorption-based heat transformation by a metal coating of highly-stable, hydrophilic aluminium fumarate MOF. *RSC Adv* 4(46):24073–24082. <https://doi.org/10.1039/C4RA03794D>
51. Cadiou, A., J.S. Lee, D. Damasceno Borges, P. Fabry, T. Devic, M.T. Wharmby, C. Martineau, D. Foucher, F. Taulelle, and C.H. Jun, Design of hydrophilic metal organic framework water adsorbents for heat reallocation. *Advanced Materials*, 2015. 27(32): p. 4775–4780. doi: <https://doi.org/10.1002/adma.201502418>
52. De Lange M, Zeng T, Vlugt T, Gascon J, Kapteijn F (2015) Manufacture of dense CAU-10-H coatings for application in adsorption driven heat pumps: optimization and characterization. *CrystEngComm* 17(31):5911–5920. <https://doi.org/10.1039/C5CE00789E>
53. Jeremias F, Lozan V, Henninger SK, Janiak C (2013) Programming MOFs for water sorption: amino-functionalized MIL-125 and UiO-66 for heat transformation and heat storage applications. *Dalton Trans* 42(45):15967–15973. <https://doi.org/10.1039/C3DT51471D>
54. Solovyeva M, Gordeeva L, Krieger T, Aristov YI (2018) MOF-801 (Zr) as a promising material for adsorption cooling: Equilibrium and dynamics of water adsorption. *Energy Convers Manage* 174:356–363. <https://doi.org/10.1016/j.enconman.2018.08.032>
55. Dechnik J, Janiak C, De S (2016) Aluminium fumarate metal-organic framework: a super adsorbent for fluoride from water. *J Hazard Mater* 303:10–20. <https://doi.org/10.1016/j.jhazmat.2015.10.030>
56. Youssef P, Mahmoud S, Al-Dadah R, Elsayed E, El-Samni O (2017) Numerical Investigation of Aluminum Fumarate MOF adsorbent material for adsorption desalination/cooling application. *Energy Procedia* 142:1693–1698. <https://doi.org/10.1016/j.egypro.2017.12.551>
57. Martinez, M.R., M.R. Hill, M. Batten, K.S. Lim, A. Polyzos, T.R. Barton, T.D. Hadley, and A.A. Monch, Production of metal-organic frameworks. 2018, Google Patents.
58. Alvarez E, Guillou N, Martineau C, Bueken B, Van de Voorde B, Le Guillouzer C, Fabry P, Nour F, Taulelle F, De Vos D (2015) The structure of the aluminum fumarate metal-organic framework A520. *Angew Chem Int Ed* 54(12):3664–3668. <https://doi.org/10.1002/ange.201410459>
59. Yot PG, Vanduyfhuys L, Alvarez E, Rodriguez J, Itié J-P, Fabry P, Guillou N, Devic T, Beurroies I, Llewellyn PL (2016) Mechanical energy storage performance of an aluminum fumarate metal-organic framework. *Chem Sci* 7(1):446–450. <https://doi.org/10.1039/C5SC02794B>
60. Furukawa H, Gándara F, Zhang Y-B, Jiang J, Queen WL, Hudson MR, Yaghi OM (2014) Water adsorption in porous metal-organic frameworks and related materials. *J Am Chem Soc* 136(11):4369–4381. <https://doi.org/10.1021/ja500330a>
61. Liu X, Demir NK, Wu Z, Li K (2015) Highly water-stable zirconium metal-organic framework UiO-66 membranes supported on alumina hollow fibers for desalination. *J Am Chem Soc* 137(22):6999–7002. <https://doi.org/10.1021/jacs.5b02276>
62. Yang J-M, Liu Q, Sun W-Y (2014) Shape and size control and gas adsorption of Ni (II)-doped MOF-5 nano/microcrystals. *Microporous Mesoporous Mater* 190:26–31. <https://doi.org/10.1016/j.micromeso.2014.01.020>
63. Zhu X-W, Zhou X-P, Li D (2016) Exceptionally water stable heterometallic gyroidal MOFs: tuning the porosity and hydrophobicity by doping metal ions. *Chem Commun* 52(39):6513–6516. <https://doi.org/10.1039/C6CC02116F>
64. Ortiz AU, Freitas AP, Boutin A, Fuchs AH, Coudert F-X (2014) What makes zeolitic imidazolate frameworks hydrophobic or hydrophilic? The impact of geometry and functionalization on water adsorption. *Phys Chem Chem Phys* 16(21):9940–9949. <https://doi.org/10.1039/C3CP54292K>
65. Waitschat S, Fröhlich D, Reinsch H, Terraschke H, Lomachenko K, Lamberti C, Kummer H, Helling T, Baumgartner M, Henninger S (2018) Synthesis of M-UiO-66 (M= Zr, Ce or Hf) employing 2, 5-pyridinedicarboxylic acid as a linker: defect chemistry, framework hydrophilisation and sorption properties. *Dalton Trans* 47(4):1062–1070. <https://doi.org/10.1039/C7DT03641H>

66. Sadakiyo M, Yamada T, Kitagawa H (2011) Hydroxyl group recognition by hydrogen-bonding donor and acceptor sites embedded in a layered metal–organic framework. *J Am Chem Soc* 133(29):11050–11053. <https://doi.org/10.1021/ja203291n>
67. Kim M, Cahill JF, Su Y, Prather KA, Cohen SM (2012) Postsynthetic ligand exchange as a route to functionalization of ‘inert’ metal–organic frameworks. *Chem Sci* 3(1):126–130. <https://doi.org/10.1039/C1SC00394A>
68. Ko N, Hong J, Sung S, Cordova KE, Park HJ, Yang JK, Kim J (2015) A significant enhancement of water vapor uptake at low pressure by amine-functionalization of UiO-67. *Dalton Trans* 44(5):2047–2051. <https://doi.org/10.1039/C4DT02582B>
69. Gee, W.J., L.K. Cadman, H. Amer Hamzah, M.F. Mahon, P.R. Raithby, and A.D. Burrows, Furnishing amine-functionalized metal–organic frameworks with the β -amidoketone group by postsynthetic modification. *Inorganic chemistry*, 2016. 55(21): p. 10839–10842. doi: <https://doi.org/10.1021/acs.inorgchem.6b01917>
70. Ma D, Li Y, Li Z (2011) Tuning the moisture stability of metal–organic frameworks by incorporating hydrophobic functional groups at different positions of ligands. *Chem Commun* 47(26):7377–7379. <https://doi.org/10.1039/C1CC11752A>
71. Asiabi M, Mehdinia A, Jabbari A (2015) Preparation of water stable methyl-modified metal–organic framework-5/polyacrylonitrile composite nanofibers via electrospinning and their application for solid-phase extraction of two estrogenic drugs in urine samples. *J Chromatogr A* 1426:24–32. <https://doi.org/10.1016/j.chroma.2015.11.036>
72. Furukawa H, Gandara F, Zhang Y-B, Jiang J, Queen WL, Hudson MR, Yaghi OM (2014) Water adsorption in porous metal–organic frameworks and related materials. *J Am Chem Soc* 136(11):4369–4381. <https://doi.org/10.1021/ja500330a>
73. Weißmann G, Schaate A, Lilienthal S, Bremer I, Schneider AM, Behrens P (2012) Modulated synthesis of Zr-fumarate MOF. *Microporous Mesoporous Mater* 152:64–70. <https://doi.org/10.1016/j.micromeso.2011.12.010>
74. Anderson R, Rodgers J, Argueta E, Biong A, Gómez-Gualdrón DA (2018) Role of pore chemistry and topology in the CO₂ capture capabilities of MOFs: from molecular simulation to machine learning. *Chem Mater* 30(18):6325–6337. <https://doi.org/10.1021/acs.chemmater.8b02257>
75. Wen H-M, Liao C, Li L, Alsahme A, Allothman Z, Krishna R, Wu H, Zhou W, Hu J, Chen B (2019) A metal–organic framework with suitable pore size and dual functionalities for highly efficient post-combustion CO₂ capture. *Journal of materials chemistry A* 7(7):3128–3134. <https://doi.org/10.1039/C8TA11596F>
76. Coelho, J.A., A.M. Ribeiro, A.F. Ferreira, S.o.M. Lucena, A.E. Rodrigues, and D.C.d. Azevedo, Stability of an Al-Fumarate MOF and its potential for CO₂ capture from wet stream. *Industrial & Engineering Chemistry Research*, 2016. 55(7): p. 2134–2143. doi: <https://doi.org/10.1021/acs.iecr.5b03509>
77. Sun B, Chakraborty A (2014) Thermodynamic formalism of water uptakes on solid porous adsorbents for adsorption cooling applications. *Appl Phys Lett* 104(20). <https://doi.org/10.1063/1.4876922>
78. Sun B, Chakraborty A (2015) Thermodynamic frameworks of adsorption kinetics modeling: Dynamic water uptakes on silica gel for adsorption cooling applications. *Energy* 84:296–302. <https://doi.org/10.1016/j.energy.2015.02.101>
79. Zhang L (2000) A three-dimensional non-equilibrium model for an intermittent adsorption cooling system. *Sol Energy* 69(1):27–35. [https://doi.org/10.1016/S0038-092X\(00\)00010-4](https://doi.org/10.1016/S0038-092X(00)00010-4)

Chapter 4

Specific Heat Capacity of Carbon-Based Composites for Adsorption Heat Pump and Desalination Applications



Kaiser Ahmed Rocky, Md. Amirul Islam, Animesh Pal, Bidyut Baran Saha, Hyun-Sig Kil, Seong-Ho Yoon, and Jin Miyawaki

Abstract Environmentally benign adsorption heat pump (AHP) and desalination (AD) systems have already attracted considerable attention for space cooling/heating and potable water production since they require no electricity and are driven by solar or waste heat. The adsorbent material is the key element of these adsorption systems. Highly porous carbon-based consolidated composites are very promising adsorbents. Specific heat capacity (c_p) of adsorbent is one of the most significant thermophysical properties. It plays a vital role in predicting the performance of the systems accurately.

K. A. Rocky · B. B. Saha (✉)

Department of Mechanical Engineering, Kyushu University, 744 Motooka, Nishi-ku, Fukuoka 819-0395, Japan

e-mail: saha.baran.bidyut.213@m.kyushu-u.ac.jp

K. A. Rocky

e-mail: kaiserrocky@du.ac.bd

K. A. Rocky · Md. A. Islam · B. B. Saha · J. Miyawaki

International Institute for Carbon-Neutral Energy Research (WPI-I2CNER), Kyushu University, 744 Motooka, Nishi-ku, Fukuoka 819-0395, Japan

e-mail: miyawaki@cm.kyushu-u.ac.jp

K. A. Rocky

Department of Physics, University of Dhaka, Dhaka 1000, Bangladesh

Md. A. Islam

Department of Electronics and Telecommunication Engineering, Bangabandhu Sheikh Mujibur Rahman Science & Technology University, Gopalganj 8100, Bangladesh

A. Pal

Department of Nuclear Engineering, University of Dhaka, Dhaka 1000, Bangladesh

e-mail: animeshpal@du.ac.bd

H.-S. Kil

C1 Gas & Carbon Convergent Research Center, Korea Research Institute of Chemical Technology, 141 Gajeong-ro, Yuseong-gu, Daejeon 34114, Republic of Korea

e-mail: kgustlr@kRICT.re.kr

Md. A. Islam · S.-H. Yoon · J. Miyawaki

Institute for Materials Chemistry and Engineering, Kyushu University, Kasuga-koen 6-1, Kasuga-shi, Fukuoka 816-8580, Japan

e-mail: yoons@cm.kyushu-u.ac.jp

However, the estimation of the c_p of adsorbent materials is a demanding issue and has not been focused sufficiently yet. Therefore, this chapter will present the significance of specific heat capacity, detailed experimental procedure, and the c_p of composites, as well as the parent materials at the operating temperature range of AHP and AD systems. Finally, all the experimental data are analyzed rigorously and correlated with the established equations of c_p . The presented experimental c_p data along with the fitted parameters are crucial in the design of AHP and AD systems.

Keywords Activated carbon · Adsorption heat pump · Composite · Specific heat capacity

4.1 Introduction

Nowadays, the energy crisis and environmental pollution are the most concern issues in the world. Therefore, conventional heating, ventilation, and air conditioning (HVAC) system is now encountering momentous challenges due to employing vapor compression technique as the basic working principle. The traditional vapor compression system uses a mechanical compressor which consumes a substantial volume of electrical energy. Besides, this system causes the increase of global warming potential (GWP) and the depletion of the ozone layer. In order to protect the ozone layer, substances that are liable for ozone layer depletion should be phased out. To execute this plan, an international agreement is signed, which is known as the Montreal Protocol. Therefore, under this protocol, hydrochlorofluorocarbons (HCFCs) and hydrofluorocarbons (HFCs) have replaced the use of chlorofluorocarbons (CFCs) in the HVAC system. However, CFCs, HCFCs, and HFCs all have large global warming potential. In the 28th meeting of the Montreal Protocol, one amendment has been included to the protocol that aims to phase out HFCs. It is expected that this phasing out could prevent global warming up to 0.5 °C by the end of this century. Therefore, conventional HVAC and refrigeration systems should replace HFCs with environmentally benign refrigerants. From the environmental issue and energy consumption perspective, researchers are trying to develop an alternate cooling/heating system that could utilize natural fluids as refrigerants and consumes almost no electrical energy. In this case, an adsorption heat pump (AHP) is strongly treated as a prospective alternate to the traditional vapor compression system. In AHP, the mechanical compressor is replaced by a thermal compressor which is driven by utilizing thermal energies. The widely used thermal energy sources are solar, geothermal and waste heat of industrial or domestic processes. Besides, the adsorption desalination (AD) system that mitigates the thirst for drinkable water also employs low-grade thermal energy activated thermal compressor [1, 2]. The working principle of these compressors is almost similar. The key element of the thermal compressor is adsorbent materials. These materials can be synthesized by adopting a green synthesis process. Silica gel, activated carbon (AC), metal–organic framework (MOF), and zeolite are extensively used adsorbent materials. Each adsorbent has a

strong affinity to a specific refrigerant. Silica gel, MOF, and zeolite have an affinity to water vapor, whereas AC has more susceptibility to carbon dioxide and ethanol. Therefore, AHP uses natural fluids such as water, CO₂, methanol, ethanol, and so on as refrigerant, which in turn makes AHP as an environmental-friendly system. However, the performance of an AHP/AD is not still satisfactory due to the low heat transfer in the adsorption bed, and the system is bulky. Usually, the adsorbents used in the adsorption bed exhibits poor thermal conductivity and packing density, which decrease the system efficiency. Hence, researchers are focusing on the consolidated composite adsorbents instead of the powder form. The consolidated composite would exhibit an improved heat transfer phenomenon, a higher volumetric capacity which would result in an efficient and compact system. Several research works related to composite adsorbents can be found in the literature [3–8]. The literature review indicates that AC-based consolidated composite could be very promising for designing the next generation cooling, heating, and desalination systems.

Before designing an AHP/AD system, the first task is to determine the thermophysical properties of the adsorbents. Specific heat capacity (c_p) is considered as the most important thermophysical property since it plays a vital role in the system characteristics, simulation, design, and analysis [9, 10]. However, few research works [11–14] are available regarding the c_p of adsorbent materials. Uddin et al. [11] investigated the c_p of several carbon-based adsorbent materials and showed c_p as an increasing function of temperature. Rahman et al. [15] calculated the adsorbed phase c_p of the AC-methane system as a function of temperature and pressure. Nevertheless, many researchers adopted c_p as a constant quantity in their simulation of adsorption processes. Boelman et al. [16], Mitra et al. [17], and Thu et al. [18] considered the c_p value of silica gel as constant in their studies. Askalany et al. [19] estimated the performance of the granular AC-based adsorption cooling system, assuming the c_p value of AC as 0.930 kJ kg⁻¹ K⁻¹. Chan et al. [20] also assumed the c_p of zeolite 13X/CaCl₂ composite as a constant value of 0.836 kJ kg⁻¹ K⁻¹ for the performance prediction of the system. Since adsorption cycles include alternate cooling and heating, considering the c_p value as constant will reflect an erroneous result which would hinder the design and the performance of the AHP or AD systems. Therefore, precise c_p measurement finds immense importance in the energetics of the systems.

This chapter, firstly, focuses on the significance of specific heat capacity in AHP/AD design and its performance analysis. Secondly, a concise description of the prospective materials for the preparation of composite adsorbents and the development procedure of consolidated composites are summarized. Thirdly, the working principle of differential scanning calorimetry (DSC) and c_p measurement procedure are summarized. Finally, specific heat capacity data of parent substances are correlated with a well-known equation, and a universal equation proposed by Rocky et al. [12] is employed to determine the specific heat capacity of composite adsorbents.

4.2 Significance of Specific Heat Capacity

The amount of input energy of an AHP/AD system strongly depends on the specific heat capacity of adsorbents and materials used for fin and heat exchanger tubes. Hence, specific heat capacity plays an important role in the design and optimization of minimum desorption temperature and adsorption cycle time. Besides, before the overall system design, the essential thermodynamic quantities such as enthalpy and entropy should be evaluated. Several researchers [21–24] showed that the enthalpy and entropy of an adsorbent-adsorbate system depend on the c_p of adsorbent and adsorbate. Rupam et al. [23] derived the equations of enthalpy and entropy for various adsorbent/adsorbate pairs. The equations can be expressed as

$$\begin{aligned}
 h = & \int_{T_o}^T c_{p,ad}(T)dT + \int_{T_o}^T \left[c_{p,ref}(P, T) + \frac{\Delta H_{ads}}{T} - \frac{\Delta H_{ads}}{v_{ref}} \frac{\partial v_{ref}}{\partial T} - \frac{\partial \Delta H_{ads}}{\partial T} \right] dT \\
 & + \int_0^q [h_{ref}(P, T) - \Delta H_{ads}]dq + \int_{P_o}^P v_{ad} \cdot dP
 \end{aligned} \tag{4.1}$$

and

$$\begin{aligned}
 s = & \int_{T_o}^T \frac{c_{p,ad}(T)}{T} dT + q \int_{T_o}^T \left(c_{p,ref}(P, T) + \frac{\Delta H_{ads}}{T} - \frac{\Delta H_{ads}}{v_{ref}} \left(\frac{\partial v_{ref}}{\partial T} \right)_p - \frac{\partial \Delta H_{ads}}{\partial T} \right) dT \\
 & + \int_0^q \left\{ s_{ref}(P, T) - \frac{\Delta H_{ads}}{T} \right\} dq
 \end{aligned} \tag{4.2}$$

Here, h and s represent enthalpy and entropy, respectively; H_{ads} denotes the heat of adsorption; q is adsorption uptake; P , v , and T carry the conventional meaning. The subscripts ad and ref stand for adsorbent and adsorbate (refrigerant), respectively.

From Eqs. (4.1) and (4.2), it is clearly observed that specific heat capacity has a significant contribution in the calculation of the enthalpy and entropy of the system. Moreover, the thermal conductivity of adsorbent strongly depends on the c_p value [25–27], whereas thermal conductivity is also considered as a key parameter for AHP/AD design.

An energy balance equation is required for the design of an AHP/AD system. The c_p of adsorbent is a significant parameter of the energy balance equation. A generalized energy balance equation [28] for an adsorber can be written as -

$$[m c_p]_{adsorber} \frac{dT_{adsorber}}{dt} = m_{ad} H_{ads} \frac{dq}{dt} + [\dot{m} c_p (T_{in} - T_{out})]_{H.Ex.fluid} \tag{4.3}$$

The heat capacity term of the left side of the Eq. (4.3) could be extended as -

$$[mC_p]_{adsorber} = m_t c_{p,t} + m_f c_{p,f} + m_{ad} c_{p,ad} \quad (4.4)$$

Here, m stands for mass. The subscript $H.Ex.fluid$ stands for the heat transfer fluid of heat exchanger; in and out represent inlet and outlet, respectively; t and f denote tubes and fins of the adsorber, respectively.

Usually, the c_p of the tube and fin materials is known, as it is provided by the manufacturing company. Thus, accurate c_p determination of adsorbents is essential since Eq. (4.3) is potentially influenced by the specific heat capacity of the adsorbents. In AHP/AD, adsorption usually occurs at room temperature, whereas regeneration is done at a higher temperature. Hence, assuming the c_p value of adsorbents as constant will result in an imprecise energy balance equation. This erroneous equation will considerably affect the performance of an AHP/AD system.

4.3 Promising Materials for Composite Adsorbents

Adsorbent materials are the heart of an AHP/ AD system. Therefore, the selection of a suitable material is one of the most important tasks. An adsorbent material should have the following properties for an efficient system:

- Stable physicochemical property
- High surface area
- Uniform pore size distribution
- Large pore volume
- High adsorption capacity
- Low specific heat capacity
- Good heat and mass transfer capacity
- High packing density
- High affordability and availability

However, a single adsorbent material cannot meet all the properties mentioned above. Hence, researchers are focusing on composite adsorbents.

Nowadays, carbon-based adsorbent materials, namely activated carbon fiber (ACF), AC, biomass-derived AC, etc., are the most promising adsorbents for their high availability and low production cost. Nevertheless, these types of materials exhibit low packing density and poor thermal conductivity, which render the system bulky and inefficient. Therefore, the composites, which consist of adsorbents, thermally conductive materials, and binder materials, are considered potential adsorbents to solve the current limitations of AHP/AD. The following sub-sections will describe the widely used carbon-based adsorbent, thermally conductive, and binder materials.

4.3.1 Adsorbent Materials

Nowadays, researchers are focusing on AC as an adsorbent material. AC is a form of graphitic materials. It occupies special attention as green energy material. This has an immense gas adsorption capacity for its high pore volume and huge surface area. Saha et al. [29] showed that 1 g of ACF of type A-20 and AC powder of type Maxsorb III could adsorb up to 1.56 g and 3.06 g of CO₂, respectively. EI-Merraoui et al. [30] considered that A-20 has a slit-shaped pore, and this ACF possesses a high specific surface area of 1770 m² g⁻¹, micropore volume of 0.96 cm³ g⁻¹, and pore width of 1.09 nm. On the other hand, Maxsorb III exhibits a huge specific surface area of 3045 m² g⁻¹, micropore volume of 1.70 cm³ g⁻¹, and average pore width of 1.12 nm [31]. Since ACs exhibit high pore volume and surface area, these might be used as promising adsorbents for adsorption applications. Akkimaradi et al. [32] presented the adsorption of HFC-134a onto three types of ACs, namely Maxsorb III, Fluka, and Chemviron for adsorption refrigeration application. Besides, several researchers are working on the adsorption of different refrigerants onto different types of ACs for the development of adsorption cooling and heating systems. Here, some notable research findings regarding the physical and adsorption properties of ACs are furnished in Table 4.1.

4.3.2 Thermal Conductive Materials

Thermal conductive materials are incorporated with the adsorbent to improve the heat transfer, packing density, and volumetric adsorption uptake. The literature review reveals that silicon carbide (SiC), expanded graphite (EG), graphene nanoplatelets (GNPs), and carbon nanotubes (CNT) are the most potential thermal conductive materials to synthesize consolidated composite adsorbents. EI-Sharkawy et al. [3] used expanded graphite, namely EC-500, to enhance the heat transfer of AC-based composite adsorbents. According to their findings, packing density and heat transfer of composite adsorbent have been increased to 2.2 and 11 times, respectively, than those of parent AC. Pal et al. [25] developed AC and GNPs based novel composites. The composite had 3.2 times higher packing density than the parent adsorbent, with an improvement of the thermal conductivity to 23.5 times. Moreover, Rocky et al. [41] and Yan et al. [42] mentioned that multi-walled carbon nanotube (MWCNT) could be used as thermal conductive material along with parent adsorbent to develop an efficient AHP. Besides, several researchers [43–47] studied the adsorption of various materials/molecules onto CNT for different applications.

Table 4.1 Physical and adsorption properties of promising carbon-based adsorbents

Adsorbent	Type	Surface area (m ² g ⁻¹)	Micropore volume (cm ³ g ⁻¹)	Average pore width (Å)	Packing density (g cm ⁻³)	Refrigerant	Adsorption uptake (g g ⁻¹)
Maxsorb III	Powder	3045 [31]	1.79 ^a [22]	11.20 [31]	0.281 [32]	n-butane	0.80 [22]
						CO ₂	3.06 ^b [29]
						HFC-134a	1.55 ^c [32]
						HFC-32	2.25 ^b [33]
						Ethanol	1.24 [34]
A-10	Fiber	1160 [30]	0.48 [30]	8.30 [30]	–	–	–
A-15	Fiber	1350 [30]	0.61 [30]	9.10 [30]	–	Ethanol	0.57 ^d [35]
A-20	Fiber	1770 [30]	0.96 [30]	10.90 [30]	–	CO ₂	1.56 ^a [29]
					–	Ethanol	0.80 ^d [35]
					–	HFC-32	2.08 ^b [33]
Fluka	Powder	1143 [36]	0.41 [36]	–	0.391 [32]	HFC-134a	0.45 ^c [32]
Chemviron	Granules	750 [32]	0.27 [32, 36]	–	0.752 [32]	HFC-134a	0.28 ^c [32]
Norit R1 extra	–	1450 [22]	0.47 [22]	–	–	–	–
Norit RB3	–	978.04 [24]	0.43 [24]	21 [24]	–	CO ₂	1.09 ^c [24]
Norit Darco	–	876.45 [24]	0.61 [24]	33.30 [24]	–	CO ₂	0.90 ^c [24]
BPL	Granules	1150 [22]	0.43 [22]	–	–	–	–
Kureha	–	1300 [22]	0.56 [22]	–	–	–	–
Phenol resin derived AC (KOH4-PR)	Powder	3060 [37]	1.85 [37]	12.50 [37]	–	Ethanol	1.43 [37]
Phenol resin derived AC (KOH6-PR)	Powder	2910 [37]	2.37 [37]	17.80 [37]	–	Ethanol	1.98 [37]
Waste Palm Trunk (WPT) derived AC (WPT-AC)	Powder	2927 [38]	2.41 [38]	16.8 [38]	–	Ethanol	1.90 ^b [38]
					–	CO ₂	3.90 ^b [39]
Mangrove derived AC	Powder	2924 [38]	2.13 [38]	14.7 [38]	–	Ethanol	1.65 ^b [38]
						CO ₂	3.85 ^b [39]

(continued)

Table 4.1 (continued)

Adsorbent	Type	Surface area (m ² g ⁻¹)	Micropore volume (cm ³ g ⁻¹)	Average pore width (Å)	Packing density (g cm ⁻³)	Refrigerant	Adsorption uptake (g g ⁻¹)
Coconut shell derived AC	Powder	2288 [40]	1.012 [40]	–	–		-

^a Total pore volume [cm³ g⁻¹]; ^b Saturated amount of adsorption uptake [g g⁻¹] determined by Tóth model.; ^c Saturated amount of adsorption uptake [cm³ g⁻¹] determined by Dubinin-Astakhov model.; ^d Saturated amount of adsorption uptake [g g⁻¹] determined by Dubinin-Radushkevich model

4.3.3 Binder Materials

Basically, carbon-based adsorbents are in powder form and have a dispersive nature. Therefore, they cannot be consolidated by applying pressure only. Consequently, a small weight percentage of binder material is assimilated with parent adsorbent to obtain the consolidation, which results in the development of thermal conductive path as well as an increase of packing density. Numerous binders such as polyvinylpyrrolidone (PVP) [48], polyvinyl alcohol (PVA) [3, 49], hydroxyethyl cellulose [50], polytetrafluoroethylene (PTFE) [51], etc., have been employed to synthesize composite adsorbents for the enhancement of the compactness of system and heat transfer in the adsorption bed. Sharafian et al. [48] showed that silica gel-PVP composite possessed 78.6% higher thermal conductivity than that of dry silica gel packed bed. Besides, Pal et al. [52] presented that Maxsorb III-PVA composite exhibited a 50% higher thermal conductivity than that of parent Maxsorb III. However, these binders have a poor affinity to the refrigerant molecules, which results in the negative adsorption effect of composite adsorbents. Thus, several researchers [5, 52] are employing polymerized ionic liquid (PIL) as a promising binder to develop consolidated composite adsorbents. Pal et al. [52] and Rocky et al. [5] revealed that amino acid-based PIL, namely poly vinylbenzyltrimethyl ammonium alanate (simply written as Poly[VBTMA][Ala]), had an affinity to refrigerant molecules. As a result, the Maxsorb III-PIL composite exhibited higher adsorption uptake of CO₂ and ethanol than that of the Maxsorb III-PVA composite. Besides, the Maxsorb III-PIL composite possessed higher packing density and thermal conductivity than that of the Maxsorb III-PVA composite.

4.4 Synthesis of Consolidated Composite Adsorbent

Reflection of the particular properties of one or more materials in a parent material to meet specific demands is the main motivation of the synthesis of composite. There exist two processes, namely chemical process, and simple mixing process to synthesize composite adsorbent. In the chemical process, basically, a chemical reaction takes place in any step of the synthesis process. A number of researchers [53–55] developed composite adsorbents adopting the chemical process. Here, we are focusing only on the simple mixing process. In this process, firstly, adsorbents and thermally conductive materials are separately regenerated in a heater at 120–150 °C for 6 h to eliminate moisture and volatile materials that might be adsorbed on the surface. After that, a certain percentage of adsorbent and thermally conductive materials are mixed. Meanwhile, water or other solvents such as ethanol, methanol is poured into the predetermined percentage of binder to make a viscous solution. Then, the mixture and the viscous solution are combined and tried to mix all the materials to get a homogeneous mixture. Hereafter, employing a compressing machine, the final mixture is compacted, which results in a consolidated composite adsorbent in a pellet form. Finally, the composite adsorbent is heated at 120–150 °C for 24 h to remove the solvent and other materials that might be adsorbed during the synthesis. The steps involved in the synthesis of consolidated composite adsorbent are depicted in Fig. 4.1.

4.5 Methodology of Specific Heat Capacity Measurement

Numerous methods [56–63] have been established to investigate the c_p of substances. Differential scanning calorimetry or simply DSC is the most well-known and efficient thermoanalytical technique. Here, the difference in the amount of heat energy required to raise the temperature of the sample and standard material is investigated as a function of temperature. In the DSC experiment, both the sample and standard

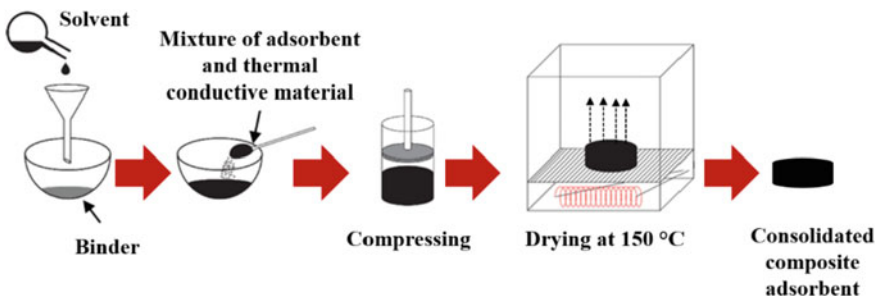


Fig. 4.1 Preparation of consolidated composite adsorbent

materials are kept at the same temperature throughout the whole measurement. Basically, in a DSC analysis, the temperature profile is programmed in such a way that the temperature of the sample holder increases linearly with time. It should be noted that the standard material should possess a well-defined heat capacity value over the measuring temperature range. In principle, differential scanning calorimeters can be categorized into two types:

- (a) Heat flux DSC
- (b) Power compensation DSC

The main difference between these DSCs lies in the measurement principle and construction. In the heat flux DSC, a single furnace is employed to heat the sample and standard material, and the difference of the temperature of the sample and standard material varies proportionally to the heat flow. Here, the amount of heat flux or heat flow is determined through the temperature difference and thermal resistance associated with the specimen and its surroundings. In this type of DSC, the temperature difference represents DSC output. On the other hand, in the power compensation DSC, two independent furnaces are used to increase the temperature of the sample and standard material. The temperatures of the sample and standard material are maintained the same through independent heating. In this case, the difference in the heating power of two furnaces is recorded against temperature or time.

In the following section of this chapter, we will present several experimental specific heat capacity data of parent substances and composite adsorbents, which are obtained employing DSC-60A. This DSC is developed by Shimadzu Corporation Ltd., Japan. DSC-60A is a heat flux type DSC. It has a built-in autosampler section that can measure samples automatically. It has a noise level of less than $1 \mu\text{W}$ and offers improved sensitivity. The heating or cooling rate can be set from $0.1 \text{ }^\circ\text{C/h}$ to $99.9 \text{ }^\circ\text{C/min}$. The major components of this type of DSC are the thermal analyzer, heater control circuit, gas flow controller, temperature sensors, and data acquisition unit. Figure 4.2 shows the schematic construction of DSC-60A.

From Fig. 4.2, it is seen that on the heating block (furnace) of the DSC section, there exist two portions—one is the reference portion (R), and the other is the sample portion (S). These two portions can be warmed or cooled by a predesigned program. When power is supplied to the heater, heating block temperature changes to T_B at a predefined rate. Q_S and Q_R heat per unit time flow from the heating block through the thermal resistance to the sample section and reference section, respectively. Therefore, the temperature of the sample section and the reference section increases/decreases to T_S and T_R , respectively. At this time, the temperature difference ($\Delta T = T_S - T_R$) between the sample section and the reference section is detected. In DSC-60A, chromel–alumel thermocouples are used for the detection of T_B and T_S , and a chromel–constantan thermocouple is employed for the detection of ΔT .

In the experimental investigation of c_p , the most important concern is to uphold uniformity in all aspects of the analysis. In DSC-60A, three successive measurements are carried out under the same conditions to investigate the c_p of any material. In

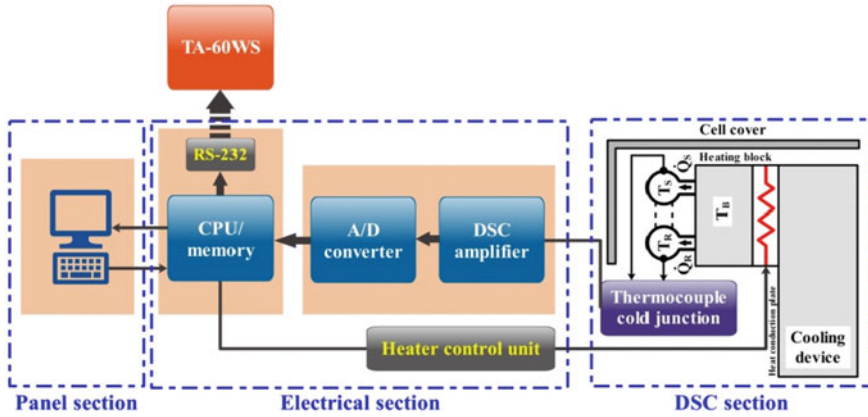


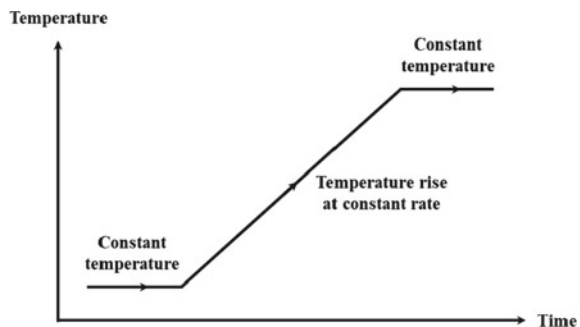
Fig. 4.2 Schematic of DSC-60A apparatus

every measurement, a blank sample crucible sealed with the lid is placed on the reference section. The three consecutive measurements are:

- (a) **Blank measurement:** In this measurement, a blank sample crucible with closed lid is kept in the sample portion (S), and the DSC output is obtained for it.
- (b) **Standard sample measurement:** A certain amount of standard material (α -Al₂O₃) is placed into the crucible and sealed with the lid. DSC data is then attained by putting the pan in the sample section (S).
- (c) **Sample measurement:** In this step, the target sample is put into an empty crucible. The sample mass should be close to the standard sample that was measured in the previous step. The crucible is then sealed, kept in the sample portion (S), and the DSC data is measured for similar operating conditions.

In the c_p measurement, the execution of a temperature program is a prerequisite. Fig. 4.3 shows a temperature program consisting of one isothermal phase followed by a heating phase and another isothermal phase. When the temperature increases at the fixed rate, the system is considered stable.

Fig. 4.3 Temperature program for c_p measurement



The relationship among the heat capacity of the sample section (sample crucible stage + sample crucible + sample) C_S , heat capacity of reference section (sample crucible stage + sample crucible + sample) C_R , and the temperature rising rate can be expressed as

$$C_S - C_R = -\frac{T_S - T_R}{\alpha R} \quad (4.5)$$

where, T_S and T_R refer to the temperature of the sample side and reference side in a stable state, respectively, α denotes the rate of temperature rise, and R is the thermal resistance between the sample/reference side and furnace. According to the principle of heat flux DSC, $(T_S - T_R)$ will represent the DSC output. If we define the DSC output as Z and the proportion constant as k , then the Eq. (4.5) can be written as

$$C_S - C_R = kZ \quad (4.6)$$

Since three successive measurements are accomplished to calculate the specific heat capacity of an unknown substance, therefore, three DSC outputs will be obtained, and they can be expressed as by Eqs. (4.7) to (4.9)

$$kZ_{blank} = C_s^l - C_r^l \quad (4.7)$$

$$kZ_{standard} = (C_s^l + m_{standard} \cdot c_{p,standard}) - C_r^l \quad (4.8)$$

$$kZ_{sample} = (C_s^l + m_{sample} \cdot c_{p,sample}) - C_r^l \quad (4.9)$$

where, Z_{blank} , $Z_{standard}$, and Z_{sample} represent the DSC outputs for blank measurement, standard sample measurement, and unknown sample measurement, respectively. All these DSC data are plotted and depicted in Fig. 4.4; C_s^l and C_r^l denote the heat capacity of sample section (sample crucible stage + sample crucible) and reference section (sample crucible stage + sample crucible), respectively; $m_{standard}$ and m_{sample} stand for the mass of standard material and the target sample, respectively; $c_{p,standard}$ and $c_{p,sample}$ are the specific heat capacity of the standard material and the unknown sample, respectively.

Now, from the Eqs. (4.7), (4.8), and (4.9), we can obtain –

$$c_{p,sample} = \frac{m_{standard}}{m_{sample}} \cdot \frac{Z_{sample} - Z_{blank}}{Z_{standard} - Z_{blank}} \times c_{p,standard} \quad (4.10)$$

As the $c_{p,standard}$ is known, then the specific heat capacity of any unknown material ($c_{p,sample}$) could be calculated by adopting the Eq. (4.10).

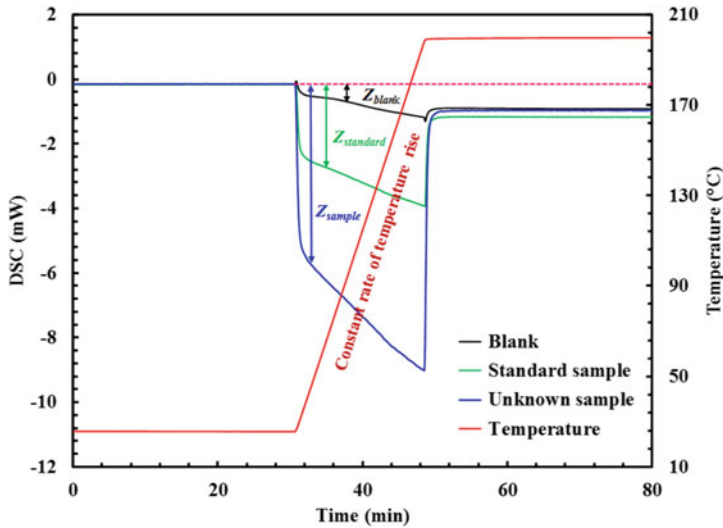


Fig. 4.4 DSC plots of blank, standard, and measured samples as a function of time

4.6 Specific Heat Capacity of Composite Adsorbents

In this section, the experimental specific heat capacity data of parent substances (adsorbent, thermal conductive, and binder materials) as well composites are reported. Here, the adopted experimental procedure is explained briefly, and the c_p data are correlated with a well-known polynomial equation. Besides, a generalized c_p equation for composite adsorbents is employed to determine the c_p of composites.

4.6.1 Experimental Procedure

The c_p measurement of adsorbents is quite challenging since they might contain water vapor or other materials into the pores. Therefore, the specimen preparation should be proper, and the final result is not affected by the adsorbed impurities. Hence, sample regeneration and accurate mass measurement of samples play significant roles for precise c_p measurement. Therefore, parent materials are degassed at 120 °C for 24 h. After that, the masses of the blank crucible (diameter: 5.6 mm, height: 2.8 mm) and the lid (diameter: 5.2 mm, height: 1.4 mm) are weighted. Then, the sample is kept in the blank sample crucible and sealed with the lid. After that, the sealed sample crucible is placed in a vacuum heater at 140 °C for 4 h, and after the drying, instantly the mass of the sealed sample crucible is weighed again. Finally, the sample mass is calculated from the two mass measurements. It should be noted that the sample mass should be very close to that of standard material. However, in the

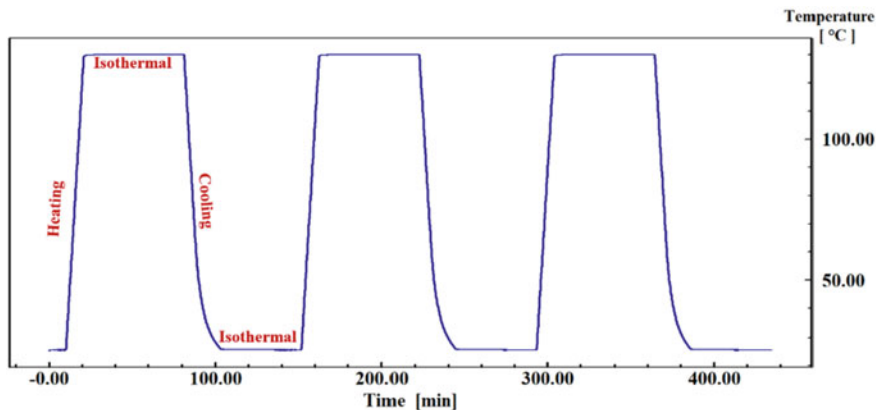


Fig. 4.5 A three-cycle temperature profile of DSC experiment

case of consolidated composite adsorbents, the specimen is prepared by resizing the larger consolidated composite into a disk of 4.5 to 5 mm diameter. After the resizing, the regeneration and mass measurement processes are also performed here. These processes are analogous to those for the parent substances.

After the preparation, samples are kept on the autosampler slots of the DSC. A suitable temperature profile is designed for the determination of c_p . The furnace of the DSC heats/cools the samples according to the designed profile. Researchers [11, 12] usually programmed three/four cycles of heating and cooling to determine the c_p of porous materials since moisture or other undesirable substances may be adsorbed at the pores during sample preparation. Each cycle consists of one heating phase, followed by one isothermal, one cooling, and another isothermal phase. It is expected that all the impurities are removed during the first two cycles, and the c_p is analyzed at the third or fourth cycle.

In our study, the adopted temperature profile is illustrated in Fig. 4.5. Here, the temperature profile comprises three cycles. Each cycle starts with heating from 25 °C to 130 °C at the rate of 10 °C/min. Just after this heating phase, the isothermal phase originates and continues for 60 min. After that, cooling starts from 130 °C to 25 °C at the same rate. Hereafter, another isothermal phase starts for 60 min. Finally, DSC analysis is carried out at the heating phase of the last cycle to determine the c_p of the substance.

4.6.2 Results and Discussion

In this section, the experimental c_p data of parent materials and composite adsorbents will be presented. Besides, we will show the correlation of the c_p data of parent materials with a c_p equation, which is a fourth-order polynomial function of temperature.

Tomeczek and Palugniok (TP) proposed this equation and correlated the c_p data of coal with this equation [64]. The equation can be expressed as

$$c_p = A + BT + CT^2 + DT^3 + ET^4 \tag{4.11}$$

Here, T represents the temperature [K]; $A, B, C, D,$ and E are coefficients.

Adsorbents: Fig. 4.6 illustrates the correlation of experimental c_p data with TP equation of several carbon-based adsorbents. Polynomial coefficients for adsorbents are also summarized in Table 4.2.

From Fig. 4.6, it is observed that c_p is an increasing function of the temperature and could be expressed as a polynomial equation since the RMSD value of the TP equation and the corresponding experimental data is very small (tabulated in Table 4.2). Among all the studied ACs, phenol resin based AC (KOH6-PR) exhibits the lowest c_p value, whereas KOH-H₂ treated Maxsorb III possesses the highest c_p value. When Maxsorb III is treated with H₂, the c_p value increases. If Maxsorb III is treated with KOH and H₂ then the c_p value further increases. In the case of WPT-AC, the c_p value lies in between Maxsorb III and H₂ treated Maxsorb III.

Thermal conductive materials: The specific heat capacity of several promising thermal conductive materials, namely multi-walled carbon nanotube (MWCNT), graphene nanoplatelets (R25-GNPs, H25-GNPs, C750-GNPs), and expanded graphite (EC-100, EC-500) are presented along with TP model fitting.

From Fig. 4.7, it is observed that all the c_p data are correlated well with the TP equation. All the polynomial coefficients and the RMSD values for these materials are listed in Table 4.3. It is investigated that H grade graphene nanoplatelets (H25-

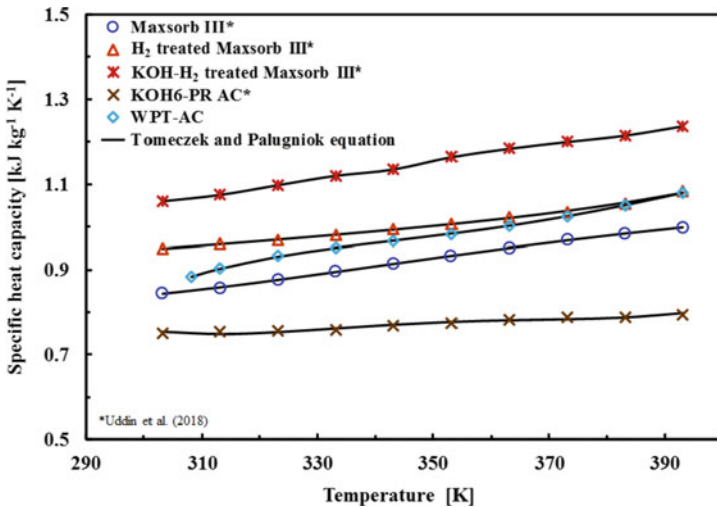


Fig. 4.6 Illustration of c_p mapping of different ACs

Table 4.2 Polynomial coefficients of TP model with RMSD value for different AC-based adsorbents

Adsorbent	Coefficients					RMSD (%)
	A _{ad} [kJ kg ⁻¹ K ⁻¹]	B _{ad} [kJ kg ⁻¹ K ⁻²]	C _{ad} [kJ kg ⁻¹ K ⁻³]	D _{ad} [kJ kg ⁻¹ K ⁻⁴]	E _{ad} [kJ kg ⁻¹ K ⁻⁵]	
Maxsorb III	11.54686	-0.11885	4.79695 × 10 ⁻⁴	-8.36726 × 10 ⁻⁷	5.39044 × 10 ⁻¹⁰	0.0964
H ₂ treated Maxsorb III	5.57681	-0.06177	3.00800 × 10 ⁻⁴	-6.43661 × 10 ⁻⁷	-10 ⁵ .19334 × 10	0.1917
KOH-H ₂ treated Maxsorb III	36.93756	-0.41431	1.77453 × 10 ⁻³	-3.34924 × 10 ⁻⁶	2.36185 × 10 ⁻⁹	0.2244
KOH6-PR AC	109.40739	-1.24928	5.36803 × 10 ⁻³	-1.02196 × 10 ⁻⁵	7.27667 × 10 ⁻⁹	0.3536
WPT-AC	-75.98262	0.83623	-3.40459 × 10 ⁻³	6.14217 × 10 ⁻⁶	-4.13186 × 10 ⁻⁹	0.0956

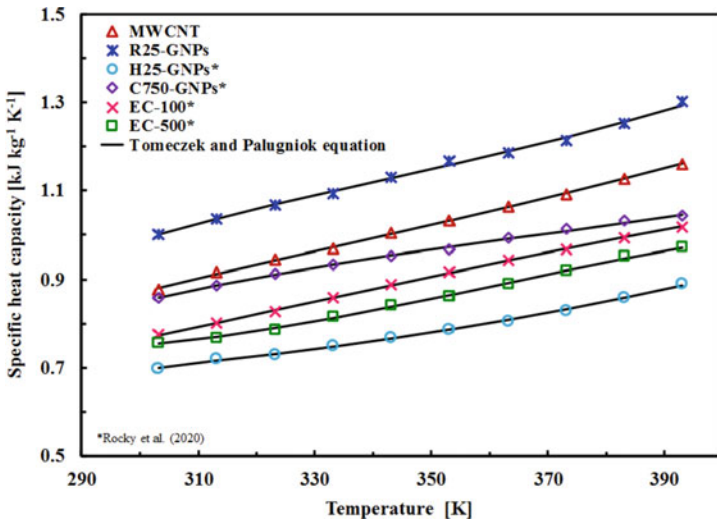


Fig. 4.7 Illustration of c_p mapping of different thermal conductive materials

GNPs) exhibit the lowest c_p value, whereas R grade graphene nanoplatelets (R25-GNPs) possess the highest c_p value. Expanded graphite of type EC-100 shows a higher c_p value than that of expanded graphite of type EC-500.

Table 4.3 Polynomial coefficients of the TP model with RMSD value for promising thermal conductive materials

Thermal conductive material	Coefficients					RMSD (%)
	A _{TCM} [kJ kg ⁻¹ K ⁻¹]	B _{TCM} [kJ kg ⁻¹ K ⁻²]	C _{TCM} [kJ kg ⁻¹ K ⁻³]	D _{TCM} [kJ kg ⁻¹ K ⁻⁴]	E _{TCM} [kJ kg ⁻¹ K ⁻⁵]	
MWCNT	-9.44522	0.10718	-4.28089 × 10 ⁻⁴	7.73244 × 10 ⁻⁷	-5.16988 × 10 ⁻¹⁰	0.3147
R25-GNPs	-16.38973	0.17742	-6.83150 × 10 ⁻⁴	1.17061 × 10 ⁻⁶	-7.37179 × 10 ⁻¹⁰	0.5054
H25-GNPs	-8.59435	0.10481	-4.47099 × 10 ⁻⁴	8.45953 × 10 ⁻⁷	-5.87069 × 10 ⁻¹⁰	0.2684
C750-GNPs	-7.13628	7.41276 × 10 ⁻²	-2.58989 × 10 ⁻⁴	4.05260 × 10 ⁻⁷	-2.32694 × 10 ⁻¹⁰	0.3226
EC-100	0.23944	-2.09282 × 10 ⁻³	2.46345 × 10 ⁻⁵	-4.95572 × 10 ⁻⁸	3.37382 × 10 ⁻¹¹	0.1405
EC-500	14.74781	-0.14925	5.79545 × 10 ⁻⁴	-9.74257 × 10 ⁻⁷	6.08081 × 10 ⁻¹⁰	0.3194

Binders: Binders play an important role to consolidate the adsorbent material. Figure 4.8 shows the c_p values of four types of binders, namely PVA, PVP, Poly[VBTMA][Ala], and poly vinylbenzyltrimethyl ammonium serinate (simply written as Poly[VBTMA][Ser]). It is clearly observed that the TP model can explain the experimental c_p data well. The fitting coefficients and RMSD values are tabulated in Table 4.4.

From Fig. 4.8, it is noticed that PVA exhibits the highest specific heat capacity among the studied binders. However, at lower temperatures, Poly[VBTMA][Ala] shows a higher c_p value than that of PVA. Besides, among the ionic liquid-based binders, Poly[VBTMA][Ser] shows the lowest c_p value.

Consolidated composite adsorbent: Since composite adsorbent consists of adsorbent, thermal conductive material, and binder, the effects of individuals are reflected

Table 4.4 Polynomial coefficients of TP model with RMSD value for binders

Binder	Coefficients					RMSD (%)
	A _b [kJ kg ⁻¹ K ⁻¹]	B _b [kJ kg ⁻¹ K ⁻²]	C _b [kJ kg ⁻¹ K ⁻³]	D _b [kJ kg ⁻¹ K ⁻⁴]	E _b [kJ kg ⁻¹ K ⁻⁵]	
PVA	939.61951	-10.56792	4.43688 × 10 ⁻²	-8.23358 × 10 ⁻⁵	5.70513 × 10 ⁻⁸	2.4637
PVP	-37.91221	0.45005	-1.98146 × 10 ⁻³	3.93575 × 10 ⁻⁶	-2.94289 × 10 ⁻⁹	0.2012
Poly[VBTMA][Ala]	-93.13202	1.10967	-4.91416 × 10 ⁻³	9.67982 × 10 ⁻⁶	-7.09499 × 10 ⁻⁹	0.1611
Poly[VBTMA][Ser]	-267.38593	3.05691	-1.30269 × 10 ⁻²	2.46086 × 10 ⁻⁵	-1.73514 × 10 ⁻⁸	0.2626

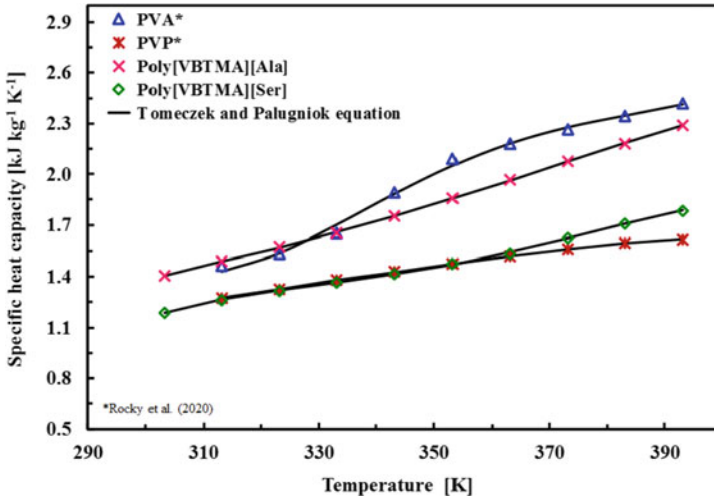


Fig. 4.8 Illustration of c_p mapping of different binders

in the c_p of composite adsorbents. Considering these effects, Rocky et al. [12] proposed a generalized temperature-dependent equation as depicted below to calculate the c_p of any composite.

$$c_{p,c} = A_c + \alpha(B_c T + C_c T^2 + D_c T^3 + E_c T^4) \quad (4.12)$$

where, $c_{p,c}$ represents the c_p of composite adsorbent and α is a dimensionless parameter. A_c , B_c , C_c , D_c , and E_c are the coefficients, which are determined by the coefficients of TP model for adsorbents, thermal conductive materials, and binders. The coefficients can be defined as

$$\begin{aligned} A_c &= xA_{ad} + yA_{TCM} + zA_b \\ B_c &= xB_{ad} + yB_{TCM} + zB_b \\ C_c &= xC_{ad} + yC_{TCM} + zC_b \\ D_c &= xD_{ad} + yD_{TCM} + zD_b \\ E_c &= xE_{ad} + yE_{TCM} + zE_b \end{aligned}$$

Here, x , y , and z denote the mass fraction of adsorbent, thermal conductive material, and binder, respectively, and it should be noted that the summation of x , y , and z will always be one. In the Eq. (4.12), if we consider $\alpha = 1$, then it will turn into Eq. (4.11) and represent that the constituent materials of the composites are well distributed. However, the value of α higher than 1 indicates that the percentage of material having a high c_p value is governing in the tested sample. On the other hand,

the value of α between 0 and 1 represents that the material of low c_p value is dominant in the sample. Rocky et al. validated the proposed equation with some experimental results shown in Figs. 4.9 and 4.10. In the legend section of the figures, the mass fractions of constituent materials of each composite are mentioned.

From Figs. 4.9 and 4.10, it is clear that the proposed equation can accurately predict the c_p of any composite adsorbent. In these figures, it is observed that the c_p of the individual components of the composites have contributed to the c_p of composites according to their mass fractions. Therefore, the c_p of several composites has been calculated employing Eq. (4.12) and illustrated in Figs. 4.11 and 4.12. From Fig. 4.11, it is seen that the increase of the mass fraction of Maxsorb III in the composites results in the decrease of c_p of composite adsorbents since Maxsorb III possesses the lowest c_p value among the comprising materials of the composites. A similar phenomenon is investigated in the case of WPT-AC, R25-GNPs, and Poly[VBtMA][Ser] based composites, which is depicted in Fig. 4.12. Here, when the mass fraction of WPT-AC increases in the composites, then c_p of the composites decreases, as WPT-AC exhibits the lowest c_p value among all the comprising substances of the composite adsorbents.

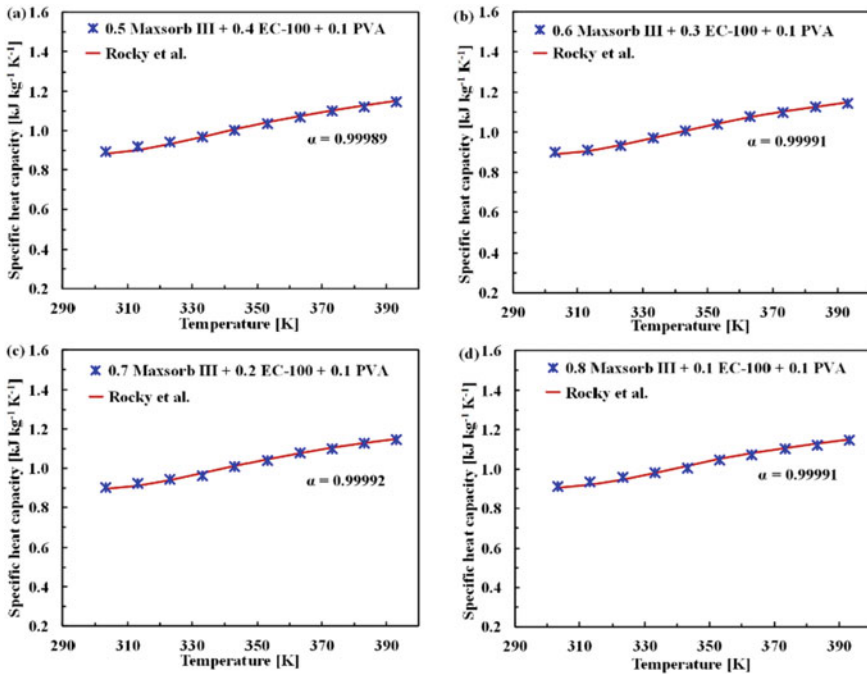


Fig. 4.9 Illustration of c_p mapping of Maxsorb III—EC-100—PVA-based consolidated composite adsorbents

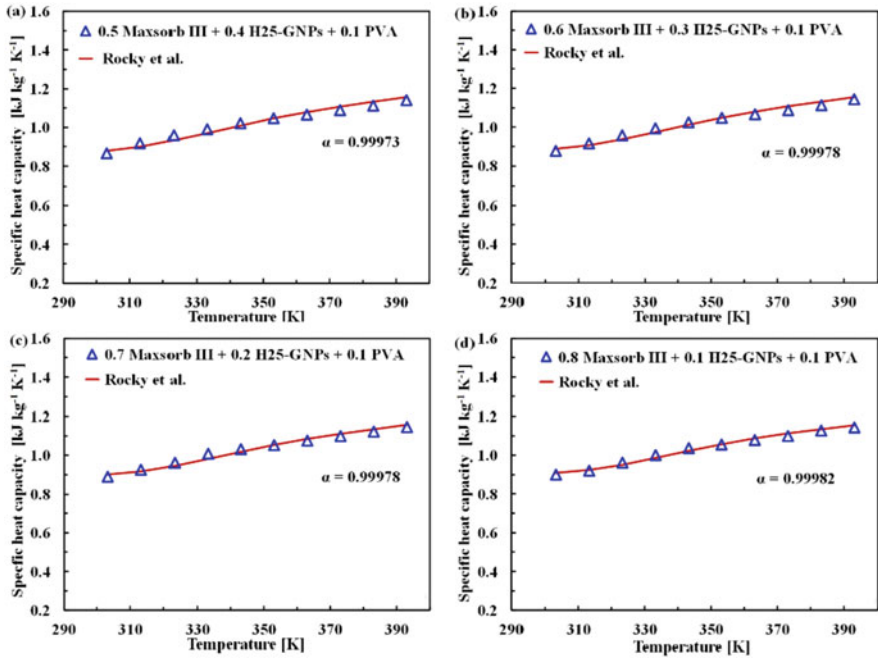


Fig. 4.10 Illustration of c_p mapping of Maxsorb III—H25-GNPs—PVA-based consolidated composite adsorbents

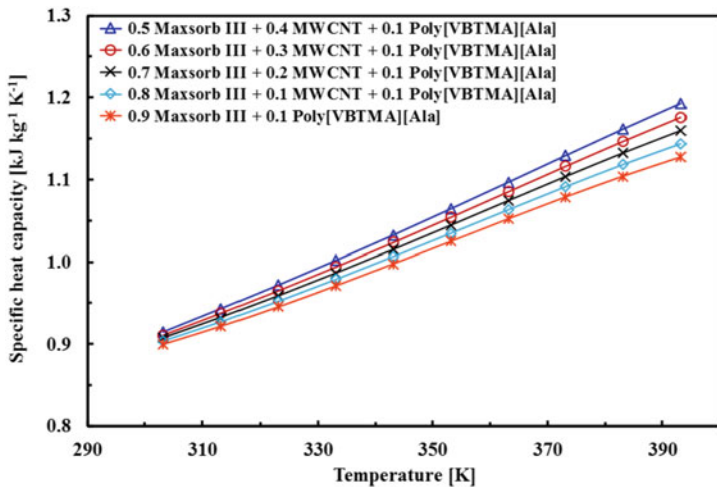


Fig. 4.11 Illustration of c_p mapping of Maxsorb III, MWCNT, and Poly[VBTMA][Ala] based composites

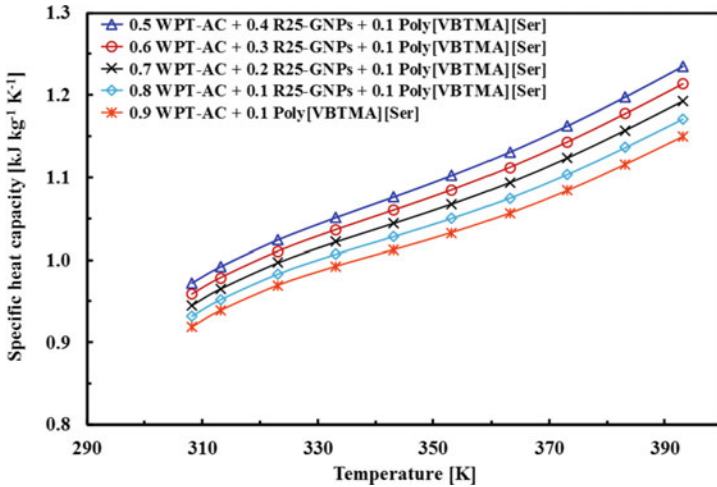


Fig. 4.12 Illustration of c_p mapping of WPT-AC, R25-GNPs, and Poly[VBtMA][Ser] based composites

4.7 Conclusions

This chapter briefly describes the significance of c_p in the design of an adsorption heat pump and desalination systems. Besides, the physical and adsorption properties of several carbon-based adsorbents are summarized here. This chapter mainly focuses on the c_p of parent substances as well carbon-based composite adsorbents. The procedure adopted to obtain the accurate specific heat capacity is also described here concisely. From the experimental c_p data, it could be concluded that c_p is the increasing function of temperature. The experimental c_p data are correlated with the well-known fourth-order polynomial equation proposed by Tomeczek and Palugniok [64], and good agreements are noticed. Besides, a universal temperature-dependent c_p equation for composite adsorbents proposed by Rocky et al. [12] is described here. Through this equation, one can determine the c_p of any composite adsorbent by knowing only the c_p value of the consisting parent substances. In this study, this generalized equation is employed to determine the c_p of several composite adsorbents. The precise c_p value of adsorbents or composites will significantly contribute to the rigorous analysis and accurate performance evaluation of an AHP/AD system.

References

1. Thu K, Ng KC, Saha BB, Chakraborty A, Koyama S (2009) Operational strategy of adsorption desalination systems. *Int J Heat Mass Transf* 52:1811–1816. <https://doi.org/10.1016/j.jheatmasstransfer.2008.10.012>
2. Saha BB, El-Sharkawy II, Shahzad MW, Thu K, Ang L, Ng KC (2016) Fundamental and application aspects of adsorption cooling and desalination. *Appl Therm Eng* 97:68–76. <https://doi.org/10.1016/j.applthermaleng.2015.09.113>
3. El-Sharkawy II, Pal A, Miyazaki T, Saha BB, Koyama S (2016) A study on consolidated composite adsorbents for cooling application. *Appl Therm Eng* 98:1214–1220. <https://doi.org/10.1016/j.applthermaleng.2015.12.105>
4. Pal A, Uddin K, Rocky KA, Thu K, Saha BB (2019) CO₂ adsorption onto activated carbon-graphene composite for cooling applications. *Int J Refrig*. <https://doi.org/10.1016/j.ijrefrig.2019.04.022>
5. Rocky KA, Pal A, Moniruzzaman M, Saha BB. Adsorption characteristics and thermodynamic property fields of polymerized ionic liquid and polyvinyl alcohol based composite/CO₂ pairs. *J Mol Liq* 2019:111555. <https://doi.org/10.1016/j.molliq.2019.111555>.
6. Zheng X, Wang LW, Wang RZ, Ge TS, Ishugah TF (2014) Thermal conductivity, pore structure and adsorption performance of compact composite silica gel. *Int J Heat Mass Transf* 68:435–443. <https://doi.org/10.1016/j.jheatmasstransfer.2013.09.075>
7. Eun T, Song H, Hun Han J, Lee K, Kim J. Enhancement of heat and mass transfer in silica-expanded graphite composite blocks for adsorption heat pumps:: Part I. Characterization of the composite blocks: Amélioration du transfert de chaleur de blocs en matériaux composite graphite-silice expansé/d. *Int J Refrig* 2000;23:64–73.
8. Kulakowska A, Pajdak A, Krzywanski J, Grabowska K, Zylka A, Sosnowski M et al (2020) Effect of metal and carbon nanotube additives on the thermal diffusivity of a silica-gel-based adsorption bed. *Energies* 16:12–16. <https://doi.org/10.3390/en13061391>
9. Aristov YI (2012) Adsorptive transformation of heat: Principles of construction of adsorbents database. *Appl Therm Eng* 42:18–24. <https://doi.org/10.1016/j.applthermaleng.2011.02.024>
10. Askalany AA, Henninger SK, Ghazy M, Saha BB (2017) Effect of improving thermal conductivity of the adsorbent on performance of adsorption cooling system. *Appl Therm Eng* 110:695–702. <https://doi.org/10.1016/j.applthermaleng.2016.08.075>
11. Uddin K, Islam MA, Mitra S, Lee JB, Thu K, Saha BB et al (2018) Specific heat capacities of carbon-based adsorbents for adsorption heat pump application. *Appl Therm Eng* 129:117–126. <https://doi.org/10.1016/j.applthermaleng.2017.09.057>
12. Rocky KA, Islam MA, Pal A, Ghosh S, Thu K, Nasruddin, et al. Experimental investigation of the specific heat capacity of parent materials and composite adsorbents for adsorption heat pumps. *Appl Therm Eng* 2020;164:114431. <https://doi.org/10.1016/j.applthermaleng.2019.114431>.
13. Islam MA, Pal A, Saha BB (2020) Experimental study on thermophysical and porous properties of silica gels. *Int J Refrig* 110:277–285. <https://doi.org/10.1016/j.ijrefrig.2019.10.027>
14. Jahan I, Islam MA, Palash ML, Rocky KA, Rupam TH, Saha BB. Experimental Study on the Influence of Metal Doping on Thermophysical Properties of Porous Aluminum Fumarate. *Heat Transf Eng* 2020:1–10. <https://doi.org/10.1080/01457632.2020.1777005>.
15. Rahman KA, Chakraborty A, Saha BB, Ng KC (2012) On thermodynamics of methane + carbonaceous materials adsorption. *Int J Heat Mass Transf* 55:565–573. <https://doi.org/10.1016/j.jheatmasstransfer.2011.10.056>
16. Boelman EC, Saha BB, Kashiwagi T (1995) Experimental investigation of a silica gel-water adsorption refrigeration cycle - the influence of operating conditions on cooling output and COP. *ASHRAE Trans* 101:358–366
17. Mitra S, Aswin N, Dutta P (2016) Scaling analysis and numerical studies on water vapour adsorption in a columnar porous silica gel bed. *Int J Heat Mass Transf* 95:853–864. <https://doi.org/10.1016/j.jheatmasstransfer.2015.12.011>

18. Thu K, Kim YD, Shahzad MW, Saththasivam J, Ng KC (2015) Performance investigation of an advanced multi-effect adsorption desalination (MEAD) cycle. *Appl Energy* 159:469–477. <https://doi.org/10.1016/j.apenergy.2015.09.035>
19. Askalany AA, Saha BB, Ahmed MS, Ismail IM (2013) Adsorption cooling system employing granular activated carbon-R134a pair for renewable energy applications. *Int J Refrig* 36:1037–1044. <https://doi.org/10.1016/j.ijrefrig.2012.11.009>
20. Chan KC, Chao CYH, Sze-To GN, Hui KS (2012) Performance predictions for a new zeolite 13X/CaCl₂ composite adsorbent for adsorption cooling systems. *Int J Heat Mass Transf* 55:3214–3224. <https://doi.org/10.1016/j.ijheatmasstransfer.2012.02.054>
21. Chakraborty A, Saha BB, Ng KC, Koyama S, Srinivasan K. Theoretical insight of physical adsorption for a single-component adsorbent + adsorbate system: I. thermodynamic property surfaces. *Langmuir* 2009. <https://doi.org/10.1021/la803289p>.
22. Saha BB, Chakraborty A, Koyama S, Yoon SH, Mochida I, Kumja M et al (2008) Isotherms and thermodynamics for the adsorption of n-butane on pitch based activated carbon. *Int J Heat Mass Transf* 51:1582–1589. <https://doi.org/10.1016/j.ijheatmasstransfer.2007.07.031>
23. Rupam TH, Islam MA, Pal A, Chakraborty A, Saha BB. Thermodynamic property surfaces for various adsorbent/adsorbate pairs for cooling applications. *Int J Heat Mass Transf* 2019;144:118579. <https://doi.org/10.1016/j.ijheatmasstransfer.2019.118579>
24. Singh VK, Kumar EA. Experimental investigation and thermodynamic analysis of CO₂adsorption on activated carbons for cooling system. *J CO₂ Util* 2017;17:290–304. <https://doi.org/10.1016/j.jcou.2016.12.004>.
25. Pal A, Uddin K, Thu K, Saha BB (2019) Activated carbon and graphene nanoplatelets based novel composite for performance enhancement of adsorption cooling cycle. *Energy Convers Manag* 180:134–148. <https://doi.org/10.1016/j.enconman.2018.10.092>
26. Jiang L, Roskilly AP (2019) Thermal conductivity, permeability and reaction characteristic enhancement of ammonia solid sorbents: A review. *Int J Heat Mass Transf* 130:1206–1225. <https://doi.org/10.1016/j.ijheatmasstransfer.2018.11.029>
27. Jiang L, Wang RZ, Roskilly AP (2018) Investigation on thermal characteristics of novel composite sorbent with carbon coated iron as additive. *Int J Heat Mass Transf* 125:543–551. <https://doi.org/10.1016/j.ijheatmasstransfer.2018.04.118>
28. Rezk ARM, Al-Dadah RK (2012) Physical and operating conditions effects on silica gel/water adsorption chiller performance. *Appl Energy* 89:142–149. <https://doi.org/10.1016/j.apenergy.2010.11.021>
29. Saha BB, Jribi S, Koyama S, El-Sharkawy II (2011) Carbon dioxide adsorption isotherms on activated carbons. *J Chem Eng Data* 56:1974–1981. <https://doi.org/10.1021/je100973t>
30. El-Merraoui M, Aoshima M, Kaneko K (2000) Micropore size distribution of activated carbon fiber using the density functional theory and other methods. *Langmuir* 16:4300–4304. <https://doi.org/10.1021/la991242j>
31. K. Hata, H.S. Kil, K. Ideta, J. Miyawaki, I. Mochida SHY. Influence of surface functionality on ethanol adsorption behavior in activated carbons analyzed by solid-state NMR. In: Saha BB et al., editor. *Proceeding Innov. Mater. Process. Energy Syst.* 2013, Fukuoka: 2013, p. 525–8.
32. Akkimaradi BS, Prasad M, Dutta P, Srinivasan K (2002) Effect of packing density and adsorption parameters on the throughput of a thermal compressor. *Carbon N Y* 40:2855–2859. [https://doi.org/10.1016/S0008-6223\(02\)00218-X](https://doi.org/10.1016/S0008-6223(02)00218-X)
33. Askalany AA, Saha BB, Uddin K, Miyzaki T, Koyama S, Srinivasan K et al (2013) Adsorption isotherms and heat of adsorption of difluoromethane on activated carbons. *J Chem Eng Data* 58:2828–2834. <https://doi.org/10.1021/je4005678>
34. Uddin K, El-Sharkawy II, Miyazaki T, Saha BB, Koyama S, Kil HS et al (2014) Adsorption characteristics of ethanol onto functional activated carbons with controlled oxygen content. *Appl Therm Eng* 72:211–218. <https://doi.org/10.1016/j.applthermaleng.2014.03.062>
35. El-Sharkawy II, Kuwahara K, Saha BB, Koyama S, Ng KC (2006) Experimental investigation of activated carbon fibers/ethanol pairs for adsorption cooling system application. *Appl Therm Eng* 26:859–865. <https://doi.org/10.1016/j.applthermaleng.2005.10.010>

36. Prasad M, Akkumardi BS, Rastogi SC, Rao RR, Srinivasan K (1996) Adsorption characteristics of the charcoal-nitrogen system at 79–320 K and pressures to 5 MPa. *Carbon N Y* 34:1401–1406. [https://doi.org/10.1016/S0008-6223\(96\)00082-6](https://doi.org/10.1016/S0008-6223(96)00082-6)
37. El-Sharkawy II, Uddin K, Miyazaki T, Baran Saha B, Koyama S, Kil HS et al (2015) Adsorption of ethanol onto phenol resin based adsorbents for developing next generation cooling systems. *Int J Heat Mass Transf* 81:171–178. <https://doi.org/10.1016/j.ijheatmasstransfer.2014.10.012>
38. Pal A, Thu K, Mitra S, El-Sharkawy II, Saha BB, Kil HS et al (2017) Study on biomass derived activated carbons for adsorptive heat pump application. *Int J Heat Mass Transf* 110:7–19. <https://doi.org/10.1016/j.ijheatmasstransfer.2017.02.081>
39. Pal A, Uddin K, Saha BB, Thu K, Kil H-S, Yoon S-H, et al. A benchmark for CO₂ uptake onto newly synthesized biomass-derived activated carbons. *Appl Energy* 2020;264:114720. <https://doi.org/10.1016/j.apenergy.2020.114720>.
40. Yang K, Peng J, Srinivasakannan C, Zhang L, Xia H, Duan X (2010) Preparation of high surface area activated carbon from coconut shells using microwave heating. *Bioresour Technol* 101:6163–6169. <https://doi.org/10.1016/j.biortech.2010.03.001>
41. Rocky KA, Pal A, Saha BB. Adsorption Characteristics of CO₂ onto Carbon Nanotube for Adsorption Cooling / Capturing Applications. *Proceeding Int. Exch. Innov. Conf. Eng. Sci., Fukuoka, Japan: Kyushu University; 2019, p. 67–9.* <https://doi.org/10.15017/2552939>.
42. Yan T, Li TX, Wang RZ, Jia R (2015) Experimental investigation on the ammonia adsorption and heat transfer characteristics of the packed multi-walled carbon nanotubes. *Appl Therm Eng* 77:20–29. <https://doi.org/10.1016/j.applthermaleng.2014.12.001>
43. Su F, Lu C, Cnen W, Bai H, Hwang JF (2009) Capture of CO₂ from flue gas via multiwalled carbon nanotubes. *Sci Total Environ* 407:3017–3023. <https://doi.org/10.1016/j.scitotenv.2009.01.007>
44. Su F, Lu C, Chung AJ, Liao CH (2014) CO₂ capture with amine-loaded carbon nanotubes via a dual-column temperature/vacuum swing adsorption. *Appl Energy* 113:706–712. <https://doi.org/10.1016/j.apenergy.2013.08.001>
45. Zhao J, Buldum A, Han J, Lu JP (2002) Gas molecule adsorption in carbon nanotubes and nanotube bundles. *Nanotechnology* 13:195–200. <https://doi.org/10.1088/0957-4484/13/2/312>
46. Wang H, Zhou A, Peng F, Yu H, Yang J (2007) Mechanism study on adsorption of acidified multiwalled carbon nanotubes to Pb(II). *J Colloid Interface Sci* 316:277–283. <https://doi.org/10.1016/j.jcis.2007.07.075>
47. Raymundo-Piñero E, Azaïs P, Cacciaguerra T, Cazorla-Amorós D, Linares-Solano A, Béguin F (2005) KOH and NaOH activation mechanisms of multiwalled carbon nanotubes with different structural organisation. *Carbon N Y* 43:786–795. <https://doi.org/10.1016/j.carbon.2004.11.005>
48. Sharafian A, Fayazmanesh K, McCague C, Bahrami M (2014) Thermal conductivity and contact resistance of mesoporous silica gel adsorbents bound with polyvinylpyrrolidone in contact with a metallic substrate for adsorption cooling system applications. *Int J Heat Mass Transf* 79:64–71. <https://doi.org/10.1016/j.ijheatmasstransfer.2014.07.086>
49. Pal A, El-Sharkawy II, Saha BB, Jribi S, Miyazaki T, Koyama S (2016) Experimental investigation of CO₂ adsorption onto a carbon based consolidated composite adsorbent for adsorption cooling application. *Appl Therm Eng* 109:304–311. <https://doi.org/10.1016/j.applthermaleng.2016.08.031>
50. Berdenova B, Pal A, Muttakin M, Mitra S, Thu K, Saha BB et al (2019) A comprehensive study to evaluate absolute uptake of carbon dioxide adsorption onto composite adsorbent. *Int J Refrig* 100:131–140. <https://doi.org/10.1016/j.ijrefrig.2019.01.014>
51. Cacciola G, Restuccia G, Mercadante L (1995) Composites of activated carbon for refrigeration adsorption machines. *Carbon N Y* 33:1205–1210. [https://doi.org/10.1016/0008-6223\(95\)00051-E](https://doi.org/10.1016/0008-6223(95)00051-E)
52. Pal A, Shahrom MSR, Moniruzzaman M, Wilfred CD, Mitra S, Thu K et al (2017) Ionic liquid as a new binder for activated carbon based consolidated composite adsorbents. *Chem Eng J* 326:980–986. <https://doi.org/10.1016/j.cej.2017.06.031>
53. Zheng W, Hu J, Rappeport S, Zheng Z, Wang Z, Han Z et al (2016) Activated carbon fiber composites for gas phase ammonia adsorption. *Microporous Mesoporous Mater* 234:146–154. <https://doi.org/10.1016/j.micromeso.2016.07.011>

54. Chan KC, Chao CYH, Wu CL (2015) Measurement of properties and performance prediction of the new MWCNT-embedded zeolite 13X/CaCl₂ composite adsorbents. *Int J Heat Mass Transf* 89:308–319. <https://doi.org/10.1016/j.ijheatmasstransfer.2015.05.063>
55. Sukhyy KM, Belyanovskaya EA, Kozlov YN, Kolomiyets EV, Sukhyy MP (2014) Structure and adsorption properties of the composites “silica gel-sodium sulphate”, obtained by sol-gel method. *Appl Therm Eng* 64:408–412. <https://doi.org/10.1016/j.applthermaleng.2013.12.013>
56. Shi Q, Snow CL, Boerio-Goates J, Woodfield BF (2010) Accurate heat capacity measurements on powdered samples using a Quantum Design physical property measurement system. *J Chem Thermodyn* 42:1107–1115. <https://doi.org/10.1016/j.jct.2010.04.008>
57. Wang MH, Tan ZC, Sun XH, Zhang HT, Liu BP, Sun LX et al (2005) Determination of heat capacities and thermodynamic properties of 2-(chloromethylthio)benzothiazole by an adiabatic calorimeter. *J Chem Eng Data* 50:270–273. <https://doi.org/10.1021/je049678a>
58. Göbel A, Hemberger F, Vidi S, Ebert HP (2013) A new method for the determination of the specific heat capacity using laser-flash calorimetry down to 77K. *Int J Thermophys* 34:883–893. <https://doi.org/10.1007/s10765-012-1255-4>
59. Cao JN, Long Y, Shanks RA (1997) Experimental investigation into the heat capacity measurement using an modulated DSC. *J Therm Anal* 50:365–373. <https://doi.org/10.1007/BF01980497>
60. Jiang CH, Song LF, Jiao CL, Zhang J, Sun LX, Xu F et al (2011) Determination of heat capacities and thermodynamic properties of two structurally unrelated but isotopic calcium and manganese(II) 2,6-naphthalene dicarboxylate-based MOFs. *J Therm Anal Calorim* 103:1095–1103. <https://doi.org/10.1007/s10973-010-1197-7>
61. Czerniecka A, Magoń A, Schliesser J, Woodfield BF, Pyda M (2014) Heat capacity of poly(3-hydroxybutyrate). *J Chem Thermodyn* 73:76–84. <https://doi.org/10.1016/j.jct.2013.10.020>
62. Wen H, Lu JH, Xiao Y, Deng J (2015) Temperature dependence of thermal conductivity, diffusion and specific heat capacity for coal and rocks from coalfield. *Thermochim Acta* 619:41–47. <https://doi.org/10.1016/j.tca.2015.09.018>
63. Deng J, Li QW, Xiao Y, Shu CM, Zhang YN (2017) Predictive models for thermal diffusivity and specific heat capacity of coals in Huainan mining area. China. *Thermochim Acta* 656:101–111. <https://doi.org/10.1016/j.tca.2017.09.005>
64. Tomeczek J, Palugniok H (1996) Specific heat capacity and enthalpy of coal pyrolysis at elevated temperatures. *Fuel* 75:1089–1093. [https://doi.org/10.1016/0016-2361\(96\)00067-1](https://doi.org/10.1016/0016-2361(96)00067-1)

Chapter 5

Characterizing Adsorbent Materials Employing Atomic Force Microscopy



Mujib L. Palash, Animesh Pal, Mir Shariful Islam, and Bidyut Baran Saha

Abstract This chapter focuses on a modern characterization technique, Atomic Force Microscopy (AFM), which uses nanoprobes to extract three-dimensional (3-D) images of surfaces. These 3-D images contain both qualitative and quantitative information. Qualitative information is useful for visually understand the differences between various adsorbents that influence the physical properties. Quantitative information is suitable for determining roughness, shape, and depth of surface pores, pore size distribution, etc. However, it is quite challenging to take images of highly coarse surfaces like the porous materials usually have. Each of the materials requires different techniques for image extraction. Therefore, this work contains a brief description of the image extraction techniques for various porous materials with quantitative analysis.

Keywords Atomic force microscopy · Porosity · Porous materials · Surface imaging

M. L. Palash

Department of Electrical and Electronic Engineering, University of Dhaka, Dhaka 1000, Bangladesh

e-mail: mlpalash@du.ac.bd

A. Pal

Department of Nuclear Engineering, University of Dhaka, Dhaka 1000, Bangladesh

e-mail: animeshpal@du.ac.bd

M. S. Islam · B. B. Saha (✉)

International Institute for Carbon-Neutral Energy Research (WPI-I2CNER), Kyushu University, 744 Motoooka, Nishi-ku, Fukuoka 819-0395, Japan

e-mail: saha.baran.bidyut.213@m.kyushu-u.ac.jp

M. S. Islam

e-mail: mirsharifuldu77@du.ac.bd

Mechanical Engineering Department, Kyushu University, 744 Motoooka, Nishi-ku, Fukuoka 819-0395, Japan

5.1 Introduction

Characterization of porous materials is essential in various areas of research. Particle size, surface area, and porosity are the three key characteristics that control various properties of materials such as adsorption, filter-ability, flowability, agglomeration, the storage capacity of fluids and gases. In the case of gas adsorption, which has a major application in energy-efficient chiller systems, specific surface area (SSA) and pore size distribution (PSD) is needed to determine quantitatively [1]. Larger SSA means higher adsorption, where PSD is directly related to the response of adsorbent to adsorbate. For example, activated carbon is considered a suitable adsorbent because of having a high SSA, which is about 3,000 m²/g [2]. Similarly, different sizes of the pores of adsorbent contribute to varying adsorption kinetics for specific adsorption. Adsorption kinetics of ethanol onto activated carbon and mesoporous silica gel is completely different due to PSD [3]. Therefore, measuring these characteristics is practiced before the primary research.

Various methods are existed to measure specific surface area and pore size distribution. One of the common practices to measure these characteristics is the gas adsorption technique. In this technique, nitrogen (N₂) or helium (He) is used at a low-pressure condition to indirectly measure the surface characteristic, and the pore size distribution is measured by capillary condensation of the adsorbate molecules [4, 5].

On the other hand, imaging techniques are more of a straight-forward method, which takes the surface images to extract the topographic information of the surface. Wide varieties of imaging techniques are present to determine the type of porosity of various porous materials. Optical Microscopy and Transmission Electron Microscopy (TEM) [6], Nuclear Magnetic Resonance Imaging (NMRI), Scanning Electron Microscopy (SEM) [7], and X-ray spectroscopy are the popular techniques in this category. Atomic Force Microscopy (AFM) is a considerably new technique with an identical feature of providing height-based information of surface [8]. This feature can be used to generate three-dimensional images and calculate the surface topographic information, such as pore size distribution, fractal dimension, roughness, etc.

In this chapter, various types of materials are used to identify the challenges of extracting topographic images of different types of surfaces. First of all, standard sample TGG1 and HOPG samples are studied to understand the limitation of AFM techniques. As a representative of porous materials, silica gels and activated carbon were studied. Three important quantitative parameters, pore size distribution, roughness, and fractal dimension, were measured, which are challenging to study using conventional characterization techniques.

5.2 Characterization Techniques

The gas adsorption method is a standard method for measuring specific surface area and pore size distribution. This method is based on the principle of gas adsorption on solid surfaces. Usually, nitrogen, helium, carbon dioxide gases are used in this method. Equilibrium gas adsorption capacity is measured under certain pressure and temperature, known as adsorption isotherm. The specific surface area and pore distribution of the studied sample can be obtained from the analysis of this adsorption isotherm curve. Nowadays, nitrogen adsorption at 77 K temperature is widely used to measure the materials' specific surface area and pore size distribution. The adsorption amount of nitrogen in a particular solid sample depends on the relative pressure of nitrogen. Capillary condensation happens in the micropores when the relative pressure is equal to or larger than 0.4. Several theoretical models such as BET (Brunauer, Emmett, and Teller), t-plot, Langmuir, Alpha-S are used for specific surface area estimation, whereas NLDFT (Non-Local Density Functional Theory) is used for the calculation of pore size distribution, which may vary according to the several parameters of the model. Calculated surface area and pore size do not reflect the actual value of the material. Because, in the gas adsorption method, some nitrogen gas molecules do not completely infuse into the pores of the material but stay on its surface due to the weak van der Waals forces. As the volume of injected nitrogen increases (equivalent to pressure increase), gas molecules occupy the surface and start to fill in the pores. Therefore, obtained pore information from the gas adsorption method is mainly a combination of both connected pore wall and pore openings [9]. As a result, the gas adsorption method is known as an indirect technique for the measurement of surface area and pores. However, AFM provides a direct measurement of surface area and counting of the surface pore numbers even at ambient conditions. AFM method is crucial for adsorption-related research to analyze the porosity at ambient conditions, which is not possible in the conventional gas adsorption method [10]. AFM provides three-dimensional topography images, and thus height, perimeter, diameter, and surface roughness can be extracted from images that can be used to compute the specific surface area and volume of each particle when the density of the sample is known [11]. However, the scanned area often doesn't represent the bulk properties of the sample, a limitation of the AFM method. This scanning area problem can be lessened by taking several images at different locations of the same sample [10].

5.3 Overview of Physical Properties of Studied Adsorbents

5.3.1 *Silica Gel*

Silica gel is mesoporous and has spherical structures, which have potential applications in the adsorption of various gases/vapors. In our experiment, three different

silica gels are studied; RD silica gel, Generic (commercial food sample) silica gel, and CaCl_2 coated silica gel, which has a specific surface area of about 768, 654, and $316 \text{ m}^2/\text{g}$, respectively.

RD-type silica gel is also used in this study, a well-known material used in a wide range of applications [12]. This silica gel sample is spherical in shape, crystalline, and mesh size is 80. The initial water content amount is nearly zero, and the pH value is 4.0. Figure 5.1a shows a picture of a typical RD-type silica gel.

5.3.2 Activated Carbon and 2-D Material

Amorphous Maxsorb III (commercial activated carbon) is used in this experiment (Fig. 5.1b). This material has a high surface area, which is around $3,000 \text{ m}^2/\text{g}$, and pores are in the micropore range ($<2 \text{ nm}$) [13]. As a 2-D material, HOPG is used in this experiment (Fig. 5.1c), which has roughness around 0.3 nm .

5.3.3 Standard Sample

Standard sample TGG1 (collected from Tipsnano OÜ, Estonia) has a reparative triangle pattern, which has regularity on both X–Y and Z directions. This sample is used to understand the effect of variation of different set points. A general description of TGG1 is given (Table 5.1). The height of the triangle is about $1.5 \text{ }\mu\text{m}$, and the edge separation is about $3 \text{ }\mu\text{m}$.

5.3.4 Methodology: Surface Porosity Using Direct Imaging

Silica gel samples were first cleaned and heated in a vacuum chamber to remove the pre-adsorbed water content. After cooling, the samples were scanned using Scanning

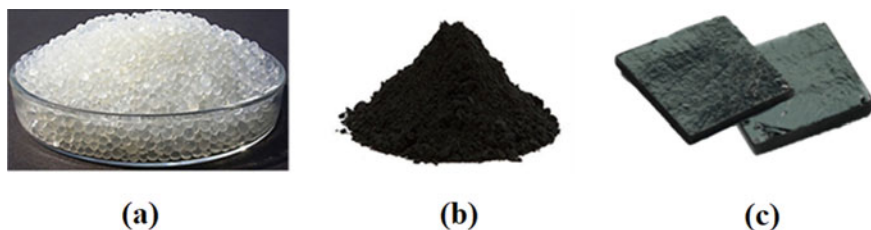
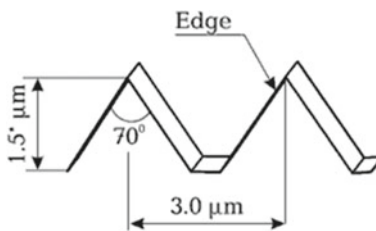


Fig. 5.1 Materials used for surface analysis **a** silica gel, **b** activated carbon, and **c** highly ordered pyrolytic graphite (HOPG)

Table 5.1 Features of TGG1. Adapted with permission from [14]

Structure	A grating is formed on Si wafer top surface	
Pattern types	1-D array of triangular steps (in X or Y direction) having precise linear and angular sizes	
Edge angle	70°	
Edge radius	≤10 nm	
Period	3 ± 0.05 μm	
Chip size	5 × 5 × 0.5 mm	
Effective area	Central square 3 × 3 mm	

Probe Microscopy (SPM) in phase mode to generate topographic images. Scanning was directed through continuous monitoring by a live scanning window with tilt correction mode. The images were then further corrected by post-image processing preserving its topographic features, specially undistorted pore structures. For detection and counting of pores, Fast Fourier Transformation was used to mitigate the parts of the images which contain high topographic variation, which was then further segmented by the Watershed method. The inverse grain detection technique counted segmented pores. NLDFT method was used on N_2 adsorption data to find the pore size distribution. The process is illustrated in Fig. 5.2.

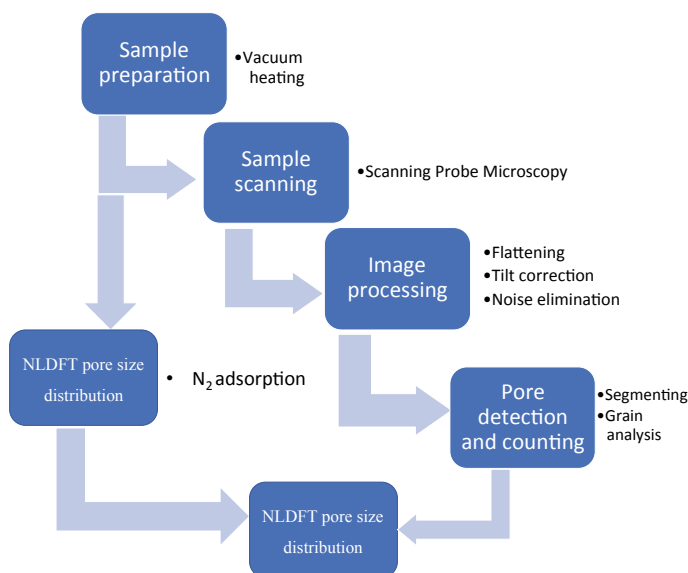
**Fig. 5.2** Concept of adsorbent characterizing procedure using a direct imaging technique

Table 5.2 Cantilever used in phase mode

Name	Company	Reflective coating	Lever shape	k (N/m)	f (kHz)
SSS-10	Nanoworld	None	Rectangle	42	(250–390) 320
NCHR-20	Nanoworld	Al	Rectangle	42	(260–410) 330
NSG-10	Single-crystal Si	Au	Rectangle	11.8	(140–390) 240

5.4 Experimental

5.4.1 Instrumentation

In this work, we have used Scanning Probe Microscopy (SPM-9700, Shimadzu corp.), where SPM is the generic term used to describe a microscope that allows the high-magnification observation of 3-D topographic variation, especially height, force modulation, magnetic force, friction force, electric-current, and electric-potential images [15]. The scanning is performed by a sharp microscopic probe (Fig. 5.3). In contrast, an AFM is a device that allows the observation of a sample's surface topography by holding a microscopic cantilever close to the sample surface and detecting the force (atomic force) acting between the cantilever and the sample.

SPM-9700 is based on AM-AFM, which can be operated in ambient conditions. Operation modes are essential to understand to use for applying scanning on different types of materials. The resolution indicates the lowest possible visible features of the sample topography. SPM head indicates the types of detection techniques. Besides these features, the maximum sample size and maximum operating frequency are also included here.

There are various kinds of cantilevers available for different modes of operation. It is very challenging to select a suitable cantilever for a specific mode of operation. In our experiment, three different kinds of the cantilever are used to observe the variation (Table 5.2).

5.4.2 Procedure

This experiment contains three major sections (Fig. 5.4). The first one is sample preparation, which is very important because SPM-9700 is designed for flat sample analysis. We have taken flat, amorphous, spherical, and 2-D material, which is treated differently before observation. The details of different types of sample preparation and their scanning process will be discussed in the next section. The second part is setting the SPM equipment, which includes selecting appropriate observation mode, setting setpoint, and scanning parameters. Though SPM-9700 is amplitude modulation-based AFM, the variation of amplitude is essential to determine. Setpoint plays a vital role in this part; error in setting may distort the image and even cause

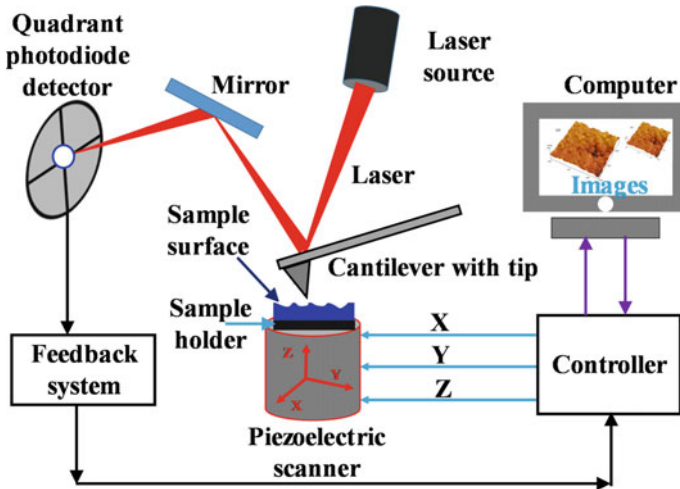


Fig. 5.3 Schematic diagram of the SPM system operated in the phase mode

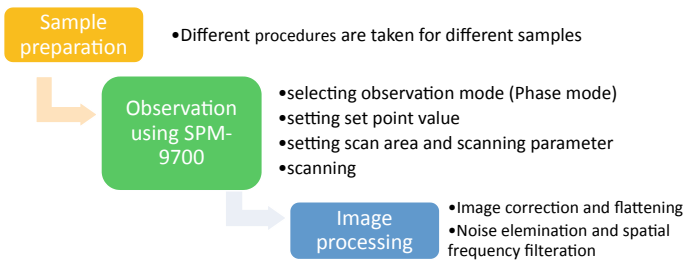


Fig. 5.4 Experimental procedure of image processing using SPM system

breaking the cantilever. Scanning parameter selection includes finding the appropriate scanning location, area, z-parameter values, etc. In most cases, these values are set on a trial and error analysis basis. The third part is image processing, which is required to get acceptable surface images. The collected image data may have tilted, drifted, or even contains thermal noises. Image processing is, in this case, useful to mitigate these effects.

5.4.2.1 Observation Using SPM-9700

The experiment is performed using phase mode. Two types of images are collected, one is a height image, and another is the phase image. In this case, phase images are only used to guide the observation, and height images are used for constructing images. The procedures of operation are illustrated in Fig. 5.5. In observation using

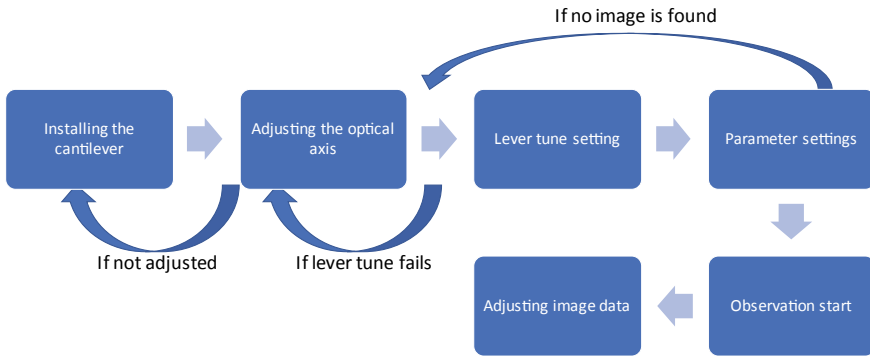


Fig. 5.5 Observation procedure using SPM-9700

SPM-9700, the observation procedures are almost similar, and the differences are in setting modes, setpoints, and scanning area.

Installing the cantilever is concerning in choosing the appropriate cantilever, placing it on the cantilever holder. In every observation, three different kinds of cantilevers are used to verify the observation. The specification of used cantilevers is shown in Table 5.2.

Laser detection is used to detect the amplitude variation. It is vital to set the optical axis properly. The laser should be incident upon the top of the lever/tip of the cantilever. The vibrating frequency of the cantilever is set to the vicinity of its resonance frequency and in the steepest descent part of the left side of the curve. If the tune is set correctly, the whole process should be started from the beginning. Another critical parameter is the operating point. For dynamic mode, zero value in the operating point indicates the tips will vibrate near the surface. It is recommended to start from a higher value to a lower one. The higher value provides safe operation but low-quality features [16]. At the same time, the lower value is risky but offers high-quality images. For high topographic variation, higher values are recommended.

A proper scanning area is required to set before starting the observation. A large scanning area with a low-resolution setting provides blur images. Nevertheless, high-resolution images are affected by the drift problem, which changes the topography entirely into a different one. In our experiment, we have optimized these values to get good images.

A live monitoring option is available in SPM-9700, which shows tilt corrected images. Observation error is possible to correct by observing these images. Troubleshooting is also possible; if data is drifted, it can be corrected by lowering the scanning resolution and frequency.

5.4.2.2 Image Processing

The raw images have tilt problems in every axis due to the hysteresis effect of the piezoelectric scanner. This can be adjusted by calibrating the scanner. Another way is to mitigating the tilt effect by various image processing mechanisms, which are subtracting average, a median of the values along a different axis, polynomial correction, line fit, plane fit, and curve fit option. For a regular-shaped sample, average subtraction is useful, but for an irregular-shaped sample, median correction is effective. If the sample is flat and similar 3 points can be determined, then the plane fit is convenient.

SPM offline module software is used to correct the raw images, which contain noise and tilt effects. Moreover, flattening is required to extract the topographic images. Gwyddion (ver. 2.47) is used for further image processing, especially for 2-D FFT operation, segmentation, pore detection, and counting.

2-D Fast Fourier Transform (FFT) is used to decompose an image to its sine and cosine components denoted at frequency domain transformation, i.e., the spatial domain images are transformed into the Fourier domain. In the Fourier domain image, each point represents a particular frequency contained in the spatial domain image [17]. In the Fourier domain, low-frequency points are aligned in the center, the high topographic variation data of the spatial image resides center of the Fourier domain. Similarly, low topographic variation data resides on the border. This is useful to remove the high topographic data by filtering.

The Watershed segmentation method is used to detect local minima determination and image segmentation. At the first step, virtual water drops are placed all over the image; drop size is selected by taking the optimum value. Then the local minima are measured under each drop and marked. Several steps are performed to find minima, which is like detecting the catchment basin. Then these multiple layers of virtual water are placed to fill up the pores. Overlapped water drops are considered as pore boundaries, and the pores are masked to identify [18].

5.4.3 *Experimental Error Analysis*

The error generated in SPM is a result of quantum and chaotic phenomena. The source of quantum phenomena is the interaction between tip and sample, whereas chaotic phenomena are associated with the dynamic behavior of measurement techniques and the control system used in SPM equipment. Therefore, the overall uncertainty effects are linked with the instantaneous phenomena both from fundamental physical limits (quantum), chaos, and various kinds of instabilities, including technical faults in the microscope. It is complex to determine the cumulative effects of the errors by analyzing individual sources and apply in the measurement to understand data integrity. Therefore, a more simplistic approach was adopted in this work, which can be termed as ‘dimensional measurement’ error correction. Dimensional measurement is vital in nanometrology because, in this method, standard three-dimensional

calibration gratings are used to measure the errors as well as the uncertainty directly from the image data.

In this work, a standard 3-D grating (TGG1, Tipsnano OÜ, Estonia) is used to determine both the lateral and vertical variances. Generally, for the evaluation of uncertainty, an average of many individual period measurements is taken from the grating profile. Additionally, the grating itself is prone to have dimensional errors generated from the synthesis process. In the case of TGG1, the dimensional error of the lateral period is $\pm 0.05 \mu\text{m}$, whereas the length is $3.0 \mu\text{m}$. Similarly, the height of the period is $1.5 \pm 0.05 \mu\text{m}$. Using the height measurement of the various periods of the 3-D calibration gratings, it is possible to evaluate the uncertainty satisfactorily. The uncertainty of the weighted average can be measured using the following equation:

$$\bar{x} = \frac{\sum_{i=1}^n \left(\frac{x_i}{\sigma_i^2}\right)}{\sum_{i=1}^n \left(\frac{1}{\sigma_i^2}\right)} \quad (5.1)$$

here σ_i is a local variance belonging to the measured height value x_i . Similarly, the variance of this average can be expressed as the following equation:

$$\sigma_{\bar{x}}^2 = \frac{1}{\sum_{i=1}^n (1/\sigma_i^2)} \times \frac{1}{n-1} \sum_{i=1}^n \frac{(x_i - \bar{x})^2}{\sigma_i^2} \quad (5.2)$$

These equations can be used to calculate the root mean square deviation of the final calibration grating pitch volume of the calibration grating pitch value. The measurement process is illustrated in Fig. 5.6.

Using the above equations, the weighted average of the height measurement is 1,440 nm, and the variance of this mean is 56 nm, which is 0.025% of the mean. Compare to the actual measurement, the variance is negligible. The SPM-9700 equipment includes a build-in calibration system, which provides the ability to correct the height measurement for each sample. In this work, mean correction is used for every measurement before image processing.

5.4.3.1 Scanning Process of Different Materials

SPM-9700 is designed for observing flat surfaces in the nanometer range. However, we have used flat, spherical, amorphous, and 2-D material for extended observation. The following sections are arranged based on sample materials. For each case, the most mentionable features are explained.

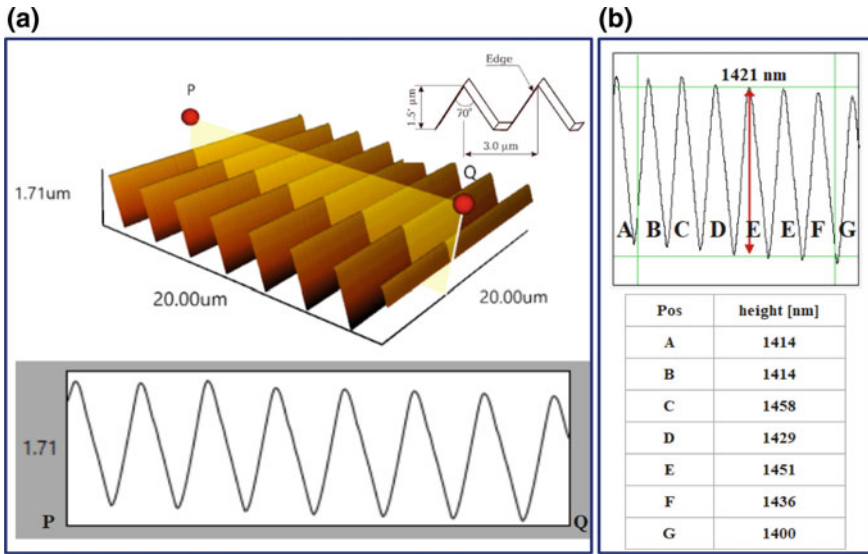


Fig. 5.6 Error measurement procedure, **a** 3-D view of the standard calibration sample and its corresponding line graph, **b** measured height of individual pitches of TGG1

5.4.3.2 TGG1

As mentioned earlier, TGG1 is a standard sample, which is used in this experiment to observe the effect of changes of different parameters, which are then applied to an unknown sample. TGG1 has a flat and guided surface that is placed on a metallic sample holder. A two-sided adhesive tape has been used to bound the sample with the holder. Sometimes dust remover is used to avoid unwanted variation due to dust. Figure 5.7a represents a top view of the sample where we can find that the height distribution of the points along the X–Y plane is uniform, and the maximum value is 1.46 μm. Figure 5.7b presents the side view of the 3D image, which is clearly helpful for visualizing and understanding the surface topography of the sample. Later in most cases, we have taken 3D side view and top view to visualize the feature. However, by changing the set value or the operating point, which determines the position of the tip, near or far from the sample, different height values are acquired. Nevertheless, the shapes of the topographies are still triangular. Some important understandings of the operation are stated briefly in the successive sub-sections.

Phase images show different information, and it is sensitive to edges rather than height values. Once the edges are detected, it shows a fixed angle a while before detecting another edge. Figure 5.8a shows a continuous red color for a while until it detects a sharp decline, which is indicated by dark color. Figure 5.8b, c show corresponding line profiles for both phase and height images, respectively.

X-direction scanning is much faster than the Y-direction in the scanner in SPM, and due to this, there is an inherent drift problem with this equipment. This problem

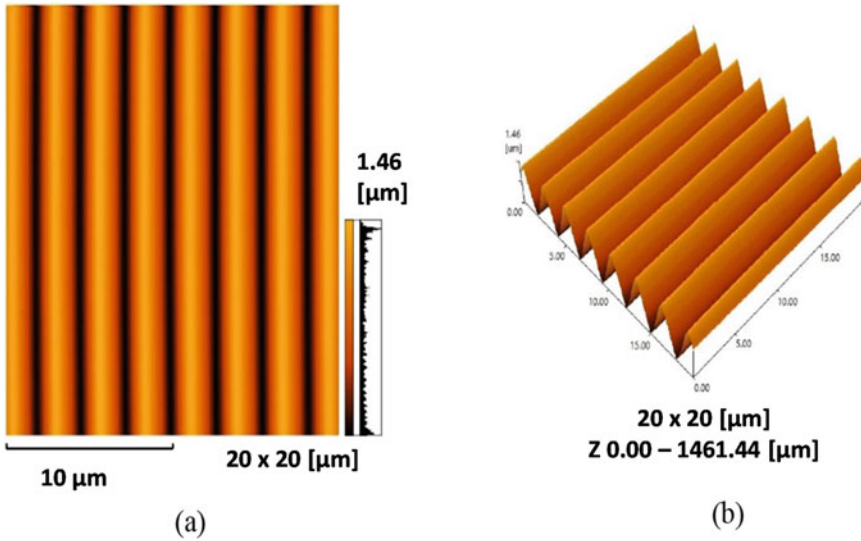


Fig. 5.7 SPM images of TGG1: a top view, b 3-D view

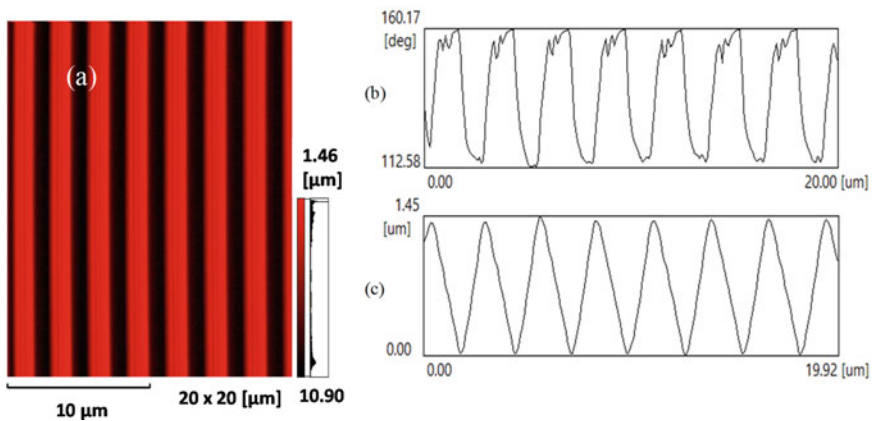


Fig. 5.8 Phase image extraction: a phase image of TGG1, b line profile of phase image, and c line profile of height image

changes the shape of the real image as the sample is first set on the holder so that the features lie parallel in the Y-direction, which suffers less drift problem, as can be seen in Fig. 5.9a. However, when rotated 90°, the same sample suffers a massive drift problem (see Fig. 5.9b). One way to overcome this problem is to set the scanning resolution as low as possible. Not to mention, faster scanning is sometimes helpful to avoid drift problems [19].

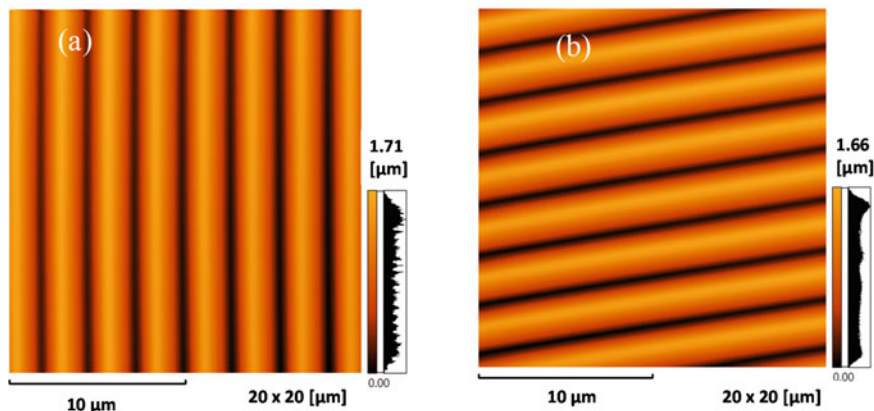


Fig. 5.9 Drift problem **a** suffers less drift problem **b** suffers a high drift problem

5.4.3.3 Silica Gel

Silica gel adsorbs vapor at room temperature, which is removed by vacuum heating at 85 °C for 2 h. Then samples are placed in the sample holder with adhesive tape. RD-type silica gel samples are first cleaned with ethanol to remove dust and other impurities. In this process, some ethanol might have been absorbed, which is removed by vacuum heating for two hours at 85 °C. Adhesive tape is used to tautly stick the silica gel particle with the AFM sample holder. An optical microscope has been used to locate the scanning location. To avoid the spherical shape problem, an optimized scanning area is taken. RD-type silica gel consists of pores in the mesoporous region (above 2 nm and below 50 nm). Considering this, the surface scanning area is taken below 5 μm². Figure 5.10 shows the images of RD-type silica gel. The first one is the position of the cantilever on the silica gel; the top and the less coercive surface are ideal for selecting the scanning area. After the scanning is finished, the second image is found, which has a severe tilt problem. To mitigate the tilt problem, post-processing such as filtering and flattening is required. Figure 5.10c is the ideal image of the surface, which is corrected by the flattening process. Orthogonal scanning is done to avoid the drift problem [19].

3-D topographic features of RD-type silica gel are also changes due to its types and location, which are shown in Fig. 5.11.

5.4.3.4 Activated Carbon

Powder like Maxsorb III is not suitable to observe using SPM. In this experiment, Maxsorb III is placed on the sample holder, then 5 MP pressure is applied to compact in a small area, and additionally flat surface is prepared for observation.

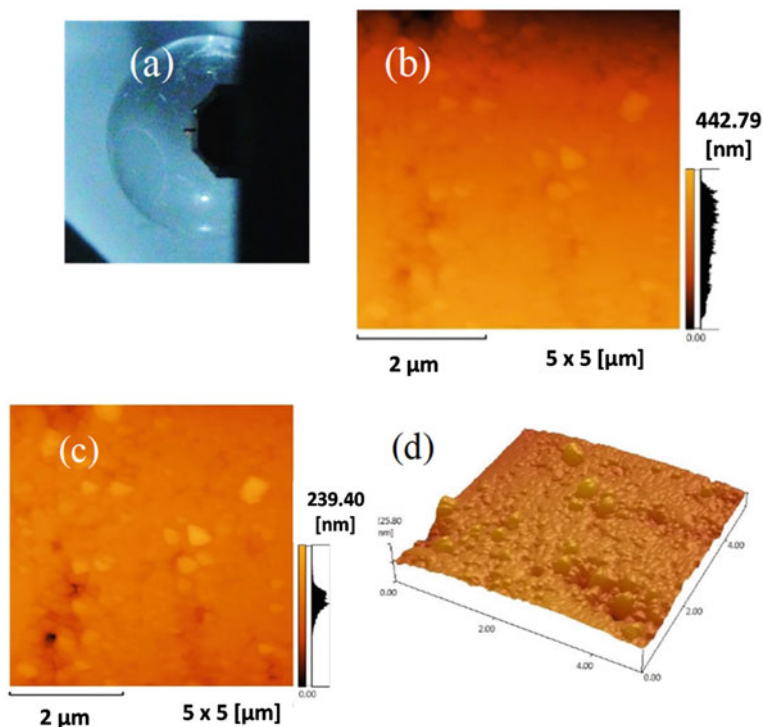


Fig. 5.10 SPM images of RD-type silica gel: **a** position of the cantilever on the sample, **b** tilted raw image, **c** flattened image, and **d** 3-D image after flattening

To get an SPM image of activated carbon, which is in powder form, it has been consolidated under a hydraulic press using 5 MPa [20]. Then the adsorbed water is removed by vacuum heating for 3 h at 200 °C temperature. As the surface is very coercive, the operating point is taken as large as possible. This value is reduced to optimum value gradually on a trial and error basis. To get a clear image, the feedback controller's P and I values are also taken with care. These values are the controlling parameters of the feedback circuits.

Firstly, the phase images are searched as the features are more visible in the phase image (Fig. 5.12); when the acceptable image [21] is found then, the parameters are changed to find the height image (Fig. 5.12b). Here, the phase image acts as a guiding image. The features of the height image are becoming visible after the flattening operation. From the live monitoring, it is complicated to find the features of this sample. The 3-D image is drawn after the post-processing (Fig. 5.12c). The explanation of the post-processing is beyond the scope of the thesis.

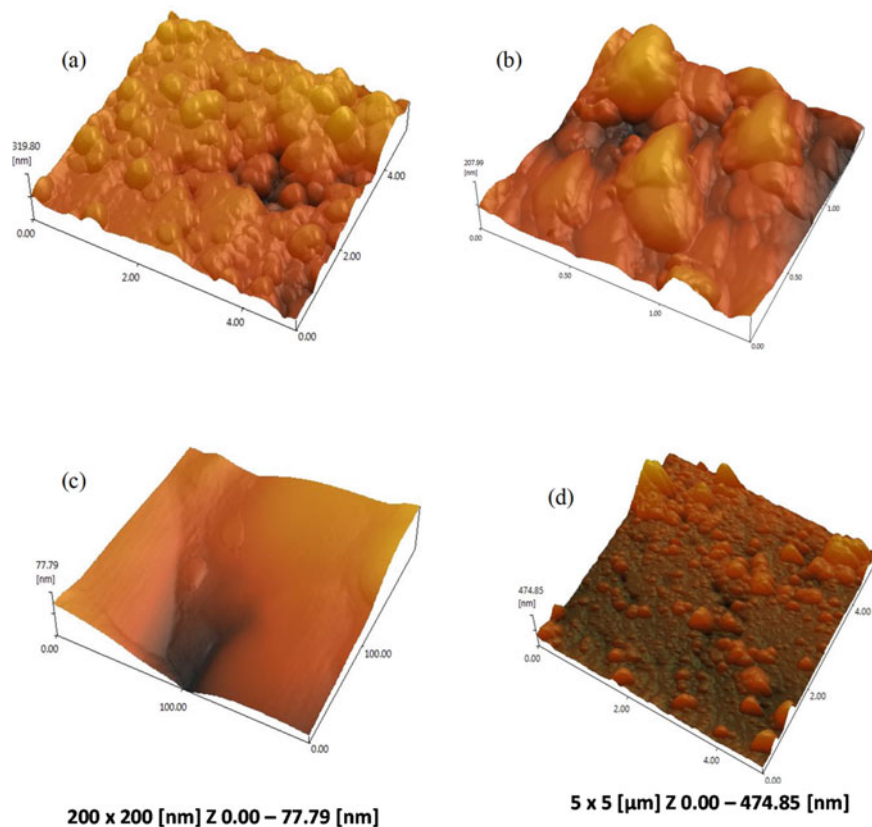


Fig. 5.11 Topographic variation of silica gel: **a** RD-type silica gel scanning area $5 \mu\text{m}^2$, **b** RD-type silica gel scanning area $1.5 \mu\text{m}^2$, **c** RD-type silica gel scanning area 200 nm^2 , and **d** Cu sputtered silica gel scanning area $5 \mu\text{m}^2$

5.4.3.5 Two Dimensional (2D) Materials

2D materials have minute variations in the surface. Our equipment has a limitation in spatial resolution, which is 0.2 nm , whereas the atomic separation of graphene is below 0.3 nm [22]. There is another influential parameter called tip radius, which is required to take as small as possible. In the case of graphene, we have used a super sharp cantilever (SSS-10, nanoworld) having a 1.0 nm tip radius. After having the images, we have used a 2-D FFT operation to extract the features (Fig. 5.13a) [23]. This time the layered structure is not visible, probably due to the operation is done in the ambient condition, and noise due to vibration is in its topographic range. However, the roughness of the image is found near the roughness of graphene (Fig. 5.13c).

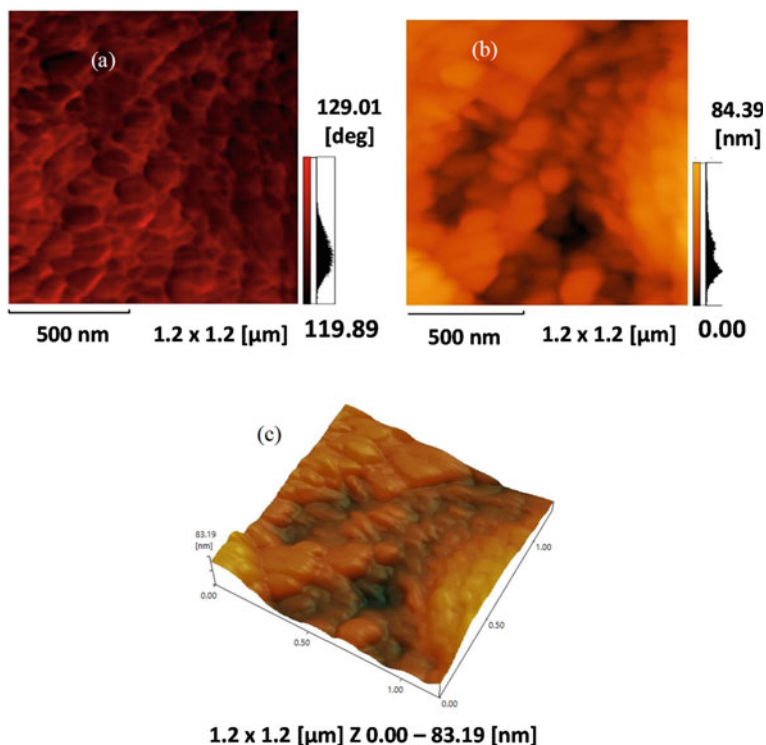


Fig. 5.12 SPM images of activated carbon: **a** phase image, **b** height image, and **c** 3-D image

5.4.3.6 Extracting Quantitative Information

Extraction of quantitative data from the surface of the porous materials is quite challenging since the surface contains various topographical irregularities such as cracks, overlapped pores, gaps, and uneven variation of structures. It is possible to extract pore-related information from the topographic images by converting the spatial domain images to that of the frequency domain. The conversion can be performed by Fast Fourier transformation (FFT). In the FFT image, the high topographic variation resides in the central region, which can be filtered out by eliminating the center frequencies. After the elimination, the FFT images can be converted to spatial domain images by Inverse Frequency Domain Transformation (IFDT). The filtered images are dominated by pore information which can be further detected by the Watershed method [10]. The pore counting procedure is applied to three different silica gel samples, and the result is shown in Fig. 5.14. Most of the detected pores reside in the nano and mesopore regions. In the case of RD silica gel, the peak of the pore count is single, and others have double, indicating the homogeneous distribution of pores for the former one.

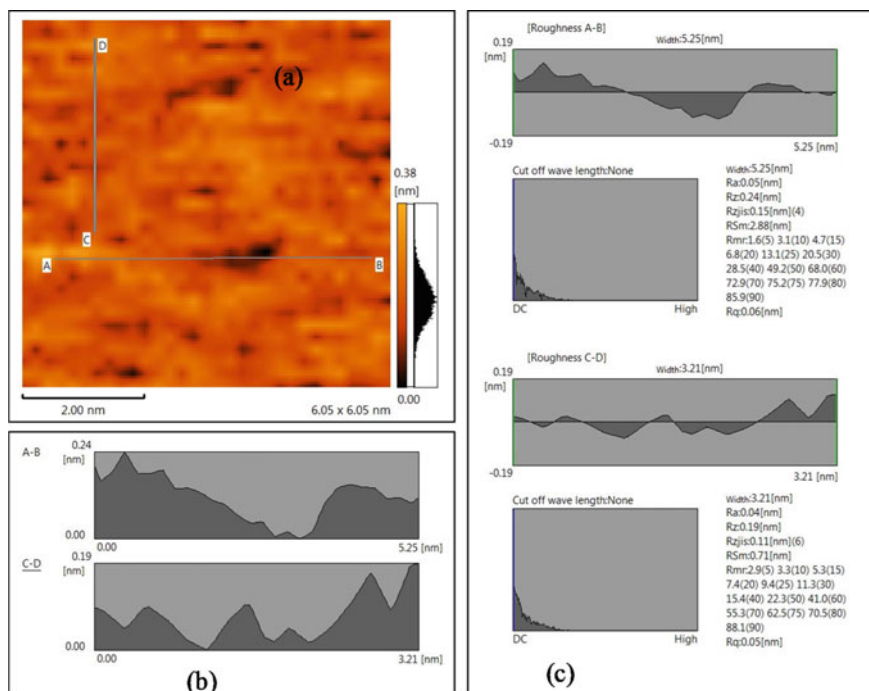


Fig. 5.13 SPM image of graphene and its features: **a** 2D image, **b** line profile, and **c** roughness profile

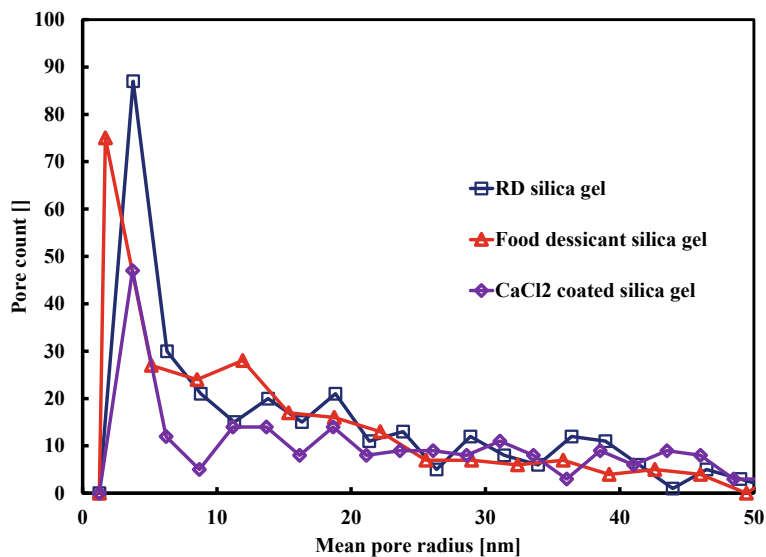


Fig. 5.14 Pore count results of three silica gel samples

Another two critical parameters, fractal dimension and roughness, can be measured using AFM. The fractal dimension is a measure of self-similarity of the surface profile, indicating the complexity and irregularity of the material surface. Whereas the roughness is the arithmetic mean deviation of the topographic height that reflects the variation of peaks and valleys of the surface. One of the disadvantages of roughness calculation is that it depends on the scanning resolution and length, while the fractal dimension is scale-independent. Moreover, it is found that the surface fractal dimension can be used to determine the critical supersaturation of cloud droplets forming on insoluble nuclei [24]. Therefore, in this work, two silica gel samples (RD and CaCl_2 coated) are used to determine the fractal dimension and the corresponding roughness. In the measurement, the scanning area was fixed to $1.2 \mu\text{m} \times 1.2 \mu\text{m}$, and the resolution was 512×512 . For each of the silica gel samples, several locations are randomly selected. The results are shown in Fig. 5.15.

The result shows that both the RMS roughness and fractal dimension of RD silica gels are slightly lower than CaCl_2 coated silica gel. When the RMS roughness is zero, i.e., in the absence of RMS roughness, the fractal dimension of RD silica gel is around 2.14, and that of CaCl_2 is 2.20. That implies the surface of RD silica gel is flatter than the other samples.

5.5 Conclusions

Atomic force microscopy can provide additional characterization information, which might carry essential values in surface property measurements. This chapter initially presented the techniques of extracting 3-D images of silica gel, activated carbon samples. These 3-D images provide additional visual understandings, which are not possible in conventional imaging techniques. Additionally, several surface parameters such as pore size distribution, fractal dimension, and roughness are calculated from the height profile data, which carries extra advantages.

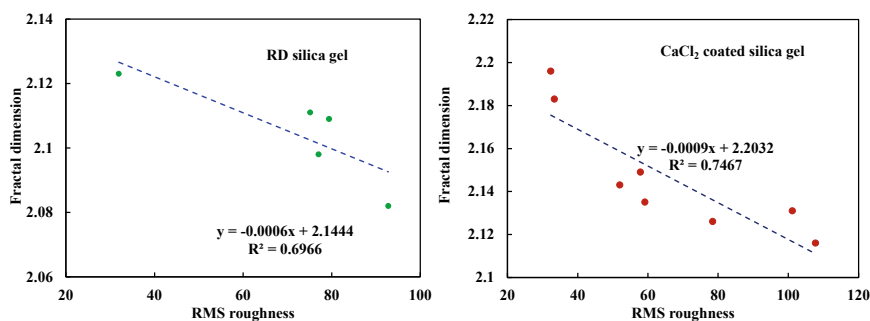


Fig. 5.15 Fractal dimension and roughness of RD and CaCl_2 coated silica gel

References

1. Saha BB, Akisawa A, Kashiwagi T (2001) Solar/waste heat driven two-stage adsorption chiller: the prototype. *Renew Energy* 23:93–101. [https://doi.org/10.1016/S0960-1481\(00\)00107-5](https://doi.org/10.1016/S0960-1481(00)00107-5)
2. Kaneko K, Ishii C, Ruike M, Kuwabara H (1992) Origin of superhigh surface area and microcrystalline graphitic structures of activated carbons. *Carbon N Y* 30:1075–1088. [https://doi.org/10.1016/0008-6223\(92\)90139-N](https://doi.org/10.1016/0008-6223(92)90139-N)
3. Do HD, Do DD (1995) Effect of pore size distribution on the surface diffusivity in activated carbon: hybrid Dubinin-Langmuir isotherm. *Adsorption*. <https://doi.org/10.1007/BF00707352>
4. Naderi M (2014) Surface area: Brunauer-Emmett-Teller (BET). *Prog Filtr Sep*. <https://doi.org/10.1016/B978-0-12-384746-1.00014-8>
5. Landers J, Gor GY, Neimark AV (2013) Density functional theory methods for characterization of porous materials. *Colloids Surf Physicochem Eng Asp* 437:3–32. <https://doi.org/10.1016/j.colsurfa.2013.01.007>
6. Wang ZL (2003) New developments in transmission electron microscopy for nanotechnology. *Adv Mater* 15:1497–1514. <https://doi.org/10.1002/adma.200300384>
7. Vanderlinde W (2011) Scanning electron microscopy. *Scan Electron Microsc*. <https://doi.org/10.1159/000265104>
8. Paredes J, Martínez-Alonso A, Tascón JM (2003) Application of scanning tunneling and atomic force microscopies to the characterization of microporous and mesoporous materials. *Microporous Mesoporous Mater* 65:93–126. <https://doi.org/10.1016/j.micromeso.2003.07.001>
9. Gas Adsorption Method—an overview (2021) ScienceDirect Topics, (n.d.). <https://www.sciencedirect.com/topics/engineering/gas-adsorption-method> (Accessed March 6 2021)
10. Palash ML, Mitra S, Harish S, Thu K, Saha BB (2019) An approach for quantitative analysis of pore size distribution of silica gel using atomic force microscopy. *Int J Refrig* 105:72–79. <https://doi.org/10.1016/J.IJREFRIG.2018.08.017>
11. Macht F, Eusterhues K, Pronk GJ, Totsche KU (2011) Specific surface area of clay minerals: Comparison between atomic force microscopy measurements and bulk-gas (N₂) and -liquid (EGME) adsorption methods. *Appl Clay Sci* 53:20–26. <https://doi.org/10.1016/j.clay.2011.04.006>
12. Ng KC, Chua HT, Chung CY, Loke CH, Kashiwagi T, Akisawa A, Saha BB (2001) Experimental investigation of the silica gel–water adsorption isotherm characteristics. *Appl Therm Eng* 21:1631–1642. [https://doi.org/10.1016/S1359-4311\(01\)00039-4](https://doi.org/10.1016/S1359-4311(01)00039-4)
13. Otowa T, Tanibata R, Itoh M (1993) Production and adsorption characteristics of MAXSORB: high-surface-area active carbon. *Gas Sep Purif* 7:241–245. [https://doi.org/10.1016/0950-4214\(93\)80024-Q](https://doi.org/10.1016/0950-4214(93)80024-Q)
14. TGG1 AFM Calibration sample, (n.d.)
15. Shimadzu, Scanning Probe Microscope SPM-9700 Hardware Instruction Manual, Kyoto, 2011
16. Eaton P, West P (2010) Atomic force microscopy. Oxford University Press, New York, NY. <https://doi.org/10.1093/acprof:oso/9780199570454.001.0001>
17. Gonzalez RC, Woods RE (2002) Digital image processing. <https://doi.org/10.1017/CBO9781107415324.004>
18. Klapetek P (2012) Quantitative data processing in scanning probe microscopy: SPM applications for nanometrology. <https://doi.org/10.1016/C2011-0-09615-1>
19. Marinello F, Bariani P, De Chiffre L, Savio E (2007) Fast technique for AFM vertical drift compensation. *Meas Sci Technol* 18:689–696. <https://doi.org/10.1088/0957-0233/18/3/019>
20. Paredes JI, Martínez-Alonso A, Hou PX, Kyotani T, Tascón JMD (2006) Imaging the structure and porosity of active carbons by scanning tunneling microscopy. *Carbon N Y* 44:2469–2478. <https://doi.org/10.1016/j.carbon.2006.04.040>
21. Kim D-W, Kil H-S, Nakabayashi K, Yoon S-H, Miyawaki J (2017) Structural elucidation of physical and chemical activation mechanisms based on the microdomain structure model. *Carbon N Y* 114:98–105. <https://doi.org/10.1016/j.carbon.2016.11.082>

22. Frank IW, Tanenbaum DM, Van Der Zande AM, McEuen PL (2007) Mechanical properties of suspended graphene sheets. *J Vac Sci Technol B Microelectron Nanom Struct* 25:2558–2561. <https://doi.org/10.1116/1.2789446>.
23. Voltolini M, Artioli G, Moret M (2003) Molecular resolution images of the surfaces of natural zeolites by atomic force microscopy. *Microporous Mesoporous Mater* 61:79–84. [https://doi.org/10.1016/S1387-1811\(03\)00357-3](https://doi.org/10.1016/S1387-1811(03)00357-3)
24. Laaksonen A, Malila J, Nenes A, Hung H-M, Chen J-P (2016) Surface fractal dimension, water adsorption efficiency and cloud nucleation activity of insoluble aerosol. *Sci Rep* 6:25504. <https://doi.org/10.1038/srep25504>

Chapter 6

Advanced Adsorbents for Ecological Applications: Water Harvesting from the Atmosphere and Recuperation of Heat and Moisture in Ventilation Systems



Larisa G. Gordeeva and Yuri I. Aristov

Abstract The Chapter addresses two emerging adsorption processes aimed at improving the Earth's ecology, namely, water harvesting from the atmosphere and recuperation of heat and moisture in ventilation systems. Both systems are open and can be examined in a unified way by analyzing a thermodynamic cycle of the process to account for various climatic conditions. Since these conditions can significantly vary for seasons and geographic locations, they have to be correctly taken into account to formulate thermodynamic requirements to an optimal adsorbent. Special attention is paid to a) harmonization of the adsorbent and the cycle, and b) the preparation of the optimal adsorbent and its testing. Advanced adsorbents selected/developed/tested for both applications are considered

Keywords Advanced adsorbents · Moisture recuperation · Water harvesting

6.1 Introduction

Many natural materials (clays, charcoals, lime, zeolitic tuffs, volcanic ash, etc.) having a good ability to concentrate various substances on the surface have been known since the earliest times. For instance, wood chars were empirically selected by the Egyptians and Sumerians for use in medicine [1], water purification and manufacture of bronze [2]. Their scientific research started only at the end of the eighteenth century [3–6], whereas the first synthetic porous solids (metal oxides) were prepared about a century later [2]. However, the first industrial production of adsorbents (activated carbons) was organized at the very beginning of the twentieth

L. G. Gordeeva (✉) · Y. I. Aristov
Boreskov Institute of Catalysis, Ac. Lavrentiev av. 5, 630090 Novosibirsk, Russia
e-mail: gordeeva@catalysis.ru

Y. I. Aristov
e-mail: aristov@catalysis.ru

century [2]. Useful historical excursus of the adsorption science development can be found elsewhere [2, 7].

By now, the main technological application of adsorbents, namely, the gas and liquid separation, has been brought to near-perfection [8]. Many other adsorptive applications, like catalysis [2], ion exchange [2], maintaining relative humidity [9], shifting chemical equilibrium [10], pharmaceuticals and medicine (drug delivery, blood cleaning, etc.) [2], active heat insulation [11], conditioning of indoor air [12], life support system on a spacecraft [13], gas storage [2], etc., are quite advanced as well. Many emerging adsorptive technologies are aimed at improving the Earth's ecology. Among them, the most needed are heat conversion/storage/amplification [14], water harvesting from the atmospheric air [15], and recuperation of heat and moisture in ventilation systems [16]. This Chapter addresses the last two applications that now attract increasing attention.

Due to the growing world population and environmental pollution, fresh water scarcity is becoming a global challenge. Nowadays, about two-thirds of the population live in regions facing water shortage [17]. Meanwhile, the atmosphere contains 13,000 km³ of water [18–20], three times more than the world water demands of 3000–4000 km³ per year, including industry, agriculture, and domestic sectors [21, 22]. For these reasons, water generation from the atmosphere has drawn human interest since immemorial time. The first attempt to collect fresh water from the air using ancient artificial “springs” and “ponds” made in Russia (Altai mountains) and England are described in [21]. Today, adsorptive water harvesting (AWH) from the atmosphere brings great promise for potable water supply for domestic purposes in water scarcity regions remote from other water sources (sea, rivers, lakes, underground water, etc.) [15, 23].

Nowadays, it is impossible to contemplate our manner of life without modern Heating, Ventilating, and Air-Conditioning Systems. It is particularly true for the urban population, which has been persistently growing for past centuries. At present, more than half of the world's population lives in cities [24]. As a result, a significant part of primary fossil fuels is spent on heating/cooling of buildings, thus, greatly contributing to GHG emissions. In Europe, the heat consumption in buildings is responsible for 24% of the total energy consumption of the EU-27 (2008) [25]. In the Russian Federation, 43% of the produced centralized heat or 138 Mtoe is used for buildings [26]. For modern dwellings with better fabric insulation, a fraction of the heat losses through ventilation system significantly increases and becomes dominant, especially in high-rise buildings. The same tendency was reported by many researchers (see e.g. [27]). Therefore, a further improvement of the dwellings thermal efficiency is associated with a decrease in heat losses through ventilation system. This can be achieved by the implementation of traditional and novel technologies of heat recovery in ventilation systems (see e.g. [16, 27, 28]).

It is especially important for the winter season in cold climates (typical for Russia, Northern Europe, the USA and Canada). At these conditions, the difference ΔT between indoor and outdoor temperature can reach 50–60 °C or even more, which leads to enormous heat losses through ventilation and moisture freezing at the system exit. As a result, common heat recovery units integrated into ventilation systems may

not work at these harsh conditions. Moreover, such systems can not manage the indoor humidity, which dramatically reduces in the winter season that greatly disbalances the indoor heat comfort. Thus, to fill these three main gaps in the current ventilation techniques, the following actions should be performed:

- efficient exchange of heat between the exhaust and supply air fluxes to reduce heat losses,
- reasonable drying of the exhaust air to avoid ice formation at the system exit,
- moisturizing the supply air to provide indoor conditions of human thermal comfort.

These problems can be solved or, at least, alleviated by an *adsorptive* heat and moisture regeneration (AHMR) approach, which was suggested in [29, 30] specifically for cold countries. This method, called VENTIREG, and its very recent modification VENTIREC [31] are comprehensively considered below.

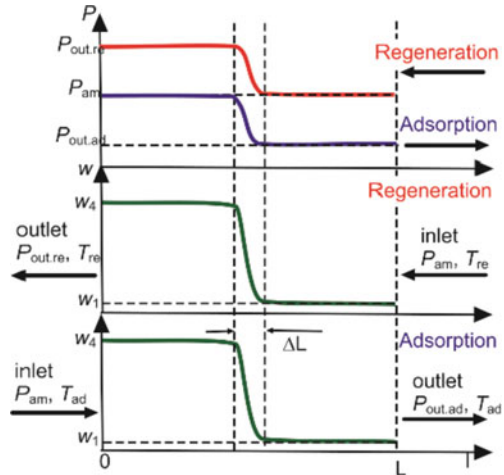
Both applications considered in this Chapter have already been realized at a prototype level. However, there is still big room for their further improvement. In our opinion, the main direction in this way is a harmonization of the adsorbent used with the particular process/cycle/unit. The main idea of this approach is that for each adsorptive process, there is an optimal adsorbent (OA), the properties of which could allow a perfect performance of this process. As a first, theoretical step, it is necessary to understand what properties the OA should have. The next, practical step is the synthesis of a real material with adsorption properties close to those predicted for the OA. The application of this strategy for several adsorption processes mentioned above was reported in the recent book [32]. Below, the nano-tailoring approach is applied to select or synthesize advanced adsorbents for the two ecological applications: water harvesting from the atmospheric air as well as heat and moisture recuperation in the ventilation systems.

6.2 Process Thermodynamic Diagrams

For formulating requirements for the adsorbent optimal for both AWH and AHMR, we consider here thermodynamic diagrams of these processes. Both technologies are realized in practice as open cycles because they exchange moisture with the ambient. Hence, AWH and AHMR can be examined in a unified way by studying the process cycle in thermodynamic diagrams to account for various climatic conditions.

We assume that the process occurs in a flow adsorber (Ad), in which the adsorption front with the thickness ΔL is much smaller than the Ad length L , $\Delta L \ll L$ (Fig. 6.1). It indicates that the equilibrium between the process air and the adsorbent is achieved, and the dynamic uptake w_d in the Ad is virtually equal to the thermodynamic (equilibrium) uptake $w(P,T)$.

Fig. 6.1 Evolution of the water vapor pressure and the water uptake along a flow adsorber. Reprinted from [33] with permission from Elsevier



6.2.1 Adsorption Water Harvesting

It is known that the air temperature in arid regions varies strongly during a day, while the absolute air humidity changes only slightly. This results in a wide variation of the air relative humidity of 15–20% between night and day-times [34]. The working cycle of AWH consists of alternating adsorption and regeneration/condensation stages (Fig. 6.2a) [35]. Let's consider the thermodynamic cycle of AWH in the Clausius-Clapeyron diagram, which represents water adsorption isosters at various uptakes w and the water liquid–vapor equilibrium line (Fig. 6.2b).

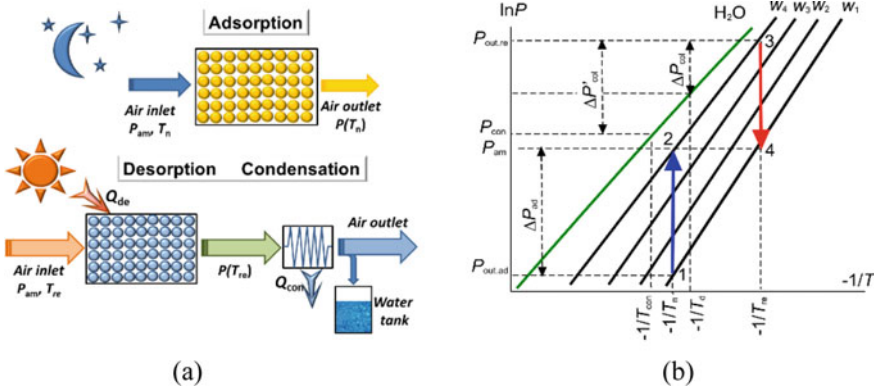


Fig. 6.2 General scheme of the AWH process (a). Adsorption isosters $w_1 - w_4$ and water–vapor equilibrium in the Clausius-Clapeyron diagram (b). Arrows denote changes in the water uptake during adsorption (1–2) and desorption (3–4) stages of the AWEA process. Fig. (b) is reprinted from [33] with permission from Elsevier

The adsorption stage (1–2 in Fig. 6.2b) takes place at night-time, when the relative humidity of the air is high. The ambient air with night temperature T_n and the water vapor pressure P_{am} enters the Ad loaded with the adsorbent regenerated during the preceding desorption stage to the uptake w_1 (Fig. 6.1, bottom). Due to water adsorption the uptake in Ad rises to $w_4 = w(T_n, P_{am})$ (point 2 in Fig. 6.2b). The vapor pressure in the process air decreases to the equilibrium value $P_{out.ad} = P(w_1, T_n)$ over the regenerated adsorbent with the minimum uptake w_1 , (Fig. 6.1, top, and point 1 in Fig. 6.2b).

During the following **desorption stage**, the adsorbent saturated with water up to the maximal uptake w_4 at the previous adsorption stage is blown with the ambient air with the vapor pressure P_{am} and heated up to temperature T_{re} . The adsorbed water is released to the air, the uptake w falls down to the value $w_1 = w(T_{re}, P_{am})$ (Fig. 6.1b middle, and point 4 in Fig. 6.2b). The vapor pressure in the air grows to equilibrium value $P_{out.re} = P(w_4, T_{re})$ over the wet adsorbent, having the uptake w_4 at T_{re} (Fig. 6.1 top and point 3 in Fig. 6.2b). If the condenser is cooled by the ambient air, the desorbed water is collected at day-time temperature T_d , and $P_{con} = P_0(T_d)$ (Fig. 6.2b).

There are two modifications of the AWH cycle: open [36, 37] and semi-open [38]. The adsorption phase is open for both cycles, and the ambient air passed through the adsorber is discharged into the ambient. The desorption/condensation stage differs: for semi-open systems, the process air circulates between the Ad, where it captures the desorbed moisture, and the condenser, where moisture is collected. The performance of the semi-open cycles can be enhanced because the rest of the moisture remaining in the air after condensation re-enters the Ad.

The main AWH performance index is the specific water productivity SWP or the ratio $\Delta w_{col} = m_{col}/m_{ads}$ of the mass m_{col} of water collected per cycle to the adsorbent mass m_{ads} . This parameter determines the mass of adsorbent, needed to harvest, let say, 1 L water and, consequently, the AWH unit volume. The SWP alone, however, is not sufficient for evaluating the actual AWH performance. Another important indicator is the specific energy consumption SEC, which includes the electric SEC_{el} for blowing the air through the Ad, and the thermal SEC_{th} for water vapor desorption:

$$\begin{aligned} SEC_{th} &= (Q_{sen} + Q_{re})/m_{col} \\ &= [m_{ad}(Cp_{ad} + w_{ad}Cp_w)(T_{re} - T_{ad}) + m_{ad}\Delta w\Delta H_{ad}]/m_{col} \end{aligned} \quad (6.1)$$

$$SEC_{el} = W_{el}\tau/m_{col}, \quad (6.2)$$

where Cp_{ad} and Cp_w are the specific heats of the adsorbent and water, w_{ad} is the specific mass of adsorbed water, T_{re} and T_{ad} are the regeneration and adsorption temperatures, and $\Delta w = w_{ad} - w_{re}$ is the mass of water released during desorption, W_{el} is the electric power consumption, and τ is the cycle duration. If Δw is large, $Q_{sen} \ll Q_{re}$, and

$$SEC_{th} \approx m_{ad}\Delta w\Delta H_{ad}/m_{col} \quad (6.3)$$

The importance of SEC_{el} can be brought to light when considering a small water vapor content of 4–15 g/(m³ air) in arid regions. Thus, even if the whole atmospheric moisture is adsorbed, 67–250 m³ of the air have to be blown through the Ad just to collect 1 L of water in the adsorbent during the adsorption stage. Air blowing is also required during the desorption/condensation stage. The SEC_{el} depends mainly on the humidity ratio of the ambient air and the efficiencies δ_{ex} of water extraction during the adsorption stage, and δ_{col} of water collection during the desorption stage (see below).

6.2.2 Heat and Moisture Recuperation in Ventilation (AHMR)

First, the principle of the common method VentireG for heat and moisture regeneration in ventilation systems in cold regions [30] is briefly described. Then, we consider its recent modification VentireC [31].

The *VentireG* unit is mounted in a ventilation system, and contains an Ad, located on the inside of the system (closer to the room), and the heat storing bed (HSB), placed on the outside (Fig. 6.3a). The process is intermittent and consists of two stages: the indoor air dehumidification and outdoor air moisturizing. During the *dehumidification* stage, the wet and warm indoor air with temperature T_{in} and relative humidity RH_{in} (point 1 in Fig. 6.4) passes through the dried Ad, where the vapor is captured. The adsorption heat is released, increasing the air and adsorbent temperature (line 1–2). If no heat is transferred from the Ad bed through the walls, the process is almost adiabatic. Then the air enters the HSB (line 2–3), where the sensible heat is absorbed. Then, cold and dry air (point 3) is discharged. During the *moisturizing* stage, the fresh outdoor air with temperature T_{out} and humidity ratio X_{out} passes through the HSB and absorbs the stored heat (line 3–2). Then, the warm and dry air enters the wet Ad, where the adsorbed water is desorbed, and enters the room, being warm and humid. Thus, the indoor heat and humidity are partially recovered.

The implementation of the VentireG reveals two main drawbacks [14]:

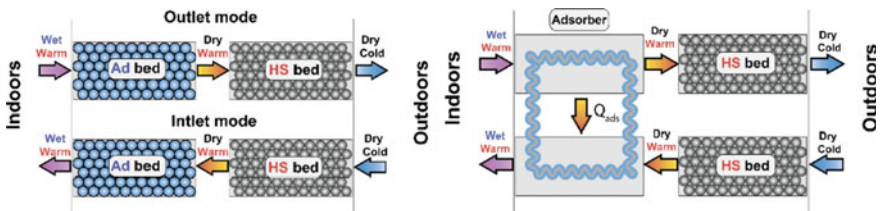


Fig. 6.3 Scheme of the common VentireG (a) and new VentireC (b) processes [30]. Reprinted from [31] with permission from Elsevier

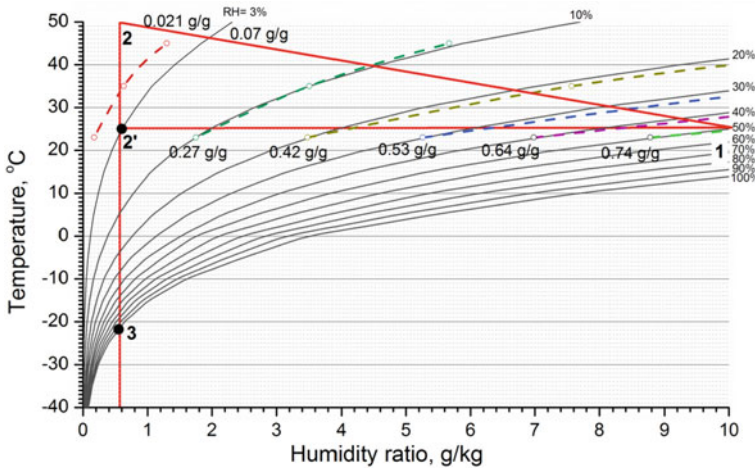


Fig. 6.4 VentireG (1-2-3) and VentireC (1-2'-3) processes in a psychrometric (Mollier) chart of wet air. Isosters of water sorption on LiCl/Davisil 646 composite for various uptakes are shown by empty symbols and dashed lines. Reprinted from [31] with permission from Elsevier

- The rise of the adsorbent temperature due to the released adsorption heat reduces the dehumidification performance of the adsorbent.
- The air blowing through the flow Ad and HS beds requires a significant power consumption that diminishes the energy efficiency of the process.

In the improved VentireC approach, a *thermal coupling* of two desiccant coated heat exchangers (DCHEs) is employed to overcome both drawbacks of the common VentireG. A VentireC unit contains two blocks of DCHE and HSB and operates continuously (Fig. 6.3b). The adsorption heat released in DCHE1 working at the air dehumidification mode is transferred by the heat transfer fluid to DCHE2, which works at the moisturizing mode. The water adsorption occurs in DCHE1 near-isothermally (line 1–2' in Fig. 6.4), facilitating air dehumidification. The heat transferred is consumed by the wet adsorbent in DCHE2, which promotes the vapor desorption and moisturizing the dry outdoor air. The sensible heat of the indoor air is recovered in the HSBs like in the conventional VentireG process.

Thus, in the VentireC process, the decoupling of the latent and sensible loads of indoor air enhance the moisture recovery. Moreover, utilization of the DCHE instead of a fixed granular Ad is expected to reduce the bed hydraulic resistance and, accordingly, the electric power consumption for the air blowing. This approach is called VentireC = Ventilation + ReCuperation. Contrary to VentireG that can be both intermittent and continuous, VentireC is an intrinsically continuous process.

The basic indexes, characterising the AHMR performance, are the efficiencies δ_{hr} of heat regeneration and δ_{mr} of moisture regeneration, equal to

$$\delta_{hr} = Q_{in}/Q_{out} \tag{6.4}$$

$$\delta_{mr} = m_{in}/m_{out}, \quad (6.5)$$

where Q_{in} and Q_{out} are the sensible heat of the air incoming to and outgoing from the room; m_{in} and m_{out} are the amounts of moisture in the air incoming to and outgoing from the room, respectively. Since the heat exchange occurs in VentireC similar to that in VentireG, we mainly consider here the moisture recuperation efficiency δ_{mr} , which depends on the degree δ_{ex} of moisture extraction during the adsorption stage and the degree δ_m of moisturizing during the desorption stage

$$\delta_{ex} = m_{ad}/m_{out}, \quad (6.6)$$

and

$$\delta_m = m_{de}/m_{ad} = m_{in}/m_{ad}, \quad (6.7)$$

where m_{ad} and m_{de} are the amounts of moisture adsorbed and desorbed, respectively. Then, $\delta_{mr} = \delta_{ex}\delta_m$.

6.3 Harmonization of the Adsorbent with the Cycle

Properties of the used adsorbent is a key factor affecting the efficiency of both AWH and AHMR systems. In our opinion, to improve the process performance these properties have to be harmonised with the specific cycle parameters, which, in their turn, depend on the ambient climatic conditions. Below we consider what adsorbent is optimal for these processes from the thermodynamic point of view.

6.3.1 Qualitative Requirements

AWH The thermodynamic requirements for the adsorbent optimal for AWH can be derived considering the SWP and the fractions δ_{ex} of water extracted and δ_{col} of water collected, as the performance indexes. Based on the AWH P - T diagram (Fig. 6.2 b), the fractions δ_{ex} and δ_{col} can be expressed as

$$\delta_{ex} = \Delta P_{ad}/P_{am} = 1 - P_{out.ad}/P_{am}, \quad (6.8)$$

$$\delta_{col} = \Delta P_{con}/P_{out.re} = 1 - P_0(T_d)/P_{out.re}. \quad (6.9)$$

To enhance the fraction δ_{ex} (Eq. 6.8), an adsorbent, which at temperature T_n adsorbs water vapor strongly at low vapor pressure $P_{\text{out,ad}} = P(T_n, w_1)$ (point 1 in Fig. 6.2b), is needed. Such an adsorbent possesses a strong affinity to water vapor.

On the contrary, to increase the fraction δ_{col} (Eq. 6.9), at temperature T_{re} the adsorbent has to release water easily at higher vapor pressure $P_{\text{out,re}} = P(T_{\text{re}}, w_4)$ (point 3 in Fig. 6.2b). Such an adsorbent possesses a weak affinity to water vapor.

AHMR. The thermodynamic requirements to the OA for the AHMR process can be formulated considering the efficiencies of the moisture extraction and humidification (Eqs. 6.6 and 6.7):

- During the *dehumidification* stage (1–2 and 1–2' for VentireG and VentireC, Fig. 6.4), the adsorbent with a strong affinity to water is needed to dry the indoor air to low humidity ratio, and to prevent the unit outlet from moisture freezing at the ambient temperature (point 3). Such an adsorbent ensures a large δ_{ex} -value.
- During the opposite *moisturising* stage, the adsorbent with a low affinity to water is required to easily disengage the adsorbed vapor at point 1 and moisturise the outdoor air to a comfortable level of 40–60% RH. It promotes large efficiency δ_{hum} .
- OA has to exchange a large amount $\Delta w = w_{\text{max}} - w_{\text{min}}$ of water between points 1 and 2 (2') in Fig. 6.4 to minimize the needed adsorbent volume.

Thus, for both AHMR and AWH, the requirements to the properties of optimal adsorbent can be formulated in a unified way by analyzing the process thermodynamic cycle in a psychrometric chart of wet air. The requirements differ for adsorption/dehumidification and regeneration/moisturizing stages. Namely, an adsorbent with a strong affinity to water vapor is needed for efficient adsorption, while a weak affinity is demanded for easy desorption. Consequently, the OA has to possess both strong and weak adsorption sites, in other words, to exhibit the affinity distributed in a wide range. The strong sites adsorb vapor at its low pressure to assure high efficiency of water extraction δ_{ex} from the ambient air in AWH and from the humid indoor air in VentireC. During the desorption stage, the weak sites disengage vapor at a high pressure to increase the efficiency δ_{hum} of the inflowing air humidification for AHMR and the efficiency δ_{col} of water collection for AWH.

6.3.2 Quantitative Requirements

Quantitative demands to the adsorbent optimal for AWH and AHMR can also be formulated in a uniform way: if the water adsorption equilibrium obeys the Polanyi principle of temperature invariance [39], the water uptake w is a function of the only parameter—the Polanyi-Dubinin adsorption potential $\Delta F = -RT \ln[P/P_0(T)]$, where P is the partial vapor pressure, P_0 is the saturation vapor pressure at temperature T . In this case, the OA should have energy different adsorption centers with the affinity distributed in a wide range between $\Delta F_{\text{ad}} = -RT_n [\ln P_{\text{am}}/P_0(T_n)]$ for rich isoster and $\Delta F_{\text{re}} = -RT_{\text{re}} [\ln P_{\text{am}}/P_0(T_{\text{re}})]$ for weak isoster. For the VentireC processes, both

stages occur at a temperature close to the indoor one (Fig. 6.3), and relative humidity $RH(1)$ and $RH(2')$ instead of ΔF can be used to formulate the requirements. The adsorption isotherm of such OA should be a curve with the uptake gradually rising at the appropriate ΔF or RH range (Fig. 6.5).

To be particular, we give below examples of *quantitative* demands for the adsorbent optimal for AWH and AHMR in various climatic regions. For making this analysis, the needed climatic data were collected from a Meteonorm database [40].

AWH. To outline the OA properties, we analyze the average night temperature T_n and the partial pressure P_{am} of water vapor in the ambient air for several regions, suffering from the fresh water scarcity, including the Sahara desert, the Mojave desert, Riyadh Old in Saudi Arabia, Noyon in Southern Mongolia, Atacama in Southern America and Alice-Spring in Central Australia (Fig. 6.6). The appropriate values ΔF_{ad} and ΔF_{re} are calculated at $T_{re} = 70$ and 80 °C for the dry season (January in Alice Spring and July for the rest). Three climatic zones are selected, namely that with extremely dry (ED), dry (D) and moderate humid (MD) climates. Riyadh

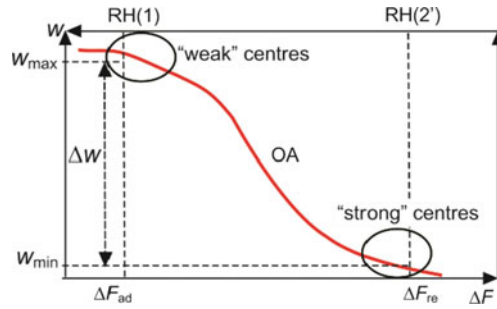


Fig. 6.5 Characteristic adsorption curve of the OA for the AWH and VentireC processes

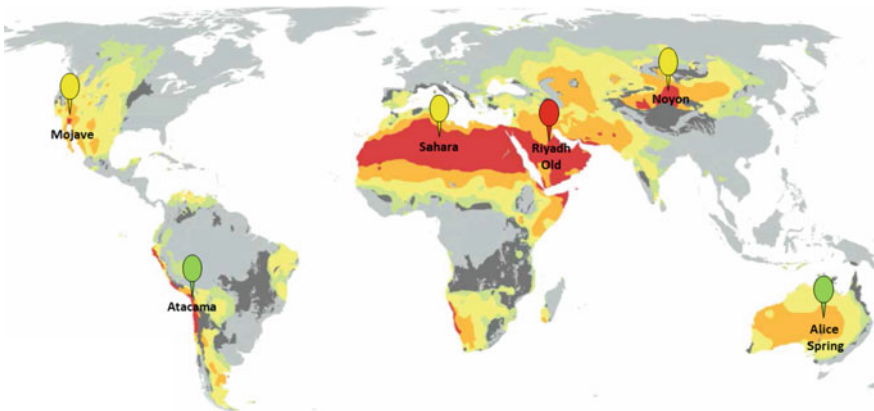


Fig. 6.6 Selected reference regions with extremely dry (red symbols), dry (yellow symbols) and moderate humid (green symbols) climate [17]

Old with $\Delta F_{\text{ad}} = 4.1$ kJ/mol during the dry season is characterized by ED climate. The Mohave and Sahara deserts and Noyon are zones with D climate ($\Delta F_{\text{ad}} = 3.2\text{--}3.4$ kJ/mol), while Atacama and Alice Spring with $\Delta F_{\text{ad}} = 2.3\text{--}2.5$ kJ/mol belong to MH zone. The ΔF_{re} -value at $T_{\text{re}} = 80$ °C varies from 10.4 for Alice Spring to 16.4 kJ/mol for Atacama. Accordingly, the OA for AWH for these climatic zones has to exchange a large amount of water between these boundary ΔF -values.

AHMR. For analyzing the *VentireC* process, the average minimum temperature $T(3)$ in the coldest month (January) (Table 6.1) is taken into account. We considered the climatic data for several zones with warm ($T(3) = -10\text{--}-3$ °C), moderate warm ($T(3) = -15\text{--}-10$ °C), moderate cold ($T(3) = -20\text{--}-15$ °C), cold ($T(3) = -25\text{--}-30$ °C), and extremely cold ($T(3) < -30$ °C) climates. Regions from Central Europe (Minsk (Belarussia), Warsaw (Poland), Prague (Czech Republic), belong to the warm zone. Northern USA (Anchorage), Northern Europe (Oulu, Finland), and Central Russia (Moscow), etc. can be assigned to the moderate warm zone. Southern Canada (Quebec, Whitehorse), can be classified as the moderate cold zone. The southern parts of Siberia (Novosibirsk, Krasnoyarsk, Irkutsk) belong to the cold zone. Northern Canada (Yellowknife, Iqaluit) and northern parts of Far East in Russia (Anadyr, Magadan, Chita, Norilsk) constitute the extremely cold zone. The comfortable indoor $T(1)$ and $RH(1)$ values are assumed to be 22 °C and 50%, respectively [41]. The relative humidity $RH(1)$ at point 2' is defined as an intersection of isotherm 1–2' and line 3–2' with constant moisture content X (Fig. 6.4). The ranges of $RH(2')$ corresponding to different climatic zones are presented in Table 6.1. Accordingly, the strongest sites of OA for *VentireC* realization in the abovementioned climatic zones have to sorb water vapor at $RH(2')$ -values, while the weak sites have to release vapor at $RH(1) = 50\%$. The uptake swing $\Delta w = w(1) - w(2')$ has to be maximized.

6.4 Tailoring Adsorbents Optimal for Heat Storage and Water Harvesting

After the properties of the OA required for AWH and AHMR (*VentireC*) have been defined, the next step is the selection of real adsorbents, which properties meet the formulated requirements. One way (**screening**) is searching for such an adsorbent among those already known and available. The other option (**nanotailoring**) is preparing a new adsorbent with the pre-requested properties. Unfortunately, the performance of traditional adsorbents used for water adsorption (silica gels, active alumina, and zeolites) is quite low due to a small amount of water exchanged under conditions of the AWH and AHMR processes.

To date, a huge number of novel materials with advanced adsorption properties have been developed, which offer new opportunities for AWH and AHMR. We mainly consider here two new families of advanced sorbents, namely, Composites based on a hygroscopic Salt inserted into Pores of a solid Matrix (CSPMs) [32,

42] and Metal–Organic Frameworks (MOFs) [43, 44]. They are characterized by advanced adsorption capacity and offer wide opportunities for the rational design of materials with predetermined adsorption properties. Below we briefly discuss the water adsorption properties of CSPMs and MOFs, and factors affecting these properties.

The **CSPMs** were shown to surpass traditional adsorbents (zeolites, silicas, etc.) in water adsorption capacity. The common adsorbents, such as silica gels, alumina, activated carbons, natural clays, etc. are matrices for CSPMs. The halides, nitrate, and sulphates of alkaline and alkaline-earth metals mainly serve as hygroscopic salts [32, 42]. The sorption of water vapor on SCPMs includes three mechanisms:

- Physical adsorption on active surface sites of the matrix;
- Formation of salt hydrates via a reaction between water and salt $S + nH_2O = S \cdot nH_2O$;
- Deliquescence of the hydrate and absorption of water by the salt solution formed inside the pores.

The active surface sites of the matrix (silica, alumina, etc.) possess a quite strong affinity to water vapor and adsorb it at high ΔF (or low RH) values; however, the impact of this mechanism is usually minor. For mesoporous and macroporous matrices commonly used for CSPMs, the uptake due to the physical adsorption on their surface usually does not exceed 0.03–0.05 g/g. At decreasing ΔF (increasing RH), the salt reacts with water, forming solid hydrates, which deliquesce and transform to the salt solution inside pores. The solution retains water weakly, thus allowing its easy release during the desorption stage. The properties of CSPMs can be tuned in a wide range by judicious selection of the active salt, being the main water absorbing component [32, 42, 45–47]. The nature and porous structure of the matrix also affect the adsorption equilibrium of CSPMs with water vapor [32, 42, 48, 49]. Besides, it can be further altered by varying the synthesis conditions [50] and embedding two salts inside the matrix [51].

MOFs consist of metal clusters bonded through polydentate organic linkers [52], forming a porous framework. Due to extremely high porosity and specific surface area, the combination of both hydrophilic and hydrophobic moieties in the same structure, MOFs possess unique adsorption properties: large water adsorption capacity and variable hydrophilicity. A wide variety of water adsorption isotherms is observed for diverse MOFs: hyper-hydrophobic ZIF-8; strongly hydrophilic HKUST-1 and CPO-27; MIL-101(Cr) and Cr-soc-MOF-1 with an extraordinary adsorption capacity of 1.6 and 1.95 g/g, respectively [53–55]. Three types of water adsorption mechanisms on MOFs are usually distinguished, namely [56, 57]:

- Chemisorption on open (or coordinatively unsaturated, CUS) metal sites via coordination bonds;
- Reversible layer or cluster adsorption, or continuous pore filling;
- Irreversible capillary condensation.

Adsorption on CUS modifies the first coordination sphere of the metal ion (e.g. MIL-100(Cr) [58], MIL-101(Cr) [54], HKUST-1 [59], MOF-74 (CPO-27), UIO-66

[60]). The water—CUS interaction is rather strong, and adsorption on CUS occurs at low P/P_0 -values. Further adsorption may occur through continuous pore filling leading to the gradual adsorption isotherms. Such a behavior is typical of microporous MOFs. For MOFs with larger pores, capillary condensation occurs at increasing P/P_0 , which is described by isotherms of type IV (MIL-100(Cr), MIL-101(Cr)) [54, 58]. Furthermore, the flexibility of the crystalline structure of several MOFs (e.g. MIL-53(Cr) [61], CAU-10 [62]) results in unique step-wise adsorption isotherms.

Various adsorption mechanisms result in a wide variety of types of adsorption isotherms reported for MOFs and CSPMs. The opportunity of rational designing the materials with the required adsorption equilibrium is a corner-stone of potentially revolutionary advancements in AWH and AHMR. Below the adsorbents, selected or tailored for these two applications are comprehensively described.

6.5 Advanced Solid Sorbents

6.5.1 MOFs for AWH

As shown above, two factors, the affinity of the strong and weak sites of the adsorbent to water vapor and uptake swing under conditions of a specific AWH cycle are corner-stones for the OA selection. Remind that the adsorption isotherm of OA for AWH is a smooth curve with the gradual gradient in uptake in the ΔF -range from ΔF_{re} to ΔF_{ad} , and large uptake variation $\Delta w = w(\Delta F_{ad}) - w(\Delta F_{re})$ (see Sects. 6.3.1 and 6.3.2). For MOFs, the hydrothermal stability is a critical issue for practical application as well.

In this section, the suitability of MOFs for AWH in regions with different climatic conditions is assessed. First, the water adsorption isotherms were collected from the literature and plotted as function $w = f(\Delta F)$ [32]. Then, considering the values ΔF_{ad} and ΔF_{re} for the three climatic zones (Sects. 6.3.2) and keeping in mind the abovementioned requirements, the most promising MOFs are selected.

Two famous mesoporous MOFs, MIL-101(Cr) [54] and Cr-socMOF-1 [55] (Fig. 6.7a) demonstrate outstanding water adsorption capacity of 1.6 and 1.95 g/g, respectively. However, the uptake rise is observed at ΔF ranges 1.8–2.2 and 0.7–1.3 kJ/mol for MIL-101(Cr) [54] and Cr-socMOF-1, respectively, which is below $\Delta F_{ad} = 2.3$ –2.5 kJ/mol even for the zone with MH climate. These MOFs can be employed for AWH in regions with a more humid climate. For MH zone, Co_2Cl_2 -BTDD [63], MIL-100(Fe) [58], MIL-101(Cr)- SO_3H [54], can be selected as promising adsorbents for AWH. The strongest sites of these MOFs adsorb vapor at ΔF range 8–9 kJ/mol that ensures large fraction δ_{ex} . At lower $\Delta F < 4$ kJ/mol, the rise on adsorption isotherms is observed up to uptake $w = 0.6$ –0.9 g/g (Fig. 6.7b), which can be attributed to capillary condensation in pores.

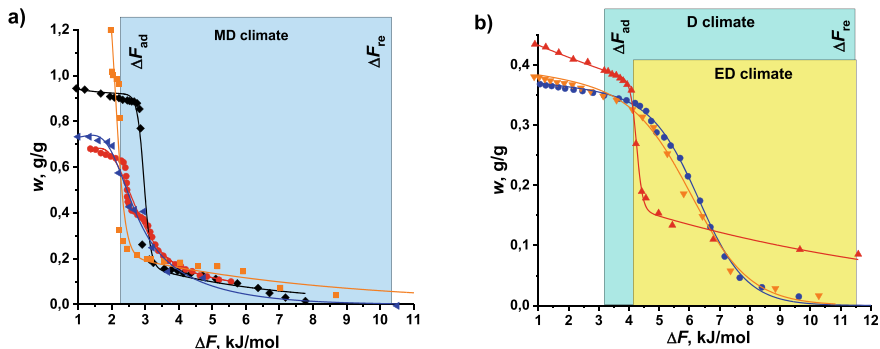


Fig. 6.7 Characteristic curves of water adsorption on (a) MIL-101(Cr) (■), $\text{Co}_2\text{Cl}_2\text{-BTDD}$ (◆), MIL-100(Fe) (◄), MIL-101(Cr)- SO_3H (●); (b) MIP-200 (▲), MIL-160, (●, ○), CAU-10(pydc) (▼). The boundary values of ΔF_{ad} and ΔF_{re} for the operating conditions of adsorption and regeneration stages in HM (a) D (b) and ED (c) climatic zones. $T_{\text{re}} = 80^\circ\text{C}$. Reprinted from [33] with permission from Elsevier

For D climatic zone with harsher conditions during the adsorption stage (higher ΔF_{ad} value), MIL-160 [64], CAU-10(pydc) [64] and MIP-200 [65] can be recommended, which gradually adsorb water vapor at $\Delta F < 10$ kJ/mol (Fig. 6.7b) up to $w = 0.35\text{--}0.36$ g/g at $\Delta F_{\text{ad}} = 3.2\text{--}3.4$ kJ/g (Fig. 6.8b). For ED climatic zone with $\Delta F_{\text{ad}} = 4.1$ kJ/g, the same adsorbents could also be appropriate with slightly lower uptake $w = 0.32\text{--}0.34$ g $\text{H}_2\text{O/g}$. It is worthy to note, that under conditions of the desorption stage at moderate temperature 80°C ($\Delta F_{\text{ad}} \geq 10.4$ kJ/g), the captured water can be completely desorbed (Fig. 6.7). If a heat source with a higher temperature is available for regeneration, MIP-200 can be recommended for D climate with maximum uptake $w = 0.4$ g/g (Fig. 6.7b).

The selected MOFs adsorb water vapor at $\Delta F \leq 8\text{--}9$ kJ/mol that promotes the high extraction fraction $\delta_{\text{ex}} = 0.78\text{--}0.93$. They can be regenerated at reasonable $T_{\text{re}} = 80^\circ\text{C}$ that allows utilization of solar heat to drive AWH cycles. At this desorption temperature, the fraction $\delta_{\text{col}} = 0.75\text{--}0.93$ can be achieved at $T_{\text{con}} = 20^\circ\text{C}$. Thus, for MOFs, the screening version of the harmonization concept demonstrates a high potential for selection of OA, which ensures efficient AWH realization.

6.5.2 LiCl/Silica Composite Specialized for VentireC

In this part, we illustrate the second version of the harmonization concept and describe the rational design of OA specialized for VentireC process for the cold climatic zone, e.g., Western Siberia. Based on the literature data on water—salt equilibrium, LiCl was selected for the preparation of the CSPM. The LiCl/silica composite was synthesized by a dry impregnation method using the mesoporous Silica Gel Davisil®grade

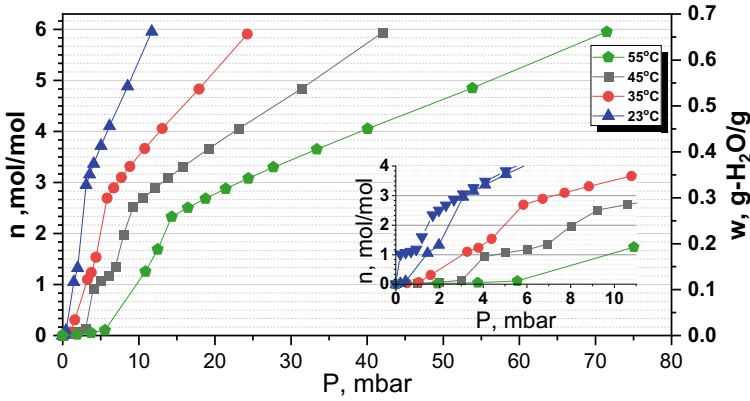


Fig. 6.8 Water sorption isotherms for the LiCl/silica composite. Reprinted from [31] with permission from Elsevier

646 (specific surface area $S_{sp} = 265 \text{ m}^2/\text{g}$, pore volume $V_p = 1.12 \text{ cm}^3/\text{g}$, average pore size $D_{av} = 17 \text{ nm}$) as a matrix. The salt content C_s was 25.7 wt.% [31].

The isotherms of water vapor adsorption (Fig. 6.8a) show three distinct ranges. At a small pressure, active sites of the silica adsorb water vapor (the uptake $w \leq 0.02 \text{ g/g}$). A step on the isotherms detected at increasing pressure, attributes to the $\text{LiCl}\cdot\text{H}_2\text{O}$ formation. Then the uptake increases slightly because the hydrate is stable. Finally, the hydrate $\text{LiCl}\cdot\text{H}_2\text{O}$ deliquesces and transforms into an aqueous LiCl solution inside the pores, which further absorbs water vapor.

The isosteric enthalpy of sorption at various water uptakes varies from $64 \pm 1 \text{ kJ/mol}$ at $n = 0.1 \text{ mol-H}_2\text{O/mol-LiCl}$, indicating a strong interaction between LiCl and water in $\text{LiCl}\cdot\text{H}_2\text{O}$, to $44\text{--}50 \text{ kJ/mol}$ at $n = 3\text{--}7 \text{ mol-H}_2\text{O/mol-LiCl}$, showing a weak interaction between water molecules and ions Li^+ and Cl^- in the solution.

Based on the water sorption equilibrium data for the LiCl/silica the feasibility of the VentireC process using this composite was assessed using a psychrometric chart of humid air combined with the isosteric chart of the composite (Fig. 6.4) [66]. During the adsorption mode, the strong sites of LiCl/silica sorb water to reach low air $RH \approx 3\%$ at point 2' with the uptake $w = 0.02 \text{ g/g}$. This assures the discharged air dehumidification to a required RH to prevent the unit outlet from moisture freezing. At increasing RH the uptake gradually rises to reach 0.73 g/g at $RH \approx 50\%$ (point 1 in Fig. 6.4). At this point, water is easily desorbed from the salt solution inside silica pores and moisturizes the dry outdoor air up to the comfort level. The uptake variation Δw can be evaluated as about $0.6\text{--}0.7 \text{ g/g}$. Assuming the recommended air change rate (ACR) for a domestic sector of 1 air change per hour, the mass of the adsorbent needed for the humidity recuperation in a room of volume $V_r = 75 \text{ m}^3$ was estimated as 530 g [31]. This reasonable result provides a good base for the design of a compact VentireC unit.

To verify the feasibility of the VentireC process employing the LiCl/silica composite, a mathematical simulation of humidity recuperation with and without

thermal coupling was carried out in [67] for a single fin-tube heat exchanger coated with the LiCl/silica composite. This analysis was based on the assumption that the adsorption heat transfer from one DCHE to another one is fast; so that the temperatures of the considered DCHE and air are equal $T_{in} = 22\text{ }^{\circ}\text{C}$ (line 1–2' in Fig. 6.4) and constant. Thus, the “ideal” VentireC system was simulated.

The results show that:

- At the beginning of the sorption stage, the humidity ratio X of the outlet air equals 1.2–2.2 g/kg for various process parameters and DCHE geometry [67]. In the course of sorption, this ratio gradually increases to 1.35–3.2 g/kg. As a result, the fraction of water removed from the room air varies from 62 to 84%.
- During the desorption stage, the VentireC unit maintains $X = 7.2 - 7.65$ g/kg for the incoming air flux. This corresponds to $RH = 42\text{--}47\%$ at $22\text{ }^{\circ}\text{C}$, which meets the required value of 40–60% for indoor humidity [41].

Thus, the harmonization of the adsorbent properties with the climatic conditions of the region, where the VentireC process to be realised, allows efficient humidity recuperation.

This analysis was carried out for other climatic zones, and appropriate adsorbents were selected for each zone (Table 6.1) [31]. For instance, for the extremely cold climatic zone, a sorbent with a stronger affinity to water vapor, which sorbs vapor at $RH < 2.4\%$ is required. The LiCl/(silica grade 636) with narrower pores ($D_{av} = 6$ nm) or LiBr/silica (15 nm), which sorbs water at $RH \geq 1\text{--}2\%$ [31, 68], could be recommended. Accordingly, for zones with warmer climates, a sorbent with a weaker affinity to water is needed. $\text{Ca}(\text{NO}_3)_2$ in the silica gel pores of 6–15 nm size, which sorbs vapor at $RH \geq 9\text{--}18\%$ [49], can be employed.

Table 6.1 Average minimum temperature $T(3)$ and relative humidity $RH(2')$ for various cold regions as well as composite sorbents potentially promising for the VentireC process in these zones

Zone	$T(3)$, $^{\circ}\text{C}$	$RH(2')$, %	Appropriate sorbents
Warm	–10– –3	9.9 – 18.0	$\text{Ca}(\text{NO}_3)_2/\text{SiO}_2$ (12 nm) $\text{Ca}(\text{NO}_3)_2/\text{SiO}_2$ (15 nm)
Moderate warm	–15– –10	6.2 – 9.9	$\text{Ca}(\text{NO}_3)_2/\text{SiO}_2$ (10 nm) $\text{Ca}(\text{NO}_3)_2/\text{SiO}_2$ (6 nm)
Moderate cold	–20– –15	3.9–6.2	$\text{Ca}(\text{NO}_3)_2/\text{SiO}_2$ (6 nm) LiCl/SiO ₂ (15 nm)
Cold	–25– –20	2.4–3.9	LiCl/SiO ₂ (15 nm)
Extremely cold	<–25	< 2.4	LiCl/SiO ₂ (6 nm) LiBr/SiO ₂ (15 nm)

6.6 Conclusions

Two emerging adsorption processes aimed at improving the Earth's ecology, namely, water harvesting from the atmosphere (AWH) and heat and moisture recuperation in ventilation systems (AHMR) are considered in this Chapter. The adsorbent and its harmonization with the process conditions are corner-stones for the effective performance of both technologies. First, the process thermodynamic cycle is analyzed to formulate qualitative and quantitative requirements for the optimal adsorbent. It is revealed that for both processes, the adsorbent has to possess energy different adsorption sites with the affinity to water distributed in a certain range. This range depends on the climatic conditions of the region, where the process is realized. The searching/tailoring of real adsorbent, which fits the formulated requirements, is discussed for two families of adsorbents, Metal Organic Frameworks (MOFs) and Composites "Salt in Porous Matrix". Several MOFs are suggested as adsorbents for AWH in three arid regions (the Sahara Desert, Saudi Arabia and Central Australia), and their potential for AWH is evaluated. The composite "LiCl in the mesoporous silica gel" is intently designed for AHMR in the cold climate of Western Siberia and Northern Canada. Its sorption equilibrium with water vapor is studied, and the performance in humidity recuperation is estimated.

Acknowledgements This work was supported by the Ministry of Science and Higher Education of the Russian Federation within the governmental order for Boreskov Institute of Catalysis (project AAAA-A21-121011390006-0).

References

1. Joachim H (1890) Papyrus Ebers, Berlin
2. Schueth F, Sing KSW, Weitkamp J (2002) Handbook of porous solids eds. Wiley-VCH, Weinheim, Germany, 1:12
3. Scheele CW (1894) Chemische Abhandlung von der Luft und dem Feuer (1773), see: Ostwald's Klassiker der exakten Wiss. 58
4. Fontana F (1777) Mem Mat Fis Soc Ital, 1: 679
5. Kehi DM (1793) Observations et Journal sur la Physique, de Chemie et d'Histoire Naturelle et des Arts, Paris: XLII, 250
6. Lowitz T (1786) Crell's Chem. Ann 1:211
7. Dabrowski A (2001) Adsorption — from theory to practice. Adv Coll Interface Sci 93:135–224
8. Yang RT (1997) Gas separation by adsorption processes. Handb Porous Solids Eds, London
9. Tomphson G (1986) The Museum Environment. London-Boston
10. Roes AWM, Swaaij WPM (1979) Hydrodynamic behaviour of a gas-solid counter-current packed column at trickle flow. Chem Engng J 17:81
11. Kaviany M (1995) Principles of heat transfer in porous media, 2nd edn. Springer, New York
12. ASHRAE, Handbook-Fundamentals American Society of Heating, Refrigeration and Air-conditioning Engineers. Atlanta, GA, USA (1997)
13. DallBauman LA, Finn JE, Dabrowski A (ed.) (1999) Adsorption and its applications in industry and environmental protection. 120B Elsevier, Amsterdam, 455.

14. Wang R, Wang L, Wu J (2014) Adsorption refrigeration technology: theory and application. John Wiley & Sons, Singapore Pte. Ltd
15. Tu YD, Wang RZ, Zhang YN, Wang JY (2018) Progress and expectation of atmospheric water harvesting. *Joule* 2:1452–1475
16. Alonso MJ, Liu P, Mathisen HM, Ge G, Simonson C (2015) Review of heat/energy recovery exchangers for use in ZEBs in cold climate countries. *Build Environ* 84:228–237
17. Food and Agriculture organization of the United Nations. Water. <http://www.fao.org/land-water/water/water-scarcity/en/>, 2012 (last access on May 4, 2020)
18. Fathieh F, Kalmutzki MJ, Kapustin EA, Waller PJ, Yang J, Yaghi OM (2018) Practical water production from desert air. *Sci Adv* 4, eaat3198.
19. Gleick PH (1993) *Water in Crisis: A Guide to the World's Fresh Water Resources*. Oxford Univ. Press, Oxford
20. Shiklomanov I (1993) World fresh water resources. *Water in Crisis: A Guide to the World's Fresh Water Resources* (Ed. P. H. Gleick), Oxford University Press, New York
21. Beysens D, Milimouk I (2000) Pour les ressources alternatives en eau (The case for alternative fresh water sources). *Sécheresse* 11:281–288
22. Wada Y, de Graaf IEM, van Beek LPH (2016) High-resolution modeling of human and climate impacts on global water resources. *J Adv Model Earth Syst* 8:735–763
23. Kogan B, Trahtman A (2003) The moisture from the air as water resource in arid region: hopes, doubts and facts. *J Arid Environ* 53:231–240
24. United Nations Population. *Fund State of the World population 2011*. (2012).
25. Eurostat Energy Yearly Statistics 2008, Publication Office of the European Union (2010).
26. Report «On enhancement of energy efficiency of the Russian economy». Arkhangelsk, April 2009; <http://www.cenef.ru/file/Report%2025.05.09.pdf> (last access on November 2, 2021).
27. Filippov SP, Dil'man MD, Ionov MS. (2013) The optimum levels of the thermal protection of residential buildings under climatic conditions of Russia. *Therm Engn* 60: 841–851
28. Riffat SB, Zhao X, Doherty PS (2006) Application of sorption heat recovery systems in heating appliances—Feasibility study. *Appl Therm Engn* 26:46–55
29. Aristov Yu.I, Mezentsev IS, Mukhin VA (2006) New approach to regenerating heat and moisture in ventilation systems. 1. Laboratory prototype. *J. Engineering and Thermophysics* 79:(3) 143–150
30. Aristov YuI, Mezentsev IS, Mukhin VA (2008) A new approach to regenerating heat and moisture in ventilation systems. *Ener Build* 40:204–208
31. Shkatulov A, Gordeeva LG, Girmik IS, Huinink H, Aristov Yu.I (2020) Novel adsorption method for moisture and heat recuperation in ventilation. Composites “LiCl/matrix” tailored for cold climate. *Energy* 201:117595
32. Aristov YuI (2020) *Nanocomposite Sorbents for Multiple Applications*. Jenny Stanford Publishing Pte. Ltd., New York
33. Gordeeva LG, Solovyeva MV, Sapienza A, Aristov YuI (2020) Potable water extraction from the atmosphere: Potential of MOFs. *Renewable Energy* 148:72–80
34. *World Survey of climatology. Vol 10. Climates of Africa* (Ed. J.F. Griffiths). Elsevier, Amsterdam, London, New York (1972).
35. Alayli Y, Hadji NE, Leblond J (1987) A new process for extraction of water from air. *Desalination* 67:227–229
36. Gordeeva LG, Tokarev MM, Parmon VN, Aristov Yu.I (1998) Selective water sorbents for multiple applications: 6. Fresh water production from the atmosphere. *React Kinet Catal Lett*, 65: 153–160
37. Aristov YuI, Tokarev MM, Gordeeva LG, Snytnikov VN, Parmon VN (1999) New composite sorbents for solar-driven technology of fresh water production from the atmosphere. *Sol Energy* 66:165–168
38. Wang JY, Wang RZ, Wang LW, Liu JY (2017) A high efficient semi-open system for fresh water production from atmosphere. *Energy* 138:542–551
39. Polanyi M (1932) Section III. Theories of the adsorption of gases. A general survey and some additional remarks. *Trans Faraday Soc* 28: 316–333

40. Meteororm n.d. <https://meteororm.com/en/> (last access on May 5, 2020)
41. Wolkoff P, Kjærgaard SK (2007) The dichotomy of relative humidity on indoor air quality. *Environ Int* 33:850–857
42. Gordeeva LG, Aristov YI (2012) Composites “salt inside porous matrix” for adsorption heat transformation: A current state-of-the-art and new trends. *Int J Low-Carbon Technol* 7:288–302
43. Ferey G (2008) Hybrid porous solids: past, present, future. *Chem Soc Rev* 37:191–214
44. Kitagawa S, Kitaura R, Noro S (2004) Functional porous coordination polymers. *Angew Chem Int Ed* 43:2334–2375
45. Grekova AD, Gordeeva LG, Aristov YI (2017) Composite “LiCl/vermiculite” as advanced water sorbent for thermal energy storage. *Appl Therm Eng* 124:1401–1408
46. Shkatulov AI, Houben J, Fischer H, Huinink HP (2019) Stabilization of K_2CO_3 in vermiculite for thermochemical energy storage. *Renew Energy* 150:990–1000
47. Calabrese L, Brancato V, Palomba V, Frazzica A, Cabeza LF (2018) Assessment of the hydration/dehydration behaviour of $MgSO_4 \cdot 7H_2O$ filled cellular foams for sorption storage applications through morphological and thermo-gravimetric analyses. *Sustain Mater Technol* 17: e00073
48. Glaznev IS, Ponomarenko IV, Kirik SD, Aristov YuI (2011) Composites $CaCl_2/SBA-15$ for adsorptive transformation of low temperature heat: pore size effect. *Int J Refrig* 34:1244–1250
49. Simonova IA, Aristov YI (2005) Sorption properties of calcium nitrate dispersed in silica gel: the effect of pore size. *Rus J Phys Chem* 79:1307–1311
50. Gordeeva LG, Glaznev IS, Savchenko EV et al (2006) Impact of phase composition on water adsorption on inorganic hybrids “salt/silica.” *J Colloid Interface Sci* 301:685–691
51. Gordeeva LG, Grekova AD, Krieger TA, Aristov YuI (2009) Adsorption properties of composite materials (LiCl + LiBr)/silica. *Micropor Mesopor Mater* 126:262–267
52. Yaghi OM, O’Keeffe M, Ockwig NW, Chae HK, Eddaoudi M, Kim J (2003) Reticular synthesis and the design of new materials. *Nature* 423:705–714
53. Kuesgens P, Rose M, Senkovska I, Froede H, Henschel A, Siegle S, Kaskel S (2009) Characterization of metal-organic frameworks by water adsorption. *Micropor Mesopor Mater* 120:325–330
54. Akiyama G, Matsuda R, Sato H, Hori A, Takata M, Kitagawa S (2012) Effect of functional groups in MIL-101 on water sorption behavior. *Micropor Mesopor Mater* 157:89–93
55. Towsif Abtab SM, Alezi D, Bhatt PM, Shkurenko A, Belmabkhout Y, Aggarwal H, Weseliński ŁJ, Alsadun N, Samin U, Hedhili MN, Eddaoudi M (2018) Reticular chemistry in action: a hydrolytically stable MOF capturing twice its weight in adsorbed water. *Chem* 4:94–105
56. Canivet J, Fateeva A, Guo Y, Coasne B, Farrusseng D (2012) Water adsorption in MOFs: fundamentals and applications. *Chem Soc Rev* 43:5594–5617
57. Burtch NC, Jasuja H, Walton KS (2014) water stability and adsorption in metal–organic frameworks *Chem. Rev* 114:10575–10612
58. Akiyama G, Matsuda R, Kitagawa S (2010) Highly Porous and Stable Coordination Polymers as Water Sorption Materials. *Chem Lett* 39:360–361
59. Schlichte K, Kratzke T, Kaskel S (2004) Improved synthesis, thermal stability and catalytic properties of the metal-organic framework compound $Cu_3(BTC)_2$. *Micropor Mesopor Mater* 73:81–88
60. Schoenecker PM, Carson CG, Jasuja H, Flemming CJJ, Walton KS (2012) Effect of water adsorption on retention of structure and surface area of metal–organic frameworks. *Ind Eng Chem Res* 51:6513–6519
61. Bourrelly S, Moulin B, Rivera A, Maurin G, Devautour-Vinot S, Serre C, Devic T, Horcajada P, Vimont A, Clet G, Daturi M, Lavalley GC, Loera-Serna S, Denoyel R, Llewellyn PL, Ferey G (2010) explanation of the adsorption of polar vapors in the highly flexible metal organic framework MIL-53(Cr). *J Am Chem Soc* 132:9488–9498
62. Frohlich D, Pantatosaki E, Kolokathis PD, Markey K, Reinsch H, Baumgartner M, van der Veen MA, De Vos DE, Stock N, Papadopoulos GK, Henninger SK, Janiak C (2016) Water adsorption behaviour of CAU-10-H: a thorough investigation of its structure–property relationships. *J Mater Chem A* 4:11859–11869

63. Rieth AJ, Yang S, Wang EN, Dinca M (2017) Record atmospheric fresh water capture and heat transfer with a material operating at the water uptake reversibility Limit. *ACS Cent Sci* 3:668–672
64. Cadiau A, Lee JS, Borges DD, Fabry P, Devic T, Wharmby MT, Martineau C, Foucher D, Taulelle F, Jun C-H, Hwang YK, Stock N, de Lange MF, Kapteijn F, Gascon J, Maurin G, Chang J-S, Serre C (2015) Design of hydrophilic metal organic framework water adsorbents for heat reallocation. *Adv Mater* 27:4775–4780
65. Wang S, Lee JS, Wahiduzzaman M, Park J, Muschi M, Martineau-Corcus C, Tissot A, Cho KH, Marrot J, Shepard W, Maurin G, Chang J-S, Serre C (2018) A robust large-pore zirconium carboxylate metal–organic framework for energy-efficient water-sorption-driven refrigeration. *Nat Energy* 3:985–993
66. Aristov Yu I, Gordeeva LG (2022) Combining the psychrometric chart of humid air with water adsorption isosters: Analysis of the Ventireg process. *Energy* 239, part C, 122278
67. Girmik I, Yang T, Gordeeva L, Wang W, Ge T, Aristov, Yu (2020) New adsorption method for moisture and heat exchange in ventilation systems in cold countries: Concept and Mathematical Simulation, *Energies*, 13: 1386
68. Gordeeva LG, Restuccia G, Cacciola G, Aristov YuI (1998) Properties of the system “Lithium bromide—water” confined to silica gel pores: Equilibrium “vapor—condensed state.” *Rus J Phys Chem* 72:1236–1240

Chapter 7

Thermochemical Conversion of Lignocellulosic Waste to Activated Carbon: A Potential Resource for Industrial Wastewater Treatment



Ahmed Elsayid Ali, Zaira Zaman Chowdhury, Abu Nasser Faisal,
Rasel Das, Yasmin Abdul Wahab, and Seeram Ramakrishnan

Abstract In the last decade, the amount of contaminated water resources has increased dramatically with the rapid growth in industrial sectors. Additionally, the growth in world population and the effects of climate changes have also increased the water contamination levels in several areas. Thus, there is a crucial need for effective and eco-friendly water treatment materials. The current available water treatment methods and materials have multiples drawbacks that limit their usability. Materials such as metal oxide nanoparticles, carbon nanotubes, and polymer membranes are used widely in the water treatment field. However, the efficiency of these materials is limited by the complexity of the water contaminants. Therefore, highly efficient activated carbon is introduced as a proper approach to treat contaminated water. Typically, activated carbon is produced from different types of biomass. Hence, activated carbon can be produced almost everywhere. Currently, Lignocellulosic biomass is provided as a reliable renewable resource that can be used to produce activated carbon. Indeed, Lignocellulosic biomass can be utilized to produce several materials such as biogases, biofuels, and biochar. Activated carbon is produced from biomass using different thermal conversion technologies such as pyrolysis, anaerobic digestion, torrefaction hydrothermal processing, and gasification. Historically, pyrolysis technology is used for hundreds of years to produce biofuel and char from

A. E. Ali · Z. Z. Chowdhury (✉) · A. N. Faisal · Y. A. Wahab
Nanotechnology and Catalysis Research Centre (NANOCAT), University of Malaya, 50603 Kuala Lumpur, Malaysia

e-mail: dr.zaira.chowdhury@um.edu.my

Y. A. Wahab

e-mail: yasminaw@um.edu.my

R. Das

Department of Chemistry, Stony Brook University, Stony Brook NY 11794-3400, USA

e-mail: rasel.das@stonybrook.edu

S. Ramakrishnan

Department of Mechanical Engineering, Centre for Nanofibers and Nanotechnology, National University of Singapore, Block E3 #05-12, Engineering Drive 3, Singapore 117581, Singapore

e-mail: seeram@nus.edu.sg

woody biomass. This chapter focuses on the different reaction phases during pyrolysis and the effect of the reaction conditions on biomass to produce activated carbon. Moreover, the impact of technological development on the energy density of the lignocellulosic residues is covered in the chapter.

Keywords Activated carbon · Pyrolysis · Biomass · Cellulose · Lignin · Water treatment

7.1 Introduction

The inevitability of seeking reliable wastewater treatment techniques is evident. Presently, the global supply of clean water relies on accessible natural resources such as rivers, lakes, and groundwater. Moreover, recent studies show a massive decrement in the amount of natural water resources. The vast demand for new water and wastewater treatment approaches is associated with the huge growth in the human population, climate changes, and industrial revolutions. The industrial revolutions have the most significant impact on the water treatment sector. In fact, the dramatic growth in the industrial fields is associated with the growth in the world population and climate change. Hence, the three factors are connected like a circle. Nonetheless, the impact of the industrial revolution on the environment is not comparable with population growth or climate change. In the last years, industrial fields have introduced new types of complex contaminants into the environment in the form of wastes known as industrial wastes. The danger of industrial wastes rises with industrial developments. Generally, industrial wastes are discharged in the natural water resources such as rivers and lakes. Consequently, the industrial waste leak from surface water to the surrounding area and groundwater. The industrial waste stored inform of wastewater causes other challenges in urban areas. Apart from the environmental effects, wastewater is associated with severe health issues in urban areas.

Researchers seek effective, inexpensive, and environmentally friendly techniques and materials for water treatment to eliminate the adverse health and environmental effects of wastewater. Lignocellulosic biomass is proposed as a promising precursor to produce highly efficient activated carbon from natural resources. The special characteristics of biomass products have drawn the attention of several researchers. Also, the inorganic component of biomass contains a few sulphur, ash, and nitrogen quantities that can be neglected or utilized for other applications. Thus, the combustion of biomass is preferable because it produces fewer toxic gases such as carbon dioxide (CO_2), sulphur dioxide (SO_2) and nitrogen oxides (NO_x). Nevertheless, photosynthesis can be used to recycle and control carbon dioxide emissions (CO_2) [1]. At present, biomass products require more practical applications and demonstrations with an appropriate calculation of materials and energy. Indeed, there are multiple methods used to produce biomass products, such as biofuel, biogases, and char. Nonetheless, the thermotical base of the methods requires more sophisticated

studies. Thermal conversion technologies such as pyrolysis, anaerobic digestion, hydrothermal processing, and gasification are used widely to produce biofuel and char from different biomass types. Typically, thermochemical production of liquids and chars is conducted via flash or fast pyrolysis on an industrial scale. However, these products have not been implemented for commercialization applications.

Several biological and thermochemical processes have been adopted to convert biomass into value-added products. In general, pyrolysis is considered the most convenient conversion process among the other processes. Indeed, the pyrolysis process is considered inexpensive, flexible, efficient, requires simple transportation methods, easy to operate, and requires simple storing of products. Despite the unique features of the pyrolysis process, some challenges face the process, such as processing solid waste and biomass. Furthermore, the pyrolysis process is considered at the initial stage; several practical challenges are facing the expansion of the process to compete with the conventional thermochemical technologies [2, 3]. The pyrolysis of different lignocellulosic residues to produce biomass products such as solid char, gas, or liquid biofuel has been intensively studied earlier. Examples of these biomass species include woody biomass [6, 7], straws [8], seedcakes [9], bagasse [5], municipal solid waste (MSW) [10, 11], and beechwood [4]. Figures 7.1, 7.2, and 7.3 illustrate the different types of biomass conversion processes with their outputs and the decomposition temperature.

Pyrolysis is a process where a thermal decomposition of lignocellulosic derivatives occurs under an inert atmosphere in the absence of oxygen. The word is derived from two Greek words: 'pyro', meaning fire, and 'lysis' which means separation into different parts. Historically, pyrolysis is used by people in Southern Europe and the Middle East to prepare charcoal as a source of energy [12]. Additionally, ancient Egyptians made tar for sealing boats using pyrolysis technology [13]. The recent widespread applications of pyrolysis technologies can be seen in the energy field in the form of char and biofuel production. The pyrolysis products are also used in multiple industries such as materials fabrication, electronics, and fertilizers. Typically, high temperature obtained from burning charcoal is used to melt copper with tin to produce bronze. Throughout the modern era, pyrolysis processes gained the attention of many researchers as an effective technology for transforming waste and biomass into bio-oil [14]. Most of the present studies revolve around eventual objectives to enhance pyrolysis processes and produce reliable high-value products that can compete and replace the non-renewable fossil fuels and conventional materials to treat wastewater. Biowaste to produce value-added products via pyrolysis shadows several global challenges such as waste management, energy, and water and wastewater treatment. However, gaining more knowledge about pyrolysis technology is the true challenge. Several ideas proposed the use of biofuel in the airplane, trains, ships, and vehicles to replace fuels such as petrol and diesel [15, 16]. Nonetheless, few studies focused on the use of biomass-based carbon materials to remediate wastewater. Pyrolysis technology is under continuous enhancements to increase the quality

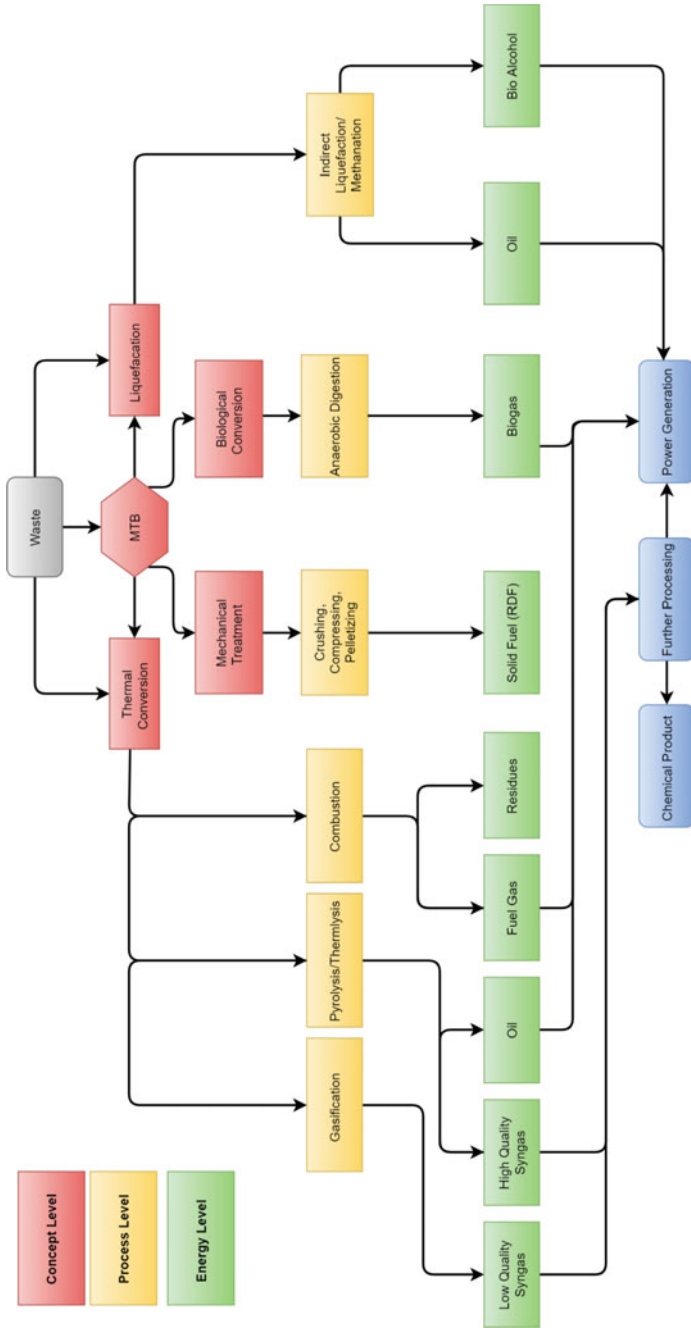


Fig. 7.1 Conversion processes of biomass feedstocks and their relative products

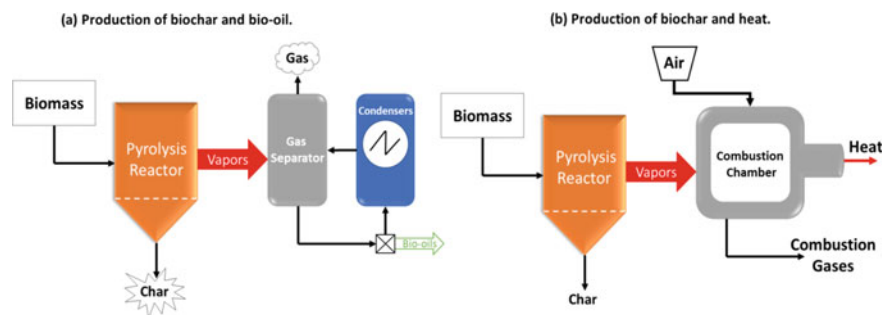


Fig. 7.2 Schematic diagram of simple pyrolysis reactors and the obtained products. **a** Production of biochar and bio-oil. **b** The production of biochar and heat

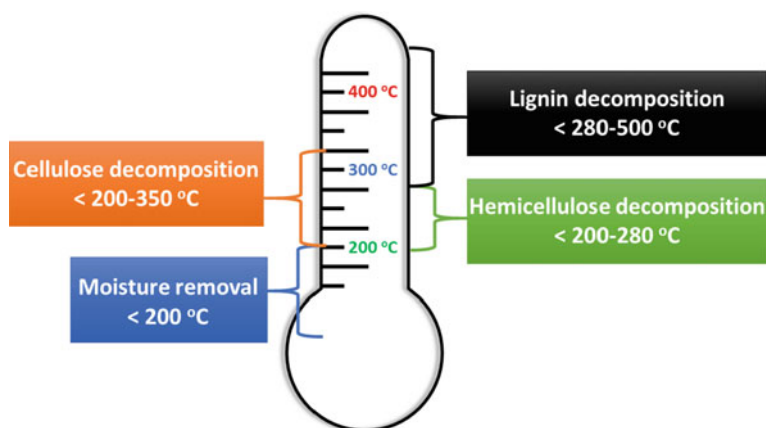


Fig. 7.3 The decomposition of lignocellulosic biomass components at different temperatures

of biomass products. Commonly, equipment such as pyrolysis reactor, lignocellulosic residues pre-treatment unit, and subsequent unit for downstream processing are parts of the pyrolysis system unit. The units are classified further into slow pyrolysis units to produce only heat and biochar or units that use fast pyrolysis to produce biochar and bio-oils.

Researchers have been working on the thermal conversion of biomass into biomass-based carbon products using advanced pyrolysis processes in the last year. The optimization of process parameters offers many advantages to pyrolysis technology over other thermochemical conversion technologies. Nevertheless, pyrolysis technology needs more improvements for commercial applications. Hence, this chapter investigates the current status of pyrolysis technology and the potential for

practical application for biochar to produce highly efficient activated carbon. Additionally, the pyrolysis products, types of pyrolysis and principles, biomass compositions and characteristics, physiochemical properties of pyrolysis products, and the economic aspects of amorphous carbon for wastewater treatment are discussed in this chapter. Moreover, the production and properties of activated carbon are stated in this chapter to study the limitations in wastewater treatment. Eventually, the future of activated carbon production from biomass is discussed to enhance the wastewater treatment process.

7.2 Classification of Thermochemical Processes to Produce Activated Carbon

Thermochemical processes are the conversion of carbonaceous materials such as biomass into value-added products like gaseous and liquid fuels, solid fuel, and chemical feedstock. Indeed, thermal conversion techniques are used in ancient India and China before 4000 BCE to produce charcoal from biomass. At present, gaseous and liquid biomass products are treated and used in several fields. Besides that, charcoal is still used by several countries as a primary source of energy. Mainly, thermochemical conversion processes are classified into pyrolysis and gasification. The significant difference between the techniques relies on the final product. Pyrolysis is primarily used to produce char and liquid fuel, whereas gasification is used to convert biomass into a conventional gaseous product. The process of producing liquid fuel from biomass is known as liquefaction. Pyrolysis is further classified into multiple methods according to the preparation temperature and final production. In general, pyrolysis is classified into pyrolysis, carbonization, and torrefaction methods. Pyrolysis is the most adopted approach to convert biomass into carbon-rich materials. Pyrolysis, carbonization, and torrefaction processes are conducted in an oxygen-starved atmosphere. Therefore, carbonaceous materials are mainly formed from biomass via thermochemical conversion processes in the absence of oxygen. The presence of oxygen during the thermochemical convention will burn the biomass precursors and produce a large amount of ashes. The thermochemical process which involves oxidation is known as combustion. As discussed before, studying and improving the thermochemical processes will produce a high quality of carbon materials from biomass. Using high-quality activated carbon will improve the quality of wastewater treatment. In several publications, thermochemical conversion processes are stated to be independent due to the different temperature values. Nevertheless, the thermochemical convention processes used to produce solid carbon substances are interconnected. In fact, carbonization and torrefaction are part of the pyrolysis process. Figure 7.4 illustrates the connection between the thermochemical processes.

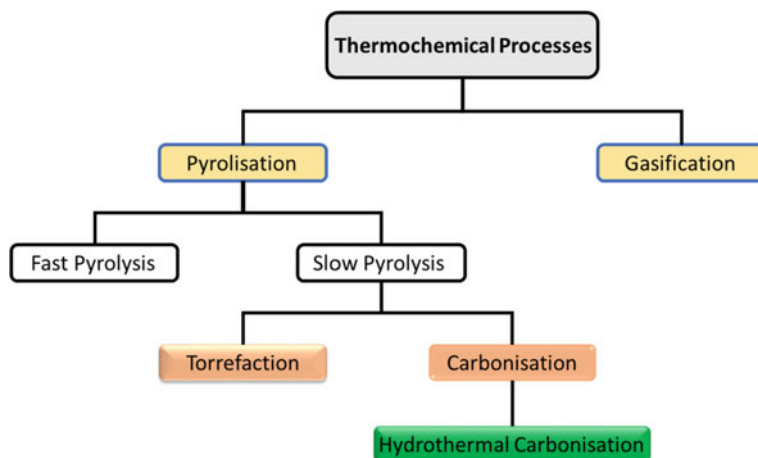


Fig. 7.4 Diagram of the relation between thermochemical processes for activated carbon, biogasses, and bio-fuels production

7.2.1 Pyrolysis

The thermal decomposition of pyrolysis using lignocellulosic biomass requires a special environment. Initially, the pyrolysis of lignocellulosic biomass occurs in an oxygen-deficient environment in an inert atmosphere. Followingly, nitrogen (N) or argon (Ar) gases are diffused into an inert atmosphere to complete the process. Generally, several steps are involved in the chemical reaction of the process, which makes it very complicated. The outputs of biomass pyrolysis are products such as biochar, gases, and bio-oil. The pyrolysis process emits materials that can be either discharged or used in further applications, such as hydrogen (H), carbon dioxide (CO₂), carbon monoxide (CO), and methane (CH₄). The decomposition of organic materials based on biomass substrate starts around 350–550 °C. However, the decomposition can proceed until 700–800 °C in the absence of oxygen/air [17, 18].

The chemical structure of biomass consists of lignin, a long polymer chain of cellulose, pectin, hemicellulose, and others. The small molecules formed from the bulky molecules of organic materials. These small molecules are then released from the pyrolysis process as solid char, steam of gases, tar, and oil as condensable vapors. Multiple factors affect the proportion of the final products, such as heat rate, temperature, and types of precursors, pressure, reactor design, and system configuration. The effect of temperature on the decomposition process of prime lignocellulosic residues is shown in Fig. 7.3 and, the effects of pyrolysis on the lignocellulose components is illustrated in Fig. 7.5. Likewise, the moisture percentage of the biomass has a vital impact on the pyrolysis processes. The raw biomass moisture percentage must be around 10% during the fast pyrolysis process [18]. The high percentage of biomass moisture will turn the major final products into liquids.

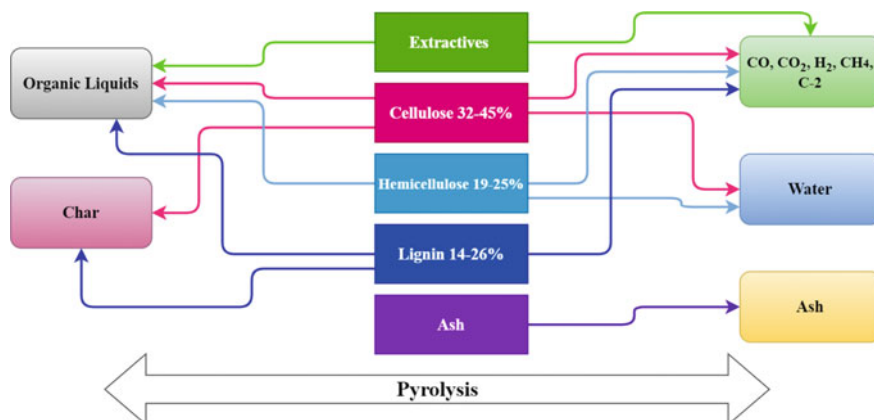


Fig. 7.5 The relationship between the composition of lignocellulosic biomass and obtained products during pyrolysis

On the other hand, the low water level will cause a high risk because the process will produce an enormous amount of dust instead of oil. Hence, it is necessary to dry the sludge produced from meat-processing wastes and waste streams before involving it in the pyrolysis process. To demonstrate, the required condition to produce biochar is a temperature less than 450 °C when the heating rate is slow. In contrast, when the heating rate is high and the temperature is higher than 800 °C, the obtained products are a large amount of gases and ash. In like manner, medium temperature when the heating rate is high, the main yield is bio-oil. When the temperature is between 250 and 300 °C at the beginning of the process, a large amount of volatile materials is disposed of almost ten times faster than the subsequent step [20].

As mentioned before, charcoal is mainly produced using woody biomass. The charcoal produced from wood has many advantages, like the production of a limited amount of smoke. Historically, charcoal is used to melt ore rocks to yield iron. Nevertheless, this process has many disadvantages, like it produces a huge amount of air pollutants, less production percentage, and less energy. Consequently, advanced technology has been adopted and developed to extract the extreme amount of energy from biomass via exothermic and endothermic processes such as combustion, gasification, and pyrolysis [21]. Combustion is used to produce heat by burning biomass in the presence of oxygen. The efficiency of combustion is not sufficient [22, 23]. Gasification may occur in an oxygen-starved environment to produce gaseous fuels. However, the pyrolysis process is more advantageous compared to combustion and gasification [24, 25]. Indeed, pyrolysis can be present as part of the combustion and gasification processes [26]. Figure 7.6 shows the products of biomass substrate during the pyrolysis process [27].

In general, the pyrolysis process is classified into slow and fast processes. The significant difference between the two types is the heating rate involved in the process. The required time of heating precursors to reach pyrolysis temperature in the slow

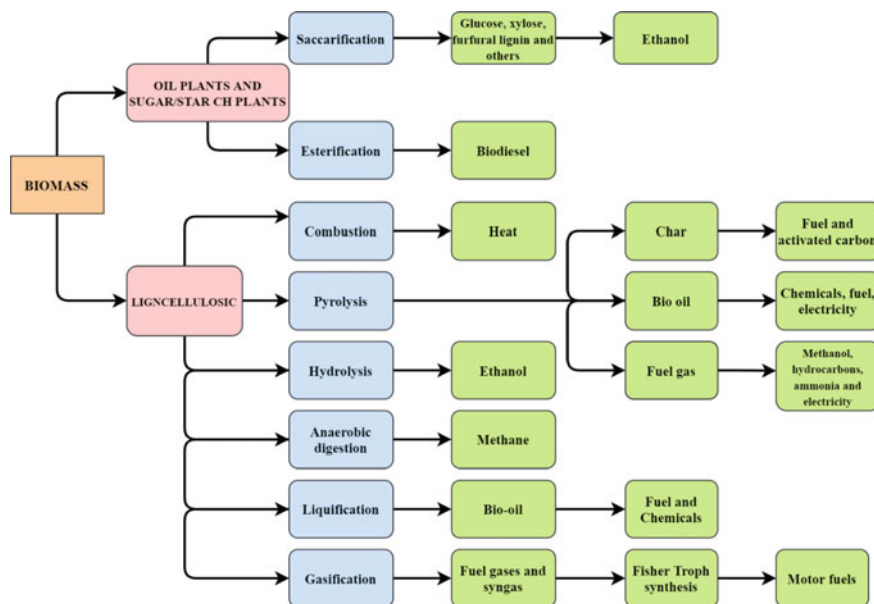


Fig. 7.6 The Conversion of biomass feedstock into value-added products through pyrolysis

pyrolysis process is longer than the time used to keep the substrate at the characteristic pyrolysis reaction temperature. On the other hand, the initial heating time of the biomass substrate in the fast pyrolysis process is less than the final retention time of the substrate at the maximum pyrolysis temperature. There are two other types of pyrolysis based on the ambiance of the process, hydro-pyrolysis and hydrous pyrolysis. As mentioned before, usually fast and slow pyrolysis process takes place in an inert atmosphere, while hydro-pyrolysis occurs in the presence of hydrogen and hydrous pyrolysis occurs in the presence of water. In the slow pyrolysis process, vapors present in the pyrolysis medium for a longer time. Hence, this process is utilized to produce more char and activated carbon. In fact, slow pyrolysis is usually classified into conventional and carbonization processes. Conversely, in fast pyrolysis vapors exist in the medium for seconds or milliseconds. Thus, fast pyrolysis is mainly utilized to produce gas and bio-oil. Fast pyrolysis is further classified into a flash and ultra-rapid pyrolysis process. Table 7.1 shows different types of pyrolysis processes with basic characteristics.

(i) Fast Pyrolysis

The fast pyrolysis process involves using a high heating rate to burn the precursors at high temperatures in the absence of oxygen. The quantity of the products produced via fast pyrolysis is related to the initial weight of the biomass. Using 15–25% of biochar precursors in the fast pyrolysis process can produce 60–75% of liquid biofuels [54]. Besides that, it is possible to obtain 10–20% of gaseous products, depending on the biomass type [54]. Fast pyrolysis

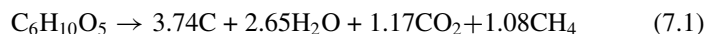
Table 7.1 Summary of pyrolysis processes for biomass

Pyrolysis process	Temperature (°C)	Heating rate	Products
Fast	500	Very high	Biofuel
Slow	400	Very low	Charcoal, biofuel, and biogas
Flash	<650	High	Chemicals, biofuel, and biogas
Ultra-fast	1,000	Very high	Chemicals and biogas
Hydro-pyrolysis	<500	High	Biofuel
Conventional	600	Low	Charcoal, biogas, and biofuel
Carbonisation	400	Very low	Charcoal
Vacuum	400	Medium	Biofuel

involves short vapors retention time. Nevertheless, the produced vapors and aerosol can be chilled quickly during the process to increase the percentage of obtained bio-oil [54]. Typically, the obtained liquid biofuels are used to operate engines, turbines, boilers, and industrial applications. Fast pyrolysis technology is receiving global attention as a liquid fuel producing process due to its practical advantages, such as the inexpensive development cost, simple storability and transportation of obtained products, and the utilization of second-generation bio-oil as industrial wastes, and municipal to produce. In addition, fast pyrolysis can derive secondary fuels and chemicals from motor fuels. Lastly, the process can assure a pre-disintegration of lignin portions and simple oligomers from lignocellulosic biomass with consecutive improvement [55–57].

(ii) **Slow Pyrolysis**

The slow pyrolysis technology uses a low heating rate and low temperature to produce a high quality charcoal. In this process, the vapor residence time is longer than flash pyrolysis, around 5–30 min. To obtain char and liquid in slow pyrolysis, a reaction occurs between the volatile organic fragments [61]. Nonetheless, the quality of the obtained bio-oil in this process is very poor. Longer vapor residence time creates further cracking, which lowers bio-oil production. Slow pyrolysis has some drawbacks, such as the higher consumption of energy due to the low heat transfer rates with longer retention time [62, 63]. The charcoal produced via slow pyrolysis is the core of activated carbon production. Basically, high-quality charcoal means the high efficiency of activated carbon. The following equation is the stoichiometric Eq. (7.1) of charcoal production by [11].



7.2.2 Carbonization

Thermochemical carbonization is a process where the pyrolysis of biomass precursors is conducted in a deficient oxygen atmosphere. Carbonization is conducted at a low temperature between 300 and 700 °C. Primarily, the carbonization process is used to produce carbon-rich char from organic substances. The carbonization of biomass is widely known in rural areas due to the simplicity of the process. Moreover, several industries are using carbonization to produce high-quality commercial char for energy sectors. Usually, carbonization is preferred to produce activated carbon as it is an inexpensive process and consumes low energy. In addition, the carbonization process produces a low amount of wastes compared to other thermochemical processes. Carbonization produces a char with a high volume of narrow pores on the surface. Frequently, a large amount of surface pores on the char are blocked by liquid tar and other substances. The tarry substances are attached to the pores of the char during the diffusion of volatile components out of carbon structure into the gas stream. Indeed, the diffusion process also forms cracks on the char structure. Thus, the structure of the char contains a high volume of pores and tunnels. The char produced by carbonization can be used for water and wastewater treatment as adsorbents. However, this char will have a poor adsorption capacity due to the existence of blocked pores. Carbonization involves four main phases at different temperatures (Table 7.2). Carbonisation of biomass is further subdivided into a process known as hydrothermal carbonization. Hydrothermal carbonization is utilized to reduce energy consumption and increase the porosity of produced char.

(i) Hydrothermal Carbonization

Hydrothermal carbonization (HTC) is a widely used process to convert industrial and agricultural wastes into green products. It produces solids, liquids, and gaseous products [44]. The solids formed are known as hydrochar (HC), while liquids and gases are known as biofuels and biogases, respectively [44, 45]. Hydrochar is a carbon-rich product that is further treated to produce activated carbon. Meanwhile, the liquids are usually used in the agricultural field as fertilizer or converted into effective biofuels. Normally, HTC is used as a pre-treatment process to optimize the surface chemistry of activated carbon [45].

Table 7.2 The phases of biomass carbonization

Phase	Temperature (°C)	Process
First	≤200	Beginning of drying process for biomass precursor
Second	170–<300	The pre-carbonization phase, few amounts of liquids and condensable gases are produced such as methanol and CO ₂
Third	250–<300	The amount of produced tar increases, and some acids are formed from the biomass precursor to produce char
Fourth	>300	The percentage of carbon content in char increase while volatile compounds are leaving the char structure

After HTC, hydrochar yields are further treated with a pyrolysis process to produce high-quality activated carbon with low moisture percentage [44–46].

The major feature of HTC is the presence of oxidants in the form of deionized water. Indeed, deionized water is used as a green solvent. During the HTC, deionized water is added to the reactor along with the biomass feedstock. Subsequently, the biomass is carbonized at a low-temperature range between 180 and 250 °C. The deionized water evaporates and creates high inner pressure [44]. Followingly, the water molecules bounce at high speed inside the reactor and break down the bulky biomass into small particles. Simultaneously, water function as an oxidation agent that optimizes the surface chemistry of the hydrochar, hence enhancing the pores volume of the material [45].

HTC is used on an industrial scale as it consumes low energy, produces a low amount of toxic gases or tars, inexpensive, easy to operate, and eco-friendly [45, 47]. Besides, the process produces high-quality hydrochar, which is further treated through the pyrolysis process to obtain highly effective activated carbon. The activated carbon is subsequently treated with physical, chemical, or physiochemical activation to increase the surface area via open blocked pores and tunnels.

(ii) **Torrefaction**

Torrefaction is a new thermal conversion process used to produce carbon-rich solids from biomass. The torrefaction process is adopted in energy sectors as it is inexpensive and requires lower operational energy compared to carbonization. The principle of torrefaction is similar to carbonization but at a lower temperature. Typically, torrefaction occurs in the absence of oxygen. However, oxygen may introduce into the reaction but in a deficient percentage to prevent combustion.

Briefly, torrefaction converts biomass precursors into solids in slow heat under temperatures between 200 and 300 °C. During the heating process, the carbon content and energy density increase while the oxygen and moisture content decrease [46]. Thus, the obtained is a charcoal-like product with a high percentage of carbon content. Torrefaction is used to reduce storability and simplify the transportation process. Therefore, torrefaction is used to enhance the commercial value of wood by-products for energy production.

7.3 Preparation of Activated Carbon

The preparation of activated carbon using biomass precursors involves two stages, thermochemical conversion, and activation. The two stages may conduct simultaneously as one-step processes or sequentially as dual steps processes. At the first stage, a thermochemical conversion such as pyrolysis, carbonization, or torrefaction is used to produce char with high carbon content. As discussed before, the obtained char may have a very poor adsorption capacity due to the existence of a high volume of blocked

pores on its structure. Thus, different activation types are used to eliminate the presence of blocked pores and increase the adsorption capacity. The activation process may include chemical activation, physical activation, or physiochemical activation. Basically, the primary objective of the activation stage is to convert biomass-based char into highly efficient activated carbon.

Briefly, the activation process is used to enhance the porosity and create a fine solid cavity on the surface of the char. Generally, the created pores are classified into three types, macropores (>50 nm), mesopores (2–50 nm), and micropores (<2 nm) [47]. Adjusting the percentage of pores type relies on the type of biomass precursor and activation process. Usually, activated carbon with a high percentage of micropores is used for gas filtration or as a base substance for other nanocarbon materials. On the other hand, macropores and mesopores are used in water and wastewater treatment to trap and hold different types of water contaminants such as heavy metals, pharmaceutical wastes, dyes, and pesticides. Chemical and physical activation processes are the most widely adopted activation methods to produce activated carbon. Physiochemical activation is a combination of physical and chemical activations which usually used to enhance the adsorption performance of activated carbon.

7.3.1 Physical Activation

Physical activation involves the oxidation of char using oxidizing agents such as air/oxygen, water steam (H_2O), diluted oxygen gas, carbon dioxide (CO_2), or their mixture [47]. Usually, physical activation conducts at an elevated temperature around 800–1,100 °C [48]. During the physical activation, the volatile chemicals on the char structure tend to skip in the form of gases. Simultaneously, existed narrow pores are widening, and new pores are formed, thence, the porosity and surface area of the char. At this stage, the modified char is known as activated carbon. Physical activation can be conducted in a single or dual stages process. There are no significant differences between the two processes on the efficiency of produced activated carbon. However, a single-stage process requires a shorter preparation time and lower operational energy.

The most remarkable oxidizing agents are water stream and carbon dioxide. Carbon dioxide has an endothermic nature and low reactivity at high temperatures [49]. Therefore, carbon dioxide is typically used to ensure high controllability of the activation process. In addition, carbon dioxide is simple to handle and provide a slow reaction rate at low temperature. Indeed, increasing the activation time and temperature will increase the CO_2 reaction. However, increasing the activation time and temperature to a certain limit may form ash residues and destroy the existed pores. Carbon dioxide as an activation agent tends to form more micropores, whereas water steam tends to expand the existed micropores. Hence, water steam generates activated carbons with low micropore volume and high meso and macropore volumes [49]. Nonetheless, both carbon dioxide and steam can be very effective activating agents because the most important factor is the conditions of the activation process. Therefore, steam and carbon dioxide can be suitable for certain types of biomass precursors.

The physical activation process is commercially favorable as it is inexpensive and requires no chemicals that will make it an environmentally friendly procedure. On the other hand, physical activation has drawbacks that limit its scalability, like it produces activated carbon with low adsorption capacity, consumes high energy, and usually, the process needs a long activation time [48, 49]. The precise selection of proper oxidizing agents for specific biomass precursors will help produce activated carbon with large pore size distribution and surface area. The detailed process for activated carbon production using physical activation is shown in Table 7.3.

7.3.2 Chemical Activation

The chemical activation method, also known as wet oxidation, uses chemical agents as dehydrating and oxidizing agents. The chemical activating agents can be acids, bases, or salt. Usually, the activation process is synchronized with the carbonization process at a temperature between 400 and 900 °C according to the used precursor and activating agents [48]. The chemical activation process is divided into three main steps. First, impregnation in which the carbonaceous materials are oxidized and dehydrated with chemicals. Subsequently, the mixture is dried and then heated for a given time at a specific temperature. Lastly, the mixture is washed repeatedly to remove the excess activating agent and obtain activated carbon [48]. Although several chemicals are studied as activating agents, only a few produce activated carbon with high efficiency. The activating agents with high potential are either alkaline or acidic groups. Examples of commonly used alkaline groups are sodium hydroxide (NaOH), potassium carbonate (K_2CO_3), potassium hydroxide (KOH), and calcium chloride ($CaCl_2$). On the other hand, the most used acidic groups are sulphuric acid (H_2SO_4) and phosphoric acid (H_3PO_4). In addition to acidic and alkaline groups, some metal salts exhibited high potential, such as zinc chloride ($ZnCl_2$) [48].

Generally, potassium hydroxide produces activated carbon with a high surface area. However, the surface area of the activated carbon is also related to the type of used precursors [47, 48]. Indeed, recent studies are focusing on enhancing the activation performance of potassium species to form different types of pores on the surface of activated carbons [50]. To obtain activated carbon with high pores size and volume, some variables need to be monitored, such as activation method, time, temperature and atmosphere, carbonization temperature and time, and impregnation ratio [45]. Although chemical activation produces activated carbons with more pores size distribution and high pores volume, the process has drawbacks that limit its applicability. For instance, the produced activated carbon by chemical activation requires repeated and long washing steps to remove the excess activating agent. Moreover, the process produces toxic wastewater, which contains some chemical agents that can be harmful to the environment upon discharging inappropriately [48]. Nonetheless, chemical activation has several advantages that make it desirable over physical activation. For instance, chemical activation produces activated carbon with a high adsorption capacity. Additionally, the process is economically viable

Table 7.3 Production of activated carbon via physical activation

Biomass	Carbonisation temperature (°C)	Carbonisation time (mins)	Activation agent	Activation temperature (°C)	Activation time (mins)	S _{BET} (m ² ·g ⁻¹)	Refs
Acrocomia karukerana	800	120	CO ₂ /Steam	850	–	1,029	[51]
Bamboo wastes	650	–	Steam	800–900	–	990–1,099	[52]
Baobab woods	–	–	CO ₂	800	–	875	[53]
Bulgarian peach stones	599.85	–	Steam	849.85	120	1,258	[54]
Coconut shell	1,000	30	N ₂ /Steam	900	120	1,926	[55]
Coconut shell	1,000	120	N ₂ /Steam	900	30	901	[55]
Cypress saw dust and palm kernel shell ash	600	–	steam	–	–	1,668.1	[56]
Camellia oleifera	–	–	Steam	820	–	1,076	[57]
Date seeds	–	–	Steam	800	120	702	[58]
Date seeds	600	280	CO ₂	900	–	490	[58]
Date palm leaves	–	–	Steam	577	30	1,094	[59]
Euterpe oleracea	800	120	Ar/CO ₂	800	180	496	[60]
Guava seeds	800	120	CO ₂ /Steam	850	–	1,201	[51]

(continued)

Table 7.3 (continued)

Biomass	Carbonisation temperature (°C)	Carbonisation time (mins)	Activation agent	Activation temperature (°C)	Activation time (mins)	S _{BET} (m ² ·g ⁻¹)	Refs
Nuati woods	–	–	CO ₂	800	–	801	[53]
Oil palm empty fruit bunch	–	–	Steam	–	–	720	[61]
Oil palm shell	–	–	CO ₂	–	–	905	[61]
Pistachio nut shells	750–850	–	Steam	850	20	2,596	[62]
Pine sawdust pellets	–	–	CO ₂	800	1	275	[63]
Phoenix dactylifera seeds	800	–	CO ₂	900	1	723.7	[64]
Rice husk	–	–	Steam	850	105	1,180	[59]
Rice bran	–	–	CO ₂	850	90	652	[59]
Tropical Almond shells	800	120	CO ₂ /Steam	850	–	1,074	[59]

because it requires a lower temperature and less activation time [48]. The detailed process for activated carbon production using chemical activation is shown in Table 7.4.

7.3.3 *Physiochemical Activation*

Physiochemical activation is a process where physical and chemical activations are performed simultaneously. The physiochemical activation is mainly used to enhance the pore volume and surface area of activated carbon. Typically, physiochemical activation is conducted via two approaches, a chemical treatment before the carbonization following by physical activation or a chemical treatment after the carbonization following by physical activation. Studies revealed that the sequence of chemical activation has negligible effects on the properties of produced activated carbon. Generally, activated carbon produced via physiochemical activation has a better pore structure and higher surface area compared to physical or chemical activations. Physiochemical activation can be used to increase the volume of mesopores on the surface of activated carbon. Thus, producing activated carbon is suitable for wastewater treatment. Apart from the advantages of physiochemical activation, the process is considered costly and time-consuming in comparison to physical activation and chemical activation. The detailed process for activated carbon production using physiochemical activation is shown in Table 7.5.

7.4 **Types of Lignocellulosic Biomass Precursors for Activated Carbon**

Lignocellulosic biomass is a natural material that is formed from living species such as animals and plants. Recently, lignocellulosic biomass is proposed as an alternative source of energy. In comparison to fossil fuel, biomass is inexpensive and environmentally friendly. Moreover, biomass is used to produce value-added products such as activated carbon and fertilizers. The new adoption of lignocellulosic biomass will solve the environmental challenges caused by waste management and fossil fuels.

Lignocellulosic biomass has a very complicated chemical structure as it is composed of several types of organic materials. In general, lignocellulosic biomass is composed of three biomacromolecules, Lignin, cellulose, and hemicellulose. In addition, the chemical structure contains minerals and extractives. Each type of biomass has a different percentage of chemicals in the structure [11, 29, 30]. Pyrolysis of cellulose and hemicellulose produce chemicals in the form of liquids and gases or condensable steam. However, the pyrolysis of lignin produces solid char, liquid, and gas. Additionally, the simplicity of extractives to evaporates and decompose

Table 7.4 Production of activated carbon via chemical activation

Biomass	Carbonisation temperature (°C)	Carbonisation time (mins)	Activation agent	Activation temperature (°C)	Activation time (mins)	SBET (m ² ·g ⁻¹)	Refs
Acacia nilotica sawdust	–	–	H ₃ PO ₄	900	60	1,701	[65]
Acacia nilotica	–	–	ZnCl ₂	600	300	403	[66]
Argan nutshell	550	60	NaOH	700	60	798	[67]
Argan nutshell	550	60	H ₃ PO ₄	700	60	1,372	[67]
Apricot stones	–	–	H ₃ PO ₄	400	120	1,382	[60]
Apricot stones	–	–	ZnCl ₂	600	60	1,111	[60]
Azadirachta indica leaves	–	–	ZnCl ₂	800	120	705.4	[68]
Bamboo	–	–	H ₃ PO ₄	600	60	1,335	[69]
Bamboo	–	–	HNO ₃	–	–	295	[70]
Baobab woods	–	–	KOH	400	–	915	[53]
Ceratonia siliqua L. residues	–	–	ZnCl ₂	600	60	1,693	[71]
Cocoa shell	110	24 (h)	ZnCl ₂	500	36	–	[70]
Chestnut oak shells	–	–	H ₃ PO ₄	450	–	989.4	[72]
Chestnut shell	–	–	ZnCl ₂	700	60	173.21	[73]
Date seed	–	–	NaOH	600	60	1,282	[74]
Distillers grain	–	–	KOH	700–900	60–120	1,430	[75]
Dry okra waste	–	–	ZnCl ₂	500	60	1,044	[59]
Euphorbia rigida	25.0	24 (h)	H ₂ SO ₄	850	30	–	[70]

(continued)

Table 7.4 (continued)

Biomass	Carbonisation temperature (°C)	Carbonisation time (mins)	Activation agent	Activation temperature (°C)	Activation time (mins)	S _{BET} (m ² ·g ⁻¹)	Refs
Euryale ferox shell	-	-	H ₃ PO ₄	700	60	2,636	[76]
Eucalyptus bark	-	-	H ₃ PO ₄	500	60	1,239	[69]
Fox nutshell	-	-	H ₃ PO ₄	700	60	2,636	[59]
Mangosteen shell	-	-	K ₂ CO ₃	900	120	1,123	[69]
Nuati woods	-	-	H ₃ PO ₄	400	-	1,660	[53]
Plum stone	400	-	KOH	800	-	2,570	[63]
Pistachio wood wastes	-	-	NH ₄ NO ₃	800	120	1,448	[77]
Pineapple plant leaves	-	-	H ₃ PO ₄	500	60	1,031	[78]
Paper mill sludge	-	-	K ₂ CO ₃	800	150	1,583	[79]
Posidonia oceanica leaves	-	-	ZnCl ₂	600	120	1,483	[69]
Rice straw	-	-	N ₂ H ₉ PO ₄	700	60	1,154	[69]
Ramulus mori	-	-	N ₂ H ₉ PO ₄	800	120	1,061	[69]
Spent mushroom compost	600	60	KOH	500	45	-	[57]
Sewage sludge	-	-	NaOH	700	60	179	[59]
Sewage sludge	-	-	NaOH	700	60	179	[59]
Sunflower oil cake	-	-	H ₂ SO ₄	-	-	241	[70]
Shorea robusta sawdust	-	-	Na ₂ CO ₃	400	180	10.45	[80]
Sunflower seed husks	-	-	ZnCl ₂	500	45	1,511	[81]

(continued)

Table 7.4 (continued)

Biomass	Carbonisation temperature (°C)	Carbonisation time (mins)	Activation agent	Activation temperature (°C)	Activation time (mins)	S _{BET} (m ² ·g ⁻¹)	Refs
Safflower biochar	–	–	ZnCl ₂	900	60	801	[69]
Tomato paste waste	500	60	KOH	500	–	283	[82]
Tea seed shell	–	–	ZnCl ₂	500	60	1,530	[69]
Walnut shell	600	–	ZnCl ₂	700	–	5.95	[83]
Walnut shell	400	–	KOH	800	–	2,305	[63]
Walnut shell	600	–	KOH	700	–	1,239.92	[83]
Waste tea	–	–	C ₂ H ₃ O ₂ K	800	120	854	[69]
Waste sludge and bagasse	800	0.5	HNO ₃	–	–	806.57	[84]
Walnut cake	–	–	H ₃ PO ₄	400	30	–	[85]
Walnut cake	–	–	H ₃ PO ₄	500	60	–	[85]

Table 7.5 Production of activated carbon via physiochemical activation

Biomass	Carbonisation temperature (°C)	Carbonisation time (mins)	Activation agent	Activation temperature (°C)	Activation time (min)	S _{BET} (m ² ·g ⁻¹)	Refs
Acacia nilotica	–	–	H ₃ PO ₄ /N ₂	250	180	–	[86]
Date seeds	–	–	KOH/CO ₂	850	120	763	[58]
Date seeds	600	–	H ₃ PO ₄ /Steam	–	180	1,100	[58]
Date seeds	600	–	HNO ₃ /Steam	–	180	950	[58]
Rambutan seed	–	–	KOH/CO ₂	802	60	–	[57]
Oil palm fronds	–	–	KOH/CO ₂	–	–	1,237.13	[87]
Oil palm shell	–	–	H ₃ PO ₄ /CO ₂	–	–	642	[87]
Oil palm empty fruit bunch	–	–	KOH/CO ₂	–	–	720	[87]
Rice husk	–	–	KOH/CO ₂	800	120	1,836	[88]
Waste sludge	–	–	HCl/CO ₂	800	–	269	[84]
Waste sludge	–	–	KOH/CO ₂	–	–	984	[84]
Pandanus amaryllifolius stem	400	120	KOH/CO ₂	794	~71	–	[57]

also helps in producing liquids and gases. The ashes in the char structure are mainly composed of minerals. To summarise, Table 7.6 shows the components of the biomass with its related products.

The obtained vapors from the primary stage of reaction go through a second stage to produce soot. This soot varies according to the type of pyrolysis, either fast or slow. Catalysts like alkali metals are added to enhance char production. The ignition properties of biochar are directly related to the percentage of minerals [11]. Typically, the cellulosic substrate produces bio-oils when the temperature is around 500 °C [31]. Lignin is mainly used to extract biochar. Hence, biomass substrate with a higher percentage of lignin derivatives is used to obtain char. Table 7.6 contains a list of biomasses with the proportion of hemicellulose, cellulose, and lignin substrate [1, 32–37].

Table 7.6 The distribution of biomass composites [1, 32–37]

Biomass	Cellulose (%)	Hemicellulose (%)	Lignin (%)
Almond shell	50.7	28.9	20.4
Bamboo	26–43	15–26	21–31
Banana waste	13.2	14.8	14
Barley straw	31–37	24–29	14–15
Corn cob	50.5	31	15
Corn stover	28	35	16–21
Cotton seed fibers	80–95	5–20	0
Coastal Bermuda grass	25	35.7	6.4
Hazelnut shell	28.8	30.4	42.9
Jute fiber	45–53	18–21	21–26
Nut shell	25–30	25–30	30–40
Oat straw	31–37	24–29	16–19
Olive husk	24	23.6	48.4
Rice straw	32.1	24	18
Rye straw	33–35	27–30	16–19
Sunflower shell	48.4	34.6	17
Sugarcane bagasse	19–24	32–48	23–32
Silvergrass	24	44	17
Tea waste	30.20	19.9	40
Wood	35–50	20–30	25–30
Walnut shell	25.6	22.7	52.3
Wheat straw	33–40	20–25	15–20

7.4.1 Cellulose

Cellulose is the most abundant organic compound on earth. The basic structure of cellulose is a linear polymer contain six-carbon glucose units. The glucose units are connected together via β -(1–4)-glycosides bonds. Typically, cellulose is insoluble in some solvents due to the connection between glucose units and cellulose polymers. Indeed, the cellulose polymers are arranged and connected parallel to each other. The cellulose connection is influenced by the presence of intermolecular and intramolecular hydrogen bonds among the hydroxide groups (OH) of the cellulose polymer. The cellulose structure has two different terminals, which allow for different reactions at the same structure. One of the cellulose terminals is known as the reducing end group as it consists of the reducing hemiacetal group in position C1. The second terminal is known as a non-reducing group and consists of an extra secondary hydroxyl group in position C4. Biomass with high content of cellulose is typically used to produce biofuel through a thermochemical convention. Therefore, the new approach of studying cellulosic materials involves the modification of chemical structure to produce a high quality biofuel and replace fossil fuel.

7.4.2 Lignin

Lignin is a complex form of organic polymers found in lignocellulosic biomass. Lignin polymers are the core of biomass structure. Lignin consists of phenyl propane building blocks and has a form similar to resin. The structure of lignin consists of hydroxyl group and methoxyl group in para and meta positions, respectively. Moreover, the aromatic rings in the structure are connected via carbon-to-carbon or carbon-to-oxygen bonds. Lignin has a complex structure that contains multiple groups such as carbonyl, hydroxyl, and methoxyl groups. Therefore, lignin has a strong structure and insoluble. The lignin present in biomass at different percentages. On average, biomass may contain 10% to 30% of lignin. Nonetheless, materials such as coconut fibers and husk may consist of 45% of lignin. Additionally, hardwood contains 16–24% of lignin, and softwood composed of 25–31%. Lignin in hardwood is connected with xylans via a covalent bond, whereas softwood is connected to galactoglucommannans. Lignocellulosic biomass with a high percentage of lignin is used to produce carbonaceous solids such as char and activated carbon. Thus, the quality and structure of biomass have a significant impact on the properties of produced activated carbon used for wastewater treatment.

7.4.3 *Hemicellulose*

Hemicellulose (also known as polyose) is a heteropolymer that has a random amorphous structure. Typically, hemicellulose exists along with cellulose in the biomass structure. Hemicellulose structure consists of several monosaccharide units joined together. The primary units of hemicellulose are pentose sugar. In comparison to cellulose, the hemicellulose chain is shorter and unorganized. Thus, hemicellulose has better solubility compared to cellulose. The hemicellulose polymer has two forms, either a homopolymer or a heteropolymer. Homopolymer structure composes of units from a single type of sugar, whereas heteropolymer structure composes of different kinds of sugar units. Hemicellulose acts as an adhesive where it holds the fiber and cellulose in biomass structure.

7.4.4 *The Physiochemical Properties of Lignocellulosic Biomass*

The final obtained products of the biomass conversion process are significantly influenced by the percentage of moisture in biomass which is further affected by the type of biomass feedstock, the design of the reactor, and process parameters [11]. As discussed before, charcoal production involves two steps: the drying and pyrolysis processes. In the primer phase of the drying step, the water contained in the pores structure as free water tends to evaporate and diffuse at a temperature around 110 °C. The higher is the percentage of water, and the more energy is required to evaporate water. Additionally, when the temperature is between 150 and 200 °C, an obvious reduction occurs for the combined water inside the cellulose chain of wood. White smoke of water vaporizes from the charcoal oven chamber during the initial stage of carbonization. Generally, the rate of temperature rise does not rely on the evaporated water because the fast pyrolysis process is effective in drying the feedstock [38]. The existence of moisture in the wood is usually around 15–20% [11]. Moisture content can significantly affect the properties of the production of activated carbon [39]. The differences between the obtained char or liquid are directly connected to the particle size of the biomass matrix. When the particle sizes of the biomass are large, char is mostly formed. However, a secondary char forming reaction is usually required due to the low rate of disintegration caused by the size of the large particles [11]. Hence, to produce more carbon, it is better to use larger particle sizes, while smaller particle sizes are used to increase the percentage of gained liquid during the fast pyrolysis process. Better biochar substrate production is related to the temperature of the pyrolysis and lignin and carbon quantity. Thus, to obtain a better biochar substrate, a higher percentage of lignin and fixed carbon is used while the pyrolysis process occurs at a medium temperature of 500 °C. On the other hand, to obtain more bio-oils and syngas, the proportion of the volatile materials must be high [29]. Precursors such as olive stone, walnut shell, and hazel nutshell are highly selected to

produce biochar because it contains a higher percentage of lignin. Furthermore, materials such as dead wood, cereal straw, and grasses are suitable to produce syngas and bio-oils [40]. Briefly, the physicochemical properties, transformation mechanisms, and composition of lignocellulosic biomass directly impact the type of final products as shown in Fig. 7.6.

7.4.5 The Influential Factors on Activated Carbon Production

(i) Temperature

Controlling the temperature profile is crucial for biomass product optimization because the heating rate, pressure, contact time, and peak temperature between solid and gaseous phases are partially affected by the temperature profile. During the fast pyrolysis, rapid heating and cooling rate are utilized to reduce the duration of secondary reactions. As a result, the product quality will be downgraded, whereas the liquid yield is reduced. Additionally, the obtained product will contain a mixture with high complexity and viscosity [38]. On the contrary, to increase the char yields, the pyrolysis process involves slow heating rates, though; this is not consistent [11]. Increasing the temperature can assure the release of more evaporative fractions, which increase the content of carbon in the biochar. At the same time, hosting the biomass for a long time under high temperatures will significantly reduce the biochar yield. In regard to liquid and gaseous products, the effect of temperature is very complicated. To obtain a higher portion of liquid, the pyrolysis temperature must reach up to 400–550 °C. Moreover, when the temperature is higher than 550 °C, the final products contain fewer liquid percentages due to the decomposition of condensable vapor via secondary reactions. A higher percentage of liquid can be obtained during the fast pyrolysis when the temperature is around 500 °C. Around 28–4% of liquid can be gained during the slow pyrolysis when the temperature is between 377 and 577 °C, and this depending on the type of biomass feedstock [13]. On the other hand, 4.93–45% of the liquid can be obtained at a temperature around 385–450 °C using different cellulose-rich feedstock [19].

(ii) Gas Flow Rate

The influence of the gas flow rate during the pyrolysis process appears on the degree of secondary char formation. Applying a low gas flow rate is preferable during the slow pyrolysis process to form char. Conversely, higher gas flows are applied during the fast pyrolysis to adequately and quickly remove formed vapors. High pressure will increase the formation of secondary char because it increases the activity of vapors at the surface of char particles and within the reactor. On the other hand, conducting pyrolysis under vacuum

produces a higher proportion of liquid and less char. Moisture that exists in the form of vapors can increase carbon production systematically when pyrolysis takes place under pressure. This occurs due to water, which acts as a catalyst and lowers the activation time of pyrolysis reactions [46]. Conspicuously, the gas flow rate affects the thermodynamics of the pyrolysis process. Using a low gas flow rate, the reaction is more exothermic when the pressure is high. The exothermic pyrolysis process assures more char yield. Additionally, these conditions are favorable because the total energy balance of the processes will seek carbon and char as prime products. Generally, to form more char and gain less liquid, it is important to increase the contact between the main generated vapors and hot char surface during the pyrolysis process. This can happen using particles with large size, high pressure, slow heating rate, or low gas flow rate.

7.5 Applications of Activated Carbon for Water Treatment

Activated carbon is used in several industrial and agricultural applications. Primarily, activated carbon is used for air and water filtration. Indeed, the use of activated carbon in water treatment to remove contaminants and pollutants has increased dramatically [89]. It is stated that water purification and filtration consume around 80% of activated carbon worldwide [90]. Activated carbon is widely adopted in the water treatment field due to its unique physical and chemical characteristics. Activated carbon is used mainly as highly efficient adsorbents for several types of contaminants. The high adsorption capacity of activated carbon is directly related to its high surface area and porous structure [91]. Moreover, the surface of activated carbon contains several types of functional groups that interact efficiently with contamination particles in water.

The recent approaches of utilizing activated carbon in water treatments revolve around enhancing the adsorption performance via nanoparticles [92, 93]. Basically, activated carbons are loaded with nanoparticles to produce nanocomposites with high adsorption capacity and high chemical and mechanical stability. Popularly adapted nanoparticles include iron nanoparticles [94], tungsten oxide nanoparticles [95], silver nanoparticles [96], and zero-valent iron nanoparticles [97]. Typically, activated carbon modified with nanoparticles is used to remove metal ions and dyes from contaminated water. However, removing these types of contaminants relies on other factors such as the solution temperature and pH level. Indeed, pH level is considered as a key factor. pH level control both the anionic and cationic nature of the surfaces and the surface charge density. Therefore, a high pH level solution will attract cations, whereas a low pH level will attract anions. In general, the pH level is considered during the synthesis of modified activated carbon. Acidic carbons are preferred to catch cations, while basic carbons are used to remove anions from polluted water [90].

7.5.1 *Elimination of Metallic Contaminants*

Metallic contaminants exist in a high percentage of wastewater. Typically, metallic contaminants present as heavy metals and/or metalloids. Generally, metallic contaminants are extremely dangerous to human health. Moreover, metallic contaminants are subject to biomagnification in plants and animals. Above all, they are non-degradable materials that make the water purification and treatment process difficult and costly. Consuming food or water contaminated with metallic pollutants for the short term may cause several diseases such as diarrhea, fever, and damage to the liver and kidney. However, long-term exposure to metallic contamination via water or food can cause liver cancer, skin cancer and may lead to death. The impact of heavy metals on human health is associated with the long-term accumulation of these materials in the human body [98]. In general, metallic contaminants are introduced to the environment from different agricultural and industrial sources. These sources include activities such as mining, the metal industry, usage of pesticides and fertilizers, and semiconductors manufacturing [99].

In the last decade, removal processes of metallic contaminants from water have developed significantly. New technologies are explicitly designed to eliminate heavy metals and loids from water. However, most of the developed technologies are expensive and have low efficiency compared to activated carbon. Thus, several studies reported the use and development of activated carbon for metallic pollutant removal. Activated carbon is considered a low-cost and highly efficient solution for water contamination [98]. Activated carbon is used to remove metals such as lead (Pb(II)), cadmium (Cd(II)), copper (Cu(II)), chromium (Cr(II)), iron (Fe), and arsenic (As) [100]. Indeed, the elimination process of metallic contaminants from the water via activated carbon is considered a simple process due to the size of metallic contaminants and the properties of activated carbon. Usually, metallic contaminants present in the water as small charged particles. Hence, the interaction between the activated carbon and the metal ions occurs directly (electrostatic interaction) [101]. Similar to other types of contaminants, the adsorption process of metallic pollutants is affected by the pH level of the solution. Moreover, there are other factors that influence the adsorption behavior, such as the structure and size of metal ions, the surface area and porosity of activated carbon, and the functional groups present on the surface of activated carbon [84].

As mentioned before, the type of biomass used to produce activated carbon greatly influences the adsorption of metallic pollutants. Min et al. has conducted a study on the removal of Cd(II) from contaminated water using oil palm shell-activated carbon [57]. Their study revealed that oil palm shell-activated carbon has 99.5% removal efficiency for Cd(II). A similar study is conducted by Ahmed, where he used chemically activated date seeds activated carbon to remove Cd(II) ions from water [58]. His results exhibited a great tendency of date seed activated carbon to adsorb cadmium ions. The reported adsorption capacities were in the range of 118.1–127 mg·g⁻¹. Sajjadi et al. have published a study on the removal of mercury (Hg) from polluted water using chemically activated pistachio wood wastes activated carbon

[77]. The study used ammonium nitrate (NH_4NO_3) as an activation agent for the carbon. The produced activated carbon has a high surface area of about $1,448 \text{ m}^2 \cdot \text{g}^{-1}$. The maximum adsorption capacity was $201.095 \text{ mg} \cdot \text{g}^{-1}$.

Heavy metals are highly toxic metallic elements that have a higher density than other common metals. Indeed, heavy metals exist naturally in many areas and contaminate soil, air, and water. The danger of heavy metals is related to their toxicity, wide distribution, and extensive usage in industrial applications. There are several types of heavy metals such as arsenic (As), lead (Pb), cadmium (Cd), nickel (Ni), mercury (Hg), chromium (Cr), selenium (Se), and cobalt (Co). These heavy metals contaminate the environmental resources at different levels. Generally, the dramatic increase in the concentration of heavy metals is associated with anthropogenic activities such as semiconductor manufacturing, mining, combustion of fossil fuel, and material fabrication.

Heavy metals can be found in natural water resources such as lakes, rivers, and groundwater. In fact, heavy metals such as arsenic can be found at high concentrations in groundwater as it leaks from surrounding soils and rocks. Such a high concentration of heavy metal above the standard level poses health risks. Moreover, in urban areas, the concentration of heavy metals increases in surface water resources, especially rivers. In general, urban areas discharge highly toxic wastes into rivers and coastal regions. The discharged wastes contain several contaminants such as heavy metals, polyaromatic hydrocarbons (PAHs), and polyfluoroalkyl substances (PFAS).

Primarily, heavy metals are removed from water using different types of adsorbents. Nonetheless, other methods such as membrane filtration and reverse osmosis are used to remove certain types of heavy metals. Generally, removing heavy metals from contaminated water using adsorbents is the most preferred treatment approach. Among the different types of adsorbents, activated carbon has exhibited an outstanding performance in removing highly toxic heavy metals such as arsenic, lead, and mercury. Activated carbon has special physical and chemical properties that make it suitable for wastewater treatment. Briefly, activated carbon is inexpensive, environmentally friendly, easy to regenerate, and has high adsorption capacity. Typically, activated carbon is used to eliminate arsenic and lead from water and wastewater. Arsenic and lead are used intensively in manufacturing and can spread quickly in the environment.

7.5.2 Elimination of Non-Metallic Contaminants

The threat of non-metallic contaminants on human health has been observed in the last few years. Similar to metal ions, anions as non-metallic contaminants are considered essential elements to human bodies. Nonetheless, excessive consumption of non-metallic pollutants can cause diseases and lead to death. Molybdate, phosphate, and fluoride are the most popular types of anions consumed by humans. These anions are detrimental not only to humans but also to other living species. Globally, millions of people have consumed excessive fluorosis and suffered from fluorosis

[102]. Typically, people consume fluoride through contaminated water, especially in developing countries. Indeed, fluoride is used in some water treatment plants as part of the process in controllable percentages. However, in some developing countries, fluorides are used in excessive amount due to the lack of monitoring and regulations. Viswanathan et al. have published a study on the impact of fluoride ions on human health [103]. In the study, they measured the level of fluoride ions in drinking water. The level of fluoride ion was 3.24 ppm, and children are the most affected with fluorosis. Like fluorides, molybdate ions can accumulate in humans and animals and cause severe diseases [104]. Anions can be removed easily via activated carbon. The removal of anions is influenced by the type of activated carbons and the pH value of the solution.

7.5.3 *Elimination of Various Dyes from Water*

In the last decades, the rapid development in the industrial sectors caused severe damage to the environment via introducing new types of complex contaminants. Dyes are one of the most extensively used materials in several industries such as textiles, papers, cosmetics, and paint production. Indeed, the textile industry is considered the major source of water contamination in several areas [105]. It is estimated that there are around 3,600 types of dyes in the industries, where 2–20% are typically discharged directly into the environment [106, 107]. Dyes discharged into the natural water resources are highly toxic and deadly. Regarding the environmental effects, the presence of dyes can reduce the photosynthesis process of the aquatic flora and fauna [89].

Several studies have proposed activated carbon as a great solution to remove different types of dyes from water. The adsorption of dyes is directly influenced by the types and properties of activated carbon, such as the porosity and high surface area, the functional groups. Besides that, the solubility and molecular size of dyes and the pH level of the aquatic medium affect the adsorption behavior [108]. Katheresan et al. stated that pretreating and activating carbon via steam could produce activated carbon with a high tendency to adsorb dye [109]. Further studies have revealed the great performance of activated carbon prepared from *Acacia Mangium* and *Acacia Nilotica* in removing different types of dyes such as Methyl orange (90.5%) and Methylene blue ($250 \text{ mg}\cdot\text{g}^{-1}$) [66, 110].

Methylene Blue (MB) is considered the most popular among the different types of dyes. In fact, MB present in wastewater at high percentages. Wang et al. have published a study on the removal of MB using activated carbon [111]. The study used potassium hydroxide (KOH) as an activation agent. The analytical data showed that activated carbon has a surface area of $1,430 \text{ m}^2\cdot\text{g}^{-1}$. Moreover, the obtained adsorption capacity was $934.579 \text{ mg}\cdot\text{g}^{-1}$ at pH 5.8. Further study has been published by Ahmed on the removal of MB via rice straw and *Ramulus mori*-based activated carbon [112]. The study involved the use of diammonium phosphate ($\text{N}_2\text{H}_9\text{PO}_4$) as

an activation agent. The adsorption capacities of both rice straw-based and *Ramulus mori*-based activated carbon was 129.5 and 1,061 mg·g⁻¹, respectively.

7.5.4 Elimination of Phenolic Compounds

Phenolic compounds are highly toxic chemicals that can affect the ecosystem for decades. Usually, phenolic compounds are discharged into the environmental system through chemicals and petrochemical industries [113]. The impact of phenolic compounds is monitored by the environmental protection agencies. Phenolic compounds are carcinogenic and can destroy the aquatic ecosystem [114]. Different standards are made to limit the amount of phenolic compounds in water bodies [115]. For instance, the Environmental Protection Agency (EPA) has limited the amount of phenolic pollutants to 0.1 mg·L⁻¹ at maximum. However, the World health organization (WHO) has made the acceptable standard lower to 0.001 mg·L⁻¹ for drinkable water [115]. Activated carbon has shown an outstanding performance in removing phenolic compounds from contaminated water. The removal of phenol via activated carbon relies mainly on surface functionality. Therefore, the presence of functional groups such as carboxyl and hydroxyl on the activated carbon surface will increase the adsorption of the phenolic compounds. The interaction between the activated carbon and phenol is directed by pi-pi bond [116]. Besides the surface functionality, the pH level of the solution has a significant impact on the removal of phenolic compounds from water. Indeed, the adsorption performance decrease for both high and low pH values [117].

7.5.5 Elimination of Pesticides

Recently, pesticides are used intensively in agricultural fields to eliminate pests and several plant diseases. However, the intensive use of pesticides has formed global environmental threats. Pesticides can leak from the agricultural fields to the surrounding water resources. As a result, the contamination level of the natural water resources increases and destroys the ecosystem. The most commonly used pesticides include. 2,4-dichlorophenoxyacetic acid, carbofuran, and bentazon. Generally, the environmental protection agencies have set a permissible concentration of these pesticides to 0.1, 0.05, and 0.09 mg·L⁻¹ for 2,4-dichlorophenoxyacetic acid, bentazon, and carbofuran, respectively [118]. Typically, pesticides are removed from water via highly efficient activated carbon. The removal process relies on the presence of organic matter and the flow rate in the adsorption [108].

7.5.6 *Elimination of Pharmaceutical Contaminants*

Recently, pharmaceutical contaminants have been introduced in the ecosystem due to the increase in the usage of medical products. Pharmaceutical contaminants involve the waste and the byproducts of pharmaceutical products discharged into the environment. The pharmaceutical compounds are difficult to remove due to their high stability and hydrophilicity. Thus, they can present in water bodies for a long time. Although the concentration of pharmaceutical contaminants is considered low, the longtime exposure to contaminated water via drinking can cause severe diseases [119–121]. Activated carbon is used as an adsorbent for different types of pharmaceutical compounds [119]. Indeed, the adsorption of pharmaceutical compounds via activated carbon relies on operational conditions, type of precursor, activation method, and the properties of a pharmaceutical compound. The operational conditions involve the pH level of the solution, temperature, organic structure, adsorbent (activated carbon) dose, and ionic capability [122].

7.6 Conclusions

In summary, the production of value-added products using proper biomass feedstock requires more studies and experiments to enhance the overall technology. There is a crucial need for more experiments on the consistency of pyrolysis reactions to be used in large-scale applications and become more sustainable. Moreover, the relation between the general operation of the pyrolysis plant and the applied feedstock or precursors must be more evident. Nevertheless, the fundamentals of pyrolysis technology have been covered elaborately in this chapter to specify the influential factors on the process performance. This includes different factors to design the process and obtain a preferred product, such as an activated carbon with high adsorption performance for wastewater. The major influential factors involve the selection of conditional parameters for the pyrolysis process, types of reactors, and the type of lignocellulosic biomass.

The suggestions for future studies on the thermochemical conversion of biomass include the improvement of the biochar separation process to enhance the quality of biofuels and activated carbon production. Moreover, the type of selected biomass is considered a vital factor in the process. Lignocellulosic biomass with a high portion of cellulose is preferred to obtain a maximum bio-oil yield. On the other hand, lignin-based biomass can be used to obtain biochar. Apart from activated carbon production, there are few studies on the enhancement of gas production from biomass precursors. Hence, there is a crucial need for sophisticated studies on the development of gaseous products via metal catalysts. Several methods can be utilized for the kinetics of the pyrolysis of biomass. Initially, to obtain char and gas, lower activation energy is used by applying a low temperature. On the other hand, applying higher temperature results in higher activation energy and produces condensable fumes, liquid aerosols,

and oils. However, heating biomass quickly at a proper high temperature will lead to obtaining a high percentage of liquid fuels. For fast biomass heating, it is preferable to use smaller particle sizes of precursors to initiate constant particle heating. The pyrolysis processes require more development from the environmental and economic aspects. As a result, the cost of biomass products will become competitive with conventional products. In addition, maximizing the activated carbon production is also related to the quality of pyrolysis reactors. Attention must be drawn towards the pyrolysis efficiency, physicochemical properties of the biochar, carbon and slag deposition, and emission of microparticles during the pyrolysis process. Presently, activated carbon exhibited a great performance in treating wastewater at an industrial scale as an alternative to metal oxides and membrane polymers. However, the need for development in activated carbon production is continuous as novel contaminants become more challenging to remove from wastewater.

Acknowledgements Authors are grateful to the University Malaya, Malaysia for the financial support (Grant IF 065-2021 and IF 073-2019).

References

1. Xu L, Xiu Y, Liu F, Liang Y, Wang S (2020) Research progress in conversion of CO₂ to valuable fuels. *Molecules* 25(16):3653. <https://doi.org/10.3390/molecules25163653>
2. Xia C, Cai L, Zhang H, Zuo L, Shi SQ, Lam SS (2021) A review on the modeling and validation of biomass pyrolysis with a focus on product yield and composition. *Biofuel Res J* 8(1):1296–1315. <https://doi.org/10.18331/brj2021.8.1.2>
3. Słasiak J, Szkodo M (2020) Thermochemical conversion of biomass and municipal waste into useful energy using advanced HiTAG/HiTSG technology. *Energies* 13(16):4218. <https://doi.org/10.3390/en13164218>
4. Idriss IM, Ahmed MM, Grema AS, Baba D (2017) Modeling and simulation of pyrolysis process for a beech wood material. *Arid Zone J Eng* 13(6):710–717
5. Saif AGH, Wahid SS, Ali MR (2020) Pyrolysis of sugarcane bagasse: the effects of process parameters on the product yields. *Mater Sci Forum* 1008:159–167. <https://doi.org/10.4028/www.scientific.net/msf.1008.159>
6. Papari S, Hawboldt K (2015) A review on the pyrolysis of woody biomass to bio-oil: focus on kinetic models. *Renew Sustain Energy Rev* 52:1580–1595. <https://doi.org/10.1016/j.rser.2015.07.191>
7. Januszewicz K, Kazimierski P, Klein M, Kardaś D, Łuczak J (2020) Activated carbon produced by pyrolysis of waste wood and straw for potential wastewater adsorption. *Materials* 13(9):2047. <https://doi.org/10.3390/ma13092047>
8. Aqsha A, Tijani MM, Moghtaderi B, Mahinpey N (2017) Catalytic pyrolysis of straw biomasses (wheat, flax, oat and barley) and the comparison of their product yields. *J Anal Appl Pyrol* 125:201–208. <https://doi.org/10.1016/j.jaap.2017.03.022>
9. Mulimani HV (2017) Production of solid fuel biochar from de-oiled seed cake by pyrolysis. *IOSR J Mech Civ Eng* 14(02):57–61. <https://doi.org/10.9790/1684-1402035761>
10. Sipra AT, Gao N, Sarwar H (2018) Municipal solid waste (MSW) pyrolysis for bio-fuel production: a review of effects of MSW components and catalysts. *Fuel Process Technol* 175:131–147. <https://doi.org/10.1016/j.fuproc.2018.02.012>

11. Świechowski K, Syguła E, Koziel JA, Stępień P, Kugler S, Manczarski P, Białowiec A (2020) Low-temperature pyrolysis of municipal solid waste components and refuse-derived fuel—process efficiency and fuel properties of carbonized solid fuel. *Data* 5(2):48. <https://doi.org/10.3390/data5020048>
12. Lofrano G, Brown J (2010) Wastewater management through the ages: a history of mankind. *Sci Total Environ* 408(22):5254–5264. <https://doi.org/10.1016/j.scitotenv.2010.07.062>
13. Parkash V, Singh S (2020) A review on potential plant-based water stress indicators for vegetable crops. *Sustainability* 12(10):3945. <https://doi.org/10.3390/su12103945>
14. Panwar NL, Paul AS (2020) An overview of recent development in bio-oil upgrading and separation techniques. *Environ Eng Res* 26(5):200382–0. <https://doi.org/10.4491/eer.2020.382>
15. Mizik T, Gyarmati G (2021) Economic and sustainability of biodiesel production—a systematic literature review. *Clean Technol* 3(1):19–36. <https://doi.org/10.3390/cleantechnol3010002>
16. Popp J, Kot S, Lakner Z, Oláh J (2018) Biofuel use: peculiarities and implications. *J Secur Sustain Issues* 7(3). [https://doi.org/10.9770/jssi.2018.7.3\(9\)](https://doi.org/10.9770/jssi.2018.7.3(9))
17. Sarkar JK, Wang Q (2020) Different pyrolysis process conditions of south asian waste coconut shell and characterization of gas, bio-char, and bio-oil. *Energies* 13(8):1970. <https://doi.org/10.3390/en13081970>
18. Pawar A, Panwar NL, Salvi BL (2020) Comprehensive review on pyrolytic oil production, upgrading and its utilization. *J Mater Cycles Waste Manage* 22(6):1712–1722. <https://doi.org/10.1007/s10163-020-01063-w>
19. Jahiril M, Rasul M, Chowdhury A, Ashwath N (2012) Biofuels production through biomass pyrolysis —a technological review. *Energies* 5(12):4952–5001. <https://doi.org/10.3390/en5124952>
20. Xu Z, Xiao X, Fang P, Ye L, Huang J, Wu H, Tang Z, Chen D (2020) Comparison of combustion and pyrolysis behavior of the peanut shells in air and N₂: kinetics thermodynamics and gas emissions. *Sustainability* 12(2):464. <https://doi.org/10.3390/su12020464>
21. Tanneberger T, Schimek S, Paschreit CO, Stathopoulos P (2019) Combustion efficiency measurements and burner characterization in a hydrogen-oxyfuel combustor. *Int J Hydrogen Energy* 44(56):29752–29764. <https://doi.org/10.1016/j.ijhydene.2019.05.055>
22. Chunbao X, Baoqiang L, Shushen P, Madhumita BR, Mohammad ST (2018) 1.19 Biomass energy, vol 19, 1st edn. Elsevier Inc., pp 770–794. <https://doi.org/10.1016/B978-0-12-809597-3.00121-8>
23. Gvero P, Papuga S, Mujanic I, Vaskovic S (2016) Pyrolysis as a key process in biomass combustion and thermochemical conversion. *Therm Sci* 20(4):1209–1222. <https://doi.org/10.2298/tsci151129154g>
24. Gądek W, Mlonka-Mędrala M, Prestipino M, Evangelopoulos P, Kalisz S, Yang W (2016) Gasification and pyrolysis of different biomasses in lab scale system: a comparative study. In: *E3S Web of Conferences*, vol 10, 00024. <https://doi.org/10.1051/e3sconf/20161000024>
25. Jayaraman K, Gökalp I (2015) Pyrolysis, combustion and gasification characteristics of miscanthus and sewage sludge. *Energy Convers Manage* 89:83–91. <https://doi.org/10.1016/j.enconman.2014.09.058>
26. Chowdhury Z, Krishnan B, Sagadevan S, Rafique R, Hamizi N, Abdul Wahab Y, Khan A, Johan R, Al-douri Y, Kazi S, Tawab Shah S (2018) Effect of temperature on the physical, electro-chemical and adsorption properties of carbon micro-spheres using hydrothermal carbonization process. *Nanomaterials* 8(8):597. <https://doi.org/10.3390/nano8080597>
27. Montoya Arbeláez JI, Chejne Janna F, Garcia-Pérez M (2015) Fast pyrolysis of biomass: a review of relevant aspects. Part I: parametric study. *DYNA* 82(192):239–248. <https://doi.org/10.15446/dyna.v82n192.44701>
28. Panchasara H, Ashwath N (2021) Effects of pyrolysis bio-oils on fuel atomisation—a review. *Energies* 14(4):794. <https://doi.org/10.3390/en14040794>
29. Fogarassy C, Toth L, Czikkely M, Finger DC (2019) Improving the efficiency of pyrolysis and increasing the quality of gas production through optimization of prototype systems. *Resources* 8(4):182. <https://doi.org/10.3390/resources8040182>

30. Álvarez-Chávez BJ, Godbout S, Le Roux T, Palacios JH, Raghavan V (2019) Bio-oil yield and quality enhancement through fast pyrolysis and fractional condensation concepts. *Biofuel Res J* 6(4):1054–1064. <https://doi.org/10.18331/brj2019.6.4.2>
31. Dellarose Boer F, Valette J, Commandre JM, Thevenon MF (2021) Slow pyrolysis of sugarcane bagasse for the production of char and the potential of its by-product for wood protection. *J Renew Mater* 9(1):97–117. <https://doi.org/10.32604/jrm.2021.013147>
32. Varma AK, Shankar R, Mondal P (2012) A review on pyrolysis of biomass and the impacts of operating conditions on product yield, quality, and upgradation. Springer, pp 227–259. https://doi.org/10.1007/978-981-13-1307-3_10
33. David E (2020) Evaluation of hydrogen yield evolution in gaseous fraction and biochar structure resulting from walnut shells pyrolysis. *Energies* 13(23):6359. <https://doi.org/10.3390/en13236359>
34. Williams CL, Emerson RM, Tumuluru JK (2017) Biomass compositional analysis for conversion to renewable fuels and chemicals. *Energy Convers Manage*. <https://doi.org/10.5772/65777>
35. Clauser NM, González G, Mendieta CM, Kruyeniski J, Area MC, Vallejos ME (2021) Biomass waste as sustainable raw material for energy and fuels. *Sustainability* 13(2):794. <https://doi.org/10.3390/su13020794>
36. Zhang S, Yang X, Zhang H, Chu C, Zheng K, Ju M, Liu L (2019) Liquefaction of biomass and upgrading of bio-oil: a review. *Molecules* 24(12):2250. <https://doi.org/10.3390/molecules24122250>
37. Fahmi R, Bridgwater A, Donnison I, Yates N, Jones J (2008) The effect of lignin and inorganic species in biomass on pyrolysis oil yields, quality and stability. *Fuel* 87(7):1230–1240. <https://doi.org/10.1016/j.fuel.2007.07.026>
38. Demirbas A (2004) Current technologies for the thermo-conversion of biomass into fuels and chemicals. *Energy Sources* 26(8):715–730. <https://doi.org/10.1080/00908310490445562>
39. Demirbaş A (1997) Calculation of higher heating values of biomass fuels. *Fuel* 76(5):431–434. [https://doi.org/10.1016/s0016-2361\(97\)85520-2](https://doi.org/10.1016/s0016-2361(97)85520-2)
40. Bridgwater A (2000) Fast pyrolysis processes for biomass. *Renew Sustain Energy Rev* 4(1):1–73. [https://doi.org/10.1016/s1364-0321\(99\)00007-6](https://doi.org/10.1016/s1364-0321(99)00007-6)
41. Zanzi R, Bai X, Capdevila P, Bjornbom E (2001) Pyrolysis of biomass in the presence of steam for preparation of activated carbon, liquid and gaseous products. In: 6th World Congress of Chemical Engineering, pp 23–27
42. Friedl A, Padouvas E, Rotter H, Varmuza K (2005) Prediction of heating values of biomass fuel from elemental composition. *Anal Chim Acta* 544(1–2):191–198. <https://doi.org/10.1016/j.aca.2005.01.041>
43. Chen X, Zhang R, Zhao B, Fan G, Li H, Xu X, Zhang M (2020) Preparation of porous biochars by the co-pyrolysis of municipal sewage sludge and hazelnut shells and the mechanism of the nano-zinc oxide composite and Cu(II) adsorption kinetics. *Sustainability* 12(20):8668. <https://doi.org/10.3390/su12208668>
44. Román S, Libra J, Berge N, Sabio E, Ro K, Li L, Ledesma B, Álvarez A, Bae S (2018) Hydrothermal carbonization: modeling, final properties design and applications: a review. *Energies* 11(1):216. <https://doi.org/10.3390/en11010216>
45. Hagemann N, Spokas K, Schmidt HP, Kägi R, Böhler M, Bucheli T (2018) Activated carbon, biochar and charcoal: linkages and synergies across pyrogenic carbon's ABCs. *Water* 10(2):182. <https://doi.org/10.3390/w10020182>
46. Basu P (2013) Biomass gasification, pyrolysis, and torrefaction practical design and theory, 2nd edn. Elsevier Inc. <https://doi.org/10.1017/CBO9781107415324.004>
47. Inagaki M, Kang F (2014) Materials science and engineering of carbon fundamentals, 2nd edn. Elsevier Ltd. <https://doi.org/10.16309/j.cnki.issn.1007-1776.2003.03.004>
48. Heidarinejad Z, Dehghani MH, Heidari M, Javedan G, Ali I, Sillanpää M (2020) Methods for preparation and activation of activated carbon: a review. *Environ Chem Lett* 18(2). <https://doi.org/10.1007/s10311-019-00955-0>

49. Pallarés J, González-Cencerrado A, Arauzo I (2018) Production and characterization of activated carbon from barley straw by physical activation with carbon dioxide and steam. *Biomass Bioenerg* 115:64–73. <https://doi.org/10.1016/j.biombioe.2018.04.015>
50. Wang B, Zhu C, Zhang Z, Zhang W, Chen X, Sun N, Wei W, Sun Y, Ji H (2016) Facile, low-cost, and sustainable preparation of hierarchical porous carbons from ion exchange resin: An improved potassium activation strategy. *Fuel* 179:274–280. <https://doi.org/10.1016/j.fuel.2016.03.088>
51. Largette L, Brudey T, Tant T, Dumesnil PC, Lodewyckx P (2016) Comparison of the adsorption of lead by activated carbons from three lignocellulosic precursors. *Microporous Mesoporous Mater* 219:265–275. <https://doi.org/10.1016/j.micromeso.2015.07.005>
52. Dong L, Liu W, Yu Y, Hou L, Gu P, Chen G (2019) Preparation, characterization, and application of macroporous activated carbon (MAC) suitable for the BAC water treatment process. *Sci Total Environ* 647:1359–1367. <https://doi.org/10.1016/j.scitotenv.2018.07.280>
53. Tchikuala EF, Mourao PAM, Nabais JMV (2017) Removal of phenol by adsorption on activated carbon from aqueous solution. *Wastes: Solutions, Treatments and Opportunities*. Faculty of Engineering of the University of Porto, Porto, Portugal, pp 1–3
54. Tsoncheva T, Mileva A, Tsyntsarski B, Paneva D, Spassova I, Kovacheva D, Petrov N (2018) Activated carbon from Bulgarian peach stones as a support of catalysts for methanol decomposition. *Biomass Bioenerg* 109:135–146. <https://doi.org/10.1016/j.biombioe.2017.12.022>
55. Zhang H, Gao Z, Liu Y, Ran C, Mao X, Kang Q, Ao W, Fu J, Li J, Liu G, Dai J (2018) Microwave-assisted pyrolysis of textile dyeing sludge, and migration and distribution of heavy metals. *J Hazard Mater* 355:128–135. <https://doi.org/10.1016/j.jhazmat.2018.04.080>
56. Li L, Sato Y, Shimizu T (2015) Promoting effect of PKS ash on activated carbon preparation from cypress Sawdust Liuyun. *Int Proc Chem, Biol Environ Eng* 51:139–142. <https://doi.org/10.7763/IPC>
57. Min HS, Abbas M, Kanthasamy R, Abdul Aziz H, Tay CC (2017) Activated Carbon: Prepared From Various Precursors. Ideal International E - Publication Pvt Ltd
58. Ahmed MJ (2016) Preparation of activated carbons from date (*Phoenix dactylifera* L.) palm stones and application for wastewater treatments: review. *Process Saf Environ Prot* 102:168–182. <https://doi.org/10.1016/j.psep.2016.03.010>
59. Menya E, Olupot P, Storz H, Lubwama M, Kiros Y (2018) Production and performance of activated carbon from rice husks for removal of natural organic matter from water: a review. *Chem Eng Res Des* 129:271–296. <https://doi.org/10.1016/j.cherd.2017.11.008>
60. Kecira Z, Benturki A, Daoud M, Benturki O (2018) Effect of chemical activation on the surface properties of apricot stones based activated carbons and its adsorptive properties toward aniline. In: *Proceedings of the third international symposium on materials and sustainable development*. Springer International Publishing, Springer Nature Switzerland AG, pp 228–240. https://doi.org/10.1007/978-3-319-89707-3_27
61. Rashidi NA, Yusup S (2017) A review on recent technological advancement in the activated carbon production from oil palm wastes. *Chem Eng J* 314:277–290. <https://doi.org/10.1016/j.cej.2016.11.059>
62. Niksiar A, Nasernejad B (2017) Activated carbon preparation from pistachio shell pyrolysis and gasification in a spouted bed reactor. *Biomass Bioenerg* 106:43–50. <https://doi.org/10.1016/j.biombioe.2017.08.017>
63. Jeguirim M, Belhachemi M, Limousy L, Bennici S (2018) Adsorption/reduction of nitrogen dioxide on activated carbons: textural properties versus surface chemistry—a review. *Chem Eng J Biochem Eng J* 347:493–504. <https://doi.org/10.1016/j.cej.2018.04.063>
64. Ogungbenro AE, Quang DV, Al-Ali K, Abu-Zahra MRM (2017) Activated carbon from date seeds for CO₂ capture applications. *Energy Procedia* 114:2313–2321. <https://doi.org/10.1016/j.egypro.2017.03.1370>
65. Gupta TB, Lataye DH (2017) Adsorption of indigo carmine dye onto *Acacia nilotica* (babool) sawdust activated carbon. *J Hazard Toxic Radioact Waste* 21(4):04017013. [https://doi.org/10.1061/\(ASCE\)HZ.2153-5515.0000365](https://doi.org/10.1061/(ASCE)HZ.2153-5515.0000365)

66. Dass B, Jha P (2015) Batch adsorption of phenol by improved activated *Acacia nilotica* branches char: equilibrium, kinetic and thermodynamic studies. *Int J ChemTech Res* 8:269–279
67. Zbair M, Ainassaari K, Drif A, Ojala S, Bottlinger M, Pirilä M, Keiski RL, Bensitel M, Brahm R (2017) Toward new benchmark adsorbents: preparation and characterization of activated carbon from argan nut shell for bisphenol A removal. *Environ Sci Pollut Res* 25(2):1869–1882. <https://doi.org/10.1007/s11356-017-0634-6>
68. Ahmed S, Parvaz M, Johari R, Rafat M (2018) Studies on activated carbon derived from neem (*Azadirachta indica*) bio-waste, and its application as supercapacitor electrode. *Mater Res Express* 5(4):045601. <https://doi.org/10.1088/2053-1591/aab924>
69. Ahmed MJ (2016) Application of agricultural based activated carbons by microwave and conventional activations for basic dye adsorption. *J Environ Chem Eng* 4(1):89–99. <https://doi.org/10.1016/j.jece.2015.10.027>
70. Din MI, Ashraf S, Intisar A (2017) Comparative study of different activation treatments for the preparation of activated carbon: a mini-review. *Sci Prog* 100(3):299–312. <https://doi.org/10.3184/003685017x14967570531606>
71. Saygılı H, Guzel F (2018) Novel and sustainable precursor for high-quality activated carbon preparation by conventional pyrolysis: optimization of produce conditions and feasibility in adsorption studies. *Adv Powder Technol* 29(3):726–736. <https://doi.org/10.1016/j.apt.2017.12.014>
72. Niazi L, Lashanizadegan A, Sharififard H (2018) Chestnut oak shells activated carbon: Preparation, characterization and application for Cr (VI) removal from dilute aqueous solutions. *J Clean Prod* 185:554–561. <https://doi.org/10.1016/j.jclepro.2018.03.026>
73. Altıntig E, Onaran M, Sari A, Altundag H, Tuzen M (2018) Preparation, characterization and evaluation of bio-based magnetic activated carbon for effective adsorption of malachite green from aqueous solution. *Mater Chem Phys* 220:313–321. <https://doi.org/10.1016/j.matchemphys.2018.05.077>
74. Islam MA, Tan IAW, Benhouria A, Asif M, Hameed BH (2015) Mesoporous and adsorptive properties of palm date seed activated carbon prepared via sequential hydrothermal carbonization and sodium hydroxide activation. *Chem Eng J Biochem Eng J* 270:187–195
75. Wang H, Xie R, Zhang J, Zhao J (2018) Preparation and characterization of distillers' grain based activated carbon as low cost methylene blue adsorbent: mass transfer and equilibrium modelling. *Adv Powder Technol* 29(1):27–35. <https://doi.org/10.1016/j.apt.2017.09.027>
76. Kumar A, Jena HM (2016) Preparation and characterization of high surface area activated carbon from Fox nut (*Euryale ferox*) shell by chemical activation with H₃PO₄. *Results Phys* 6:651–658. <https://doi.org/10.1016/j.rinp.2016.09.012>
77. Sajjadi SA, Mohammadzadeh A, Tran HN, Anastopoulos I, Dotto GL, Lopičić ZR, Sivamani S, Rahmani-Sani A, Ivanets A, Hosseini-Bandegharai A (2018) Efficient mercury removal from wastewater by pistachio wood wastes-derived activated carbon prepared by chemical activation using a novel activating agent. *J Environ Manage* 223:1001–1009. <https://doi.org/10.1016/j.jenvman.2018.06.077>
78. Beltrame KK, Cazetta AL, de Souza PSC, Spessato L, Silva TL, Almeida VC (2018) Adsorption of caffeine on mesoporous activated carbon fibers prepared from pineapple plant leaves. *Ecotoxicol Environ Saf* 147:64–71. <https://doi.org/10.1016/j.ecoenv.2017.08.034>
79. Jaria G, Silva CP, Oliveira JA, Santos SM, Gil MV, Otero M, Calisto V, Esteves VI (2019) Production of highly efficient activated carbons from industrial wastes for the removal of pharmaceuticals from water—a full factorial design. *J Hazard Mater* 370:212–218. <https://doi.org/10.1016/j.jhazmat.2018.02.053>
80. Shrestha D, Gyawali G, Rajbhandari AR (2009) Preparation and characterization of activated carbon from waste sawdust from saw mill. *J Hazard Mater* 165:481–485. <https://doi.org/10.1016/j.jhazmat.2008.10.011>
81. Tsoncheva T, Mileva A, Tsyntsarski B, Paneva D, Spassova I, Kovacheva D, Velinov N, Karashanova D, Georgieva B, Petrov N (2018) Activated carbon from Bulgarian peach stones as a support of catalysts for methanol decomposition. *Biomass Bioenerg* 109:135–146. <https://doi.org/10.1016/j.biombioe.2017.12.022>

82. Ozbay N, Yargic AS (2016) Comparison of surface and structural properties of carbonaceous materials prepared by chemical activation of tomato paste waste: the effects of activator type and impregnation ratio. *J Appl Chem* 2016:1–10. <https://doi.org/10.1155/2016/8236238>
83. Li K, Ruan H, Ning P, Wang C, Sun X, Song X, Han S (2018) Preparation of walnut shell-based activated carbon and its properties for simultaneous removal of H₂S, COS and CS₂ from yellow phosphorus tail gas at low temperature. *Res Chem Intermed* 44(2):1209–1233. <https://doi.org/10.1007/s11164-017-3162-6>
84. Bian Y, Yuan Q, Zhu G, Ren B, Hursthouse A, Zhang P (2018) Recycling of waste sludge: preparation and application of sludge-based activated carbon. *Int J Polym Sci* 2018:1–17. <https://doi.org/10.1155/2018/8320609>
85. Maguana Y, El E, N., Bouchdoug, M., & Benchanaa, M. (2018) Study of the influence of some factors on the preparation of activated carbon from walnut cake using the fractional factorial design. *J Environ Chem Eng* 6(1):1093–1099. <https://doi.org/10.1016/j.jece.2018.01.023>
86. Amin MT, Alazba AA (2017) Comparative study of the absorptive potential of raw and activated carbon *Acacia nilotica* for Reactive Black 5 dye. *Environ Earth Sci* 76:581. <https://doi.org/10.1007/s12665-017-6927-8>
87. Rashidi NA, Yusup S (2017) A review on recent technological advancement in the activated carbon production from oil palm wastes. *Chem Eng J Biochem Eng J* 314:277–290. <https://doi.org/10.1016/j.cej.2016.11.059>
88. Shen Y, Fu Y (2018) KOH-activated rice husk char via CO₂ pyrolysis for phenol adsorption. *Materials Today Energy* 9:397–405. <https://doi.org/10.1016/j.mtener.2018.07.005>
89. Wong S, Ngadi N, Inuwa IM, Hassan O (2018) Recent advances in applications of activated carbon from biowaste for wastewater treatment: A short review. *J Clean Prod* 175:361–375. <https://doi.org/10.1016/j.jclepro.2017.12.059>
90. Rivera-Utrilla J, Sánchez-Polo M, Ferro-García MN, Prados-Joya G, Ocampo-Pérez R (2013) Pharmaceuticals as emerging contaminants and their removal from water. A review. *Chemosphere* 93(7):1268–1287. <https://doi.org/10.1016/j.chemosphere.2013.07.059>
91. Briones R, Serrano L, Younes RB, Mondragon I, Labidi J (2011) Polyol production by chemical modification of date seeds. *Ind Crops Prod* 34(1):1035–1040. <https://doi.org/10.1016/j.indcrop.2011.03.012>
92. Fu X, Yang H, Lu G, Tu Y, Wu J (2015) Improved performance of surface functionalized TiO₂/activated carbon for adsorption–photocatalytic reduction of Cr(VI) in aqueous solution. *Mater Sci Semicond Process* 39:362–370. <https://doi.org/10.1016/j.mssp.2015.05.034>
93. Jamshidi M, Ghaedi M, Dashlian K, Ghaedi A, Hajati S, Goudarzi A, Alipanahpour E (2016) Highly efficient simultaneous ultrasonic assisted adsorption of brilliant green and eosin B onto ZnS nanoparticles loaded activated carbon: artificial neural network modeling and central composite design optimization. *Spectrochim Acta Part A Mol Biomol Spectrosc* 153:257–267. <https://doi.org/10.1016/j.saa.2015.08.024>
94. Sahu UK, Sahu S, Mahapatra SS, Patel RK (2017) Cigarette soot activated carbon modified with Fe₃O₄ nanoparticles as an effective adsorbent for As(III) and As(V): material preparation, characterization and adsorption mechanism study. *J Mol Liq* 243:395–405. <https://doi.org/10.1016/j.molliq.2017.08.055>
95. Anfar Z, Zbair M, Ahsaine HA, Ezahri M, Alem NE (2018) Well-designed WO₃/Activated carbon composite for Rhodamine B Removal: synthesis, characterization, and modeling using response surface methodology. *Fullers Nanotub Carbon Nanostruct* 26(6):389–397. <https://doi.org/10.1080/1536383x.2018.1440386>
96. Tuan TQ, Son NV, Dung HTK, Luong NH, Thuy BT, Anh NTV, Hoa ND, Hai NH (2011) Preparation and properties of silver nanoparticles loaded in activated carbon for biological and environmental applications. *J Hazard Mater* 192(3):1321–1329. <https://doi.org/10.1016/j.jhazmat.2011.06.044>
97. Khosravi R, Moussavi G, Ghaneian MT, Ehrampoush MH, Barikbin B, Ebrahimi AA, Sharifzadeh G (2018) Chromium adsorption from aqueous solution using novel green nanocomposite: Adsorbent characterization, isotherm, kinetic and thermodynamic investigation. *J Mol Liq* 256:163–174. <https://doi.org/10.1016/j.molliq.2018.02.033>

98. Burakov AE, Galunin EV, Burakova IV, Kucherova AE, Agarwal S, Tkachev AG, Gupta VK (2018) Adsorption of heavy metals on conventional and nanostructured materials for wastewater treatment purposes: a review. *Ecotoxicol Environ Saf* 148:702–712. <https://doi.org/10.1016/j.ecoenv.2017.11.034>
99. Azimi A, Azari A, Rezakazemi M, Ansarpour M (2017) Removal of heavy metals from industrial wastewaters: a review. *ChemBioEng Reviews* 4(1):37–59. <https://doi.org/10.1002/cben.201600010>
100. Yusuff, A. S. (2018). Optimization of adsorption of Cr(VI) from aqueous solution by *Leucaena leucocephala* seed shell activated carbon using design of experiment. *Appl Water Sci* 8(8). <https://doi.org/10.1007/s13201-018-0850-3>
101. Yang X, Wan Y, Zheng Y, He F, Yu Z, Huang J, Wang H, Ok YS, Jiang Y, Gao B (2019) Surface functional groups of carbon-based adsorbents and their roles in the removal of heavy metals from aqueous solutions: a critical review. *Chem Eng J* 366:608–621. <https://doi.org/10.1016/j.cej.2019.02.119>
102. Alagumuthu G, Rajan M (2010) Equilibrium and kinetics of adsorption of fluoride onto zirconium impregnated cashew nut shell carbon. *Chem Eng J* 158(3):451–457. <https://doi.org/10.1016/j.cej.2010.01.017>
103. Viswanathan G, Jaswanth A, Gopalakrishnan S, Siva Ilango S (2009) Mapping of fluoride endemic areas and assessment of fluoride exposure. *Sci Total Environ* 407(5):1579–1587. <https://doi.org/10.1016/j.scitotenv.2008.10.020>
104. Namasivayam C, Sangeetha D (2006) Removal of molybdate from water by adsorption onto ZnCl₂ activated coir pith carbon. *Biores Technol* 97(10):1194–1200. <https://doi.org/10.1016/j.biortech.2005.05.008>
105. Oladipo AA, Ifebajo AO (2018) Highly efficient magnetic chicken bone biochar for removal of tetracycline and fluorescent dye from wastewater: Two-stage adsorber analysis. *J Environ Manage* 209:9–16. <https://doi.org/10.1016/j.jenvman.2017.12.030>
106. Bernhardt A, Gysi N (2016) World's worst pollution problems: the toxics beneath our feet. *Fabrikstrasse 17:8005. Zurich, Switzerland*
107. Ahmed TF, Sushil M, Krishna M (2012) Impact of dye industrial effluent on physicochemical characteristics of Kshipra River, Ujjain City, India. *Int Res J Environ Sci* 1:41–45
108. Sharma P, Kaur H, Sharma M, Sahore V (2011) A review on applicability of naturally available adsorbents for the removal of hazardous dyes from aqueous waste. *Environ Monit Assess* 183(1–4):151–195. <https://doi.org/10.1007/s10661-011-1914-0>
109. Katheresan V, Kansedo J, Lau SY (2018) Efficiency of various recent wastewater dye removal methods: a review. *J Environ Chem Eng* 6(4):4676–4697. <https://doi.org/10.1016/j.jece.2018.06.060>
110. Danish M, Hashim R, Ibrahim MNM, Sulaiman O (2013) Characterization of physically activated *Acacia mangium* wood-based carbon for the removal of methyl orange dye. *BioResources* 8(3). <https://doi.org/10.15376/biores.8.3.4323-4339>
111. Wang H, Xie R, Zhang J, Zhao J (2018) Preparation and characterization of distillers' grain based activated carbon as low cost methylene blue adsorbent: mass transfer and equilibrium modeling. *Adv Powder Technol* 29(1):27–35. <https://doi.org/10.1016/j.apt.2017.09.027>
112. Ahmed MJ (2016) Application of agricultural based activated carbons by microwave and conventional activations for basic dye adsorption: review. *J Environ Chem Eng* 4(1):89–99. <https://doi.org/10.1016/j.jece.2015.10.027>
113. Hammani H, Boumya W, Laghrib F, Farahi A, Lahrich S, Aboulkas A, El Mhammedi M (2017) Electrocatalytic effect of NiO supported onto activated carbon in oxidizing phenol at graphite electrode: application in tap water and olive oil samples. *J Assoc Arab Univ Basic Appl Sci* 24(1):26–33. <https://doi.org/10.1016/j.jaubas.2017.06.006>
114. Theydan SK, Ahmed MJ (2012) Adsorption of methylene blue onto biomass-based activated carbon by FeCl₃ activation: equilibrium, kinetics, and thermodynamic studies. *J Anal Appl Pyrol* 97:116–122. <https://doi.org/10.1016/j.jaap.2012.05.008>
115. Chowdhury ZZ, Abd Hamid, SB, Das R, Hasan MR, Zain SM, Khalid K, Uddin, MN (2013) Preparation of carbonaceous adsorbents from lignocellulosic biomass and their use in removal

- of contaminants from aqueous solution. *BioResources* 8(4). <https://doi.org/10.15376/biores.8.4.6523-6555>
116. González-García P (2018) Activated carbon from lignocellulosics precursors: a review of the synthesis methods, characterization techniques and applications. *Renew Sustain Energy Rev* 82:1393–1414. <https://doi.org/10.1016/j.rser.2017.04.117>
 117. El Gamal M, Mousa HA, El-Naas MH, Zacharia R, Judd S (2018) Bio-regeneration of activated carbon: a comprehensive review. *Sep Purif Technol* 197:345–359. <https://doi.org/10.1016/j.seppur.2018.01.015>
 118. Salman JM, Hussein FH (2014) Batch adsorber design for different solution volume/adsorbate mass ratios of bentazon, carbofuran and 2,4-D adsorption on to date seeds activated carbon. *J Environ Anal Chem* 02(01). <https://doi.org/10.4172/2380-2391.1000120>
 119. Ahmed MJ (2017) Adsorption of non-steroidal anti-inflammatory drugs from aqueous solution using activated carbons: review. *J Environ Manage* 190:274–282. <https://doi.org/10.1016/j.jenvman.2016.12.073>
 120. Boudrahem N, Delpeux-Ouldriane S, Khenniche L, Boudrahem F, Aissani-Benissad F, Gineys M (2017) Single and mixture adsorption of clofibric acid, tetracycline and paracetamol onto activated carbon developed from cotton cloth residue. *Process Saf Environ Prot* 111:544–559. <https://doi.org/10.1016/j.psep.2017.08.025>
 121. Mansour F, Al-Hindi M, Yahfoufi R, Ayoub GM, Ahmad MN (2017) The use of activated carbon for the removal of pharmaceuticals from aqueous solutions: a review. *Rev Environ Sci Bio/Technol* 17(1):109–145. <https://doi.org/10.1007/s11157-017-9456-8>
 122. Chayid MA, Ahmed MJ (2015) Amoxicillin adsorption on microwave prepared activated carbon from *Arundo donax* Linn: isotherms, kinetics, and thermodynamics studies. *J Environ Chem Eng* 3(3):1592–1601. <https://doi.org/10.1016/j.jece.2015.05.021>

Chapter 8

Carbon Nanomaterial-Based Adsorbents for Water Protection



Umma Habiba and Tawsif Ahmed Siddique

Abstract The pollution of water resources with different inorganic and organic pollutants and deterioration of drinkable water quality is pressing the need for the introduction of new and advanced material for water treatment technology. Nanomaterials are being very popular in water purification technology because of their excellent removal efficiency for a vast spectrum of pollutants via the adsorption process. Nowadays, carbon nanomaterials (carbon nanofiber, carbon nanotube, graphene, and its derivatives, etc.) have attracted great attention as adsorbents because of their extraordinary physicochemical properties for water treatment. This chapter explores the adsorption performance of carbon nanotube, carbon nanofiber, graphene, and its derivatives, etc., for organic dye, heavy metal, and pharmaceutical pollutants. It starts with the fundamental of the adsorption mechanism and isotherms. The chapter describes all the details on material from the synthesis process to the application and concisely states that adsorption performance can be improved by functionalization and modification of the pristine material. The current hurdle and prospects of the carbon nanomaterial also have been discussed. This chapter will contribute to a proper understanding of the implementation of carbon nanomaterials in the field of adsorption for environmental remediation and designing future experiments for water treatment.

Keywords Adsorption · Carbon nanotube · Graphene · Organic dye · Heavy metal

U. Habiba (✉)

Department of Chemical and Biological Engineering, Faculty of Engineering, Monash University, Clayton, VIC, Australia

e-mail: Umma.Habiba@monash.edu

U. Habiba · T. A. Siddique

Department of Mechanical Engineering, University of Creative Technology Chittagong, Chittagong (UCTC), Bangladesh

T. A. Siddique

Department of Chemical Engineering, RMIT University, Melbourne, VIC, Australia

8.1 Introduction

Water an indispensable component to survive in this world. Unfortunately, the quality of water is deteriorating because of environmental pollution and climate change effect. Moreover, the steep increases in the world population at a rate of 80 million per year causes increasing the demand for water by 64 billion cubic meters per annum [1–3]. Therefore, there is a pressing need to search for new technologies for water purification. Different technologies such as adsorption, flocculation, coagulation, aerobic and anaerobic treatments, and membrane filtration are used to get pure water from primary resources and contaminated water [4]. Among them, adsorption is mostly implemented for water purification due to its easy operation, reusability, and availability of a vast range of the adsorbent [5]. A wide range of materials has been reported as an adsorbent for water purification. However, various nanomaterials-based adsorbents are being examined for the removal of different contaminants from water as their size-dependent property like large surface area and high density of low coordinated atoms facilitate the adsorbent rate. The most common nanomaterial adsorbents are different metal oxides (TiO_2 , titanates, CuO , Fe_3O_4 , etc.) [6, 7], hexagonal boron nitride [8, 9], transition metal carbides, and carbonitrides (MXenes) [10, 11], layered double hydroxides [12], zeolites [13], magnetic nanomaterials [14], polymer nanocomposite and carbon nanomaterials [15–18] or their superstructures or hybrid [19, 20]. Carbon nanomaterials are graphene and its derivatives, carbon nanotubes (CNT), activated carbon, nanoporous carbons, carbon nanofibers (CNF), fullerenes, nanodiamonds, and graphite-carbon nitride [21–28]. These materials are receiving more attention as they ensure fast adsorbent kinetics as a consequence of high specific surface area and active sites of the nanomaterials [29, 30].

In this chapter, the application of carbon-based adsorbent for water purification will be discussed, focusing on CNT, CNF and graphene and its family, etc. The adsorption performance depends on the adsorption kinetics, the adsorption isotherm of pollutants such as dye, heavy metal, pharmaceutical, and other organic compounds. Besides, the high surface area, easy synthesis process, and low energy demand determine its practical applicability. The adsorption performance and prospects of different carbon-based nano-adsorbent have been presented.

8.2 Adsorption Isotherms and Fundamentals

Adsorption is an exothermic surface phenomenon that helps to transfer a substance from a liquid or gaseous phase to the surface or pores of a solid called adsorbent. The adsorption occurs when the attraction between the surface of the adsorbent and the adsorbate overcomes the cohesive energy of the adsorbate itself [31]. Usually, the adsorbent is agitated with the solution containing the pollutants, and the pollutants adhere to the adsorbent. The adsorption occurs via different interactions such

as chemical or physiochemical interactions and can be categorized as chemisorption and physisorption. The driving force in the chemisorption process is the strong chemical interaction among the adsorbent and adsorbates via electron exchange [32]. On the other hand, physisorption is a reversible process, where the driving forces for adsorption are van der Waals forces, hydrogen bonding, dipole–dipole interactions, π - π interactions, etc. [33, 34]. The adsorption performance is defined by several factors such as the adsorbent dosage, surface area of adsorbent, reaction time, operational temperature, and pH of the contaminate solution [34, 35].

The characteristics of the adsorption process are investigated by adsorption kinetic models, adsorption isotherms, and thermodynamic parameters. Among them, the isotherms contain most of the information about adsorption behavior and proficiency [36, 37]. The adsorption mechanism can be homogeneous/heterogeneous or monolayer/multilayer. Several adsorption isotherms such as Henry, Freundlich, Langmuir, Temkin, Dubinin-Radushkevich, Halsey, Koble-Corrigan, Redlich-Peterson, and Jovanovic have been developed to define the adsorption mechanism. The Langmuir isotherm model is designed for homogeneous monolayer adsorption with two parameters. This model indicates the maximum number of occupied adsorption sites [38]. The Freundlich model is based on multilayer adsorption on the nonuniform surface [39]. Redlich-Petersen and Sips model abided the parameters of Langmuir and Freundlich to present the difference between adsorption of low concentration and high concentration solution [40]. The Fritz-Schlunder is a three-component model and also a combination of Langmuir and Freundlich isotherms [41]. The Toth isotherm model is for heterogeneous adsorption for both low and high-end boundaries of the concentration [42]. Hill's model assumes the adsorption process is a shared incident with the ligand-binding ability at one site on the molecule, where the different binding sites on the same molecule are also considered [43]. Among different isotherms model, the Langmuir and Freundlich adsorption isotherms are widely used as it helps to measure the ultimate adsorption capacity of an adsorbent for a specific adsorbate. These two models also symbolize the surface roughness of the adsorbent by fitting the experimental data fitting whether with Langmuir (monolayer surface) or Freundlich model (heterogeneous surface) [38, 39]. The Langmuir model is presented by the Eq. 8.1 written below [44].

$$q_e = \frac{q_m k_a C_e}{1 + k_a C_e} \quad (8.1)$$

where q_m (mg/g) represents maximum adsorption capacity and K_a (L/mg) is the Langmuir constant related to the affinity of the binding sites.

The Freundlich model is described by the following Eq. 8.2 [45]

$$q_e = K_F C_e^{1/n} \quad (8.2)$$

The K_F is the adsorption constant that represents the adsorption capacity. The magnitude of $1/n$ signifies the favorability of the adsorption process. It can be classified as irreversible ($1/n = 0$), favourable ($0 < 1/n < 1$) and unfavourable ($1/n > 1$) [46–48].

8.3 Carbon Nanostructures

8.3.1 Carbon Nanotube

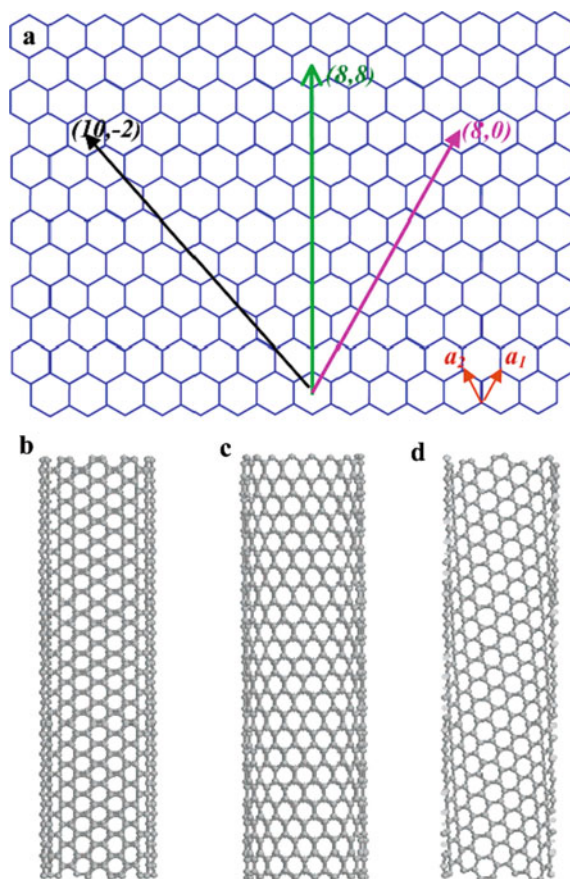
The CNTs are distinctive nanostructured materials, which are prepared by the bottom-up synthesis process. They are a 1-dimensional tube-like rolled-up graphite sheet and hollow structured material with thin carbon walls [49]. A rolled-up sheet along lattice vector (m, n) [50] in the graphene plane has been shown in Fig. 8.1. The tube diameter is in the range of a nanometer and is made up of the allotropes of carbon molecules [51]. The structure of CNTs is classified as single-walled, and multi-walled CNTs based on the number of CNTs rolled up to form the tube structure and denoted as SWCNTs and MWCNTs, respectively [52]. The structures of these two types of CNTs have been shown in Fig. 8.2.

Although the chemical composition and bonding structure of CNTs are ordinary, its unique cylindrical molecular structure ensures diverse applications in different fields because it is advantageous with large surface area, high electrical conductivity, mechanical, thermal, and chemical stability [54]. However, synthesized CNTs using CVD [55] have few impurities, and methods are there to purify these CNTs [56–58] that is important prior to water purification technology design [59, 60].

CNTs are considered as an efficient adsorbent of water purification [62] because of its inbuilt structural porosity, layered structure, the small diameter of the tube and high surface area, where the driving forces for adsorption are electrostatic interactions, charge transfer, π – π and hydrophobic interaction [63–67]. There are four possible adsorption sites of CNTs such as internal sites of the hollow tube, the interstitial channels among the tube walls, the grooves among the peripheral nanobundles, and exposed external surface area (Fig. 8.3a,b) [68, 69].

The adsorption capacity of CNTs for organic and inorganic pollutants is a rising topic for research. A highly toxic chemical named dioxin was removed from water by MWCNTs, where the adsorption was occurred because of the strong interactions between aromatic dioxin and hexagonal array of carbon atoms [71]. Pristine MWCNT was also used for the removal of dye, and a high adsorption capacity of 409.4 mg/g at lower pH was reported for Direct Blue 53 [72]. The adsorption rate was high due to the 3.7 nm diameter of the tube, which was able to accommodate three molecules of dye molecule at a time. Moreover, Xia et al. reported a low adsorption capacity of CNTs relative to graphene oxide because of its small particle size [73]. It means that the architecture of CNTs is a role-defining property for adsorption performance. Another effective parameter is the morphology of the adsorbate.

Fig. 8.1 **a** Two-dimensional graphene sheet structure with lattice vector along which it can be folded to CNTs, **b** zigzag, **c** chiral, and **d** tube orientation for a different angle of folding. The figure is adapted with permission from [53]



The planar polynuclear organic dyes such as anthracene, acridine orange, alizarin red, and Rhodamine B (RhB) are more susceptible to adhere to the CNT surface. On the other hand, non-planar and conjugated molecules such as xylenol orange, 1-(2-pyridylazo)-2-naphthol, and orange G are less efficiently attached to the surface. Besides, the adsorption efficiency of CNTs for non-conjugated molecules such as bromothymol blue and diiodofluorescein is very insignificant [74].

Although the SWCNTs are very expensive, their adsorption capacity is very high relative to the MWCNTs [75]. So, the concern of the economy is influencing the enhancement of the adsorption capacity by surface functionalization [76]. Kim et al. prepared graphene-CNT nanohybrid aerogel, which has a highly porous structure with very high specific surface area and the inbuilt properties of both components for treatment of wastewater containing both anionic dyes e.g., methyl orange (MO) and congo red (CR) and cationic dyes e.g., crystal violet (CV), methylene blue (MB), where high adsorption rate was observed [77]. CNTs are functionalized with magnetic particles to ease the separation process after the operation to ensure recycle

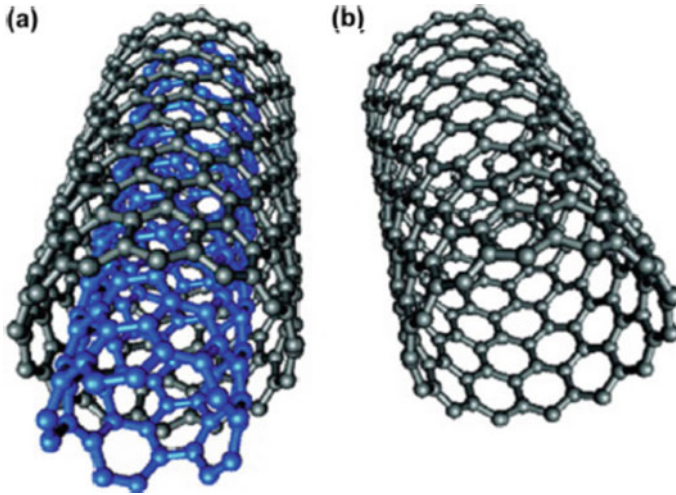


Fig. 8.2 Schematic representation of **a** MWCNT and **b** SWCNT. The figure is adapted with permission from [61]

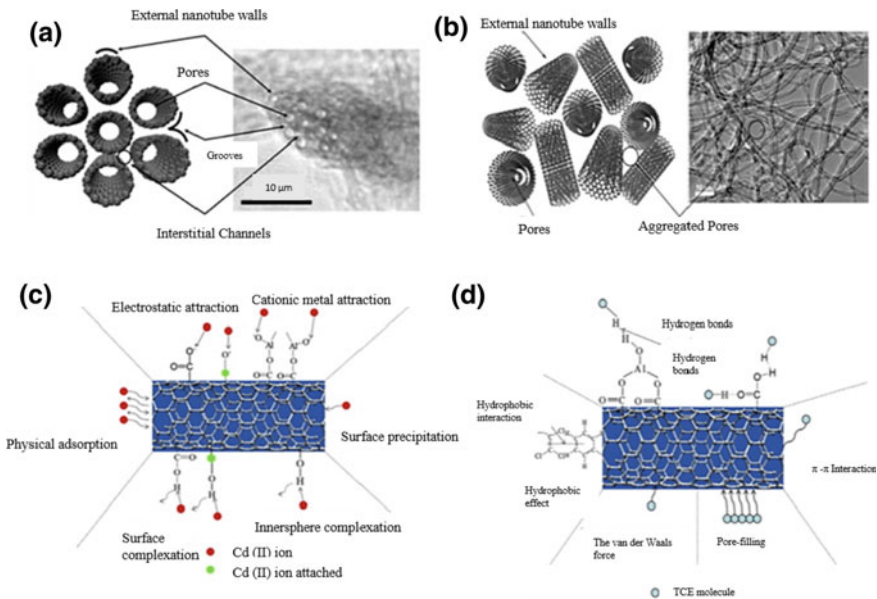


Fig. 8.3 **a** adsorption points of CNTs and TEM images of SWCNTs, **b** model and TEM image of aggregated pores, **c** interactions that cause the Cd adsorption on Al₂O₃/MWCNTs (II) and (d) TCE molecule [70].

of the adsorbent. Jin et al. prepared nanohybrids containing porous carbon, CNTs, and Ni nanoparticles for adsorption of anionic dyes (MO, CR) and cationic dyes, e.g., MB and RhB, etc. The adsorbent was very effective for Malachite green (MG) (898 mg/g) and easily separated from the solution [78]. The magnetic MnFe₂O₄/MWCNTs were applied for adsorption of direct red 16 and yellow 40. Being anionic, the direct red was efficiently removed from the water at lower pH as the number of protons was increased and eventually causes strong electrostatic interaction with the negative dye molecule. The opposite result was obtained for cationic dye yellow 40, where maximum adsorption was observed at higher pH [79]. The amino-functionalized magnetic MWCNTs adsorbed MB with a q_e of 178.8 mg/g, where the adsorption mechanism was well described by the Freundlich isotherm model. The adsorption capacity was prominent up to 6 cycles [80].

The size and radius of pollutants are very important parameters for the alternation of the performance of CNTs. Stacie et al. investigate the effect of the radius of heavy metal ions and reported that the adsorption rate decreased in the following manner, Cu (II) > Pb (II) > Co (II) > Zn (II) > Mn (II). Tofighy et al. also reported the relation of adsorption performance with the radius of ion in the following order, Pb (II) > Cd (II) > Co (II) > Zn (II) > Cu (II) [72, 81]. Therefore, the radius of the ion is an important factor for controlling the adsorption affinity and mechanism. Functionalized CNTs are also employed for the adsorption of heavy metal ions. Chen et al. functionalized the MWCNTs with iron oxide for adsorption of Ni (II) and Sr (II). The adsorption capacity was increased after functionalization, and the adsorbent was easily removed from the solution. The adsorption process is pH-dependent and follows the Langmuir isotherm model [82]. A similar study found enhancement of adsorption capacity CNT for Cr (III) after functionalization with magnetic Fe₃O₄ probably because of oxygen functionalities of the oxide, which add more active sites for adsorption [83]. Lu et al. reported enhanced adsorption of Cr (VI) at lower pH by MWCNTs/Fe₃O₄. Adsorption performance was increased with temperature and fitted well with Langmuir isotherm [84].

The research study for the application of CNTs to remove pharmaceuticals is very limited. Ncibi et al. used MWCNTs for carbamazepine and dorzolamide, and high adsorption capacity was observed comparatively with other studies [97]. Xu et al. used hybrid CNTs bead with a polymer comprising a smooth outer surface and hierarchical porous inner structure for adsorption of p-chlorophenol. The adsorption capacity was prominent for neutral p-chlorophenol, where the adsorption interaction was assumed to be π - π electron coupling and hydrophobic interactions [98]. Zhao et al. used MWCNTs for the removal of a wide range of pharmaceuticals such as dichlorofenac, ibuprofen, carbamazepine, chloramphenicol, thiamphenicol, florfenicol, sulfadiazine, sulfapyridine, sulfamethoxazole, sulfathiazole, sulfamerazine, sulfamethazine, and sulfaquinoxalin. The adsorption followed the Freundlich isotherm model. The adsorption performance was increased with the surface area of MWCNTs [99]. Moodley et al. functionalized the CNTs with ionic liquid (CNT-ILs), and they studied the adsorption behavior for sulfamethoxazole (SMZ) and ketoprofen (KET) at various pH [100]. The adsorption capacity was higher at higher pH, possibly due to the presence of strong electron acceptor, benzene and heterocyclic rings of

the pharmaceutical that dissociate to negatively charge hydrophilic species at higher pH and positively charged surface of the (CNT-ILs), which results in an electrostatic interaction [101, 102]. The adsorption at low pH indicates that the mechanism of adsorption also relied on other phenomena such as pore trapping, hydrophobic interaction, etc.

Tables 8.1 and 8.2 summarized the performances of CNTs and functionalized CNTs-based different adsorbents for the removal of organic dye and heavy metals, respectively. The availability and scope of functionality will ensure the future application of CNTs with improved adsorption capacity and selectivity.

8.3.2 Carbon Nanofiber

CNFs are 1-dimensional nanomaterial having diameters of 3–100 nm, usually prepared by electrospinning method, CVD, and templating method, being studied extensively for different practical applications [120–123]. The porous scaffold structure of CNFs is very favorable to its multifunctional pertinence [121, 124]. Besides, different advantageous properties such as high tensile strength, low density, high conductivity, outstanding thermal and chemical stability justify its application in different fields [125–128]. Electrospinning is the most favorable process for making CNF, where a polymer solution is loaded in a syringe, and voltage is applied between a collector and the tip of syringe spinneret to create the fluid jet, and eventually, fiber is accumulated in the collector. Usually, phenolic resins, polyvinyl alcohol, cellulose, polyacrylonitrile, polybenzimidazole, polyvinyl pyrrolidone, etc., are electrospun to make carbon nanofiber. Figure 8.4 represents the morphology of the carbonized electrospun polyacrylonitrile nanofiber.

The high surface area, active sites, and porous scaffold structure of CNFs suggest its relevance as an adsorbent [120]. Minmin et al. prepared three different mesoporous CNFs via the electrospinning method for adsorption of cationic (methylthionine chloride, MC) and anionic dye (MO and AR1). The adsorption capacity of CNFs was increased with pH for cationic dye, while the adsorption for anionic dye was superior at low pH. The CNFs with larger pore sizes showed the prominent adsorption performance as it helps to hold more dye molecules [130]. Al Saadi et al. used Design-Expert software for modeling the adsorption of Pb (II) [131].

The insertion of magnetic particles in the CNFs facilitates the adsorption capacity. Several research reports have described the fabrication of magnetic CNFs for the adsorption of organic molecules and heavy metals. Yang et al. prepared magnetic Fe₃O₄/CNF for adsorption of organic dyes, where the polybenzoxazine was used as the precursor for electrospinning. The final product, Fe₃O₄/CNF contains different porous structures, was prepared via a combination of in situ polymerization and electrospinning (Fig. 8.5). The mesoporous structure facilitates the adsorption of dye as well as the recovery process [132]. The same research group prepared magnetic Fe₃O₄@CNF with a very high surface area (1885 m²/g) via in situ polymerization which ensured high adsorption of cationic dye (MB and RhB) and eased the recovery

Table 8.1 CNT-based different adsorbents for organic dye removal from water

Water pollutants	Adsorbent	Adsorption isotherm Kinetics q_e (mg/g)	Refs.
MB	Ni ^a PC-CNT	Langmuir Pseudo Second Order 312	[78]
	^b P-CSCNT	Langmuir Pseudo Second Order 319	[85]
	CNT- ^c MSN	Langmuir Pseudo First Order 524	[86]
	^d G-CNT	Freundlich Pseudo Second Order 82	87[]
MO	Magnetic CNTs	Freundlich Pseudo Second Order 28	[88]
	CNT@NiCo ₂ O ₄	Freundlich Pseudo second order 1188	[89]
	CNT@MnCo ₂ O ₄	Freundlich Pseudo second order 790	[89]
	CNT@CuCo ₂ O ₄	Langmuir Pseudo second order 826	[89]
	CNT@ZnCo ₂ O ₄	Langmuir and Temkin Pseudo second order 935	[89]
	Al-doped CNTs	Langmuir Pseudo second order 69.7	[90]

(continued)

Table 8.1 (continued)

Water pollutants	Adsorbent	Adsorption isotherm Kinetics q_e (mg/g)	Refs.
	Ni ^a /PC-CNT	Langmuir and Freundlich Pseudo second order 271	[78]
MG	ZIF-CNT	Langmuir Pseudo second order 2034	[91]
	Ni ^a /PC-CNT	Freundlich Pseudo second order 898	[78]
AR18	^e mCS/CNT	Freundlich and Redlich–Peterson Pseudo Second Order 771	[92]
Direct Red 80	^f SF-CNT	Langmuir Pseudo second order 120	[93]
Direct Red 23	SF-CNT	Freundlich Pseudo second order 188	[93]
CR	CNT/Mg(Al)O	Langmuir Pseudo second order 1250	[94]
	Ni/PC-CNT	Freundlich Pseudo second order 818	[78]
Acid Blue 45	CNT-NH ₂	Langmuir Pseudo second order 714	[95]
Acid Black 1	CNT-NH ₂	Langmuir Pseudo second order 666	[95]

(continued)

Table 8.1 (continued)

Water pollutants	Adsorbent	Adsorption isotherm Kinetics q_e (mg/g)	Refs.
Basic Blue 41	CNT	Langmuir Pseudo second order 123	[96]
Cd Basic Red 18	CNT	Freundlich Pseudo second order 80	[96]
Basic Violet 16	CNT	Langmuir Pseudo second order 84	[96]

^aporous carbon, ^bporous cup-stacked carbon nanotube, ^cmesostructured silica nanoparticles, ^dgraphene-carbon nanotube, ^emagnetically retrievable chitosan, ^fcationic surfactant carbon nanotubes

of the adsorbent [25]. Sun et al. prepared magnetic CNFs using α -Fe nanoparticles for adsorption of dye and phenol. The CNFs acted as prominent adsorbent and was easily recovered from the solution [133]. Verma et al. preparation of Fe-grown CNF for removal of As(V) [134]. However, the application of CNFs for environmental remediation is still very limited.

8.3.3 Graphene Family Members

Graphene is a two-dimensional material of sp^2 hybridized carbon atoms arranged in a hexagonal close-packed crystal lattice. It is receiving attention as an adsorbent because of its prominent chemical and physical properties. Its good chemical and mechanical stability, high surface area (~ 2600 m²/g), and large delocalized π -electron systems make it a suitable adsorbent of different pollutants of water [135–137]. Graphene can be fabricated using different methods such as reduction of graphite oxide, unzipping of carbon nanotubes, electromechanical, micromechanical, and sonochemical exfoliation, acidic oxidation of graphite and arc discharge method [70]. Figure 8.6 represents the fabrication method of graphene.

However, there is a drive to make graphene derivatives, e.g., graphene oxide (GO), reduced graphene oxide (rGO), and functionalized graphene oxide (fGO) for practical application due to challenges in graphene fabrication such as small yields, a limited number of layers and minimization of folds. GO has received attention due to its easy and inexpensive fabrication process [138]. It is a single layer graphene

Table 8.2 CNT-based different adsorbents for heavy metals removal from water

Water pollutants	Adsorbent	Adsorption isotherm Kinetics q_e (mg/g)	Ref
Pb (II)	MWCNT	Langmuir – 97	[103]
	MoS ₂ / ^a SH-MWCNT	Freundlich Pseudo second order 90	[104]
	CNT/ ^b TNT	Langmuir – 588	[105]
	Oxidized CNT	Freundlich Pseudo second order 101	[106]
	CNT/Sand	Langmuir Pseudo second order 92	[107]
	Graphene–c-MWCNT hybrid aerogel	Freundlich Pseudo second order 105	[108]
	MWCNT-f	Freundlich Pseudo second order 14	[109]
	O-MWCNTs	Langmuir Pseudo second order 76	[110]
	MWCNT/SiO ₂	Langmuir and Temkin Pseudo second order 13	[111]
	^c KTEG-CNTs	Langmuir Pseudo second order 288	[112]
	mHAP-oMWCNTs	Langmuir and Freundlich Pseudo second order 698	[113]
	^e PAMAM/CNT	Langmuir Pseudo second order 4870	[114]
NiO/CNT	Freundlich Pseudo second order 24	[115]	
Cu(II)	MWCNT	Langmuir – 24	[103]

(continued)

Table 8.2 (continued)

Water pollutants	Adsorbent	Adsorption isotherm Kinetics q_e (mg/g)	Ref
	CNT/TNT	Langmuir – 116	[105]
	Oxidized CNT	Freundlich Pseudo second order 50	[106]
	CNT/Sand	Langmuir Pseudo second order 67	[107]
	Graphene–c-MWCNT hybrid aerogel	Freundlich Pseudo second order 33	[108]
	O-MWCNTs	Langmuir Pseudo second order 15	[110]
	^f DTC-MWCNT	Langmuir Pseudo second order 98	[116]
	PAMAM/CNT	Langmuir Pseudo second order 3333	[114]
Cd(II)	MoS ₂ /SH-MWCNT	Freundlich Pseudo second order 66	[104]
	MWCNT	Langmuir – 10	[103]
	Oxidized CNT	Freundlich Pseudo second order 75	[106]
	O-MWCNTs	Langmuir Pseudo second order 32	[110]
	DTC-MWCNT	Langmuir Pseudo second order 167	[116]
Hg(II)	MnO ₂ /CNT	Freundlich Pseudo second order 58	[117]
	Graphene–c-MWCNT hybrid aerogel	Freundlich Pseudo second order 93	[108]

(continued)

Table 8.2 (continued)

Water pollutants	Adsorbent	Adsorption isotherm Kinetics q_e (mg/g)	Ref
Zn (II)	Oxidized CNT	Freundlich Pseudo second order 58	[106]
	O-MWCNTs	Langmuir Pseudo second order 13	[110]
	DTC-MWCNT	Langmuir Pseudo second order 11	[116]
	CNT	Langmuir Pseudo second order –	[118]
	SWCNTs	Langmuir – 43.66	[119]
	MWCNTs	Langmuir – 32.68	

^athiol-functionalized MWCNT, ^btitanate nanotubes, ^cfunctionalised triethylene glycol, ^dmagnetic hydroxyapatite-immobilized oxidized MWCNT, ^epoly-amidoamine dendrimer, ^fdithiocarbamate carbon

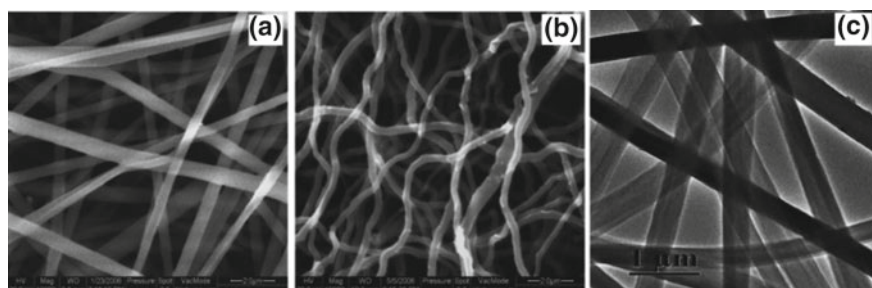


Fig. 8.4 a, b SEM, c TEM image of carbonized polyacrylonitrile nanofiber. Reproduced with permission from [129]

oxides having oxygen with functional groups contributing high hydrophilicity and negative charge density, which enable its profound adsorption capacity [139–141]. GO is prepared by exfoliation of graphite oxide into detached layers using different methods such as mechanical stirring, sonication, rapid heating, applying microwave or arc discharge [142].

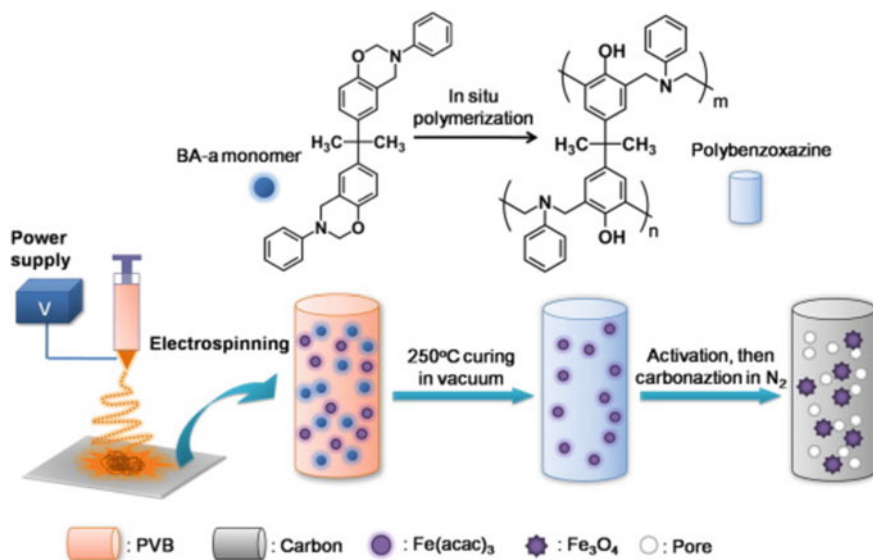


Fig. 8.5 Preparation of magnetic Fe_3O_4 /CNFs. Reproduced with permission from [132]

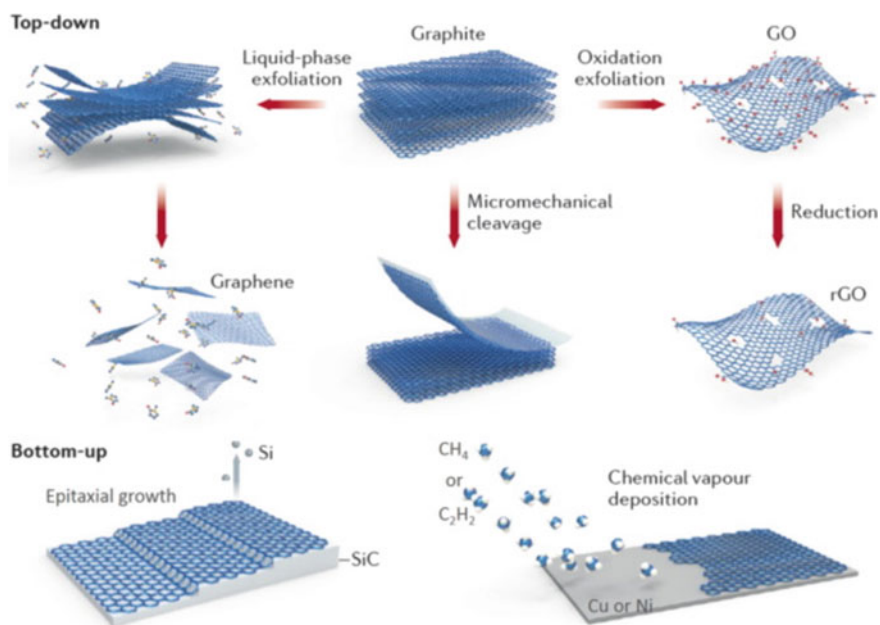


Fig. 8.6 Graphene fabrication methods. Reproduced with permission from [70]

rGO is imperfect graphene oxide but more conductive, where the graphitic system is renovated in the basal plane. rGOs are fabricated by reducing GO using chemical and hydrothermal reactions and thermal annealing [142]. rGO is a fascinating adsorbent than graphene and GO as it enables non-covalent physical sorption by π - π stacking or van der Waals interactions [139].

In recent years, many research studies reported successful application of graphene, graphene derivatives such as GO, rGO, and functionalized GO, and graphene-based composite as an adsorbent for pollutants from wastewater. A considerable amount of research reports proved the dynamic adsorption capacity of graphene and graphene-based material for the removal of organic dyes, phenol, heavy metal ions, and pharmaceutical compound [143–145]. The adsorption mechanism of graphene and its derivatives is controlled by the electrostatic interaction via physisorption and follows Langmuir adsorption isotherm, which implies monolayer formation of contaminant on the adsorbent surface. The negatively charged oxygen functionality of GO and rGO, such as $-\text{OH}$, $-\text{COOH}$, $-\text{COO}^-$ and $-\text{C}-\text{O}-\text{C}-$, makes it more attractive towards positively charged contaminants [23, 146].

Several studies have reported a significant adsorption capacity of GO/rGO for organic pollutants and metal ions. The interaction between the cationic dye and GO is controlled by electrostatic attraction between the positive charge of dye and negative charge density of GO, and π - π interaction between aromatic rings of dye and electron cloud of GO rings. [147]. Electrostatic attraction is more dominating to control the adsorption behavior of GO [148, 149]. The adsorption of cationic dye increases exponentially with increasing oxygen density of GO [150, 151]. Peng et al. reported a very high MB uptake of 2255.35 mg/g by GO [152]. Gupta et al. reported high adsorption capacity of rGO with a high number of voids for (MG) dye, where the adsorption mechanism was governed by π - π interaction between graphene and moieties of dye, and electrostatic interaction of positive center of MG dye with residual oxygen functional groups and electron clouds of rGO [23]. Liu et al. reported a 99.68% removal rate of MB by graphene nanosheet at pH 10. The high pH has dominated the dye uptake as the more negative charge was present on the GO surface, and consequently increases the electrostatic attraction between the positive dye and GO [153, 154]. Many researchers have studied the thermodynamics of dye adsorption and found it endothermic and spontaneous. The kinetic study showed that it mostly obeys the pseudo-second-order kinetic model [141, 152, 153, 155, 156]. The rGOs are mostly effective for the adsorption of anionic dyes to non-covalent and charge interactions. It was found that the adsorption rate was faster and uptake of anionic dye was higher by rGO from a comparative adsorption study on cationic and anionic dye by GO and rGO [146]. Table 8.3 lists the adsorption of organic dyes using graphene and its derivatives.

The graphene and its derivatives are often susceptible to agglomerate because of strong interplanar interactions and stacking [157]. Therefore, the surface of graphene, GO and rGO are modified by a surfactant or organic compound to regulate the aggregation. The most common surfactant cetyltrimethylammonium bromide (CTAB) has been successfully used to modify GO and rGO. CTAB modified GO, and rGO successfully adsorbed DR80 and DR23 dyes [158]. The adsorption mechanism of

Table 8.3 Graphene and its family members-based adsorbents for organic dyes removal from water

Pollutant	Adsorbent	Adsorption isotherm Kinetics q_e (mg/g)	Refs.
MB	rGO	Langmuir Pseudo Second Order 145	[146]
	^a HPA-GO	Langmuir Pseudo Second Order 740	[164]
	^b GO-SH	Langmuir Pseudo Second Order 763	[165]
	^c GO-N	Langmuir Pseudo Second Order 636	[165]
	GO/Fauasite	Freundlich – 92.4	[166]
	Graphene	Langmuir and Freundlich Pseudo Second Order 481	[167]
	^d SGO	Langmuir Pseudo Second Order 2530	[168]
	rSGO	Langmuir Pseudo Second Order 2187	[168]
	G-Fe	Langmuir Pseudo Second Order 402	[169]
	GO0123	Langmuir Pseudo Second Order 365	[170]
	GO0125	Langmuir Pseudo Second Order 504	[170]
	GO-calcium alginate Gel	Freundlich Pseudo first order 122	[171]
	^e GO-MNP	Langmuir and Freundlich Pseudo Second Order 1428	[172]

(continued)

Table 8.3 (continued)

Pollutant	Adsorbent	Adsorption isotherm Kinetics q_e (mg/g)	Refs.
	MgO-GO	Langmuir Pseudo Second Order 237	[173]
	GO-FeCl ₃	Pseudo Second Order 200 –	[174]
	^f PDA/RGO/HNTs	Langmuir Pseudo Second Order 12	[175]
	GO/MOF	Langmuir Pseudo Second Order 274	[176]
	rGO/Cu(4)	Langmuir Pseudo Second Order 1200	[177]
	^g SDS exfoliated graphene	Freundlich Pseudo Second Order 782	[178]
	MnFe ₂ O ₄ -GO nanocomposite	Langmuir Pseudo Second Order 177	[179]
	5% GO/MIL-100(Fe)	Langmuir Pseudo Second Order 1231	[180]
	rGO- ^h MMT	Langmuir Pseudo Second Order 227	[181]
	ⁱ PmPD/rGO/NFO	Langmuir Pseudo Second Order 103	[182]
	NG-2	Langmuir Pseudo first order 156	[183]
	Fe ₃ O ₄ @GNs	Langmuir Pseudo Second Order 211	[148]
	Fe ₃ O ₄ @SiO ₂ @CS- ^j TETA-GO	Langmuir Pseudo Second Order 529	[184]
	Fe ₃ O ₄ -GS	Temkin Pseudo Second Order 526	[185]

(continued)

Table 8.3 (continued)

Pollutant	Adsorbent	Adsorption isotherm Kinetics q_e (mg/g)	Refs.
	^k CA-mGO5CS	Freundlich Pseudo Second Order 315	[186]
	MgSi/RGO	Langmuir Pseudo Second Order 433	[187]
	MrGO/TiO ₂	Langmuir Pseudo Second Order 845	[188]
	mGO/PVA-50%	Langmuir Pseudo Second Order 271	[189]
	3D RGO-based hydrogels	Freundlich, Pseudo Second Order, 8	[190]
CR	^m CTAB-GO	Langmuir Pseudo Second Order 2767	[159]
	G-Fe	Langmuir Pseudo Second Order 970	[169]
	PDA/RGO/HNTs	Langmuir Pseudo Second Order 11	[175]
	RGO/NMA	Langmuir Pseudo Second Order 474	[191]
	PmPD/rGO/NFO	Langmuir Pseudo Second Order 285	[182]
	ⁿ pTSA-Pani@GO-CNT	Langmuir Pseudo Second Order 66	[192]
	MoS ₂ -rGO	Langmuir Pseudo First Order 441	[193]
	^o PPD-GO	Langmuir Pseudo Second Order 892	[194]
	Ce-Fe/RGO	Langmuir, Pseudo Second Order 179	[195]

(continued)

Table 8.3 (continued)

Pollutant	Adsorbent	Adsorption isotherm Kinetics q_e (mg/g)	Refs.
RhB	GS	Langmuir, Pseudo Second Order 56	[196]
	3D RGO-based hydrogels	Freundlich Pseudo Second Order 29	[190]
	^p TA-G	Langmuir Pseudo Second Order 201	[197]
	Bi ₂ O ₃ @GO	Langmuir & Temkin Pseudo first order and intraparticle diffusion 320	[198]
	^q SIS/RGO-2.5%	Langmuir Pseudo Second Order 174	[199]
	A-rGO/Co ₃ O ₄	Freundlich & Tempkin Pseudo first order 434	[200]
Crystal violet (CV)	rGO/ZIF-67 aerogel	Pseudo first order 1714	[201]
	G-Fe	Langmuir Pseudo Second Order 909	
	rGO/Cu(4)	Langmuir Pseudo Second Order 238	[177]
	Fe ₃ O ₄ /porous graphene nanocomposite	Langmuir Pseudo Second Order 460	[202]
	^r LI-MGO	Langmuir Pseudo Second Order 69	[203]
MG	^s N/S-GHs	Langmuir Pseudo Second Order 738	[204]
	rGO	Langmuir Pseudo Second Order 476	[23]
	GO-SBA-16	Langmuir Pseudo Second Order 358	[205]

(continued)

Table 8.3 (continued)

Pollutant	Adsorbent	Adsorption isotherm Kinetics q_e (mg/g)	Refs.
	GO–Au	Freundlich Pseudo Second order 71	[206]
MO	rGO/ZIF-67 aerogel	Pseudo first order 426	[201]
	G-Fe	Langmuir Pseudo Second Order 664	[169]
	5% GO/MIL-100(Fe)	Langmuir Pseudo Second Order 1189	[180]
	NG-6	Langmuir Pseudo first Order 232	[183]
	PmPD/rGO/NFO	Langmuir Pseudo Second Order 136	[182]
	rGO	Langmuir Pseudo Second Order 244	[146]
DR80	rGO/CTAB	Langmuir Pseudo Second Order 213	[158]
	^u mimGO sponge	Langmuir Pseudo Second Order 501	[163]
Orange IV (OIV)	LI-MGO	Langmuir Pseudo Second Order 57	[203]
	GO _{KOH}	Langmuir Pseudo Second Order 606	[207]

^ahyperbranched polyamine functionalized graphene, ^b4-aminothiophenol modified GO, ^c3-aminopropyltriethoxysilane modified GO, ^dSulfonated graphene, ^egraphene oxide- magnetic iron oxide nanoparticles, ^fpolydopamine modified reduced graphene oxide/halloysite nanotubes, ^gSodium dodecyl sulfate, ^hmontmorillonite, ⁱpoly (m-phenylenediamine)/reduced graphene oxide/nickel ferrite, ^jtriethylenetetramine, ^kcitric acid functionalized magnetic graphene oxide coated corn straw, ^mCetrimonium bromide, ⁿNH₂-MIL-68 (Al), ^opara toluene sulphonic acid, ^pp-phenylenediamine, ^rtannic acid, ^qSnO. 215In0. 38S, ^r1-amine-3-methyl imidazole chloride-functionalized magnetized graphene oxide, ^snitrogen and sulphur co-doped three-dimensional (3D) graphene hydrogels, ^tmesoporous silica, ^umethylimidazolium ionic-liquid-functionalized graphene oxide

anionic dye obeys the Langmuir isotherm and pseudo-second-order kinetic model. A very high CR uptake of 2767 mg/g was reported by CTAB-GO at low pH [159]. Non covalently functionalized GO with organic gelator 1-OA, tetrazolyl derivative (1) (1,3-di(1Htetrazol- 5-yl) benzene) and octadecylamine showed concurrent adsorption of primary, binary and mixed pollutants from water [160]. The OA helps to restrict the agglomeration of nanosheet and consequently ensure synergistic interaction such as hydrogen bonding, π - π stacking, hydrophobic interaction, and van der Waal forces to boost the adsorption efficiency. The adsorption of cationic dye is higher at high pH, where low pH leads to promote adsorption of anionic dye.

The GO or rGO is often functionalized with Fe_3O_4 nanoparticles to expedite the recovery process of the adsorbent by using an eternal magnet [161]. However, the Fe_3O_4 nanoparticles reduce the active sites of GO which reduces the adsorption. Jiao et al. prepared magnetic nanohybrid Fe_3O_4 -GO for adsorption of cationic dyes. The tuned geometry and dimensions of Fe_3O_4 ensured very high adsorption of MB and RhB [162].

A methylimidazolium ionic-liquid-functionalized graphene oxide (mimGO) sponge was used to remove Direct Red 80 from water. The mimGO was prepared by the functionalization of GO sponge with methylimidazole ionic liquid. The adsorption mechanism has been shown in Fig. 8.7. The interaction between the sulfonic group of dye and imidazolium rings of the mimGO increased the adsorption rate. Besides, π - π interaction and hydrogen bonding between dye and adsorbent also

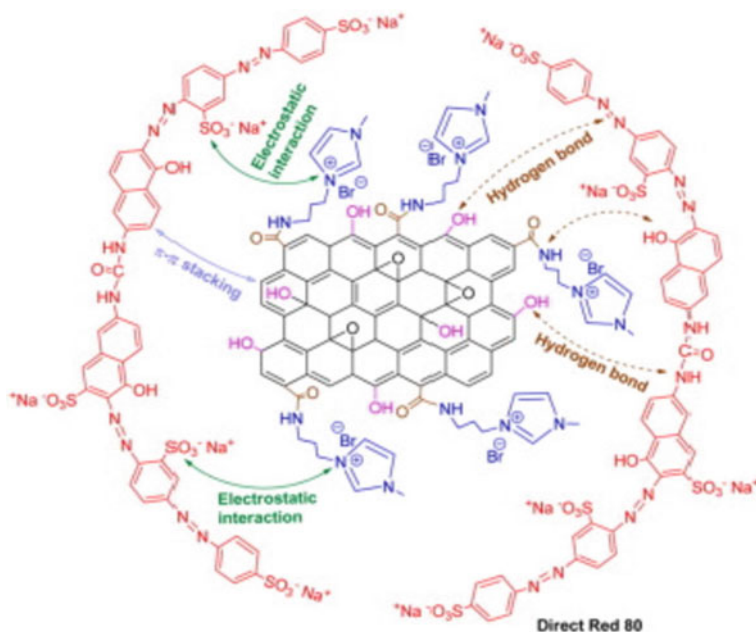


Fig. 8.7 Adsorption mechanism of DR80 by ionic liquid functionalized GO [163]

participate in the adsorption process. The adsorbent was regenerated and performed efficiently until 4 cycles (99.2% of removal efficiency at the 4th cycle) [163].

The adsorption capacity of GO for the metal ion is higher than graphene as oxidation of graphene introduces a hydrophilic oxygen functional group. Wu et al. used GO nanosheets for the removal of Cu (II), where the adsorption data was fitted well with the Freundlich isotherm and attributed to electrostatic interactions and complexation [208]. Priestly et al. compared the adsorption capacity of EDTA-GO, amine-GO, and GO for Ni (II) and reported the superiority of functionalized GO [209]. The EDTA-GO was more selective to Ni (II) competing for other ions such as Cu (II), Cd (II), and Fe (II). The magnetic nanohybrid of GO with MnFe₂O₄ showed very good removal efficiency for Pb (II), As (III), and As (IV) and easy separation after adsorption [22]. The efficient removal of two types of Arsenic is also reported by using Fe₃O₄/non-oxidative graphene composite adsorbent [210].

The functionalization of GO/rGO is a well-practiced technique for enhancement of its performance, such as adsorption efficiency and selectivity. Functionalization is done with metal, metal chalcogenides, biopolymers, and by doping with a different element such as nitrogen, Sulphur, etc. [211–214]. Doping of graphene with sulfur results in increasing the adsorption capacity by 5 times that of GO and excellent recyclability, where the main interaction causing the adsorption is pH-independent [214]. Wei et al. compared the adsorption performance of GO, rGO, sulfonated GO (SGO), and rGO (SrGO) and found that SGO performed best for adsorption of Pb (II) and MB. The functional groups such as –COOH, –SO₃H and –OH has contributed to the enhancement of adsorption capacity. The functional groups at the edges of the sp³ hybridized graphene of SGO and rGO influence the remarkable adsorption capacity for Pb (II) [168]. The graphene nanosheet (GNSs) which was prepared using vacuum-promoted low-temperature exfoliation was used to adsorb Pb (II) ions from water. The adsorption capacity pristine GNSs and thermally treated GNSs were compared, and enhanced adsorption was found for thermally treated GNSs. Moreover, increased Pb (II) uptake was increased at high pH probably because of improved Lewis basicity caused by heat treatment under a high vacuum [215]. However, the adsorption efficiency was not significant (35.46 mg/g). Deng et al. reported higher removal efficiency of Pb (II) using functionalized graphene with potassium hexafluorophosphate which was fabricated by the electrolysis process [216]. Madandarg et al. found that the adsorption capacity of EDTA-GO was 1–2 times higher than GO for Pb (II) [217]. Zhao et al. prepared few-layered graphene oxide and found that adsorption efficiency increases with temperature. The highest adsorption for Pb (II) was 1850 mg/g at 333 k [218]. The adsorption of heavy metal ions using graphene and its different derivatives have been listed in Table 8.4.

The adsorption capacity of functionalized GO is supreme towards pharmaceutical pollutants. Zanella et al. studied the adsorption of sodium diclofenac on graphene and functionalized graphene nanoribbons. The adsorption performance was improved because of the presence of functional groups that improve the binding energies [255]. Saha et al. reported a faster adsorption rate of fulvic acid from water in low pH using rGO functionalized with Fe. The electronegativity at rGO surface is increased at high pH and eventually creates difficulties in the adsorption process [256]. Mamani

Table 8.4 Graphene-based nanomaterial for adsorption of metal ions in water

Metal ion	Adsorbent	Adsorption isotherm kinetics q_e (mg/g)	Refs.
Pb(II)	Graphene	Langmuir and Freundlich – 35.46	[215]
	Functionalized graphene	Langmuir and Freundlich Pseudo Second Order 406.4	[216]
	Functionalized graphene	Langmuir and Freundlich Pseudo Second Order 74.18	[216]
	GO	Langmuir – 367	[217]
	GO	– – 35.6	[219]
	GO	Langmuir – 692.66	[220]
	GO	Langmuir Pseudo Second Order 1119	[221]
	^a EDTA modified GO	Langmuir – 525	[217]
	EDTA modified rGO	Langmuir – 228	[217]
	FGO	Langmuir – 842	[218]
	SiO ₂ /graphene	Langmuir Pseudo Second Order 113.6	[222]
	Graphene/c-MWCNT	– – 104.9	[108]
	Graphene/MWCNT	– – 44.5	[108]
	GO–iron oxide	Langmuir – 588.24	[223]

(continued)

Table 8.4 (continued)

Metal ion	Adsorbent	Adsorption isotherm kinetics q_e (mg/g)	Refs.
	^b GO-SO _x R@TiO ₂	Redlich Peterson Pseudo Second Order 285	[224]
	^c IT-PRGO	Langmuir Pseudo Second Order 101.563	[225]
	^d GO-W-MC	Langmuir Pseudo Second Order 253	[226]
	^e GI-RGO	Freundlich Elovich 101	[227]
	MoS ₂ -rGO	Langmuir Pseudo Second Order 322	[228]
	GO- ^f DPA	Langmuir Pseudo Second Order 360	[229]
	HPA-GO	Langmuir Pseudo Second Order 819	[164]
	GO- ^g HPEI1.8 K ge	Langmuir Pseudo Second Order 438	[230]
	^h LS-GH	Langmuir Pseudo Second Order 1308	[231]
	ⁱ PAS-GO	Langmuir Pseudo Second Order 312	[232]
	^j GO-BPEI	Langmuir Pseudo Second Order 3390	[233]
Cu (II)	GO	Langmuir Pseudo Second Order 294	[221]
	GO/CdS	Langmuir – 137	[234]
	GO membrane	Langmuir Pseudo Second Order 72	[235]

(continued)

Table 8.4 (continued)

Metal ion	Adsorbent	Adsorption isotherm kinetics q_e (mg/g)	Refs.
	Xanthated Fe_3O_4 -CS-GO	Langmuir Pseudo Second Order 426	[236]
	GO-DPA	Langmuir Pseudo Second Order 347	[229]
	IT-PRGO	Langmuir Pseudo Second Order 19	[225]
	CS/GO/ Fe_3O_4 -IIP	Freundlich Pseudo Second Order 132	[238]
	^k GO-CTPy	Langmuir Pseudo Second Order 119	[239]
	^l SA/PVA/GO	Langmuir Pseudo Second Order 247	[240]
	GO-BPEI	Langmuir Pseudo Second Order 1096	[233]
Co(II)	Few layered graphene oxide	Langmuir – 68	[241]
	Amination graphene oxide	Langmuir Pseudo Second Order 116	[242]
Cr (VI)	Nitrogen doped graphene oxide aerogel	Langmuir Pseudo Second Order 408	[243]
	Bio-GM nanocomposite	Langmuir Pseudo Second Order 189	[244]
	IT-PRGO	Langmuir Pseudo Second Order 37	[225]
	Amino functionalized graphene oxide decorated with Fe_3O_4 nanoparticles	Langmuir Pseudo Second Order 123	[245]
Zn(II)	GO	Langmuir Pseudo Second Order 345	[221]

(continued)

Table 8.4 (continued)

Metal ion	Adsorbent	Adsorption isotherm kinetics q_e (mg/g)	Refs.
	GO	Langmuir Pseudo Second Order 246	[246]
	GO-SO _x R@TiO ₂	Redlich Peterson Pseudo Second Order 196	[224]
Mn (II)	GO/SA	Freundlich Pseudo Second Order 56	[247]
	GO-NH ₂	Freundlich Pseudo Second Order 161	[237]
	GN-SDS	Langmuir Pseudo Second Order 223	[237]
Cd (II)	GO	Langmuir Pseudo Second Order 530	[221]
	MGO	Langmuir Pseudo Second Order 91	[248]
	Few layered graphene oxide	Langmuir – 106	[241]
	^m 3D-SRGO	Langmuir Pseudo Second Order 234	[249]
	GO membranes	Langmuir Pseudo Second Order 83	[235]
	GO-DPA	Langmuir Pseudo Second Order 253	[229]
	GO-SO _x R@TiO ₂	Redlich Peterson Pseudo Second Order 217	[224]
	GO-BPEI	Langmuir Pseudo Second Order 2051	[233]
Hg (II)	GO@SnS ₂	Langmuir Pseudo Second Order 342	[250]

(continued)

Table 8.4 (continued)

Metal ion	Adsorbent	Adsorption isotherm kinetics q _e (mg/g)	Refs.
	IT-PRGO	Langmuir Pseudo Second Order 624	[225]
	PPy-GO	Langmuir Pseudo Second Order 400	[251]
	GO/Fe-Mn	Sips Pseudo Second Order 33	[252]
	^a MBT-functionalized graphene oxide	Langmuir Pseudo Second Order 107	[253]
As(V)	^o GNP/Fe – Mg	Freundlich Pseudo Second Order 104	[254]
	M-nOG	Sips Pseudo Second Order 14	[210]
	IT-PRGO	Langmuir Pseudo Second Order –	[225]
	MnFe ₂ O ₄ -GO	Langmuir Pseudo Second Order 240	[179]

^aEthylenediaminetetraacetic acid, ^bsulfur functionalized graphene oxide, ^c2-imino-4-thiobiuret-partially reduced graphene oxide, ^dgraphene oxide-covalently encapsulated magnetic composite, ^eglycol, ^f2,2'-dipyridylamine, ^ghyperbranched polyethylenimines, ^hlignosulfonate-modified graphene hydrogel, ⁱpoly3-aminopropyltriethoxysilane, ^jGraphene oxide-branched polyethylenimine foams, ^k4'-carboxy-2,2':6',2''-terpyridine modified GO, ^lGraphene oxide encapsulated polyvinyl alcohol/sodium alginate hydrogel, ^m3D sulfonated reduced graphene oxide, ⁿmercaptobenzothiazole, ^oGraphene nanoplates

et al. prepared rGONH₂, which was immobilized with Horseradish Peroxide (HRP) for adsorption of phenol. The HRP enzyme was immobilized onto rGONH₂ via physical adsorption and π - π interaction. The resulting adsorbent efficiently adsorbed the phenol, where the complex formation between the HRP and phenol was a key driving force for adsorption. Besides, rGO-NH₂ adsorb phenol via hydrogen bonding, electrostatic interaction, and π - π interaction, which results in very high adsorption of high concentration of phenol with the synergic effect of HRP-phenol complex formation. The adsorbent was efficiently regenerative up to ten cycles [257]. The magnetic recovery of adsorbent has been practiced for the removal of pharmaceutical products using graphene-based adsorbent. Boruah et al. reported magnetic recovery

Table 8.5 Graphene and its derivatives for adsorption of pharmaceutical pollutants in water

Pollutant	Adsorbent	Adsorption isotherm Kinetics q_e (mg/g)	Refs.
Phenol	Graphene	Langmuir Pseudo Second Order 233	[260]
	Graphene	Langmuir and Freundlich Pseudo Second Order 28	[261]
	T-rGO	Langmuir Pseudo Second Order 23	[262]
	H-rGO	Langmuir Pseudo Second Order 38	[262]
	Graphene aerogels–mesoporous silica	Langmuir and Freundlich Pseudo Second Order 90	[263]
	Reduced graphene oxide–sodium alginate (rGO–SA)	Langmuir pseudo-second-order 26.126	[264]
Bisphenol A (BPA)	GO	Langmuir & Freundlich Pseudo Second Order 10	[265]
	Graphene oxide incorporated Alginate hydrogel beads	Langmuir Pseudo-second-order 342	[266]
	Magnetic reduced graphene oxide composites-1	Langmuir Pseudo-second-order 93	[267]
	Magnetic reduced graphene oxide composites-2	Langmuir Pseudo-second-order 71	[267]
	T-rGO	Langmuir Pseudo-second-order 96	[262]
	H-rGO	Langmuir Pseudo-second-order 81	[262]
	Reduced graphene oxide–sodium alginate (rGO–SA)	Langmuir Pseudo-second-order 14.123	[264]
Aniline	Fe ₃ O ₄ /graphene	Freundlich Pseudo Second Order 202.84	[268]
	Cu ²⁺ -binded graphene oxide	Langmuir Pseudo-second-order 79	[269]

(continued)

Table 8.5 (continued)

Pollutant	Adsorbent	Adsorption isotherm Kinetics q_e (mg/g)	Refs.
Naphthalene	ZnO/Ag/GO	Freundlich/Langmuir Pseudo second order 500	[270]
ciprofloxacin (CIP)	Activated graphene adsorbents (G-KOH)	Langmuir Pseudo-second-order/Intra-particle diffusion 194.6	[271]
	Modified alginate/graphene double network porous hydrogel	Langmuir Pseudo second order 344.83	[272]
	GO	Freundlich/Langmuir Pseudo second order/Elovich models 379.0	[273]
	GO-SA gel	Langmuir Pseudo Second Order 86	[274]
	Reduced graphene oxide/magnetite composites	Langmuir and Temkin – 18.22	[275]
	Diethylenetriaminepentaacetic acid-functionalized magnetic graphene oxide (DDMGO)	Freundlich isotherm Pseudo-second-order –	[276]
Aspirin	Graphene nanoplatelet	– Pseudo-second-order 12.98	[277]
acetaminophen	Graphene nanoplatelet	– Pseudo-second-order 18.07	[277]
caffeine	Graphene nanoplatelet	– Pseudo-second-order 19.72	[277]
Ibuprofen	Reduced graphene oxide-based hydrogel	Langmuir Pseudo second order 466	[278]
Diclofenac	Reduced graphene oxide-based hydrogel	Langmuir Pseudo second order 489	[278]
Tetracycline	Modified alginate/graphene double network porous hydrogel	Langmuir Pseudo Second Order 290.7	[272]
	Magnetic graphene oxide sponge	Langmuir model /Temkin model Pseudo-second-order 473	[279]
	Reduced graphene oxide–sodium alginate (rGO–SA)	Langmuir Pseudo second order 17.312	[264]
	Diethylenetriaminepentaacetic acid-functionalized magnetic graphene oxide (DDMGO)	Freundlich Pseudo-second-order –	[276]

(continued)

Table 8.5 (continued)

Pollutant	Adsorbent	Adsorption isotherm Kinetics q_e (mg/g)	Refs.
sulfamethoxazole	Graphene nanosheet	Redlich–Peterson and Koble–Corrigan isotherm Pseudo second-order 103	[280]
	Graphene oxide nanosheet	Redlich–Peterson and Koble–Corrigan isotherm Pseudo second-order 127	[280]
	GO	Freundlich/Langmuir Pseudo second order/Elovich models 240	[273]

of Fe_3O_4 -rGO from water for the removal of trizine pesticides such as ametryn, simeton, simazine, prometeyn and atrazine [258]. Ionic liquid functionalized GO has been applied for adsorption of different organic chemicals. Zhou et al. used 4 types of GO-ILs for the adsorption of different types of phthalates which is a plasticizer. As the ionic liquid is composed of anion and cation, the adsorption capacity is dependent on the design of the anion and cation. The adsorption of anionic ionic liquid was superior for phthalates. Moreover, the smaller carbon chain in GO-ILs is beneficial for extraction. On the other hand, from the comparative adsorption study with magnetic GO, the GO-ILs was superior [259]. The Table 8.5 presents the list of graphene and graphene-based adsorbent for pharmaceutical compounds.

In summary, graphene and graphene oxide can be modified and functionalized to different derivatives, according to the nature of the pollutant to be adsorbed. Its unique property and versatility in application make it consider a prominent adsorption nanomaterial for future applications.

8.4 Research Gaps

Although carbon nanomaterial offers several lucrative properties for water purification, large-scale application is still in the premature stage because of several obstacles such as high cost, toxic effects, and complicated fabricated processes [281]. Research efforts for the large-scale application of carbon nanomaterials are crucial. Although few industries have scaled up the production of CNT using CVD and arc-discharge methods, the cost is very high. Moreover, methods for large-scale graphene production have not been developed. On the other hand, high energy is required for the electrospinning process for the fabrication of CNF. Therefore, more investigation is certainly required to find low cost, feasible, and environmentally friendly fabrication process.

Although adsorption is an efficient process for water purification, it generates secondary waste. It is encouraged to mitigate the problem by a circular approach, where the secondary waste will be the source of a new cycle. Therefore, the nano adsorbent should sustain its functionality after several adsorption cycles to minimize waste. More research attention is required to increase the reusability of the adsorbent by retaining its functionality or activity. The types and number of oxygen functionality depend on the oxidation or reduction process used during synthesis and governs the adsorption performance. The current research reports do not represent a clear and consistent image of the relation between the adsorption performance and the number and types of the functional group. Therefore, more investigation is required to establish a correlation between adsorption performance and functional groups. Moreover, the impact of exposure of carbon nanomaterial in the environment and natural ecosystem is not well understood. Before approaching large-scale production, the behavior of carbon nanomaterial under severe conditions and long exposure should be investigated. An immense research effort is essential to understand the toxicity of this material to ensure a safer application.

8.5 Conclusion

Adsorption, principally physisorption, chemisorption, and ion-exchange mechanism, is an established method for the treatment of wastewater. Adsorption performance depends on many factors such as type of adsorbent, adsorbate, and process parameters, and usually measured using different isotherms and kinetic models. Nanomaterials are a booming field for the adsorption of pollutants from water. Different nano adsorbents, either in pristine form or a modified version, are being studied widely. Among them, carbon nanomaterials are leading because of their impressive properties. Although there are several limitations, the current research focuses on improving the performance of carbon nano adsorbents. In this chapter, the role of carbon nanomaterials such as CNF, CNT, and graphene for the adsorption of organic dye, heavy metal, and pharmaceutical pollutants has been summarized. The pristine adsorbents have impressive adsorption capacity for the aromatic pollutant. However, pristine adsorbent has several disadvantages, such as low adsorption capacity for a broad spectrum of pollutants and difficulty in segregation. Larger surface area, charged functional groups, and porosity of the surface improve adsorption capacity. This chapter revealed the emerging techniques for the modification of carbon nanomaterials. Functionalization and modification of adsorbent not only enhances the adsorption capacity but also improve recyclability, ease the recovery process, and helps to avoid aggregation of adsorbent particle. The magnetic composite of carbon nanomaterial is very useful for the separation and reusability of the adsorbent. The trend in research of graphene-based adsorbents shows the improvement of adsorption capacity largely depends on the functional groups.

To establish the carbon nanomaterial as a pioneer in the field of adsorption technology, more research is required to overcome the current challenges. Even though

the application of carbon nano adsorbents for water purification is still confined to the lab scale, the bright future of these materials cannot be denied.

References

1. Grafton RQ, Horne J (2014) Water markets in the Murray-Darling basin. *Agricultural Water Management* **145**(C): p. 61–71.
2. Programme WWA and UN-Water (2009) *Water in a changing world*, vol 1. Earthscan
3. Das R et al (2014) Multifunctional carbon nanotubes in water treatment: The present, past and future. *Desalination* **354**:160–179
4. Das R et al (2017) Recent advances in nanomaterials for water protection and monitoring. *Chem Soc Rev* **46**(22):6946–7020
5. Burakov AE et al (2018) Adsorption of heavy metals on conventional and nanostructured materials for wastewater treatment purposes: A review. *Ecotoxicol Environ Saf* **148**:702–712
6. Hu JS et al (2008) Synthesis of hierarchically structured metal oxides and their application in heavy metal ion removal. *Adv Mater* **20**(15):2977–2982
7. Upadhyay RK, Soin N, Roy SS (2014) Role of graphene/metal oxide composites as photocatalysts, adsorbents and disinfectants in water treatment: a review. *RSC Adv* **4**(8):3823–3851
8. Lei W et al (2013) Porous boron nitride nanosheets for effective water cleaning. *Nat Commun* **4**(1):1–7
9. Das R et al. (2020) High flux and adsorption based non-functionalized hexagonal boron nitride lamellar membrane for ultrafast water purification. *Chem Eng J* **127721**
10. Zhang Y et al (2018) Adsorptive environmental applications of MXene nanomaterials: a review. *RSC Adv* **8**(36):19895–19905
11. Zhang Q et al (2016) Efficient phosphate sequestration for water purification by unique sandwich-like MXene/magnetic iron oxide nanocomposites. *Nanoscale* **8**(13):7085–7093
12. Chubar N et al (2017) Layered double hydroxides as the next generation inorganic anion exchangers: Synthetic methods versus applicability. *Adv Coll Interface Sci* **245**:62–80
13. Wang S, Peng Y (2010) Natural zeolites as effective adsorbents in water and wastewater treatment. *Chem Eng J* **156**(1):11–24
14. Ambashta RD, Sillanpää M (2010) Water purification using magnetic assistance: a review. *J Hazard Mater* **180**(1–3):38–49
15. Yin J, Deng B (2015) Polymer-matrix nanocomposite membranes for water treatment. *J Membr Sci* **479**:256–275
16. Unuabonah EI, Taubert A (2014) Clay-polymer nanocomposites (CPNs): Adsorbents of the future for water treatment. *Appl Clay Sci* **99**:83–92
17. Zhao G et al (2018) Polymer-based nanocomposites for heavy metal ions removal from aqueous solution: a review. *Polym Chem* **9**(26):3562–3582
18. Das R (2019) *Polymeric materials for clean water*. Springer
19. Alayan HM et al (2018) The formation of hybrid carbon nanomaterial by chemical vapor deposition: an efficient adsorbent for enhanced removal of methylene blue from aqueous solution. *Water Sci Technol* **77**(6):1714–1723
20. Haiyam MA et al (2017) Hybridizing carbon nanomaterial with powder activated carbon for an efficient removal of Bisphenol A from water: the optimum growth and adsorption conditions. *Desalin Water Treat* **95**:128–143
21. Mauter MS, Elimelech M (2008) Environmental applications of carbon-based nanomaterials. *Environ Sci Technol* **42**(16):5843–5859
22. Kumar S et al (2014) Graphene oxide-MnFe₂O₄ magnetic nanohybrids for efficient removal of lead and arsenic from water. *ACS Appl Mater Interfaces* **6**(20):17426–17436
23. Gupta K, Khatri OP (2017) Reduced graphene oxide as an effective adsorbent for removal of malachite green dye: Plausible adsorption pathways. *J Colloid Interface Sci* **501**:11–21

24. Gupta VK, Saleh TA (2013) Sorption of pollutants by porous carbon, carbon nanotubes and fullerene—an overview. *Environ Sci Pollut Res* 20(5):2828–2843
25. Si Y et al (2012) Synthesis of mesoporous magnetic Fe₃O₄@ carbon nanofibers utilizing in situ polymerized polybenzoxazine for water purification. *J Mater Chem* 22(11):4619–4622
26. Fu Y et al (2019) Chitosan functionalized activated coke for Au nanoparticles anchoring: green synthesis and catalytic activities in hydrogenation of nitrophenols and azo dyes. *Appl Catal B: Environ* 255:117740
27. Fu Y et al (2019) Au nanoparticles decorated on activated coke via a facile preparation for efficient catalytic reduction of nitrophenols and azo dyes. *Appl Surf Sci* 473:578–588
28. Chowdhury ZZ et al (2013) Preparation of carbonaceous adsorbents from lignocellulosic biomass and their use in removal of contaminants from aqueous solution. *BioResources* 8(4):6523–6555
29. Kim H, Hwang YS, Sharma VK (2014) Adsorption of antibiotics and iopromide onto single-walled and multi-walled carbon nanotubes. *Chem Eng J* 255:23–27
30. Fang Q, Shen Y, Chen B (2015) Synthesis, decoration and properties of three-dimensional graphene-based macrostructures: a review. *Chem Eng J* 264:753–771
31. Chiou CT (2003) Partition and adsorption of organic contaminants in environmental systems. John Wiley & Sons
32. Takijiri K et al (2017) Highly stable chemisorption of dyes with pyridyl anchors over TiO₂: application in dye-sensitized photoelectrochemical water reduction in aqueous media. *Chem Commun* 53(21):3042–3045
33. Dunne LJ, Manos G (2009) Adsorption and phase behaviour in nanochannels and nanotubes. Springer Science & Business Media
34. Kumar N et al (2016) Efficient removal of rhodamine 6G dye from aqueous solution using nickel sulphide incorporated polyacrylamide grafted gum karaya bionanocomposite hydrogel. *RSC Adv* 6(26):21929–21939
35. Gao Z et al (2009) Investigation of factors affecting adsorption of transition metals on oxidized carbon nanotubes. *J Hazard Mater* 167(1–3):357–365
36. Ayawei N, Ebelegi AN, Wankasi D (2017) Modelling and interpretation of adsorption isotherms. *J Chem* 2017
37. Kavitha D, Namasivayam C (2007) Experimental and kinetic studies on methylene blue adsorption by coir pith carbon. *Biores Technol* 98(1):14–21
38. Langmuir I (1917) The constitution and fundamental properties of solids and liquids. II. Liquids. *J Am Chem Soc* 39(9):1848–1906
39. Freundlich H (1906) Over the adsorption in solution. *J Phys Chem* 57(385471):1100–1107
40. Redlich O, Peterson DL (1959) A useful adsorption isotherm. *J Phys Chem* 63(6):1024–1024
41. Fritz W, Schlueder E-U (1974) Simultaneous adsorption equilibria of organic solutes in dilute aqueous solutions on activated carbon. *Chem Eng Sci* 29(5):1279–1282
42. Tóth J (1995) Uniform interpretation of gas/solid adsorption. *Adv Coll Interface Sci* 55:1–239
43. Hill TL, Emmett PH, Joyner LG (1951) Calculation of thermodynamic functions of adsorbed molecules from adsorption isotherm measurements: nitrogen on Graphon 1, 2. *J Am Chem Soc* 73(11):5102–5107
44. Kannan N, Sundaram MM (2001) Kinetics and mechanism of removal of methylene blue by adsorption on various carbons—a comparative study. *Dyes Pigment* 51(1):25–40
45. Febrianto J et al (2009) Equilibrium and kinetic studies in adsorption of heavy metals using biosorbent: a summary of recent studies. *J Hazard Mater* 162(2–3):616–645
46. Greluk M, Hubicki Z (2010) Kinetics, isotherm and thermodynamic studies of Reactive Black 5 removal by acid acrylic resins. *Chem Eng J* 162(3):919–926
47. Yang H, Feng Q (2010) Characterization of pore-expanded amino-functionalized mesoporous silicas directly synthesized with dimethyldecylamine and its application for decolorization of sulphonated azo dyes. *J Hazard Mater* 180(1):106–114
48. Özcan A et al (2007) Modification of bentonite with a cationic surfactant: an adsorption study of textile dye Reactive Blue 19. *J Hazard Mater* 140(1):173–179

49. Janas D (2018) Towards monochiral carbon nanotubes: a review of progress in the sorting of single-walled carbon nanotubes. *Materials Chemistry Frontiers* 2(1):36–63
50. Das R et al (2015) Carbon nanotubes characterization by X-ray powder diffraction—a review. *Curr Nanosci* 11(1):23–35
51. Dai H (2002) Carbon nanotubes: opportunities and challenges. *Surf Sci* 500(1–3):218–241
52. Das R et al (2016) Can we optimize arc discharge and laser ablation for well-controlled carbon nanotube synthesis? *Nanoscale Res Lett* 11(1):1–23
53. Dai H (2002) Carbon nanotubes: synthesis, integration, and properties. *Acc Chem Res* 35(12):1035–1044
54. Dresselhaus, M.S., G. Dresselhaus, and P.C. Eklund, *Science of fullerenes and carbon nanotubes: their properties and applications*. 1996: Elsevier.
55. Das R, Tuhi SD (2018) Carbon nanotubes synthesis. *Carbon Nanotubes for Clean Water*. Springer, pp 27–84
56. Das, R., et al., *Common wet chemical agents for purifying multiwalled carbon nanotubes*. *Journal of Nanomaterials*, 2014. **2014**.
57. Das R et al (2015) Covalent functionalization schemes for tailoring solubility of multi-walled carbon nanotubes in water and acetone solvents. *Sci Adv Mater* 7(12):2726–2737
58. Das R (2017) Carbon nanotube purification. *Nanohybrid Catalyst based on Carbon Nanotube*. Springer, pp 55–73
59. Das R, Leo BF, Murphy F (2018) The toxic truth about carbon nanotubes in water purification: a perspective view. *Nanoscale Res Lett* 13(1):1–10
60. Das R, Abd Hamid SB, Annuar MSM (2016) Highly efficient and stable novel nanobiohybrid catalyst to avert 3, 4-dihydroxybenzoic acid pollutant in water. *Sci Rep* 6(1):1–11.
61. Zhao Y-L, Stoddart JF (2009) Noncovalent functionalization of single-walled carbon nanotubes. *Acc Chem Res* 42(8):1161–1171
62. Das R (2017) Carbon nanotube in water treatment. *Nanohybrid Catalyst Based on Carbon Nanotube*. Springer, pp 23–54
63. Abbas A et al (2016) Heavy metal removal from aqueous solution by advanced carbon nanotubes: critical review of adsorption applications. *Sep Purif Technol* 157:141–161
64. Upadhyayula VK et al (2009) Application of carbon nanotube technology for removal of contaminants in drinking water: a review. *Sci Total Environ* 408(1):1–13
65. Yan Y et al (2005) Adsorption of methylene blue dye onto carbon nanotubes: a route to an electrochemically functional nanostructure and its layer-by-layer assembled nanocomposite. *Chem Mater* 17(13):3457–3463
66. Ali ME et al (2014) Multifunctional carbon nanotubes (CNTs): a new dimension in environmental remediation. In *Advanced Materials Research*. Trans Tech Publ
67. Das, R., *Carbon Nanotubes for Clean Water*. 2018: Springer.
68. Machado FM et al (2015) Carbon nanoadsorbents. *Carbon nanomaterials as adsorbents for environmental and biological applications*. Springer, pp 11–32
69. Ren X et al (2011) Carbon nanotubes as adsorbents in environmental pollution management: a review. *Chem Eng J* 170(2–3):395–410
70. Gusain R, Kumar N, Ray SS (2020) Recent advances in carbon nanomaterial-based adsorbents for water purification. *Coord Chem Rev* 405:213111
71. Long RQ, Yang RT (2001) Carbon nanotubes as superior sorbent for dioxin removal. *J Am Chem Soc* 123(9):2058–2059
72. Prola LD et al (2013) Adsorption of Direct Blue 53 dye from aqueous solutions by multi-walled carbon nanotubes and activated carbon. *J Environ Manage* 130:166–175
73. Li Y et al (2013) Comparative study of methylene blue dye adsorption onto activated carbon, graphene oxide, and carbon nanotubes. *Chem Eng Res Des* 91(2):361–368
74. Liu C-H et al (2008) Structure dependent interaction between organic dyes and carbon nanotubes. *Colloids Surf, A* 313:9–12
75. Gupta VK et al (2013) Adsorptive removal of dyes from aqueous solution onto carbon nanotubes: a review. *Adv Coll Interface Sci* 193:24–34

76. Lu C, Chiu H, Liu C (2006) Removal of zinc (II) from aqueous solution by purified carbon nanotubes: kinetics and equilibrium studies. *Ind Eng Chem Res* 45(8):2850–2855
77. Lee B et al (2015) Carbon nanotube-bonded graphene hybrid aerogels and their application to water purification. *Nanoscale* 7(15):6782–6789
78. Jin L et al (2018) Nickel nanoparticles encapsulated in porous carbon and carbon nanotube hybrids from bimetallic metal-organic-frameworks for highly efficient adsorption of dyes. *J Colloid Interface Sci* 509:245–253
79. Kafshgari LA, Ghorbani M, Azizi A (2017) Fabrication and investigation of MnFe₂O₄/MWCNTs nanocomposite by hydrothermal technique and adsorption of cationic and anionic dyes. *Appl Surf Sci* 419:70–83
80. Ahamad T et al (2019) Effective and fast adsorptive removal of toxic cationic dye (MB) from aqueous medium using amino-functionalized magnetic multiwall carbon nanotubes. *J Mol Liq* 282:154–161
81. Stafiej A, Pyrzynska K (2007) Adsorption of heavy metal ions with carbon nanotubes. *Sep Purif Technol* 58(1):49–52
82. Chen C et al (2009) Adsorption behavior of multiwall carbon nanotube/iron oxide magnetic composites for Ni (II) and Sr (II). *J Hazard Mater* 164(2–3):923–928
83. Gupta V, Agarwal S, Saleh TA (2011) Chromium removal by combining the magnetic properties of iron oxide with adsorption properties of carbon nanotubes. *Water Res* 45(6):2207–2212
84. Lu W et al (2017) One-pot synthesis of magnetic iron oxide nanoparticle-multiwalled carbon nanotube composites for enhanced removal of Cr (VI) from aqueous solution. *J Colloid Interface Sci* 505:1134–1146
85. Gong J et al (2015) A facile approach to prepare porous cup-stacked carbon nanotube with high performance in adsorption of methylene blue. *J Colloid Interface Sci* 445:195–204
86. Karim A et al (2014) Influence of multi-walled carbon nanotubes on textural and adsorption characteristics of in situ synthesized mesostructured silica. *J Colloid Interface Sci* 421:93–102
87. Ai L, Jiang J (2012) Removal of methylene blue from aqueous solution with self-assembled cylindrical graphene–carbon nanotube hybrid. *Chem Eng J* 192:156–163
88. Yu F et al (2012) Magnetic carbon nanotubes synthesis by Fenton’s reagent method and their potential application for removal of azo dye from aqueous solution. *J Colloid Interface Sci* 378(1):175–183
89. Li H et al (2015) Facile and cost-effective synthesis of CNT@ MCo₂O₄ (M= Ni, Mn, Cu, Zn) core–shell hybrid nanostructures for organic dye removal. *RSC Adv* 5(97):79765–79773
90. Kang D et al (2017) Novel Al-doped carbon nanotubes with adsorption and coagulation promotion for organic pollutant removal. *J Environ Sci* 54:1–12
91. Abdi J et al (2017) Synthesis of metal-organic framework hybrid nanocomposites based on GO and CNT with high adsorption capacity for dye removal. *Chem Eng J* 326:1145–1158
92. Wang S et al (2014) Highly efficient removal of acid red 18 from aqueous solution by magnetically retrievable chitosan/carbon nanotube: batch study, isotherms, kinetics, and thermodynamics. *J Chem Eng Data* 59(1):39–51
93. Ghobadi J et al (2014) Modification of carbon nanotubes with cationic surfactant and its application for removal of direct dyes. *Desalin Water Treat* 52(22–24):4356–4368
94. Yang S et al (2015) Enhanced adsorption of Congo red dye by functionalized carbon nanotube/mixed metal oxides nanocomposites derived from layered double hydroxide precursor. *Chem Eng J* 275:315–321
95. Maleki A et al (2017) Amine functionalized multi-walled carbon nanotubes: single and binary systems for high capacity dye removal. *Chem Eng J* 313:826–835
96. Mahmoodi NM, Ghobadi J (2015) Extended isotherm and kinetics of binary system dye removal using carbon nanotube from wastewater. *Desalin Water Treat* 54(10):2777–2793
97. Ncibi MC, Sillanpää M (2017) Optimizing the removal of pharmaceutical drugs Carbamazepine and Dorzolamide from aqueous solutions using mesoporous activated carbons and multi-walled carbon nanotubes. *J Mol Liq* 238:379–388

98. Xu L et al (2017) Removal of p-chlorophenol from aqueous solutions by carbon nanotube hybrid polymer adsorbents. *Chem Eng Res Des* 123:76–83
99. Zhao H et al (2016) Adsorption behavior and mechanism of chloramphenicol, sulfonamides, and non-antibiotic pharmaceuticals on multi-walled carbon nanotubes. *J Hazard Mater* 310:235–245
100. Lawal IA et al (2018) Theoretical and experimental adsorption studies of sulfamethoxazole and ketoprofen on synthesized ionic liquids modified CNTs. *Ecotoxicol Environ Saf* 161:542–552
101. Ji L et al (2009) Adsorption of sulfonamide antibiotics to multiwalled carbon nanotubes. *Langmuir* 25(19):11608–11613
102. Meloun M, Bordovská S, Galla L (2007) The thermodynamic dissociation constants of four non-steroidal anti-inflammatory drugs by the least-squares nonlinear regression of multiwavelength spectrophotometric pH-titration data. *J Pharm Biomed Anal* 45(4):552–564
103. Li Y-H et al (2003) Competitive adsorption of Pb²⁺, Cu²⁺ and Cd²⁺ ions from aqueous solutions by multiwalled carbon nanotubes. *Carbon* 41(14):2787–2792
104. Gusain R et al (2019) Efficient Removal of Pb(II) and Cd(II) from Industrial Mine Water by a Hierarchical MoS₂/SH-MWCNT Nanocomposite. *ACS Omega* 4(9):13922–13935
105. Doong R-A, Chiang L-F (2008) Coupled removal of organic compounds and heavy metals by titanate/carbon nanotube composites. *Water Sci Technol* 58(10):1985–1992
106. Tofighy MA, Mohammadi T (2011) Adsorption of divalent heavy metal ions from water using carbon nanotube sheets. *J Hazard Mater* 185(1):140–147
107. Tian Y et al (2012) Methods of using carbon nanotubes as filter media to remove aqueous heavy metals. *Chem Eng J* 210:557–563
108. Sui Z et al (2012) Green synthesis of carbon nanotube–graphene hybrid aerogels and their use as versatile agents for water purification. *J Mater Chem* 22(18):8767–8771
109. Jahangiri M et al (2015) The removal of lead ions from aqueous solutions by modified multi-walled carbon nanotubes with 1-isatin-3-thiosemicarbazone. *J Mol Liq* 212:219–226
110. Ma X et al (2015) Competitive adsorption of heavy metal ions on carbon nanotubes and the desorption in simulated biofluids. *J Colloid Interface Sci* 448:347–355
111. Saleh TA (2016) Nanocomposite of carbon nanotubes/silica nanoparticles and their use for adsorption of Pb (II): from surface properties to sorption mechanism. *Desalin Water Treat* 57(23):10730–10744
112. AlOmar MK et al (2016) Lead removal from water by choline chloride based deep eutectic solvents functionalized carbon nanotubes. *J Mol Liq* 222:883–894
113. Wang Y et al (2017) Removal of Pb (II) and methylene blue from aqueous solution by magnetic hydroxyapatite-immobilized oxidized multi-walled carbon nanotubes. *J Colloid Interface Sci* 494:380–388
114. Hayati B et al (2017) Super high removal capacities of heavy metals (Pb²⁺ and Cu²⁺) using CNT dendrimer. *J Hazard Mater* 336:146–157
115. Diva TN et al (2017) Synthesis, characterization, and application of nickel oxide/CNT nanocomposites to remove Pb²⁺ from aqueous solution. *Journal of Nanostructure in Chemistry* 7(3):273–281
116. Li Q et al (2015) Synthesis and characterization of dithiocarbamate carbon nanotubes for the removal of heavy metal ions from aqueous solutions. *Colloids Surf, A* 482:306–314
117. Moghaddam HK, Pakizeh M (2015) Experimental study on mercury ions removal from aqueous solution by MnO₂/CNTs nanocomposite adsorbent. *J Ind Eng Chem* 21:221–229
118. Aliyu A (2019) Synthesis, electron microscopy properties and adsorption studies of Zinc (II) ions (Zn²⁺) onto as-prepared Carbon Nanotubes (CNTs) using Box-Behnken Design (BBD). *Scientific African* 3:e00069
119. Lu C, Chiu H (2006) Adsorption of zinc(II) from water with purified carbon nanotubes. *Chem Eng Sci* 61(4):1138–1145
120. De Jong KP, Geus JW (2000) Carbon nanofibers: catalytic synthesis and applications. *Catalysis Reviews* 42(4):481–510

121. Feng L, Xie N, Zhong J (2014) Carbon nanofibers and their composites: a review of synthesizing, properties and applications. *Materials* 7(5):3919–3945
122. Huang X (2009) Fabrication and properties of carbon fibers. *Materials* 2(4):2369–2403
123. Mustafa MA et al (2019) Embedded high-hydrophobic CNMs prepared by CVD technique with PVDF-co-HFP membrane for application in water desalination by DCMD. *Desalin Water Treat* 142:37–48
124. Roberts AD, Li X, Zhang H (2014) Porous carbon spheres and monoliths: morphology control, pore size tuning and their applications as Li-ion battery anode materials. *Chem Soc Rev* 43(13):4341–4356
125. Zhu J et al (2011) Strain-sensing elastomer/carbon nanofiber “metacomposites.” *The Journal of Physical Chemistry C* 115(27):13215–13222
126. Qie L et al (2012) Nitrogen-doped porous carbon nanofiber webs as anodes for lithium ion batteries with a superhigh capacity and rate capability. *Adv Mater* 24(15):2047–2050
127. Serp P, Corrias M, Kalck P (2003) Carbon nanotubes and nanofibers in catalysis. *Appl Catal A* 253(2):337–358
128. Barcena J et al (2010) Processing of carbon nanofiber reinforced ZrB₂ matrix composites for aerospace applications. *Adv Eng Mater* 12(7):623–626
129. Guo Q et al (2009) Supercapacitors based on hybrid carbon nanofibers containing multiwalled carbon nanotubes. *J Mater Chem* 19(18):2810–2816
130. Teng M et al (2012) Electrospun mesoporous carbon nanofibers produced from phenolic resin and their use in the adsorption of large dye molecules. *Carbon* 50(8):2877–2886
131. Ahmed YM et al (2015) Efficient lead sorption from wastewater by carbon nanofibers. *Environ Chem Lett* 13(3):341–346
132. Si Y et al (2012) Fabrication of magnetic polybenzoxazine-based carbon nanofibers with Fe₃O₄ inclusions with a hierarchical porous structure for water treatment. *Carbon* 50(14):5176–5185
133. Zhu Z et al (2017) Adsorption-intensified degradation of organic pollutants over bifunctional α -Fe@ carbon nanofibres. *Environ Sci Nano* 4(2):302–306
134. Gupta AK et al (2010) Fe-grown carbon nanofibers for removal of arsenic (V) in wastewater. *Ind Eng Chem Res* 49(15):7074–7084
135. Amin M, Alazba A, Manzoor U (2014) A review of removal of pollutants from water/wastewater using different types of nanomaterials. *Adv Mater Sci Eng* 2014
136. Bi H et al (2012) Graphene: spongy graphene as a highly efficient and recyclable sorbent for oils and organic solvents. *Adv. Funct. Mater.* 22(21):4401–4401
137. Chowdhury S, Balasubramanian R (2014) Recent advances in the use of graphene-family nanoadsorbents for removal of toxic pollutants from wastewater. *Adv Coll Interface Sci* 204:35–56
138. Novoselov KS et al (2012) A roadmap for graphene. *Nature* 490(7419):192–200
139. Dreyer DR et al (2010) The chemistry of graphene oxide. *Chem Soc Rev* 39(1):228–240
140. Li J-L et al (2006) Oxygen-driven unzipping of graphitic materials. *Phys Rev Lett* 96(17):176101
141. Ramesha G et al (2011) Graphene and graphene oxide as effective adsorbents toward anionic and cationic dyes. *J Colloid Interface Sci* 361(1):270–277
142. Zhao J, Liu L, Li F (2015) Graphene oxide: physics and applications, vol 1. Springer
143. Yusuf M et al (2015) Applications of graphene and its derivatives as an adsorbent for heavy metal and dye removal: a systematic and comprehensive overview. *RSC Adv* 5(62):50392–50420
144. Carmalin Sophia A et al (2016) Application of graphene based materials for adsorption of pharmaceutical traces from water and wastewater-a review. *Desalin Water Treat* 57(57):27573–27586
145. Cortés-Arriagada D, Toro-Labbé A (2015) Improving As (iii) adsorption on graphene based surfaces: impact of chemical doping. *Phys Chem Chem Phys* 17(18):12056–12064
146. Minitha C et al (2017) Adsorption behaviour of reduced graphene oxide towards cationic and anionic dyes: Co-action of electrostatic and π - π interactions. *Mater Chem Phys* 194:243–252

147. Lee D-W, Kim T, Lee M (2011) An amphiphilic pyrene sheet for selective functionalization of graphene. *Chem Commun* 47(29):8259–8261
148. Wang F (2017) Effect of oxygen-containing functional groups on the adsorption of cationic dye by magnetic graphene nanosheets. *Chem Eng Res Des* 128:155–161
149. Tan P et al (2017) Effect of the degree of oxidation and defects of graphene oxide on adsorption of Cu²⁺ from aqueous solution. *Appl Surf Sci* 423:1141–1151
150. Pandey A et al (2018) 3D oxidized graphene frameworks: An efficient adsorbent for methylene blue. *JOM* 70(4):469–472
151. Yan H et al (2014) Effects of the oxidation degree of graphene oxide on the adsorption of methylene blue. *J Hazard Mater* 268:191–198
152. Peng W et al (2016) Adsorption of methylene blue on graphene oxide prepared from amorphous graphite: Effects of pH and foreign ions. *J Mol Liq* 221:82–87
153. Yang S-T et al (2011) Removal of methylene blue from aqueous solution by graphene oxide. *J Colloid Interface Sci* 359(1):24–29
154. Liu T et al (2012) Adsorption of methylene blue from aqueous solution by graphene. *Colloids Surf, B* 90:197–203
155. Zhang W et al (2011) Fast and considerable adsorption of methylene blue dye onto graphene oxide. *Bull Environ Contam Toxicol* 87(1):86
156. Zamani S, Tabrizi NS (2015) Removal of methylene blue from water by graphene oxide aerogel: thermodynamic, kinetic, and equilibrium modeling. *Res Chem Intermed* 41(10):7945–7963
157. Hernandez Y et al (2008) High-yield production of graphene by liquid-phase exfoliation of graphite. *Nat Nanotechnol* 3(9):563
158. Mahmoodi NM et al (2017) Preparation of modified reduced graphene oxide nanosheet with cationic surfactant and its dye adsorption ability from colored wastewater. *J Surfactants Deterg* 20(5):1085–1093
159. Su J et al (2018) Efficient preparation of cetyltrimethylammonium bromide-graphene oxide composite and its adsorption of Congo red from aqueous solutions. *Colloids Surf, A* 554:227–236
160. Lv M et al (2018) Non-covalent functionalized graphene oxide (GO) adsorbent with an organic gelator for co-adsorption of dye, endocrine-disruptor, pharmaceutical and metal ion. *Chem Eng J* 349:791–799
161. Yao Y et al (2012) Synthesis, characterization, and adsorption properties of magnetic Fe₃O₄@ graphene nanocomposite. *Chem Eng J* 184:326–332
162. Jiao T et al (2015) Facile and scalable preparation of graphene oxide-based magnetic hybrids for fast and highly efficient removal of organic dyes. *Sci Rep* 5:12451
163. Zambare R et al (2017) Ultrafast dye removal using ionic liquid–graphene oxide sponge. *ACS Sustainable Chemistry & Engineering* 5(7):6026–6035
164. Hu L et al (2016) Fabrication of hyperbranched polyamine functionalized graphene for high-efficiency removal of Pb (II) and methylene blue. *Chem Eng J* 287:545–556
165. Chen D et al (2016) Functionalization of 4-aminothiophenol and 3-aminopropyltriethoxysilane with graphene oxide for potential dye and copper removal. *J Hazard Mater* 310:179–187
166. Kim DW et al (2018) Preparation of a graphene oxide/faujasite composite adsorbent. *Microporous Mesoporous Mater* 268:243–250
167. El Essawy NA et al (2017) Green synthesis of graphene from recycled PET bottle wastes for use in the adsorption of dyes in aqueous solution. *Ecotoxicol Environ Saf* 145:57–68
168. Wei M-P et al (2018) Sulfonated graphene oxide as an adsorbent for removal of Pb²⁺ and methylene blue. *J Colloid Interface Sci* 524:297–305
169. Mahto A et al (2018) Solvent-free production of nano-FeS anchored graphene from *Ulva fasciata*: A scalable synthesis of super-adsorbent for lead, chromium and dyes. *J Hazard Mater* 353:190–203
170. de Araujo, CMB et al (2018) Systematic study of graphene oxide production using factorial design techniques and its application to the adsorptive removal of methylene blue dye in aqueous medium. *Mater Res Express* 5(6):065042

171. Balkız G et al (2018) Graphene oxide/alginate quasi-cryogels for removal of methylene blue. *Water Air Soil Pollut* 229(4):131
172. Othman NH et al (2018) Adsorption kinetics of methylene blue dyes onto magnetic graphene oxide. *J Environ Chem Eng* 6(2):2803–2811
173. Xu J et al (2018) Adsorptive removal of an anionic dye Congo red by flower-like hierarchical magnesium oxide (MgO)-graphene oxide composite microspheres. *Appl Surf Sci* 435:1136–1142
174. Ojha A, Thareja P (2018) Electrolyte induced rheological modulation of graphene oxide suspensions and its applications in adsorption. *Appl Surf Sci* 435:786–798
175. Liu Y et al (2018) A mussel-induced method to fabricate reduced graphene oxide/halloysite nanotubes membranes for multifunctional applications in water purification and oil/water separation. *Chem Eng J* 336:263–277
176. Zhao S et al (2018) Synthesis of graphene oxide/metal–organic frameworks hybrid materials for enhanced removal of Methylene blue in acidic and alkaline solutions. *J Chem Technol Biotechnol* 93(3):698–709
177. Aboelfetoh EF, Elhelaly AA, Gemeay AH (2018) Synergistic effect of Cu (II) in the one-pot synthesis of reduced graphene oxide (rGO/CuxO) nanohybrids as adsorbents for cationic and anionic dyes. *J Environ Chem Eng* 6(1):623–634
178. Sham AY, Notley SM (2018) Adsorption of organic dyes from aqueous solutions using surfactant exfoliated graphene. *J Environ Chem Eng* 6(1):495–504
179. Huong PTL et al (2018) Functional manganese ferrite/graphene oxide nanocomposites: effects of graphene oxide on the adsorption mechanisms of organic MB dye and inorganic As (v) ions from aqueous solution. *RSC Adv* 8(22):12376–12389
180. Luo S, Wang J (2018) MOF/graphene oxide composite as an efficient adsorbent for the removal of organic dyes from aqueous solution. *Environ Sci Pollut Res* 25(6):5521–5528
181. Zhang Y et al (2018) The utilization of a three-dimensional reduced graphene oxide and montmorillonite composite aerogel as a multifunctional agent for wastewater treatment. *RSC Adv* 8(8):4239–4248
182. Wang W et al (2017) A novel poly (m-phenylenediamine)/reduced graphene oxide/nickel ferrite magnetic adsorbent with excellent removal ability of dyes and Cr (VI). *J Alloy Compd* 722:532–543
183. Geng J et al (2018) Correction: 3D nitrogen-doped graphene gels as robust and sustainable adsorbents for dyes. *New J Chem* 42(3):2321–2322
184. Wang F et al (2017) Fe₃O₄@ SiO₂@ CS-TETA functionalized graphene oxide for the adsorption of methylene blue (MB) and Cu (II). *Appl Surf Sci* 420:970–981
185. Yu B et al (2015) Magnetic graphene sponge for the removal of methylene blue. *Appl Surf Sci* 351:765–771
186. Ge H et al (2016) Synthesis of citric acid functionalized magnetic graphene oxide coated corn straw for methylene blue adsorption. *Biores Technol* 221:419–429
187. Gui C-X et al (2014) Sandwichlike magnesium silicate/reduced graphene oxide nanocomposite for enhanced Pb²⁺ and methylene blue adsorption. *ACS Appl Mater Interfaces* 6(16):14653–14659
188. Wang H et al (2016) Microwave-assisted synthesis of reduced graphene oxide/titania nanocomposites as an adsorbent for methylene blue adsorption. *Appl Surf Sci* 360:840–848
189. Cheng Z et al (2015) One-step fabrication of graphene oxide enhanced magnetic composite gel for highly efficient dye adsorption and catalysis. *ACS Sustainable Chemistry & Engineering* 3(7):1677–1685
190. Tiwari JN et al (2013) Reduced graphene oxide-based hydrogels for the efficient capture of dye pollutants from aqueous solutions. *Carbon* 56:173–182
191. Wu Z et al (2017) Highly efficient adsorption of Congo red in single and binary water with cationic dyes by reduced graphene oxide decorated NH₂-MIL-68 (Al). *J Mol Liq* 247:215–229
192. Ansari MO et al (2017) Anion selective pTSA doped polyaniline@ graphene oxide-multiwalled carbon nanotube composite for Cr (VI) and Congo red adsorption. *J Colloid Interface Sci* 496:407–415

193. Xie H, Xiong X (2017) A porous molybdenum disulfide and reduced graphene oxide nanocomposite (MoS₂-rGO) with high adsorption capacity for fast and preferential adsorption towards Congo red. *J Environ Chem Eng* 5(1):1150–1158
194. Wu Z-L et al (2016) A sandwich-structured graphene-based composite: preparation, characterization, and its adsorption behaviors for Congo red. *Colloids Surf, A* 509:65–72
195. Ling Q et al (2014) Preparation of highly dispersed Ce–Fe bimetallic oxides on graphene and their superior adsorption ability for Congo red. *RSC Adv* 4(8):4020–4027
196. Cheng Z-L, Li Y-X, Liu Z (2017) Fabrication of graphene oxide/silicalite-1 composites with hierarchical porous structure and investigation on their adsorption performance for rhodamine B. *J Ind Eng Chem* 55:234–243
197. Liu K et al (2015) Adsorption and removal of rhodamine B from aqueous solution by tannic acid functionalized graphene. *Colloids Surf, A* 477:35–41
198. Das TR et al (2018) Bismuth oxide decorated graphene oxide nanocomposites synthesized via sonochemical assisted hydrothermal method for adsorption of cationic organic dyes. *J Colloid Interface Sci* 509:82–93
199. Wu Z et al (2018) Effective removal of high-chroma rhodamine B over Sn_{0.215}In_{0.385}/reduced graphene oxide composite: synergistic factors and mechanism of adsorption enrichment and visible photocatalytic degradation. *Powder Technol* 329:217–231
200. Alwan SH, Alshamsi HAH, Jasim LS (2018) Rhodamine B removal on A-rGO/cobalt oxide nanoparticles composite by adsorption from contaminated water. *J Mol Struct* 1161:356–365
201. Yang Q et al (2018) Three dimensional reduced graphene oxide/ZIF-67 aerogel: effective removal cationic and anionic dyes from water. *Chem Eng J* 348:202–211
202. Bharath G et al (2017) Development of adsorption and electrosorption techniques for removal of organic and inorganic pollutants from wastewater using novel magnetite/porous graphene-based nanocomposites. *Sep Purif Technol* 188:206–218
203. Wang H, Wei Y (2017) Magnetic graphene oxide modified by chloride imidazole ionic liquid for the high-efficiency adsorption of anionic dyes. *RSC Adv* 7(15):9079–9089
204. Shi Y-C et al (2016) Green-assembly of three-dimensional porous graphene hydrogels for efficient removal of organic dyes. *J Colloid Interface Sci* 484:254–262
205. Chaudhuri H et al (2017) Room-temperature in-situ design and use of graphene oxide-SBA-16 composite for water remediation and reusable heterogeneous catalysis. *ChemistrySelect* 2(5):1835–1842
206. Naeem H et al (2018) Synthesis and characterization of graphene oxide sheets integrated with gold nanoparticles and their applications to adsorptive removal and catalytic reduction of water contaminants. *RSC Adv* 8(7):3599–3610
207. Guo Y et al (2016) Removal of anionic azo dye from water with activated graphene oxide: kinetic, equilibrium and thermodynamic modeling. *RSC Adv* 6(46):39762–39773
208. Wu W et al (2013) Highly efficient removal of Cu (II) from aqueous solution by using graphene oxide. *Water Air Soil Pollut* 224(1):1372
209. Zhao C et al (2016) EDTA- and amine-functionalized graphene oxide as sorbents for Ni (II) removal. *Desalin Water Treat* 57(19):8942–8951
210. Yoon Y et al (2017) Synthesis of magnetite/non-oxidative graphene composites and their application for arsenic removal. *Sep Purif Technol* 178:40–48
211. Sreepasad TS et al (2011) Reduced graphene oxide–metal/metal oxide composites: facile synthesis and application in water purification. *J Hazard Mater* 186(1):921–931
212. Kumar ASK, Jiang S-J (2016) Chitosan-functionalized graphene oxide: A novel adsorbent an efficient adsorption of arsenic from aqueous solution. *J Environ Chem Eng* 4(2):1698–1713
213. Fan L et al (2013) Highly selective adsorption of lead ions by water-dispersible magnetic chitosan/graphene oxide composites. *Colloids Surf, B* 103:523–529
214. Zhao L et al (2015) Facile hydrothermal preparation of recyclable S-doped graphene sponge for Cu²⁺ adsorption. *J Hazard Mater* 286:449–456
215. Huang Z-H et al (2011) Adsorption of lead (II) ions from aqueous solution on low-temperature exfoliated graphene nanosheets. *Langmuir* 27(12):7558–7562

216. Deng X et al (2010) The adsorption properties of Pb (II) and Cd (II) on functionalized graphene prepared by electrolysis method. *J Hazard Mater* 183(1–3):923–930
217. Madandarg, C., H. Kim, and G. GAO, Adsorption behavior of EDTA-graphene oxide for Pb(II) removal. *ACS Applied Materials Interfaces*, 2012. 4(3): p. 1186–1193.
218. Zhao G et al (2011) Removal of Pb(ii) ions from aqueous solutions on few-layered graphene oxide nanosheets. *Dalton Trans* 40(41):10945–10952
219. Lee Y-C, Yang J-W (2012) Self-assembled flower-like TiO₂ on exfoliated graphite oxide for heavy metal removal. *J Ind Eng Chem* 18(3):1178–1185
220. Musico YLF et al (2013) Improved removal of lead (II) from water using a polymer-based graphene oxide nanocomposite. *Journal of Materials Chemistry A* 1(11):3789–3796
221. Sitko R et al (2013) Adsorption of divalent metal ions from aqueous solutions using graphene oxide. *Dalton Trans* 42(16):5682–5689
222. Hao L et al (2012) SiO₂/graphene composite for highly selective adsorption of Pb(II) ion. *J Colloid Interface Sci* 369(1):381–387
223. Yang X et al (2012) Graphene oxide-iron oxide and reduced graphene oxide-iron oxide hybrid materials for the removal of organic and inorganic pollutants. *RSC Adv* 2(23):8821–8826
224. Pirveysian M, Ghiaci M (2018) Synthesis and characterization of sulfur functionalized graphene oxide nanosheets as efficient sorbent for removal of Pb²⁺, Cd²⁺, Ni²⁺ and Zn²⁺ ions from aqueous solution: A combined thermodynamic and kinetic studies. *Appl Surf Sci* 428:98
225. Awad FS et al (2017) Efficient removal of heavy metals from polluted water with high selectivity for mercury (II) by 2-imino-4-thiobiuret–partially reduced graphene oxide (IT-PRGO). *ACS Appl Mater Interfaces* 9(39):34230–34242
226. Hu Z et al (2017) Recyclable graphene oxide-covalently encapsulated magnetic composite for highly efficient Pb (II) removal. *J Environ Chem Eng* 5(5):4630–4638
227. Fang Q et al (2017) Hydroxyl-containing organic molecule induced self-assembly of porous graphene monoliths with high structural stability and recycle performance for heavy metal removal. *Chem Eng J* 308:1001–1009
228. Aghagoli MJ, Shemirani F (2017) Hybrid nanosheets composed of molybdenum disulfide and reduced graphene oxide for enhanced solid phase extraction of Pb (II) and Ni (II). *Microchim Acta* 184(1):237–244
229. Zare-Dorabei R et al (2016) Highly efficient simultaneous ultrasonic-assisted adsorption of Pb(II), Cd(II), Ni(II) and Cu (II) ions from aqueous solutions by graphene oxide modified with 2,2'-dipyridylamine: Central composite design optimization. *Ultrason Sonochem* 32:265–276
230. Liu Y et al (2016) Graphene oxides cross-linked with hyperbranched polyethylenimines: preparation, characterization and their potential as recyclable and highly efficient adsorption materials for lead (II) ions. *Chem Eng J* 285:698–708
231. Li F et al (2016) A lignosulfonate-modified graphene hydrogel with ultrahigh adsorption capacity for Pb (II) removal. *Journal of Materials Chemistry A* 4(30):11888–11896
232. Luo S et al (2014) Amino siloxane oligomer-linked graphene oxide as an efficient adsorbent for removal of Pb (II) from wastewater. *J Hazard Mater* 274:145–155
233. Pakulski D et al (2018) Graphene oxide-branched polyethylenimine foams for efficient removal of toxic cations from water. *Journal of Materials Chemistry A* 6(20):9384–9390
234. Jiang T et al (2015) Adsorption behavior of copper ions from aqueous solution onto graphene oxide–CdS composite. *Chem Eng J* 259:603–610
235. Tan P et al (2015) Adsorption of Cu(2+), Cd(2+) and Ni(2+) from aqueous single metal solutions on graphene oxide membranes. *J Hazard Mater* 297:251–260
236. Liu J et al (2016) A novel reusable nanocomposite adsorbent, xanthated Fe₃O₄-chitosan grafted onto graphene oxide, for removing Cu (II) from aqueous solutions. *Appl Surf Sci* 367:327–334
237. Suddai A et al (2018) Feasibility of hard acid–base affinity for the pronounced adsorption capacity of manganese (ii) using amino-functionalized graphene oxide. *RSC Adv* 8(8):4162–4171

238. Kong D et al (2017) Facile preparation of ion-imprinted chitosan microspheres enwrapping Fe₃O₄ and graphene oxide by inverse suspension cross-linking for highly selective removal of copper (II). *ACS Sustainable Chemistry & Engineering* 5(8):7401–7409
239. Guo Y, Jia Z, Cao M (2017) Surface modification of graphene oxide by pyridine derivatives for copper (II) adsorption from aqueous solutions. *J Ind Eng Chem* 53:325–332
240. Yi X et al (2018) Graphene oxide encapsulated polyvinyl alcohol/sodium alginate hydrogel microspheres for Cu (II) and U (VI) removal. *Ecotoxicol Environ Saf* 158:309–318
241. Zhao G et al (2011) Few-layered graphene oxide nanosheets as superior sorbents for heavy metal ion pollution management. *Environ Sci Technol* 45(24):10454–10462
242. Fang F et al (2014) Removal of cobalt ions from aqueous solution by an amination graphene oxide nanocomposite. *J Hazard Mater* 270:1–10
243. Liang Q et al (2018) Facile one-pot preparation of nitrogen-doped ultra-light graphene oxide aerogel and its prominent adsorption performance of Cr (VI). *Chem Eng J* 338:62–71
244. Ramalingam B et al (2018) Biomaterial functionalized graphene-magnetite nanocomposite: a novel approach for simultaneous removal of anionic dyes and heavy-metal ions. *ACS Sustainable Chemistry & Engineering* 6(5):6328–6341
245. Zhao D et al (2016) Facile preparation of amino functionalized graphene oxide decorated with Fe₃O₄ nanoparticles for the adsorption of Cr (VI). *Appl Surf Sci* 384:1–9
246. Wang H et al (2013) Adsorption characteristics and behaviors of graphene oxide for Zn (II) removal from aqueous solution. *Appl Surf Sci* 279:432–440
247. Yang X et al (2018) Removal of Mn (II) by sodium alginate/graphene oxide composite double-network hydrogel beads from aqueous solutions. *Sci Rep* 8(1):1–16
248. Deng J-H et al (2013) Simultaneous removal of Cd (II) and ionic dyes from aqueous solution using magnetic graphene oxide nanocomposite as an adsorbent. *Chem Eng J* 226:189–200
249. Wu S et al (2015) Enhanced adsorption of cadmium ions by 3D sulfonated reduced graphene oxide. *Chem Eng J* 262:1292–1302
250. Rathore E, Biswas K (2018) Selective and ppb level removal of Hg (ii) from water: synergistic role of graphene oxide and SnS₂. *Journal of Materials Chemistry A* 6(27):13142–13152
251. Zhou C et al (2017) Adsorption of mercury (II) with an Fe₃O₄ magnetic polypyrrole–graphene oxide nanocomposite. *RSC Adv* 7(30):18466–18479
252. Chen X et al (2016) Photocatalytic oxidation of methane over silver decorated zinc oxide nanocatalysts. *Nat Commun* 7:12273
253. Kumar ASK, Jiang S-J, Tseng W-L (2016) Facile synthesis and characterization of thiol-functionalized graphene oxide as effective adsorbent for Hg (II). *J Environ Chem Eng* 4(2):2052–2065
254. La DD et al (2017) Fabrication of a GNP/Fe–Mg binary oxide composite for effective removal of arsenic from aqueous solution. *ACS Omega* 2(1):218–226
255. Jauris I et al (2016) Adsorption of sodium diclofenac on graphene: a combined experimental and theoretical study. *Phys Chem Chem Phys* 18(3):1526–1536
256. Indrawirawan S et al (2015) Nanocarbons in different structural dimensions (0–3D) for phenol adsorption and metal-free catalytic oxidation. *Appl Catal B* 179:352–362
257. Vineh MB et al (2018) Physical adsorption of horseradish peroxidase on reduced graphene oxide nanosheets functionalized by amine: A good system for biodegradation of high phenol concentration in wastewater. *International Journal of Environmental Research* 12(1):45–57
258. Boruah PK et al (2017) Magnetically recoverable Fe₃O₄/graphene nanocomposite towards efficient removal of triazine pesticides from aqueous solution: investigation of the adsorption phenomenon and specific ion effect. *Chemosphere* 168:1058–1067
259. Zhou X et al (2016) Ionic liquids modified graphene oxide composites: a high efficient adsorbent for phthalates from aqueous solution. *Sci Rep* 6(1):38417
260. Gaber D et al (2017) Graphene as an efficient and reusable adsorbent compared to activated carbons for the removal of phenol from aqueous solutions. *Water Air Soil Pollut* 228(9):320
261. Li Y et al (2012) Equilibrium, kinetic and thermodynamic studies on the adsorption of phenol onto graphene. *Mater Res Bull* 47(8):1898–1904

262. Kwon J, Lee B (2015) Bisphenol A adsorption using reduced graphene oxide prepared by physical and chemical reduction methods. *Chem Eng Res Des* 104:519–529
263. Wang X et al (2015) Three-dimensional graphene aerogels–mesoporous silica frameworks for superior adsorption capability of phenols. *Sep Purif Technol* 153:7–13
264. Feng J et al (2017) Preparation of black-pearl reduced graphene oxide–sodium alginate hydrogel microspheres for adsorbing organic pollutants. *J Colloid Interface Sci* 508:387–395
265. Catherine HN et al (2018) Adsorption mechanism of emerging and conventional phenolic compounds on graphene oxide nanoflakes in water. *Sci Total Environ* 635:629–638
266. Gan L et al (2018) Graphene oxide incorporated alginate hydrogel beads for the removal of various organic dyes and bisphenol A in water. *Colloid Polym Sci* 296(3):607–615
267. Wang P et al (2016) Synthesis and application of magnetic reduced graphene oxide composites for the removal of bisphenol A in aqueous solution—a mechanistic study. *RSC Adv* 6(104):102348–102358
268. Chang Y-P et al (2012) Preparation and characterization of Fe₃O₄/graphene nanocomposite and investigation of its adsorption performance for aniline and p-chloroaniline. *Appl Surf Sci* 261:504–509
269. Zavareh S, Norouzi E (2017) Impregnation of GO with Cu²⁺ for enhancement of aniline adsorption and antibacterial activity. *Journal of water process engineering* 20:160–167
270. Mukwevho N et al (2020) Removal of naphthalene from simulated wastewater through adsorption-photodegradation by ZnO/Ag/GO nanocomposite. *J Ind Eng Chem* 81:393–404
271. Yu F, Ma J, Bi D (2015) Enhanced adsorptive removal of selected pharmaceutical antibiotics from aqueous solution by activated graphene. *Environ Sci Pollut Res* 22(6):4715–4724
272. Zhuang Y et al (2017) Enhanced adsorption removal of antibiotics from aqueous solutions by modified alginate/graphene double network porous hydrogel. *J Colloid Interface Sci* 507:250–259
273. Chen H, Gao B, Li H (2015) Removal of sulfamethoxazole and ciprofloxacin from aqueous solutions by graphene oxide. *J Hazard Mater* 282:201–207
274. Fei Y et al (2016) Adsorptive removal of ciprofloxacin by sodium alginate/graphene oxide composite beads from aqueous solution. *J Colloid Interface Sci* 484:196–204
275. Tang Y et al (2013) Synthesis of reduced graphene oxide/magnetite composites and investigation of their adsorption performance of fluoroquinolone antibiotics. *Colloids Surf, A* 424:74–80
276. Li M-F et al (2018) Performance of magnetic graphene oxide/diethylenetriaminepentaacetic acid nanocomposite for the tetracycline and ciprofloxacin adsorption in single and binary systems. *J Colloid Interface Sci* 521:150–159
277. Al-Khateeb LA, Almotiry S, Salam MA (2014) Adsorption of pharmaceutical pollutants onto graphene nanoplatelets. *Chem Eng J* 248:191–199
278. Umbreen N et al (2018) Self-assembled three-dimensional reduced graphene oxide-based hydrogel for highly efficient and facile removal of pharmaceutical compounds from aqueous solution. *J Colloid Interface Sci* 527:356–367
279. Yu B et al (2017) Adsorption behaviors of tetracycline on magnetic graphene oxide sponge. *Mater Chem Phys* 198:283–290
280. Rostamian R, Behnejad H (2016) A comparative adsorption study of sulfamethoxazole onto graphene and graphene oxide nanosheets through equilibrium, kinetic and thermodynamic modeling. *Process Saf Environ Prot* 102:20–29
281. Ying Y et al (2017) Recent advances of nanomaterial-based membrane for water purification. *Appl Mater Today* 7:144–158

Chapter 9

Nanoparticles-Based Adsorbents for Water Pollutants Removal



Ayushi Jain, Shweta Wadhawan, and S. K. Mehta

Abstract Water pollution can cause severe health hazards in living organisms since most of the contaminants are toxic, mutagenic, and carcinogenic. There is a critical need to decontaminate the water from industrial effluents preceding their discharge into water bodies. The current chapter explores the potential of various nanoparticle-based adsorbents with special reference to nano zero-valent iron (NZVI), iron oxide, titanium, alumina, and silica in the field of adsorptive hosting of inorganic and organic pollutants from aqueous solutions. The nano adsorbents exhibit greater adsorption capacity, rapid adsorption rate, and competence to host various pollutants, recyclability, and reusability when compared to conventional adsorbents. These properties emphasize the relevance of nano adsorbents for the remediation of water contaminated with heavy metal ions, dyes, and chlorinated organic compounds. This chapter gives an overview of the progress and application of bare and functionalized metal and metal oxide nanoparticles for this purpose. Moreover, the mechanism of heavy metal ions, dyes, and organic chlorinated compounds removal by nanoparticles has also been discussed. The present chapter offers advanced information about the imperative characteristics of some metal and metal oxide-based nanoparticles and demonstrates their advantages as adsorbents in water remediation.

Keywords Degradation · Functionalization · Nano adsorbents · Water remediation

A. Jain · S. Wadhawan (✉)

Department of Chemistry, Panjab University Research Centre, Goswami Ganesh Dutta Sanatan Dharma College, Sector 32C, Chandigarh, U.T. 160031, India
e-mail: shewta.wadhawan@ggdsd.ac.in

A. Jain · S. K. Mehta

Department of Chemistry and Centre for Advanced Studies in Chemistry, Panjab University, Sector 14, Chandigarh, U.T. 160014, India
e-mail: skmehta@pu.ac.in

9.1 Introduction

Extensive growth in the population of the world, along with urbanization, has led to the rising demand for fresh water [1]. About 1.2 billion people in the world do not have access to hygienic and safe drinking water, and this issue is anticipated to augment in the years to come [2]. In addition, contamination of water with a variety of pollutants such as heavy metal ions, dyes, chlorinated organic compounds, pharmaceuticals, sediments, and radioactive contaminants has intensified the problem [3]. Among these contaminants, heavy metal ions, even in relatively small quantities, cause severe health vulnerability to human beings since they are poisonous, persistent, and non-biodegradable in nature. The effluence of heavy metal ions into water bodies caused by widespread industrialization and unsystematic removal results in contamination of aquatic ecosystems [4]. For instance, Pb^{2+} is employed in various industrial products, i.e., battery, pigments, printing, explosive, and fuel manufacturing. The Environmental Protection Agency (EPA) has recommended that the maximum Pb^{2+} contamination level in drinking water is $15 \text{ l } \mu\text{g L}^{-1}$. The toxic effects of Pb^{2+} ions in human beings include inhibition of hemopoiesis, germinal cell dysfunction, hypertension, cognitive deformities, miscarriages, renal dysfunctions, and nervous disorders. Therefore, the elimination of Pb^{2+} from water is necessary to save living organisms [5]. Another heavy metal ion, Hg^{2+} is the common inorganic form of Hg, which can be transformed into more poisonous organic forms through biological methylation [6]. Undesirable effects of Cu^{2+} in human beings encompass an accumulation of this ion in the liver leading to Wilson's disease, which further causes psycho-neurotic defects [7, 8]. The intake of Cu for humans should be below 5.0 mg d^{-1} , as recommended by the European Commission [9] and made mandatory in the WHO guidelines. As a result, the concentration of Cu in drinking water has been stipulated to below 2.0 mg L^{-1} [10]. Similar to Cu^{2+} , the devastating effects of numerous other heavy metal ions on the human body have been discussed by different scientists from time to time. In this regard, Cd leads to multiple chronic organ damage [11, 12], and Mn affects the CNS and respiratory system. Some of the ions like Ag^+ and Zn^{2+} are important trace elements but turn toxic when taken in higher amounts. The removal of Ag could protect the resources and benefit human beings' sustainable development [13]. Zn^{2+} in high doses can be toxic and cause detrimental health hazards to many biological and biochemical processes [14, 15].

Organic dyes constitute another category of pollutants that are released from several industries such as paint, cosmetics, textile, leather, pigment, paper, etc. [16]. Dyeing runoff has a dangerous impact on the environment since its presence in water causes carcinogenic effects. Moreover, colored effluents can decrease the level of O_2 in water by affecting the photosynthesis of aquatic plants, and in extreme cases, leading to the suffocation of aquatic plants and animals [17]. Amongst the diverse kinds of dyes, Methylene blue (MB) and Rhodamine B (RhB) are mainly used in textile manufacture. These dyes may lead to eye burns and, in extreme cases, result in permanent damage to the vision of humans and animals [18]. Literature studies reveal that inhalation or ingestion of RhB may cause harm to the liver and thyroid [19].

The stability and persistence of the dyes in the water increase if not treated properly. Consequently, it is essential to eliminate the perilous dyes from wastewater before disposing of these into the aquatic ecosystem with an appropriate treatment process [20]. Malachite green (MG), a triphenylmethane cationic water-soluble dye [21], has carcinogenic, mutagenic, and teratogenic effects on humans. Noxious substances are produced on MG degradation that causes damage to the liver, lungs, and bones [22–24]. For that reason, it is obligatory to eliminate these contaminants from effluents prior to their discharge into water bodies.

With the increasing water pollution resulting from various kinds of pollutants, it becomes of utmost importance to develop and apply water remediation techniques to diminish the effects of contaminants. Significant efforts have been dedicated to developing effective physical and chemical treatment processes for removing inorganic and organic pollutants from contaminated water [25]. The methods such as adsorption, ion exchange, ozonation, precipitation, membrane separation, etc., are being employed (Fig. 9.1) to eliminate pollutants from aqueous runoffs [26]. However, some of these techniques have limitations, such as high processing cost, sludge formation, and inappropriateness at a large scale (Fig. 9.1) [27].

Amongst different methods, huge consideration has been gained by the adsorption phenomenon because of its benefits such as simplicity, easy operation, recyclability, uncomplicated removal, and reusability [28]. The characteristics of a particular adsorbent depend on its specific surface area, composition, and accessibility of various functional groups; therefore, the effectiveness of an adsorption process

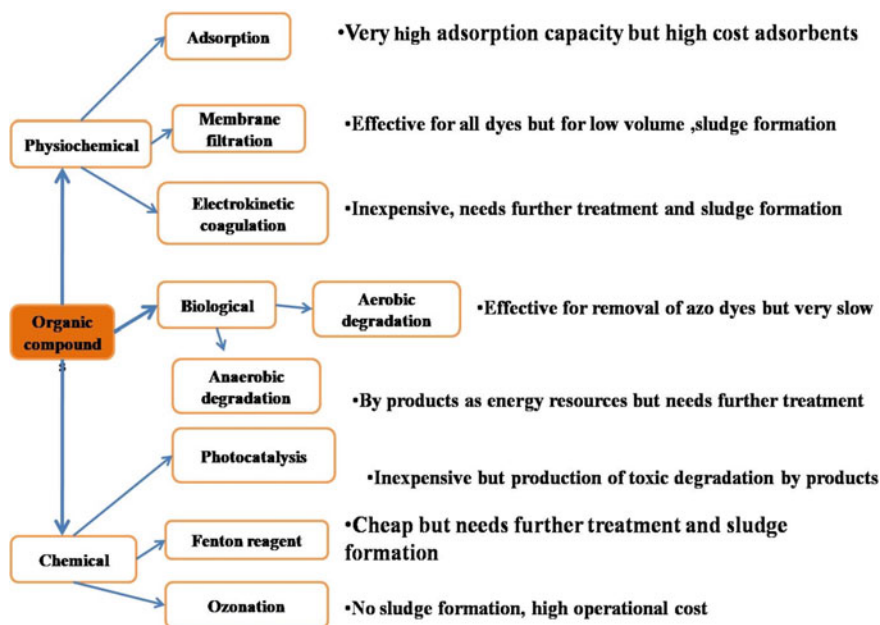


Fig. 9.1 Different techniques for the removal of dyes with positive and negative points

is controlled by these factors. Numerous adsorbents like ion-exchange resins, activated carbons [29–32], natural zeolites [33], chitosan [34], bio sorbents [35–37], and chelating materials [38, 39] have been investigated by the researchers for the elimination of pollutants from aqueous solutions. The ability of adsorbents depends on the presence of functional groups on their surfaces. For instance, an adsorbent with nitrogen-containing ligands (amino, amidoxime, hydrazine, and imidazole) are efficient in complexing metal ions [40–46].

In recent times, the production of nanomaterials with greater surface area, improved absorption capacity, and superior regeneration performance has exhibited immense potential in eliminating a wide range of pollutants [47]. For example, manganese oxides have been found to be excellent nano adsorbents for the uptake of heavy metal ions due to their greater adsorption ability, enhanced stability, and low price [48–50]. Also, the rational design and adsorbents possessing outstanding adsorption ability and easy separation are of paramount importance [51]. Compared with traditional adsorbents, magnetic nanoparticles have attracted intensive attention of many researchers and been widely used for the removal of heavy metals in wastewater treatment due to their excellent physical and chemical properties, such as super paramagnetism, high surface area, easy separation under external magnetic field and strong adsorption [52–55]. Based on these advantages, Fe_3O_4 nanoparticles were exploited to remove heavy metals from water by strong adsorption [56–60]. Not only heavy metal ions, metal oxide nano adsorbents also were extensively used for the hosting of dye pollutants owing to their enhanced surface area, improved photocatalytic properties, and reusability. The nanoparticle-based adsorbent can be recycled, thus leading to the production of very small volumes of sludge. A variety of metal and metal oxide nanoparticles like Fe/Ni [61], Ni [62], TiO_2 [63–66], ZnO [67–70], Fe_3O_4 , Fe_2O_3 [71–74], SnO_2 [75, 76] ZnS [77], CdS [78], WO_3 [79, 80] etc. have been utilized for hosting of both cationic and anionic dyes.

In addition to heavy metal ions and dyes, chlorinated organic compounds have also been effectively hosted mainly by metallic and bimetallic nanoparticles. Yet, there are fewer reports available on the use of metal oxide nanoparticles for the hosting of organo chlorines. The successful use of NZVI and Fe-based bimetallic in the hosting of organo chlorines has been demonstrated both in situ and ex situ, attributing to their high active surface area and higher number of adsorption sites. NZVI has been used for the effective hosting of heptachlor, lindane, pentachlorobenzene, and hexachlorobenzene [81].

The aim of this chapter is to explore the use of various types of metal and metal oxide-based nanomaterials for the adsorptive hosting of different water pollutants, particularly organo chlorinated compounds, dyes, and heavy metal ions, along with their mechanism of hosting. Further, the role and need for functionalization of these nanomaterials for the improved pollutant hosting performance has also been discussed in detail. The last section depicts the future perspective and research gaps regarding the use of these nanomaterials in the hosting of water pollutants.

9.2 Metal and Metal Oxide Nanoparticles

The hosting of water pollutants using metal and metal oxide-based nano adsorbents has emerged as the most promising approach for researchers. Many metal and metal oxide nanoparticles have been synthesized and employed for the removal of both organic (dyes and pesticides) and inorganic (heavy metal ions) pollutants present in the waste water. Among the metal nanoparticles, nanoscale zero-valent iron (NZVI) has emerged as the most successful nano adsorbent for hosting water pollutants, whereas a variety of metal oxide nanoparticles viz TiO_2 , iron oxides (Fe_2O_3 and Fe_3O_4), silicon dioxide (SiO_2), aluminium oxide (Al_2O_3), etc. have also been fabricated for adsorptive removal of water pollutants (Fig. 9.2). The role of these nano adsorbents in the removal of pollutants from water has been proved very significant.

9.2.1 Nanoscale Zero-Valent Iron (NZVI)

Zero valent iron has been widely used for the breakdown of chlorinated organic compounds and inorganic pollutants for water remediation. Iron in zero oxidation state (Fe^0) is known as zero-valent iron. Bulk zero-valent iron is a strong reducing agent that gets oxidized to Fe^{2+} upon reduction of pollutant molecules. Further, the properties of ZVI are improved when it is converted into nano-sized zero-valent iron. NZVI is of utmost importance owing to its improved properties like high surface area, greater thermal stability, less toxicity, better adsorption efficiency, and reducing properties as compared to bulk zero-valent iron. NZVI is obtained by both top-down and bottom-up approaches. Various studies describe the successful utilization of NZVI in the treatment of water containing pollutants viz heavy metals, dyes, and pesticides. An investigation [82] illustrated the use of NZVI for the complete removal of multiple heavy metal ions like Ni^{2+} , Hg^{2+} , and As^{5+} from water. In another study, the complete removal of As^{5+} from ground water was demonstrated [83] using NZVI,

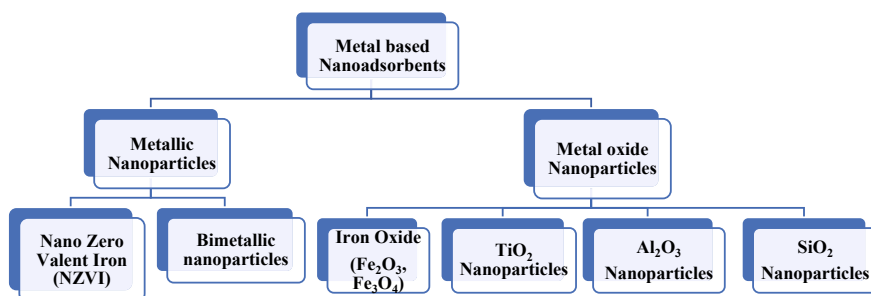


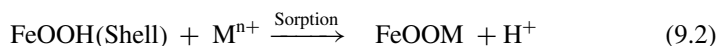
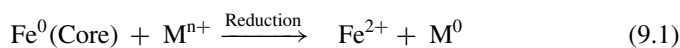
Fig. 9.2 Different types of metal-based nano adsorbents for hosting of water pollutants

where adsorption of As^{5+} was followed by precipitation. NZVI was found to be more effective as compared to ZVI in terms of efficiency and time duration.

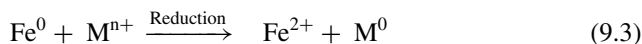
Most of the studies demonstrate that when bare NZVI is exposed to an aquatic system containing dissolved oxygen, an oxide layer is formed on its surface, which provides core-shell nature to NZVI, where the shell forms the oxidized layer that protects the Fe^0 state in the core. Consequently, the direct implication of using bare NZVI for hosting the pollutants leads to iron pollution as well as deactivation of NZVI. This issue can be resolved by functionalizing and entrapping the NZVI with some stabilizing agents, which not only prevents the quick oxidation of NZVI to magnetite but also provides functional groups for better hosting of contaminants. For example, NZVI can be entrapped into some non-toxic biomolecules like chitosan, cyclodextrins, cellulose, etc. One of the research studies demonstrated the use of functionalized NZVI, where it was entrapped into a complex of chitosan and cyclodextrin for the complete adsorptive hosting of Cr^{6+} and Cu^{2+} ions. The mechanism of metal ions hosting was supposed to be physisorption for both metal ions followed by their reduction i.e., Cr^{6+} and Cu^{2+} to Cr^{3+} and Cu^0 , respectively, by NZVI. In this case, NZVI itself gets oxidized from Fe^0 to Fe^{3+} [84].

NZVI has also found a promising use in the hosting of organic pollutants, i.e., organochlorinated pesticides and dyes, followed by their degradation in the waste water. NZVI has been employed for more than 97% removal of many pesticides, including lindane, hexachlorobenzene, pentachlorobenzene, and hexachlorobutadiene [81]. Similarly, some experimental studies describe that bare and functionalized NZVI can act as effective adsorbents for remediation of water contaminated by colored pollutants, i.e., dyes. The studies for the removal of various dyes viz. Basic Blue-3 [85], MB [86], AB24 [87], Reactive Red [88] etc. have been reported from time to time.

The possible mechanism of removal of heavy metal ions is based upon adsorption followed by reduction, precipitation, and co-precipitation depending upon the standard electrode potential of heavy metal ions (Fig. 9.3). The heavy metal ions like Pb^{2+} , Ni^{2+} and Cd^{2+} which possess reduction potential slightly higher than Fe^{2+} are reduced by Fe^0 core which is followed by their sorption on ferric hydroxide (FeOOH) shell (Eqs. 9.1 and 9.2)



On the other hand, for the heavy metal ions such as Cr^{6+} , Se^{2+} , Cu^{2+} and Hg^{2+} whose electrode potential is significantly higher than Fe^{2+} ions, the mechanism involves reduction by Fe^0 core followed by precipitation or co-precipitation by ferric hydroxide (FeOOH) shell (Eqs. 9.3–9.5).



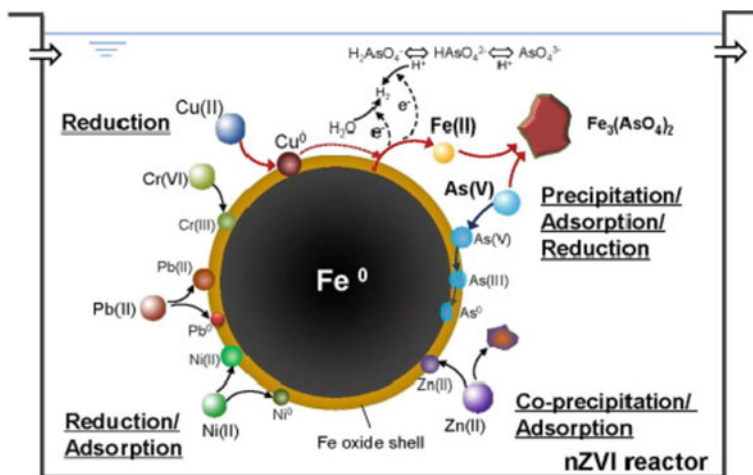
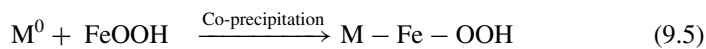
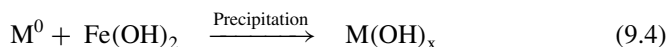
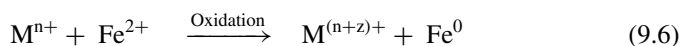


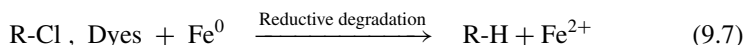
Fig. 9.3 Different possible mechanisms of heavy metal ions removal in NZVI reactor (adapted from 89 with permission)



Further, the metal ions such as Ba^{2+} and Zn^{2+} , whose standard electrode potential is lower than iron, get oxidized on the iron hydroxide shell (Eq. 9.6).



The mechanism of hosting of chlorinated pesticides and dyes generally comprises physisorption followed by reduction (Eq. 9.7)



The literature illustrates a variety of studies describing the use of bare as well as functionalized NZVI for the hosting of organic and inorganic water pollutants. In one of the reports [90], NZVI obtained from a plant extract of *Syzygium jambos* (Malabar plum) was employed for the effective hosting of Cr^{6+} with an adsorption capacity of 983.2 mg g^{-1} . In another study [91], 99% of As^{5+} was also removed using NZVI. Even though the use of NZVI for waste water treatment has many advantages still there are certain shortcomings with their use. NZVI gets easily agglomerated, resulting in reduced surface area for adsorption. Also, their oxidation in water hinders the reduction process leading to their deactivation. In order to

overcome these limitations, various functionalization strategies like a surface modification or doping (discussed in Sect. 9.2.5) have been developed. In a study, NZVI was surface functionalized by chitosan and employed for the removal of Cr^{6+} ions [92]. Also, the chitosan carboxymethyl β -cyclodextrin NZVI complex was fabricated for the effective removal of Cr^{6+} and Cu^{2+} ions [93]. The chitosan functionalized NZVI nanostructure possessed higher removal efficiency towards Cr^{6+} ions as compared to bare NZVI.

In addition to this, the use of NZVI for the decontamination of dyes and chlorinated organic compounds (R-Cl) from water has also been investigated. The hosting of these organic pollutants is based upon adsorption of pollutants on NZVI surface followed by their reductive degradation (Fig. 9.4). For example, an azo dye, i.e., Reactive Red A, was effectively removed using NZVI in the presence of hydrogen peroxide within 40 min [88]. The mechanism was based on the Fenton process where -OH free radicals are formed in two steps which lead to enhanced efficiency.

Adsorptive removal of a cationic dye, i.e., methylene blue with 100% efficiency using NZVI with adsorption capacity of 208.33 mg g^{-1} was reported [94], where the mechanism of removal was physisorption of dye onto the surface of NZVI via electrostatic interactions. Also, the NZVI supported on the surface of pillared clay for the effective hosting of Acid Red 315 dye where the removal efficiency of clay supported NZVI was found to be higher (100%) as compared to alone NZVI (80%), attributing to the enhanced surface area and higher number of functional groups [95].

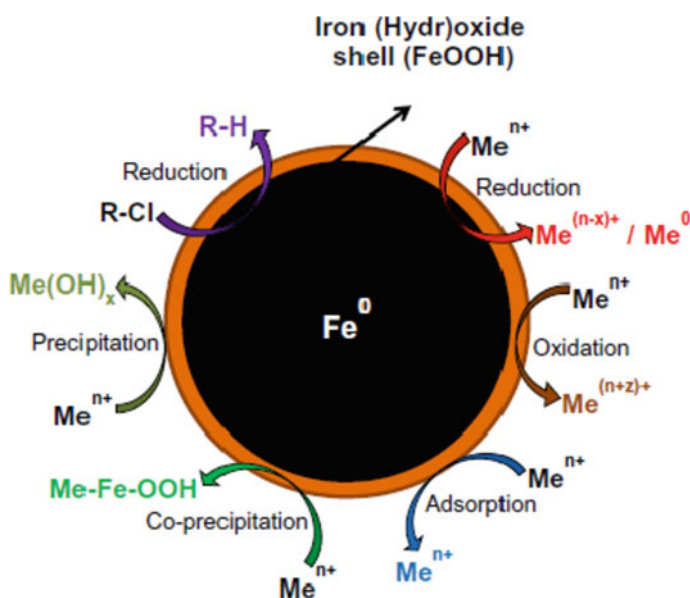


Fig. 9.4 Mechanisms of hosting of different water pollutants by NZVI (adapted with permission from [3])

NZVI alone or in combination with hydrogen peroxide has also been found effective in the hosting of chlorinated organic compounds from waste water in a Fenton-like process. The Fenton process using NZVI showed higher efficiency for hosting of pollutants attributing to the double formation of -OH radicals in contrast to conventional process which involves the use of bulk iron (Eqs. 9.8–9.10). This is the most important process for the removal of organic pollutants like dyes and organo chlorines.



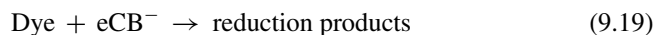
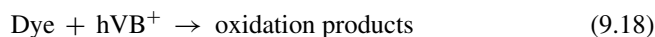
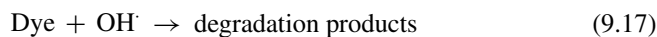
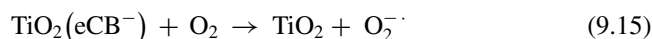
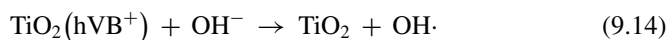
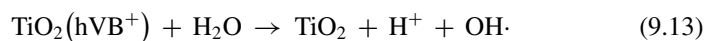
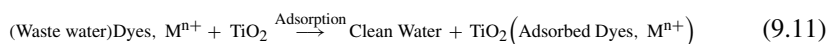
9.2.2 Nano Titanium Dioxide (TiO_2)

Nano TiO_2 generally exists in three forms; two of them are active crystalline phases, i.e., anatase and rutile, and the third is an amorphous phase, i.e., brookite. The anatase phase is distinguished for its photo catalytic behavior and used in sunscreen for protection to the skin against UV rays. In contrast, the rutile phase of TiO_2 is a stable phase. Photocatalytic behavior of nano TiO_2 (anatase) depends upon the band gap of the material, which in turn is dependent upon the size and mode of synthesis. Nano titanium oxide has been comprehensively used for hosting various organic and inorganic contaminants via both adsorption and photocatalytic degradation. This can be attributed to its excellent stability, less toxicity, biocompatibility, and strong oxidizing nature. Bare nano- TiO_2 has been employed for more than 95% removal of various organic dyes like Eriochrome Black T [96], Indigo Carmine [97], Methyl Orange [98], and Malachite Green [78]. The commercial use of bare TiO_2 nanoparticles is limited because these can be activated only through UV radiation due to the high energy band gap of 3.2 eV. Moreover, their separation from the dispersion solution is very complicated. These limitations can be overcome by the functionalization of nano TiO_2 . For this, TiO_2 NPs can be entrapped into a polymer matrix which not only increases the volume to surface area ratio of the polymer but also enhances the number of adsorption sites. A study illustrates the complete adsorptive removal of MB dye by employing a nanocomposite where TiO_2 nanoparticles were filled into polyacrylamide-based hydrogel [99]. Here, the mechanism of adsorption was mainly based upon the ion exchange process accompanying the adsorption of dye molecules on the surface of the adsorbent.

In addition to the fact that nano TiO_2 has been extensively employed for hosting of organic pollutants, it also found its use in the adsorptive removal of heavy metal ions. Many reports have described the use of mesoporous nano titania for the effective

removal of Cr^{6+} [100], Pb^{2+} , Cu^{2+} , Fe^{3+} , Cd^{2+} , Zn^{2+} [101], Fe^{3+} and As^{5+} [102]. The functionalized nano titania has proved to be a superior adsorbent as compared to bare TiO_2 NPs due to their greater surface area and easy separation. In addition, TiO_2 embedded in the polymer matrix has also been employed for the hosting of heavy metal ions via adsorption. For example, in a study, polyvinyl alcohol (PVA) coated TiO_2 was employed to host Cd^{2+} , Ni^{2+} , U^{6+} , and Th^{4+} ions [103–105] from an aqueous solution.

The mechanism of removal of heavy metal ions by TiO_2 usually consists of physical or chemical adsorption, whereas for organic dye pollutants, the adsorption process is followed by photocatalytic degradation (Eqs. 9.11–9.19).



Irradiation with UV light leads to the generation of electron–hole ($\text{hVB}^+ - \text{eCB}^-$) pair in TiO_2 . The positively charged hole interacts with water to produce $\cdot\text{OH}$ and H^+ ions, whereas electrons interact with dissolved O_2 to give superoxide ions ($\text{O}_2^{\cdot-}$) which further reacts with water to give rise to hydroxide (OH^-) ions and ($\cdot\text{OOH}$) peroxide radicals. Further, OH is formed by the combination of H^+ with $\cdot\text{OOH}$ and hole with OH^- . These $\cdot\text{OH}$ free radicals, holes, and electrons are responsible for the degradation of organic pollutants.

Researchers have illustrated the enormous use of bare and modified TiO_2 NPs and nanocomposites for the efficient hosting of heavy metal ions and organic dye pollutants. In this context, the mesoporous TiO_2 nanoparticles were fabricated with the highest Cr^{6+} ion uptake capacity of 26.1 mg g^{-1} than ever reported [100]. Not

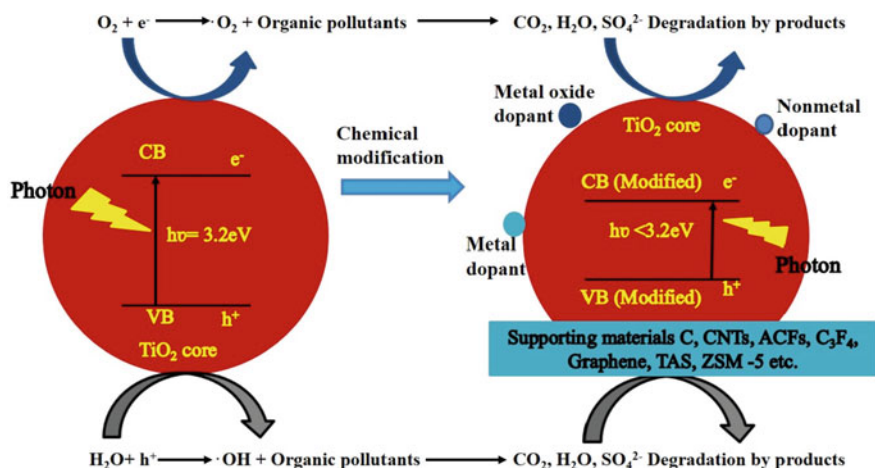


Fig. 9.5 Mechanism of hosting of organic pollutant by pure and modified nano titania (adapted with permission from [106])

only the nanoparticles, but nanowires of TiO_2 having a diameter of 30–50 nm were also established for the adsorptive hosting of different heavy metal ions viz Pb^{2+} , Fe^{3+} , Cu^{2+} , Cd^{2+} , and Zn^{2+} ions. The TiO_2 nanowires were found to be selectively effective for the maximum uptake, i.e., 97 and 80% towards Pb^{2+} and Fe^{3+} ions, respectively [101].

In addition to bare TiO_2 , functionalized and doped TiO_2 nanocomposites have also been investigated for the adsorptive uptake of metal ion pollutants. The addition of metal and non-metal dopant or different supporting materials results in enhanced removal efficiency of TiO_2 by reducing the band gap (Fig. 9.5). Razzaz et al. developed a nano fibrous nanocomposite of TiO_2 with chitosan for the adsorptive hosting of Pb^{2+} and Cu^{2+} ions [107]. Another nanocomposite, i.e., TiO_2 -chitosan fabricated using microwave synthesis technique were used for the 88, and 72.56% adsorption of Cu^{2+} and Cd^{2+} ions, respectively, and maximum adsorption capacity was obtained to be $1,800\text{ mol g}^{-1}$ [92]. Also, the nano TiO_2 coated with a biomolecule, i.e., starch, was also investigated for the hosting of Cd^{2+} , Cu^{2+} , Co^{2+} , Ni^{2+} and Pb^{2+} ions with 90% removal efficiency [108]. Besides this, doped nano TiO_2 has also been employed in heavy metal ions remediation, e.g., Fe-doped nano titania was used for the higher uptake of As^{5+} ions where the adsorption efficiency of doped nano titania was found to be higher than that of pure TiO_2 attributing to the enhanced surface area by grain growth termination and photo catalytic response [102]. Further, pure and modified nano TiO_2 can also be employed for the removal of organic dyes. The mechanism of removal of dyes is based on adsorption followed by photo catalytic degradation. In a batch adsorption experiment, Malachite Green dye was hosted by nano TiO_2 with 85% removal efficiency [77]. Sood et al. and Yang et al. investigated the use of nano TiO_2 for the 95% photo catalytic removal of Indigo Carmine dye [97] and 98.6% removal of Methyl Orange dyes [98]. Not only bare nano titania, functionalized or

doped nano TiO₂ have also been utilized for the removal of dyes. In a report, nano TiO₂ doped with Niobium (Nb), i.e., TiO₂: (Nb, N-x), were fabricated for the photocatalytic hosting of Methylene Blue dye (MB). The effect of doping was investigated on the removal efficiency, indicating the sixfold increased adsorption performance in doped NPs compared to bare ones [109], attributing to decreased band gap from 2.7 to 2.3 eV. In a batch experiment, TiO₂ nanoparticles doped with 0.5–2.5% Bi³⁺ were employed for the removal of Alizarin Red S dye, where removal efficiency was found to be as high as 80% [110]. Similarly, Pd and N co-doped nano TiO₂ were tested for the effective removal of Eosin Yellow dye [111]. Also, Ag⁺ doped TiO₂ was reported for 99% degradation of MB dye [112].

9.2.3 Nano Iron Oxide

Iron is the fourth most abundant element found in Earth's crust. It exists in divalent and trivalent oxidation states. There are three types of iron oxides, i.e., hematite (α -Fe₂O₃), maghemite (γ -Fe₂O₃), and magnetite (Fe₃O₄) whereas Fe exists in trivalent oxidation state in α -Fe₂O₃ and γ -Fe₂O₃, while in Fe₃O₄, both divalent and trivalent states exist. Nano iron oxide has received the great attention of researchers for hosting both organic and inorganic water pollutants through adsorption due to its abundance and simplicity of fabrication.

Both hematite (α -Fe₂O₃) and maghemite (γ -Fe₂O₃) nanoparticles possess great potential for the adsorptive removal of heavy metal ions from waste water. For this application, both have their own advantages. α -Fe₂O₃ is one of the most stable forms of nano iron oxide and exhibits corrosion resistant nature, whereas maghemite possesses a large surface area and is magnetically separable. Bare nano iron oxide (both α -Fe₂O₃ and γ -Fe₂O₃) have been employed for the removal of heavy metal ions like Cr⁶⁺, Cd²⁺, Cu²⁺, Pb²⁺, Zn²⁺, Al³⁺, Ni²⁺ and Mn²⁺ ions [113, 114] from the waste water. The mechanism of removal of heavy metal ions was based on electrostatic interactions, which were responsible for the adsorption of these metal ions. The surface of nano iron oxide is covered with FeOH due to water which forms either Fe⁺ OH₂ or FeO⁻ depending upon the pH of the solution. The increased number of FeO⁻ sites leads to increased adsorption of positively charged heavy metal ions and vice versa. Another simple, low cost and eco-friendly iron oxide, i.e., magnetite (Fe₃O₄), is also widely used as a nano adsorbent for hosting heavy metal ions. Magnetite also exhibits the property of magnetism which enables its easy separation from the solution after adsorption. Magnetite has also been used for the removal of Cr⁶⁺, Pb²⁺, Cu²⁺, Zn²⁺, Mn²⁺ [115–117] etc. Different values of adsorption capacities were obtained for diverse heavy metal ions using different iron oxide-based nano adsorbents. This can be accredited to the fact that various metal ions have different hydrated ionic radii in the aqueous solutions, which interact differently with dissimilar negatively charged adsorption sites. Metal ions with higher hydrated ionic radii adsorb weakly as compared to metal ions with lower hydrated ionic radii [118]. Scientific reports illustrate the extensive use of magnetic and non-magnetic nano

iron oxide for the hosting of organic and inorganic pollutants. In a study carried out by Iconaru et al., magnetite, i.e., nano Fe_3O_4 , was utilized for the removal of As^{5+} and Cu^{2+} ions where better efficiency of nano-magnetite was observed as compared to commercial magnetite [119]. In a batch adsorption experiment, nano-magnetite were demonstrated for the removal of Cu^{2+} , Pb^{2+} , Mn^{2+} and Zn^{2+} ions where highest and lowest adsorption capacities were observed towards Pb^{2+} and Mn^{2+} , respectively [120]. This is attributed to the difference in hydrated ionic radii of metal ions resulting in different electrostatic interactions of metal ions on the surface of the nanoparticle. Similarly, non-magnetic haematite, i.e., nano $\alpha\text{-Fe}_2\text{O}_3$, was investigated for the effective adsorption of Cd^{2+} and Cr^{6+} with the adsorption capacities of 146.41 and 16.17 mg g^{-1} , respectively [121, 122].

Nevertheless, the use of bare iron oxide nanoparticles suffers from the limitation of their easy oxidation in water due to the presence of Fe^{2+} ions, the tendency to agglomerate, and corrosion by acids and bases as well. These limitations can be overcome by the functionalization of nanoparticles with organic and inorganic shell materials, which not only prevent their oxidation but also provide sites for enhanced metal ion adsorption. Functionalization not merely improves the adsorption efficiency of the adsorbent but also provides chemical binding to the pollutant via electrostatic and Van der Waals interactions for the adsorptive hosting of pollutants on the surface of the adsorbent [123, 124]. Enhanced adsorption capacities have been reported with polymer functionalized iron oxide nanoparticles. The surface modification of these nanoparticles combines the advantage of a magnetic core with organic and inorganic shell. Many materials like polypyrrole, polyaniline, polyvinyl imidazole, silica, polyethylene glycol, chitosan, tannin and surfactants have been used for the functionalization which improved the adsorption capacity and stability of nano iron oxide [125–133]. A variety of studies demonstrated the use of functionalized nano iron oxide for the improved adsorption efficiency towards heavy metal ions. In a scientific investigation, improvement in stability, mechanical strength, and removal performance was observed where nano Fe_3O_4 were functionalized with a polymer, i.e., polymeric mercaptoethylamino [134] for the removal of Ag^+ , Hg^{2+} , Pb^{2+} , and Cd^{2+} ions and with polyacrylic acid and diethylenetriamine for the uptake of Cu^{2+} and Cr^{6+} with higher removal efficiency towards Cu^{2+} as compared to Cr^{6+} [135]. The higher adsorption capacity was calculated for Cu^{2+} ions as compared to Cr^{6+} ions. Furthermore, the toxicity of nano iron oxide was minimized along with improved metal ion uptake capacity by functionalization with some biomolecules like glycine [136] and carboxy methyl cellulose [137] for improved hosting of Pb^{2+} ions. The incorporation of amino functional groups in the former and chelation in the latter was responsible for the enhanced removal performance. Also, some organic molecules have been used as chelating ligands to increase the adsorption capacity and selectivity of nano iron oxide. In a scientific investigation, nano Fe_3O_4 were amino-functionalized with a chelating ligand, i.e., triethylenetetramine [138] for the 85% removal of Cu^{2+} ions and with humic acid [139] for the removal of Hg^{2+} , Pb^{2+} , Cd^{2+} , and Cu^{2+} ions where the adsorption capacity was found higher than bare nano- Fe_3O_4 .

In addition, nano iron oxides have also found their application in the removal of dyes. Both bare and coated iron oxide nanoparticles have been investigated for dye

adsorption. In a report, Reactive Red 2/A [140] was 95% removed adsorptively using nano-magnetite within 10 min. Another magnetite adsorbent functionalized by 3-aminopropyltriethoxysilane (APTES) was illustrated for the 96% adsorptive hosting of Sunset Yellow [141]. Similarly, surfactant i.e. sodium dodecyl sulphate (SDS) and hyperbranched polyglycerol modified Fe_3O_4 based nano adsorbent, were successfully demonstrated for the efficient removal of Crystal Violet [72] and MB [142] dyes, respectively. Scientists have also employed amino acids, i.e., L-arginine coated magnetite nano adsorbent for the elimination of Reactive Blue 19 dye [143] through adsorption. Not only bare and modified, but nano-magnetite supported on activated carbon surface have also proved as an efficient candidate for the dye pollutant hosting, attributing to the highly enhanced surface area of nano adsorbent. Magnetite mounted on activated carbon and Mn-doped magnetite doped on activated carbon have shown their implication in the elimination of MB [144] and MG [145] dyes with adsorption capacities of 117 and 87.5 mg g^{-1} , respectively.

9.2.4 Nano Silicon Dioxide

Silicon dioxide i.e., silica is a known inorganic material due to its applications in chromatographic columns. It is a porous material with high specific surface area of $700 \text{ m}^2 \text{ g}^{-1}$ which makes it suitable for the adsorptive removal of water pollutants. Nano silica exhibits great potential in adsorptive removal of organic and inorganic pollutants owing to its unique properties i.e. increased surface area, tailorable surface properties, and well-defined pore size. Further, the adsorption capacity and selectivity can be enhanced by modification of nano silica with different organic functional groups like $-\text{NH}_2$, $-\text{SH}$, $-\text{OH}$, etc., or by using as support for other NPs and nanocomposites. Biofunctionalized silica nanospheres were fabricated and were modified with 3-aminopropyl and phenyl groups for the hosting of Cu^{2+} ions and a cationic dye, i.e., MB [146]. The adsorption capacity was increased towards Cu^{2+} ions and MB upon increasing the number of amino groups, which may be due to the rise in the number of binding sites on the surface of silica nanospheres. To enhance the adsorption capacity of nano silica, a nanocomposite of nano polyaniline and nano silica, as well as a crosslinked nano polyaniline immobilized on the surface of nano silica, was developed for the removal of different ions like Cu^{2+} , Hg^{2+} , Cd^{2+} , and Pb^{2+} . Higher adsorption capacities were noticed towards each metal ion in the case of crosslinked nanocomposite [147]. Not only the surface-modified but magnetic nano silica also gained considerable interest for hosting different pollutants from waste water. In this perspective, nano magnetite coated with silica showed their ability in this application at an industrial scale. In addition, core-shell nanoparticles of Ni@SiO_2 were fabricated where magnetic properties of Ni were combined with porous silica for the enhanced and cost-effective removal of different dyes containing $-\text{OH}$ group, i.e., Rhodamine B and Orange II and dye without $-\text{OH}$ groups, i.e., Methylene Blue and Methyl Orange. Here, the effect of functional groups and charge on dye structures on

the removal performance of nano adsorbent was examined, indicating higher adsorption capacity towards negatively charged dyes with $-OH$ group with respect to the positively charged without $-OH$ groups [148].

9.2.5 Nano Aluminum Oxide

Nano aluminum oxide is another low-cost and effective adsorbent for hosting waste water contaminants with efficient decontamination ability [149, 150]. Aluminium oxide possesses different crystalline structures like α , γ , η and θ where γ -alumina (γ - Al_2O_3) is most widely used. The bulk γ - Al_2O_3 has been utilized as a conventional natural adsorbent for the elimination of water pollutants due to its interesting properties viz high compressive strength, resistance to corrosion, good thermal conductivity, and high electrical insulation [151]. The use of Al_2O_3 in the form of nano significantly enhances the capability as compared to bulk alumina. This can be accredited to the increased specific surface area, which leads to outstanding adsorption capacity and mechanical strength, low-temperature modification process [152]. The nano alumina has been used for hosting a number of organic and inorganic water pollutants. Tabesh et al. fabricated nano Al_2O_3 for the 97 and 87% adsorptive removal [153] of Pb^{2+} and Cd^{2+} ions, respectively. The maximum adsorption capacities of 47.08 and 17.22 $mg\ g^{-1}$ were obtained for Pb^{2+} and Cd^{2+} , respectively. The adsorption potential of nano alumina was also investigated for the removal of Zn^{2+} , Cr^{6+} , Ni^{2+} , Cu^{2+} , As^{2+} , and Hg^{2+} [154–158] ions. Excellent adsorption capacities were observed for these metal ions. Further, the removal capacity of nano alumina can be enhanced by their surface modification with surfactants. The modification process not only improves the adsorption efficiency but also enhances their stability by preventing them from agglomeration. The surface of nano Al_2O_3 was modified with two different surfactants, i.e., SDS and Sodium tetra decyl sulphate (STS), for the enhanced removal of NH_4^+ and Cd^{2+} ions, respectively [159–161]. It was proposed that surface coating of anionic surfactant leads to alteration in surface charge which was responsible for the improvement in adsorption capacity. Nano alumina has also been found effective in boosting the adsorption performance of polyethersulfone (PES) membrane matrix towards Cu^{2+} ions [162].

Along with the hosting of heavy metal ions, nano-alumina has also found applications in the removal of organic pollutant dyes from the waste water. The high specific surface area and charged surface enable them to be effective in the adsorptive elimination of dyes. A number of scientific studies report the exclusion of different cationic and anionic dyes from the waste water. Scientists employed bare nano γ - Al_2O_3 , and SDS modified nano γ - Al_2O_3 for the removal of a cationic dye i.e., Rhodamine B. The adsorption performance of SDS modified nano γ - Al_2O_3 (97.7%) was found to be better as compared to bare γ - Al_2O_3 (40%) [163]. This was due to the higher negative charge on the surface of SDS modified nano γ - Al_2O_3 providing enhanced interaction towards cationic dye. Another cationic dye i.e., MB was also removed using nano γ - Al_2O_3 with adsorption capacity of 1000 $mg\ g^{-1}$ [164]. Electrostatic interactions

between γ -Al₂O₃ and MB were responsible for high adsorption capacity. In addition to cationic dyes, nano γ -Al₂O₃ have also been found effective in the hosting of anionic dye i.e. Orange G where adsorption occurred via physisorption with 100% removal efficiency [165].

9.2.6 Bimetallic Nanoparticles

The name bimetallic nanoparticles indicate the blend of two different metals providing an assortment of new, different, and improved properties. Bimetallic nanoparticles are obtained in different forms like alloys, core–shell, and contact aggregate. In alloyed structure, two different metals are present homogeneously, whereas in core–shell type arrangement, one of the metals usually the inexpensive one is made core and the other acts as a shell. Bimetallic nanoparticles are fabricated by co-reduction or successive reduction of two metals. The properties of bimetallic nanoparticles depend upon the metals combined, mode of combination, size, and difference in reduction rates of two different metals. The process of bi-metallization results into improved and flexible electronic, structural, catalytic and surface properties. These bimetallic nanoparticles have received great attention among industrial and scientific areas owing to their novel properties. In the field of catalysis, bimetallic nanoparticles have demonstrated improved performance as compared to their monometallic counterparts. The mono metal and metal oxide nanoparticles exhibit the limitation of easy deactivation [166–170] and are easily affected by pH [171, 172] of the solution, which can be conquered by coating a small amount of noble metals on the surface of other active metals. Till date, a variety of bimetallic nanoparticles have been explored for the hosting of various organic compounds like chlorinated organic compounds, dyes, and inorganic metal ions from waste water. Fe-based bimetallic nanoparticles containing Ni, Cu, Al, and Pd as second metals have been investigated for the hydro dechlorination of polychlorine organic pollutants (Table 9.1).

Table 9.1 Removal of various chlorinated water pollutants using bimetallic nanoparticles

Sl. no	Chlorinated pollutant	Bimetallic NPs	% Removal	Refs
1	2,4-Dichlorophenol	Pd–Fe	99.0	[174]
2	Hexachlorobenzene	Cu–Fe	99.4	[175]
3	2,4,6-Trichlorophenol	Pd–Zn	100.0	[176]
4	3-Chlorophenol	Pd–Al	99.7	[177]
5	Pentachlorophenol	Ni–Fe	100.0	[178]
6	γ -Hexachlorocyclohexane	Pd–Fe	100.0	[179]
7	Dichloromethane	Cu–Al	98.0	[180]

The use of Fe-based bimetallic nanoparticles suffers from the certain limitations of spontaneous corrosion of Fe surface, which causes easy deactivation of nanoparticles system. This issue can be addressed by loading of bimetallic nanoparticles on carbon microspheres, or by adsorption of surfactants or polymers on the nanoparticles surface for prevention of agglomeration and corrosion [179] which can lead to increased cost-effectiveness of the process. Therefore, substantial attempts are being made to replace Fe with other active metals Al, Pd, Zn, Mg, etc. [180, 181]. Scientists have also synthesized Pd–Mg [182] and Pd–Al [183] bimetallic nanoparticles for the dechlorination of 2-chlorobiphenyl.

In addition to the hosting of chlorinated organic compounds, bimetallic nanoparticles have also emerged as a promising candidate for heavy metal removal. Bimetallic nanoparticles pose higher redox activity and adsorption capacity as compared to their mono metallic counterparts. Again, the Fe-based bimetallic nanoparticles containing other metals have achieved great success for the reductive hosting of Cu^{2+} , Cd^{2+} and Cr^{6+} ions [184–186]. Further, the removal performance of bimetallic nanoparticles can be ameliorated by supporting them on polymeric surface. Enhanced removal capacity of Fe-nanoparticles supported on montmorillonite clay towards Cr^{6+} was observed because of the combined adsorption tendency of montmorillonite clay and reduction capacity of nanoparticles [187]. Other toxic metals like As^{5+} and Se^{4+} have also been successfully removed using bimetallic nanoparticles. Fe–Mn nanoparticles were synthesized [188] for the oxidation of As^{3+} to As^{5+} followed by complete removal of both ions owing to the oxidation capacity of Mn and adsorption efficiency of iron oxide. Similarly, Fe–Al nanoparticles (Fig. 9.6) were also employed for the complete elimination of As^{3+} to As^{5+} ions via simultaneous oxidation and reduction

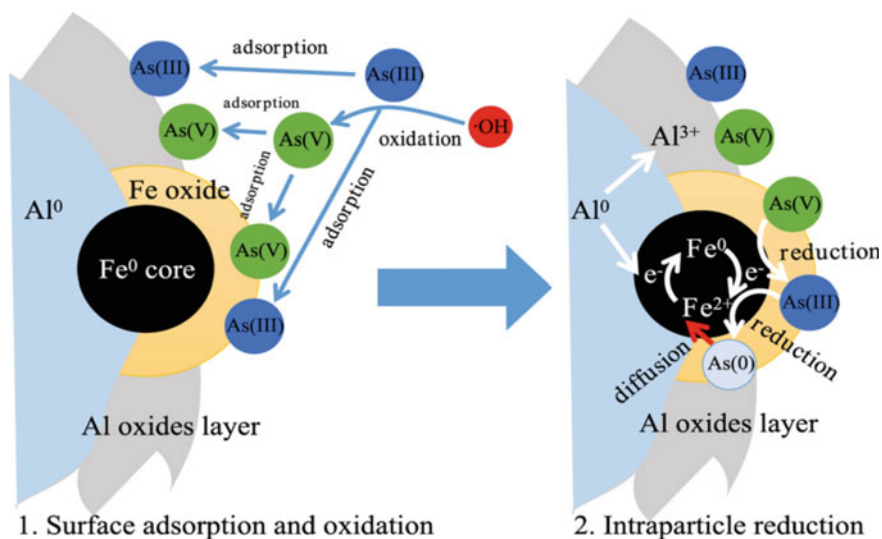


Fig. 9.6 Possible mechanism of As ions hosting by Fe–Al bimetallic nanoparticles (adapted with permission from [188])

followed by adsorptive hosting [188]. The As^{5+} ions adsorbed on the Fe oxide layer get diffused to Al part where these get reduced to As^{3+} which further reduced to As^0 via oxidation of Al and Fe into Al^{3+} and Fe^{2+} ions.

Bimetallic NPs have also gained a lot of attention from researchers for the removal of other organic and colored pollutants, i.e., dyes from the waste water. The scientific literature describes the outstanding behavior of bimetallic nanoparticles for the effective removal of dyes containing azo ($-\text{N}=\text{N}-$) functional groups, i.e., azo dyes. Scientists utilized Fe–Ni NPs for the effective hosting of Orange G in the waste water. The complete reductive degradation of dyes into by-products like aniline and naphthol was observed, which was followed by adsorption of byproducts [189]. Similarly, Fe–Cu [190] nanoparticles were developed for the complete decolorization of MB dye. Fe–Zn nanoparticles [191] were also exploited for the effective removal of Congo Red and MG dyes.

Further, to reduce the toxicity and threats caused by the leaching of toxic metal from bimetallic metals, these nanoparticles can be immobilized on many versatile catalytic supports. These nanoparticles supported on catalytic surfaces considerably enhance the removal performance and eco-friendliness of the system. Fe–Cu and Fe–Pd supported on agar gel were employed for the removal of Methylene Blue and Rhodamine B dyes with 90 and 80% efficiency, respectively [20].

9.3 Research Gaps

Although these nano adsorbents have emerged as the most promising candidates for effective hosting of contaminants from waste water, however, there are some issues in the bottleneck which are required to overcome for making them a superior host of water pollutants. Most metal oxide nanoparticles exhibit the limitation of instability, dispensability, and agglomeration, which lessens their removal performance. Also, their nano scale size makes separation from the waste water difficult. The use of modified and doped nano composites can provide the solution to these problems as it not only enhances the removal capacity but also provides stability and selectivity to the nano adsorbents. These metal oxide nanomaterials have been modified with a variety of polymeric, organic, and inorganic compounds to increase their removal capacity and selectivity towards the target contaminant. However, their synthesis and long-term performance is an issue. Similarly, bare NZVI and bimetallic nanoparticles containing iron suffer from the disadvantage of loss of activity due to corrosion and agglomeration. This problem has been solved by supporting nanomaterials on the surface of polymeric or surfactant support which combines the advantage of the high surface area of support with the removal activity of bimetallic nanoparticles by preventing them from agglomeration and corrosion. Although functionalized, doped, and supported metal-based nanoadsorbents have emerged as a promising solution. However, their synthesis and long-term performance are still an issue.

The commercial availability and use of nanoparticle-based adsorbents used for the hosting of water pollutants are rare; therefore, it is required to fabricate these

nano adsorbents at an industrial scale. Also, from the economic point of view, the development and production cost of nano adsorbents should be optimized. Further, the application of nano adsorbents for onsite treatment is simple, more effective, and also reduces the operational cost of waste water treatment. Therefore, there is a strong need to develop the nano adsorbents which can be utilized and recycled for the onsite treatment of waste water.

Last but not one, the escalated use of nano adsorbents at an industrial scale could impart toxicity to fauna and flora persistent in the environment. Therefore, the toxicity evaluation and biocompatibility of developed nano adsorbents towards the environment and human beings should be investigated prior to their implication in the field of hosting of water pollutants. The synthetic procedure for the development of nano adsorbents should meet the requirements of green chemistry. However, the reports on the toxicity evaluation of synthesized nano adsorbents are fewer.

9.4 Conclusions

The metal oxide-based nanostructures have been extensively utilized for the complete removal of inorganic and organic water pollutants owing to their excellent properties. The current chapter describes the extensive applicability of different metal, metal oxide-based nanomaterials, viz. NZVI, nano iron oxide nano alumina, nanosilica, nanotitania, and bimetallic nanomaterials for the removal of heavy metal ions, dyes, and chlorinated organic compounds from waste water. The mechanism of hosting of water pollutants using NZVI and bimetallic nanoparticles is usually based upon the adsorption followed by oxidative or reductive degradation of contaminants. Therefore, these have found great success in the complete removal of organic compounds, i.e., dyes and chlorinated organic compounds. The hosting of heavy metal ions using NZVI depends upon the standard reduction potential of heavy metal ions being hosted. Fewer reports on the reductive removal of metal ions, specially As^{5+} , Cu^{2+} , Cd^{2+} , and Cr^{6+} involving the use of bimetallic nanoparticles are available. Among all the metal oxides, oxides of iron, i.e., Fe_2O_3 and Fe_3O_4 have been exploited the most for the adsorptive hosting of heavy metal ions owing to their magnetic properties. Further, ceramic-based nano adsorbents like nano silica and nano alumina have also established their higher applicability on the hosting of heavy metal ions as compared to organic contaminants. Nevertheless, the commercial availability of such nanomaterials and their toxicity imparted on fauna and flora are also the issue of concern. To minimize the harmful effects of nano adsorbents, regulatory measures on their use are also recommended. So, nano adsorbents have emerged as an excellent alternative to conventional adsorbents due to their unique and remarkable properties. Still, there is a long way to go to use nano adsorbents in practical applications of the hosting of waste water pollutants.

References

1. Shannon MA, Bohn PW, Elimelech M, Georgiadis JG, Marinakos BJ, Mayes AM (2008) Science and technology for water purification in the coming decades. *Nature* 452:301–310
2. Manawi Y, Kochkodan V, Hussein MA, Khaleel MA, Khraisheh M, Hilal N (2016) Can carbon-based nanomaterials revolutionize membrane fabrication for water treatment and desalination? *Desalination* 391:69–88
3. Carroll DO, Sleep B, Boparai H, Kocur C (2013) Nanoscale zero valent iron and bimetallic particles for contaminated site remediation. *Adv Water Resources* 51:104–122
4. Kumar V, Jain A, Wadhawan S, Mehta SK (2018) Synthesis of biosurfactant-coated magnesium oxide nanoparticles for methylene blue removal and selective Pb²⁺ sensing. *IET Nanobiotechnol* 12(3):241–253
5. Dil EA, Ghaedi M, Asfaram A, Hajati S, Mehrabi F, Goudarzi A (2017) Preparation of nanomaterials for the ultrasound-enhanced removal of Pb²⁺ ions and malachite green dye: Chemometric optimization and modeling. *Ultrason Sonochem* 34:677–691
6. Mautner A, Kwaw Y, Wieland K, Mvubuc M, Bothac A, Jacob M, John MA, Siqueira G, Bismarck A (2019) Natural fibrenanocellulose composite filters for the removal of heavy metal ions from water. *Ind Crops Prod* 133:325–332
7. Araya M, Mc Goldrick MC, Klevay LM, Strain JJ, Robson P, Nielsen F, Olivares M, Pizarro F, Johnson L, Poirier KA (2001) Determination of an acute no-observed adverse effect level (NOAEL) for copper in water. *Regul Toxicol Pharmacol* 34:137–145
8. Zamani HA, Rajabzadeh G, Firouz A, Ganjali MR (2007) Determination of copper (II) in wastewater by electroplating samples using a PVC membrane copper (II) selective electrode. *J Anal Chem* 62:1080–1087
9. European-Commission (2003) Opinion of the scientific committee on food on the tolerable upper intake level of copper (SCF/CS/NUT/UPPLEV/57 Final)
10. WHO (2004) Copper in Drinking-Water (WHO/SDE/WSH/03.04/88).
11. Zhao GX, Li JX, Ren XM, Chen CL, Wang XK (2011) Few-layered graphene oxide nanosheets as superior sorbents for heavy metal ion pollution management. *Environ Sci Technol* 45:10454–10462
12. Jarup L, Åkesson A (2009) Current status of cadmium as an environmental health problem. *Toxicol Appl Pharmacol* 238:201–208
13. Pourreza N, Rastegarzadeh S, Larki A (2014) Nano TiO₂ modified with 2- mercaptobenzimidazole as an efficient adsorbent for removal of Ag (I) from aqueous solutions. *J Ind Eng Chem* 20:127–132
14. ATSDR (Agency for Toxic Substances and Disease Registry) (2005) Toxicological profile for zinc. (Available online: <http://www.atsdr.cdc.gov/toxprofiles/tp60.pdf>. Accessed on 20/03/2015)
15. Fu F, Wang Q (2011) Removal of heavy metal ions from wastewaters: a review. *J Environ Manag* 92(3):407–418
16. Ghasemi E, Heydari A, Sillanp M (2017) Superparamagnetic Fe₃O₄@EDTA nanoparticles as an efficient adsorbent for simultaneous removal of Ag(I), Hg(II), Mn(II), Zn(II), Pb(II) and Cd (II) from water and soil environmental samples. *Microchem J* 131:51–56
17. Minh Chu TP, Nguyen NT, Vu TL, Dao TH, Dinh LC, Nguyen HL, Hoang TH, Le TS, Pham TD (2019) Synthesis, characterization, and modification of alumina nanoparticles for cationic dye removal. *Materials* 12:450
18. Mahmoud HR, Ibrahim SM, El-Molla SA (2016) Textile dye removal from aqueous solutions using cheap MgO nanomaterials: adsorption kinetics, isotherm studies and thermodynamics. *Adv Powder Technol* 27:223–231
19. Jain R, Sharma N, Bhargava M (2003) Electrochemical degradation of rhodamine dye in textile and paper industries effluent. *J Sci Ind Res* 62:1138–1144
20. Patra S, Roy E, Madhuri R, Sharma PK (2016) Agar based bimetallic nanoparticles as high-performance renewable adsorbent for removal and degradation of cationic organic dyes. *J Ind Eng Chem* 33:226–238

21. Bhagya NP, Prashantha PA, Raveendra RS, Sathyanarayani S, Ananda S, Nagabhushanad BM, Nagabhushanae RH (2016) Adsorption of hazardous cationic dye onto the combustion derived SrTiO₃ nanoparticles: kinetic and isotherm studies. *J Asian Ceramic Soc* 4(1):68–74
22. Syed P, Shabudeen S (2011) Study of the removal of malachite green from aqueous solution by using solid agricultural waste research journal of chemical sciences res. *J Chem Sci* 1:88–104
23. Srivastava S, Sinha R, Roy D (2004) Toxicological effects of malachite green. *Aquat Toxicol* 66:319–329
24. Kushwaha AK, Gupta N, Chattopadhyaya MC (2010) Removal of cationic methylene blue and malachite green dyes from aqueous solution by waste materials of *Daucuscarota*. *J Chem Pharm Res* 2:34–45
25. Efome JE, Rana D, Matsuura T, Lan CQ (2019) Effects of operating parameters and coexisting ions on the efficiency of heavy metal ions removal by nano fibrous metal-organic framework membrane filtration process. *Sci Total Environ* 674:355–362
26. Martína DM, Faccinia M, García MA, Amantia D (2018) Highly efficient removal of heavy metal ions from polluted water using ion selective polyacrylonitrile nanofibers. *J Environ Chem Eng* 6:236–245
27. Naseem K, Begum R, Wu W, Usman M, Irfan A, Al-Sehemi AG, Farooqi ZH (2019) Adsorptive removal of heavy metal ions using polystyrene-poly isopropylmethacrylamide-acrylic acid core/shell gel particles: adsorption isotherms and kinetic study. *J Mol Liq* 277:522–531
28. Yuan X, Anc N, Zhu Z, Sun H, Zhengb J, Jia M, Lud C, Zhang W, Liu N (2018) Hierarchically porous nitrogen-doped carbon materials as efficient adsorbents for removal of heavy metal ions. *Proc Saf Environ Prot* 119:320–329
29. Cegłowski M, Gierczyk B, Frankowski M, Pepend Ł (2018) A new low-cost polymeric adsorbents with polyamine chelating groups for efficient removal of heavy metal ions from water solutions. *React Funct Polym* 131:64–74
30. Kwiatkowski M, Broniek E (2017) An analysis of the porous structure of activated carbons obtained from hazelnut shells by various physical and chemical methods of activation, *Colloids Surf A* 529:443–453
31. Valderrama C, Barios JI, Caetano M, Farran A, Cortina JL (2010) Kinetic evaluation of phenol/aniline mixtures adsorption from aqueous solutions onto activated carbon and hyper crosslinked polymeric resin (MN200). *React Funct Polym* 70:142–150
32. Otero M, Grande CA, Rodrigues AE (2004) Adsorption of salicylic acid onto polymeric adsorbents and activated charcoal. *React Funct Polym* 60:203–213
33. Narkiewicz U, Pelech I, Podsiadły M, Cegłowski M, Schroeder G, Kurczewska J (2009) Preparation and characterization of magnetic carbon nanomaterials bearing APTS silica on their surface. *J Mater Sci* 45:1100–1106
34. Jian M, Liu B, Zhang G, Liu R, Zhang X (2015) Adsorptive removal of arsenic from aqueous solution by zeoliticimidazolate framework-8 (ZIF-8) nanoparticles. *Colloid Surf A* 465:67–76
35. Wadhawan S, Jain A, Nayyar J, Mehta S K (2020) Role of nanomaterials as adsorbents in heavy metal ion removal from waste water: a review. *J Water Process Eng* 33:101038
36. Figueroa RA, MacKay AA (2005) Sorption of oxytetracycline to iron oxides and iron oxide-rich soils. *Environ Sci Technol* 39:6664–6671
37. Mon J, Flury M, Harsh JB (2006) Sorption of four triarylmethane dyes in a sandy soil determined by batch and column experiments. *Geoderma* 133:217–224
38. Wang S, Wang H (2015) Adsorption behavior of antibiotic in soil environment: a critical review. *Front Environ Sci Eng* 9:565–574
39. Maleki A, Hayati B, Najafi F, Gharibi F, Joo SW (2016) Heavy metal adsorption from industrial wastewater by PAMAM/TiO₂nanohybrid: preparation, characterization and adsorption studies. *J Mol Liq* 224:95–104
40. Demirbilek C, Dinç CO (2012) Synthesis of diethylaminoethyl dextran hydrogel and its heavy metal ion adsorption characteristics. *Carbohydr Polym* 90:1159–1167
41. Bilba N, Bilba D, Moroi G (2004) Synthesis of a polyacrylamidoxime chelating fiber and its efficiency in the retention of palladium ions. *J Appl Polym Sci* 92:3730–3735

42. Gong B (2002) Synthesis of polyacrylaminoimidazole chelating fiber and properties of concentration and separation of trace Au Hg and Pd from samples. *Talanta* 57:89–95
43. Chang X, Su Q, Liang D, Wei X, Wang B (2002) Efficiency and application of poly (acryl dinitro phenyl amidrazone -dinitroacrylphenylhydrazine) chelating fiber for pre-concentrating and separating trace Au(III), Ru(III), In(III), Bi(III), Zr(IV), V(V), Ga(III) and Ti(IV) from solution samples. *Talanta* 57:253–261
44. Deng S, Bai R (2004) Removal of trivalent and hexavalent chromium with aminatedpolyacrylonitrile fibers: performance and mechanisms. *Water Res* 38:2424–2432
45. Deng S, Bai R, Chen JP (2003) Aminatedpolyacrylonitrile fibers for lead and copper removal. *Langmuir* 19:5058–5064
46. Ma N, Yang Y, Chen S, Zhang Q (2009) Preparation of amine group containing chelating fiber for thorough removal of mercury ions. *J Hazard Mater* 171:288–293
47. Martínez DM, Faccin M, GMA, Amantia D (2018) Highly efficient removal of heavy metal ions from polluted water using ion selective polyacrylonitrile nanofibers. *J Environ Chem Eng* 6:236–245
48. Kim EJ, Lee CS, Chang YY (2013) Hierarchically structured manganese oxide-coated magnetic nanocomposites for the efficient removal of heavy metal ions from aqueous systems. *ACS Appl Mater Interfaces* 5:9628–9634
49. Wang X, Ding X, Yao S, Vu X, Feng Q, Wang Z (2014) High super capacitor and adsorption behaviors of flower-like MoS₂ nanostructures. *J Mater Chem A* 2:15958–15963
50. Guo YY, Guo H, Wang YP (2014) Designed hierarchical MnO₂ microspheres assembled from nanofilms for removal of heavy metal ions. *RSC Adv* 4:14048–14054
51. Kim EJ, Lee CS, Chang YY, Chang YS (2013) Hierarchically structured manganese oxide-coated magnetic nanocomposites for the efficient removal of heavy metal ions from aqueous systems. *ACS Appl Mater Interfaces* 5(19):9628–9634
52. Zeng T, Yu Y, Li Z, Zuo J, Kuai Z, Jin Y, Wang Y, Wu A, Peng C (2019) 3D MnO₂ nanotubes reduced graphene oxide hydrogel as reusable adsorbent for the removal of heavy metal ions. *Mater Chem Phys* 231:105–108
53. Kharissova OV, Dias HVR, Kharisov BI (2015) Magnetic adsorbents based on micro and nano-structured materials. *RSC Adv* 5(9):6695–6719
54. Reddy DHK, Lee SM (2013) Application of magnetic chitosan composites for the removal of toxic metal and dyes from aqueous solutions. *Adv Colloid Interface Sci* 201–202:68–93
55. Xu PA, Zeng GM, Huang DL, Feng CL, Hu S, Zhao MH, Liu ZF (2012) Use of iron oxide nanomaterials in wastewater treatment: a review. *Sci Total Environ* 424:1–10
56. Zhang XM, Liu JY, Kelly SJ, Huang XJ, Liu JH (2014) Biomimetic snowflake shaped magnetic micro-/nanostructures for highly efficient adsorption of heavy metal ions and organic pollutants from aqueous solution. *J Mater Chem A* 2(30):11759–11767
57. Fan H, Mab X, Zhou S, Huang J, Liu Y, Liu Y (2019) Highly efficient removal of heavy metal ions by carboxymethyl cellulose immobilized Fe₃O₄ nanoparticles prepared via high-gravity technology. *Carbohydr Polym* 213:39–49
58. Huang XG, Zhan XZ, Wen CL, Xu F, Luo LJ (2018) Amino-functionalized bacterial cellulose activated carbon composite for Pb²⁺ and methyl orange sorption from aqueous solution. *J Mater Sci Technol* 34(5):855–863
59. Mahdavi S, Jalali M, Afkhami A (2012) Removal of heavy metals from aqueous solutions using Fe₃O₄, ZnO and CuO nanoparticles. *J Nanopart Res* 14:846–863
60. Pylypchuk IV, Kessler VG, Seisenbaeva GA (2018) Simultaneous removal of acetaminophen, diclofenac, and Cd(II) by *trametes versicolor* laccase immobilized on Fe₃O₄/SiO₂-DTPA hybrid nanocomposites. *ACS Sustain Chem Eng* 6(8):9979–9989
61. Yu Y, Li Y, Wang YQ, Zou BF (2018) Self-template etching synthesis of urchin like Fe₃O₄ microspheres for enhanced heavy metal ions removal. *Langmuir* 34(32):9359–9365
62. Liu Y, Zeng G, Tang L, Cai Y, Pang Y, Zhang Y, Yang G, Zhou Y, He X, He Y (2015) Highly effective adsorption of cationic and anionic dyes on magnetic Fe/Ni nanoparticles doped bimodal mesoporous carbon. *J Colloid Interface Sci* 448:451–459

63. Pandian CJ, Palanivel R, Dhananasekaran S (2015) Green synthesis of nickel nanoparticles using *Ocimum sanctum* and their application in dye and pollutant adsorption. *Chin J Chem Eng* 23:1307–1315
64. Gamra MA, Ahmed MA (2015) TiO₂ nanoparticles for removal of malachite green dye from waste water. *Adv Chem Eng Sci* 5:373–388
65. Kansal SK, Sood S, Umar A, Mehta SK (2013) Photocatalytic degradation of Eriochrome Black T dye using well-crystalline anatase TiO₂ nanoparticles. *J Alloys Comp* 581(25):392–397
66. Sood S, Umar A, Mehta SK, Kansal SK (2015) Highly effective Fe-doped TiO₂ nanoparticles photocatalysts for visible-light driven photocatalytic degradation of toxic organic compounds. *J Colloid Interface Sci* 450:213–222
67. Sood S, Umar A, Mehta SK, Sinha ASK, Kansal SK (2015) Efficient photocatalytic degradation of brilliant green using Sr-doped TiO₂ nanoparticles. *Ceramic Int* 41(3):3533–3540. <https://www.sciencedirect.com/science/article/pii/S027288421401743X>
68. Kataria N, Garg VK, Jain M, Kadirvelu K (2016) Preparation, characterization and potential use of flower shaped Zinc oxide nanoparticles (ZON) for the adsorption of Victoria Blue B dye from aqueous solution. *Adv Powder Technol* 27(4):1180–1188
69. Saharan P, Chaudhary GR, Lata S, Mehta SK, Mor S (2015) Ultra fast and effective treatment of dyes from water with the synergistic effect of Ni doped ZnO nanoparticles and ultrasonication. *Ultrason Sonochem* 22:317–325
70. Chaudhary GR, Saharan P, Ahmad U, Mehta SK, Mor S (2013) Well-Crystalline ZnO nanostructures for the removal of acridine orange and C. brilliant blue R-250 hazardous dyes, *Sci Adv Mater* 5(12):1886–1894
71. Kansal SK, Lamba R, Mehta SK, Umar A (2013) Photocatalytic degradation of Alizarin Red S using simply synthesized ZnO nanoparticles *Mater. Lett* 106(1):385–389
72. Rajabi HR, Arjmand H, Hoseini SJ, Nasrabadi H (2015) Surface modified magnetic nanoparticles as efficient and green sorbents: synthesis, characterization, and application for the removal of anionic dye. *J Magn Magn Mater* 394:7–13
73. Aashima US, Arora A, Gautam S, Singh S, Choudhary RJ, Mehta SK (2019) Magnetically retrievable Ce-doped Fe₃O₄ nanoparticles as scaffolds for the removal of azo dyes. *RSC Adv* 9:23129
74. Saharan P, Chaudhary GR, Mehta SK, Umar A (2016) Efficient photocatalytic degradation of victoria blue R and fast green FCF dyes using γ -Fe₂O₃ and Fe₃O₄ nanoparticles. *Nanosci Nanotechnol Lett* 8(11):965–971
75. Chaudhary GR, Saharan P, Kumar A, Mehta SK, Mor S, Ahmad U (2013) Adsorption studies of cationic, anionic and azo-dyes via monodispersed Fe₃O₄ nanoparticles. *J Nanosci Nanotechnol* 13(5):3240–3245
76. Lamba R, Umar A, Mehta SK, Kansal SK (2015) Well-crystalline porous ZnO–SnO₂ nanosheets: an effective visible-light driven photocatalyst and highly sensitive smart sensor material. *Talanta* 131:490–498
77. Lamba R, Umar A, Mehta SK, Kansal SK (2015) ZnO doped SnO₂ nanoparticles hetero junction photo-catalyst for environmental remediation. *J Alloys Comp* 653(25):327–333
78. Kaur S, Sharma S, Umar A, Singh S, Mehta SK, Kansal SK (2017) Solar light driven enhanced photocatalytic degradation of brilliant green dye based on ZnS quantum dots. *Superlattices Microstruct* 103:365–375
79. Kaur M, Mehta SK, Kansal SK (2018) Visible light driven photocatalytic degradation of ofloxacin and malachite green dye using cadmium sulphide nanoparticles. *J Environ Chem Eng* 6(3):3631–3639
80. Shukla S, Chaudhary S, Umar A, Chaudhary GR, Kansal SK, Mehta SK (2016) Surfactant functionalized tungsten oxide nanoparticles with enhanced photocatalytic activity. *Chem Eng J* 288:423–443
81. Shukla S, Chaudhary S, Umar A, Chaudhary GR, Mehta SK (2015) Dodecyl ethyl dimethyl ammonium bromide capped WO₃ nanoparticles: efficient scaffolds for chemical sensing and environmental remediation. *Dalton Trans* 44:17251–17260

82. Simkovic K, Derco J, Valicova M (2015) Removal of selected pesticides by nano zero-valent iron. *Acta Chim Slov* 8(2):152–155
83. Zhang WX (2003) Nano scale iron particles for environmental remediation: an overview. *J Nanopart Res.* 5:323–332
84. Kanet SR, Greneche JM, Choi H (2006) Arsenic (V) removal from groundwater using nano scale zero-valent iron as a colloidal reactive barrier. *Mater Environ Sci Technol* 40:2045–2050
85. Sikder MT, Mihara Y, Islam MS, Saito T, Tanaka S, Kurasaki M (2015) Preparation and characterization of chitosan-caboxymethyl- β -cyclodextrin entrapped nanozero-valent iron composite for Cu (II) and Cr (IV) removal from wastewater. *Chem Eng J* 236:378–387
86. Khan MS, Khan AA, Bangash FU, Shah SS, Khan P (2013) Removal of basic dye from aqueous solutions using nano scale zero valent iron (NZVI) as adsorbent, *J Chem Soc Pak* 35(3)
87. Arabi S, Sohrabi MR (2014) Removal of methylene blue, a basic dye, from aqueous solutions using nanozerovalent iron Water science and technology. *Water Sci Technol* 70(1):24–31
88. Lin TY, Weng HC, Chen YF (2008) Effective removal of AB24 dye by nano/micro-size zero-valent iron, separation and purification effective removal of AB24 dye by nano/micro-size zero-valent iron. *Sep Purif Technol* 64(1):26–30
89. Shojaei S, Khammaria S, Shojaei S, Sasani M (2017) Removal of reactive red 198 by nanoparticle zero valent iron in the presence of hydrogen peroxide. *J Water Environ Nanotechnol* 2(2):129–135
90. Li S, Wang W, Yi Y, Zhnag LW (2014) Zero-valent iron nanoparticles (nZVI) for the treatment of smelting wastewater: a pilot-scale demonstration. *Chem Eng J* 254:115–123
91. Xiao ZH, Xu Y, Yuan M, Jing X, Huang J, Li Q, Sun D (2017) Ultra-efficient removal of chromium from aqueous medium by biogenic iron based nanoparticles. *Sep Purif Technol* 174:466–473
92. Kanet SR, Greneche JM, Choi H (2006) Arsenic (V) removal from groundwater using nano scale zero-valent iron as a colloidal reactive barrier. *Environ Sci Technol* 40:2045–2050
93. Zimmermann AC, Mecabo A, Fagundes T, Rodrigues CA (2010) Adsorption of Cr (VI) using Fe-crosslinked chitosan complex (Ch–Fe). *J Hazard Mater* 179:192–196
94. Sikder MT, Mihrac Y, Islam MS, Saitod T, Tanaka S, Kurasaki M (2014) Preparation and characterization of chitosan-caboxymethyl- β -cyclodextrin entrapped nano zero-valent iron composite for Cu (II) and Cr (IV) removal from wastewater. *Chem Eng J* 236:378–387
95. Arabi S, Sohrabi MR (2014) Removal of methylene blue, a basic dye, from aqueous solutions using nano-zerovalent iron. *Water Sci Technol* 70(1):24–31
96. Hassan MMA, Hamad HA, Shther DE (2019) Treatment of contaminated water with industrial dyes by using nano zero valent iron (NZVI) and supported on pillared clay. *Adv Anal Chem* 9(1):1–7
97. Kansal SK, Sood S, Umar A, Mehta SK (2013) Photocatalytic degradation of Eriochrome Black T dye using well-crystalline anatase TiO₂ nanoparticles. *J Alloys Compd* 581:392–397
98. Sood S, Kumar S, Umar A, Kaur A, Mehta SK, Kansal SK (2015) TiO₂ quantum dots for the photocatalytic degradation of indigo carmine dye. *J Alloys Compd* 650:193–198
99. Yang Y, Flatebo C, Liang J, Dong P, Yuan J, Wang T, Zhang J, Chen W, Wu J, Ajayan PM, Ci L, Li Q, Lou J (2016) Towards methyl orange degradation by direct sunlight using coupled TiO₂ nanoparticles and carbonized cotton T-shirt. *Appl Mater Today* 3:57–62
100. Mittal H, Ray SS (2016) A study on the adsorption of methylene blue onto gum ghatti/TiO₂ nanoparticles-based hydrogel nanocomposite. *Int J Biol Macromol* 88:66–80
101. Seisenbaeva GA, Daniel G, Nedelec JM, Gunko YK, Kessler VG (2012) High surface area ordered mesoporous nano-titania by a rapid surfactant-free approach. *J Mater Chem* 22:20374–20380
102. Malhat FM, Youssef A (2014) Selective removal of heavy metal from drinking water using titanium oxide nanowire. *Macromol Symp* 337:96–101
103. Deedar N, Irfan A, Qazi IA (2009) Evaluation of the adsorption potential of titanium dioxide nanoparticles for arsenic removal. *J Environ Sci* 21:402–408

104. Abbasizadeh S, Keshtkar AR, Mousavian MA (2013) Preparation of a novel electrospun polyvinyl alcohol/titanium oxide nanofiber adsorbent modified with mercapto groups for uranium (VI) and thorium (IV) removal from aqueous solution. *Chem Eng J* 220:161–171
105. Abbasizadeh S, Keshtkar A, R, Mousavian M A, (2014) Sorption of heavy metal ions from aqueous solution by a novel cast PVA/TiO₂nanohybrid adsorbent functionalized with amine groups. *J Ind Eng Chem* 20:1656–1664
106. Him C, Tsang A, Zeng KY, Zhao W, Zhang T, Zhan Y, Ruijie X, Leung DYC, Huang H (2019) Titanium oxide based photocatalytic materials development and their role of in the air pollutants degradation: overview and forecast. *Environ Int* 125:200–228
107. Tsang CHA, Zeng KY, Zhao W, Zhang T, Zhan Y, Xie R, Dennis YC, Huang LH (2019) Titanium oxide based photocatalytic materials development and their role of in the air pollutants degradation: overview and forecast. *Environ Int* 125:200–228
108. Razzaz A, Ghorban S, Hosayni L, Irani M, Aliabadi M (2016) Chitosan nanofibers functionalized by TiO₂ nanoparticles for the removal of heavy metal ions. *J Taiwan Inst Chem E* 58:333–343
109. Baysal A, Kuznek C, Ozcan M (2018) Starch coated titanium dioxide nanoparticles as a challenging sorbent to separate and pre concentrate some heavy metals using graphite furnace atomic absorption spectrometry. *Int J Environ Anal Chem* 98(1):45–55
110. Breault TM, Bartlett BM (2013) Composition dependence of TiO₂: (Nb, N)-x compounds on the rate of photocatalytic methylene blue dye degradation. *J Phys Chem C* 117:8611–8618
111. Sood S, Mehta SK, Umar A, Kansal SK (2014) The visible light-driven photocatalytic degradation of Alizarin red S using Bi-doped TiO₂ nanoparticles. *New. J Chem* 38:3127–3136
112. Kuvarega AT, Krause RWM, Mamba BB (2011) Nitrogen/palladium Co doped TiO₂ for efficient visible light photocatalytic dye degradation. *J Phys Chem C* 115:22110–22120
113. Sahoo C, Gupta AK, Pillai IMS (2012) Photocatalytic degradation of methylene blue dye from aqueous solution using silver ion-doped TiO₂ and its application to the degradation of real textile waste water. *J Environ Sci Health A Tox Hazard Subst Environ Eng* 47(10):1428–1438
114. Akhbarizadeh R, Shayestefar DMRE (2014) Competitive removal of metals from wastewater by maghemite nanoparticles: a comparison between simulated wastewater and AMD. *Mine Water Environ* 33:89–96
115. Rajput S, Singh LP, Jr CUP, Mohan D (2017) Lead (Pb²⁺) and copper (Cu²⁺) remediation from water using Super paramagnetic maghemite (–Fe₂O₃) nanoparticles synthesized by Flame Spray Pyrolysis (FSP). *J Colloid Interface Sci* 492:176–190
116. Watts MP, Coker VS, Parry SA, Patrick RAD, Thomas RAP, KalinR LJR (2015) Biogenic nano-magnetite and nano-zero valent iron treatment of alkaline Cr(VI) leachate and chromite ore processing residue. *Appl Geochem* 54:27–42
117. Shan C, Ma Z, Tong M, Ni J (2015) Removal of Hg(II) by poly(1-vinylimidazole)-grafted Fe₃O₄ @SiO₂ magnetic nanoparticles. *Water Res* 69:252–260
118. Mahmoud ME, Abdelwahab MS, Abdou AEH (2016) Enhanced removal of lead and cadmium from water by Fe₃O₄ cross linked-O-phenylenediaminenano-composite. *Sep Sci Technol* 51:237–247
119. Lide DR (1992) Handbook of chemistry and physics. 73rd edn. CRC Press, Boca Raton, FL, pp 12–18
120. Iconaru SL, Guégan R, Popa CL, MotelicaHeino M, Ciobanu CS, Predoi D (2016) Magnetite (Fe₃O₄) nanoparticles as adsorbents for As and Cu removal. *Appl Clay Sci* 134:128–135
121. Giraldo L, Erto A, Carlos J, Piraján M (2013) Magnetite nanoparticles for removal of heavy metals from aqueous solutions: synthesis and characterization. *Adsorption* 19(2):465–474
122. Zhu X, Song T, Lv Z, Ji G (2016) High-efficiency and low-cost α-Fe₂O₃ nanoparticles coated volcanic rock for Cd (II) removal from wastewater. *Process Saf Environ* 104:373–381
123. Ren T, He P, Niu W, Wu Y, Ai L, Gou X (2013) Synthesis of α-Fe₂O₃ nanofibers for applications in removal and recovery of Cr(VI) from wastewater. *Environ Sci Pollut Res* 20:155–162
124. Patwardhan SV (2012) Chemistry of aqueous silica nanoparticles surfaces and the mechanism of selective peptide adsorption. *J Am Chem Soc* 134:6244–6256

125. Wang X, Guo Y, Yang L, Han M, Zhao J, Cheng X (2012) Nanomaterials as sorbents to remove heavy metal ions in water treatment. *J Environ Analyt Toxicol* 2:2–7
126. Takafuji M, Ide S, Ihara H, Xu ZH (2004) Preparation of poly(1-vinylimidazole)-grafted magnetic nanoparticles and their application for removal of metal ions. *Chem Mater* 16:1977–1983
127. Song J, Kong H, Jang J (2011) Adsorption of heavy metal ions from aqueous solution by polyrhodanine encapsulated magnetic nanoparticles. *J Colloid Interface Sci* 359:505–511
128. Chávez-Guajardo AE, Medina-Llama JC, Maqueira L, Andrade CAS, Alves KGB, Melo CPD (2015) Efficient removal of Cr(VI) and Cu(II) ions from aqueous media by use of polypyrrole/maghemite and polyaniline/maghemite magnetic nanocomposites. *Chem Eng J* 281:826–836
129. Madrakian T, Afkhami A, Zolfigol MA, Ahmadi M, Koukabi N (2012) Application of modified silica coated magnetite nanoparticles for removal of iodine from water samples. *Nano-Micro Lett* 4:57–63
130. Adeli M, Yamini Y, Faraji M (2017) Removal of copper, nickel and zinc by sodium dodecyl sulphate coated magnetite nanoparticles from water and wastewater samples. *Arab J Chem* 10:S514–S521
131. Magnet C, Lomenech C, Hurel C, Reilhac P, Giulieri F, Chaze AM, Persello J, Kuzhir P (2017) Adsorption of nickel ions by oleate-modified magnetic iron oxide nanoparticles. *Environ Sci Pollut R* 24:7423–7435
132. Madrakian T, Afkhami A, Rezvani-jalal N, Ahmadi M (2014) Removal and preconcentration of lead(II), cadmium(II) and chromium(III) ions from wastewater samples using surface functionalized magnetite nanoparticles. *J Iran Chem Soc* 11:489–498
133. Behbahani NS, Rostamizadeh K, Yaftian MR, Zamani A, Ahmadi H (2014) Covalently modified magnetite nanoparticles with PEG: preparation and characterization as nano-adsorbent for removal of lead from wastewater. *J Environ Health Sci* 12:103
134. Rahbar N, Jahangiri A, Boumi S, Khodayar MJ (2014) Mercury removal from aqueous solutions with chitosan-coated magnetite nanoparticles optimized using the Box-Behnken design. *Jundishapur J Nat Pharm Prod* 9(2)
135. Madrakian T, Afkhami A, ZadpourB AM (2015) New synthetic mercaptoethylaminohomopolymer-modified maghemite nanoparticles for effective removal of some heavy metal ions from aqueous solution. *J Ind Eng Chem* 21:1160–1166
136. Huang SH, ChenD H (2009) Rapid removal of heavy metal cations and anions from aqueous solutions by amino-functionalized magnetic nano-adsorbent. *J Hazard Mater* 16:174–179
137. Verma M, Tyagi I, Chandra R, Gupta VK (2017) Adsorptive removal of Pb (II) ions from aqueous solution using CuO nanoparticles synthesized by sputtering method. *J Mol Liquids* 225:936–944
138. Fan H, Ma X, Zhou S, Huang J, Liu Y, Liu Y (2019) Highly efficient removal of heavy metal ions by carboxymethylcelluloseimmobilized Fe₃O₄ nanoparticles prepared via high-gravity technology. *Carbohydr Polym* 213:39–49
139. Gao J, He Y, Zhao X, Ran X, Wuc Y, Su Y, Dai J (2016) Single step synthesis of amine-functionalized mesoporous magnetite nanoparticles and their application for copper ions removal from aqueous solution. *J Colloid Interface Sci* 481:220–228
140. Liu JF, Shanzhao Z, Binjiang G (2008) Coating of Fe₃O₄ magnetic nanoparticles with humic acid for high efficient removal of heavy metals in water. *Environ Sci Technol* 42:6949–6954
141. Lin C, Lin YS, Ho JM (2016) Adsorption of Reactive Red 2 from aqueous solutions using Fe₃O₄ nanoparticles prepared by co-precipitation in a rotating packed bed. *J Alloy Comp* 666:153–158
142. Muthukumar C, Sivakumar VM, Thirumarimurugan M (2016) Adsorption isotherms and kinetic studies of crystal violet dye removal from aqueous solution using surfactant modified magnetic nanoadsorbent. *J Taiwan Inst Chem Eng* 63:354–362
143. He Y, Cheng Z, Qin Y, Xu B, Ning L, Zhou L (2015) Facile synthesis and functionalization of hyperbranched polyglycerol capped magnetic Fe₃O₄ nanoparticles for efficient dye removal. *Mater Lett* 151:100–103

144. Dalvand A, Nabizadeh R, Ganjali MR, Khoobi MS, Nazmara A, Mahvi H (2016) Modeling of reactive blue 19 azo dye removal from colored textile wastewater using L-arginine-functionalized Fe_3O_4 nanoparticles: Optimization, reusability, kinetic and equilibrium studies. *J Mag Mater* 404:179–189
145. Wu R, Liu JH, Zhao L, Zhang X, Xie J, Yu B, Ma X, Yang ST, Wang H, Liu Y (2014) Hydrothermal preparation of magnetic Fe_3O_4 @C nanoparticles for dye adsorption. *J Environ Chem Eng* 2:907–913
146. Asfaram A, Ghaedi M, Hajati S, Goudarzi A, Dil EA (2017) Screening and optimization of highly effective ultrasound-assisted simultaneous adsorption of cationic dyes onto Mn-doped Fe_3O_4 nanoparticle-loaded activated carbon. *Ultrason Sonochem* 34:1–12
147. Kotsyuda SS, Tomina VV, Zub YL, Furtat IM, Melnyk IV (2017) Bifunctional silica nanospheres with 3-aminopropyl and phenyl groups. Synthesis approach and prospects of their applications. *Appl Surf Sci* 420:782–791
148. Mahmoud ME, Fekry NA, El-Latif MMA (2016) Nanocomposites of nanosilica-immobilized-nanopolyaniline and cross linked nanopolyaniline for removal of heavy metals. *Chem Eng J* 304:679–691
149. Jiang Z, Xie J, Jiang D, Yan Z, Jing J, Liu D (2014) Enhanced adsorption of hydroxyl contained/anionic dyes on non functionalized Ni@ SiO_2 core-shell nanoparticles: kinetic and thermodynamic profile. *Appl Surface Sci* 292:301–310
150. Giles D, Mohapatra M, Issa TB, Anand S, Singh P (2011) Iron and aluminium based adsorption strategies for removing arsenic from water. *J Environ Manag* 92:3011–3022
151. Prabhakar R, Samadder SR (2018) Low cost and easy synthesis of aluminium oxide nanoparticles for arsenite removal from groundwater: a complete batch study. *J Mol Liquids* 250:192–201
152. Hojamberdiev M, Daminova SS, Kadirova ZC, Sharipov KT, Mtalo F, Hasegawa M (2018) Ligand-immobilized spent alumina catalyst for effective removal of heavy metal ions from model contaminated water. *J Environ Chem Eng* 6:4623–4633
153. Saadi Z, Saadi R, Fazaeli R (2013) Fixed-bed adsorption dynamics of Pb (II) adsorption from aqueous solution using nanostructured alumina. *J Nanostruct Chem* 3:1–8
154. Tabesh S, Davar F, LoghmanEstarki RM (2018) Preparation of Al_2O_3 nanoparticles using modified sol-gel method and its use for the adsorption of lead and cadmium ions. *J Alloys Compd* 730:441–449
155. Stietiya MH, Wang JJ (2014) Zinc and cadmium adsorption to aluminum oxide nanoparticles affected by naturally occurring ligands. *J Environ Qual* 43:498
156. Poursani AS, Nilchi A, Hassani AH, Shariat M, Nouri J (2015) A novel method for synthesis of nano Al_2O_3 : Study of adsorption behavior of chromium, nickel, cadmium and lead ions. *Int J Environ Sci Technol* 12:2003–2014
157. Mahdavi S, Jalali M, Afkhami A (2015) Heavy metals removal from aqueous solutions by Al_2O_3 nanoparticles modified with natural and chemical modifiers. *Clean Technol Environ Policy* 17:85–102
158. Patra AK, Dutta BAA (2012) Self-assembled mesoporous Al_2O_3 spherical nanoparticles and their efficiency for the removal of arsenic from water. *J Hazard Mater* 201:170–177
159. Wang X, Zhan C, Kong B, Zhu X, Liu J, Xu W, Cai W, Wang H (2015) Self-curved coral like Al_2O_3 nanoplates for use as an adsorbent. *J Colloid Interface Sci* 453:244–251
160. Nguyen TMT, Do TPT, Hoang TS, Nguyen NV, Pham HD, Nguyen TD, Pham TNM, Le TS, Pham TD (2018) Adsorption of anionic surfactants onto alumina: characteristics, mechanisms, and application for heavy metal removal. *Int J Polym Sci* 2830286(11)
161. Pham T D, Tran T T, Le V A, Pham T T, Dao T H, Le T S (2019) Adsorption characteristics of molecular oxytetracycline onto alumina particles: the role of surface modification with an anionic surfactant. *J Mol Liquids* 287:110900
162. Pham T, Do TU, Pham TT, Nguyen TAH, Nguyen TKT, Vu ND, Le TS, Vu CM, Kobayashi M (2019) Adsorption of poly (styrenesulfonate) onto different-sized alumina particles: characteristics and mechanisms. *Colloid Polym Sci* 297:13–22

163. Ghaemi N (2016) A new approach to copper ion removal from water by polymeric nanocomposite membrane embedded with γ -alumina nanoparticles. *Appl Surface Sci* 364:221–228
164. Chu TPM, Nguyen NT, Vu TL, Dao TH, Dinh LC, Nguyen HL, Hoang TH, Le TS, Pham TD (2019) Synthesis, characterization, and modification of alumina nanoparticles for cationic dye removal. *Mater* 12:450
165. Ali S, Abbas Y, Zuhra Z, Butler IS (2019) Synthesis of γ -alumina (Al_2O_3) nanoparticles and their potential for use as an adsorbent in the removal of methylene blue dye from industrial wastewater. *Nanoscale Adv* 1:2–13
166. Banerjee S, Dubey S, Gautam RK, Chattopadhyaya MC, Sharma YC (2019) Adsorption characteristics of alumina nanoparticles for the removal of hazardous dye, Orange G from aqueous solutions. *Arab J Chem* 12(8):5339–5354
167. Huang CC, Lo SL, Lien HL (2015) Vitamin B_{12} -mediated hydro dechlorination of dichloromethane by bimetallic Cu/Al particles. *Chem Eng J* 273:413–420
168. Wang HW, Peng P, Fennell DE (2015) Rapid dechlorination of 1,2,3,4-TCDD by Ag/Fe bimetallic particles. *Chem Eng J* 273:465–471
169. Hong HJ, Farooq W, Yang JS, Yang JW (2010) *Separ Sci Technol* 45(688):1975–1981
170. Chen LH, Huang CC, Lien HL (2008) Bimetallic iron–aluminum particles for dechlorination of carbon tetrachloride. *Chemosphere* 73:692–697
171. Lin CJ, Liou YH, Lo SL (2009) Supported Pd/Sn bimetallic nanoparticles for reductive dechlorination of aqueous trichloroethylene. *Chemosphere* 74(2):314–319
172. Ma L, Ding Z, Gao T, Zhou R, Xu W, Liu J (2004) Discoloration of methylene blue and wastewater from a plant by a Fe/Cu bimetallic system. *Chemosphere* 55(9):1207–1212
173. Fang W, Xu C, Zheng J, Chen G, Jiang K (2015) Fabrication of Cu–Ag bimetal nanotube-based copper silicates for enhancement of antibacterial activities. *RSC Adv* 5(694):39612–39619
174. Zhang Z, Shen Q, Cissoko N, Wo J, Xu X (2010) Catalytic dechlorination of 2,4-dichlorophenol by Pd/Fe bimetallic nanoparticles in the presence of humic acid. *J Hazard Mater* 182(867):252–258
175. Choi JH, Kim YH (2009) Reduction of 2, 4, 6-trichlorophenol with zero-valent zinc and catalyzed zinc. *J Hazard Mater* 166:984–991
176. Yang B, Deng S, Yu G, Lu Y, Zhang H, Xiao J, Chen G, Cheng X, Shi L (2013) Pd/Al bimetallic nanoparticles for complete hydro dechlorination of 3-chlorophenol in aqueous solution. *Chem Eng J* 219:492–498
177. Lin Y, Shih, Mac Farlane J (2015) Amphiphilic compounds enhance the dechlorination of pentachlorophenol with Ni/Fe bimetallic nanoparticles. *Chem Eng J* 262:59–67
178. Nagpal V, Bokare AD, Chikate RC, Rode CV, Paknikar KM (2010) Reductive dechlorination of γ -hexachlorocyclohexane using Fe–Pd bimetallic nanoparticles. *J Hazard Mater* 175:680–687
179. Bleyl S, Kopinke FD, Mackenzie K (2012) Carbo-Iron Synthesis and stabilization of Fe(0)-doped colloidal activated carbon for in situ groundwater treatment. *Chem Eng J* 191:588–595
180. DeVor R, Knighton KC, Aitken B, Maloney P, Holland E, Talalaj L, Fidler ES, Clausen CA, Geiger CL (2008) Dechlorination comparison of mono-substituted PCBs with Mg/Pd in different solvent systems. *Chemosphere* 73:896–900
181. Yang B, Zhang Y, Deng S, Yu G, Lu Y, Wu J, Xiao J, Chen G, Cheng X, Shi L (2013) Reductive degradation of chlorinated organic pollutants-contaminated water by bimetallic Pd/Al nanoparticles: effect of acidic condition and surfactants. *Chem Eng J* 234:346–353
182. Agarwal S, Al-Abed SR, Dionysiou DD (2009) Impact of organic solvents and common anions on 2-chlorobiphenyl dechlorination kinetics with Pd/Mg. *Appl Catal B: Environ* 92:17–22
183. Yang B, Deng S, Yu G, Zhang H, Wu J, Zhuo Q (2011) Bimetallic Pd/Al particles for highly efficient hydrodechlorination of 2-chlorobiphenyl in acidic aqueous solution. *J Hazard Mater* 189:76–83
184. Kuang Y, Du J, Zhou R, Chen Z, Megharaj M, Naidu R (2015) Calcium alginate encapsulated Ni/Fe nanoparticles beads for simultaneous removal of Cu (II) and monochlorobenzene. *J Colloid Interface Sci* 447:85–91

185. Weng X LS, Zhong Y, Chen Z (2013) Chitosan stabilized bimetallic Fe/Ni nanoparticles used to remove mixed contaminants-amoxicillin and Cd (II) from aqueous solutions. *Chem Eng J* 229:27–34
186. Huguet MR, Marshall WD (2009) Reduction of hexavalent chromium mediated by micro- and nano-sized mixed metallic particles. *J Hazard Mater* 169:1081–1087
187. Kadu BS, Sathe YD, Ingle AB, Chikate RC, Patil KR, Rode CV (2011) Efficiency and recycling capability of montmorillonite supported Fe–Ni bimetallic nanocomposites towards hexavalent chromium remediation. *Appl Catal B Environ* 104:407–414
188. Zhang G, Qu J, Liu H, Liu R, Wu R (2007) Preparation and evaluation of a novel Fe–Mn binary oxide adsorbent for effective arsenite removal. *Water Res* 41:1921–1928
189. Cheng Z, Fu F, Dionysiou DD, Tang B (2016) Adsorption, oxidation, and reduction behavior of arsenic in the removal of aqueous As (III) by mesoporous Fe–Al bimetallic particles *Water Res* 96:22–31
190. Bokare AD, Chikate RC, Rode CV, Paknikar KM (2008) Iron-nickel bimetallic nanoparticles for reductive degradation of azo dye Orange G in aqueous solution. *Appl Catal B Environ* 79:270–278
191. Ma LM, Ding ZG, Gao TY, Zhou RF, Xu WY, Liu J (2004) Discoloration of methylene blue and wastewater from a plant by a Fe/Cu bimetallic system. *Chemosphere* 55:1207–1212
192. Gautam R K, Rawat V, Banerjee S, Sanroman MA, Soni S, Singh SK, Chattopadhyaya MC (2015) Synthesis of bimetallic Fe–Zn nanoparticles and its application towards adsorptive removal of carcinogenic dye malachite green and Congo red in water. *J Mol Liq* 212:227–236